Searching for cosmological B-modes in the presence of astrophysical contaminants and instrumental effects

Clara Vergès

Université de Paris
École doctorale 560 STEP'UP
Laboratoire AstroParticule & Cosmologie

Searching for cosmological B-modes in the presence of astrophysical contaminants and instrumental effects

Thèse de doctorat de **Physique de l'Univers**

par
Clara **Vergès**
dirigée par
Dr. Radek **Stompor**

présentée et soutenue publiquement le
18 septembre 2020

devant un jury composé de

Pr. Danièle Steer (APC)	Présidente
Dr. Sophie Henrot-Versillé (IJC Lab)	Rapporteure
Dr. Nicolas Ponthieu (IPAG)	Rapporteur
Pr. Joanna Dunkley (Princeton University)	Examinatrice
Dr. Tomotake Matsumura (Kavli IPMU)	Examinateur
Dr. Radek Stompor (APC)	Directeur de thèse
Dr. Josquin Errard (APC)	Co-encadrant de thèse

Il se tint immobile, face au ciel renversé, plein de lune et d'étoiles.
Albert Camus, *La Peste*

Acknowledgements

First of all, I would like to thank my two advisers, Josquin Errard and Radek Stompor, for supervising my work over the last three years. I am very grateful for everything you have taught me and helped me accomplish. I have learned much more with you than just CMB science, and this thesis would not have been the same without your advice and support.

I thank Sophie Henrot-Versillé and Nicolas Ponthieu who have agreed to report on this thesis. Thanks to your careful reading of my work, you have given valuable advice and contributed much to the improvement of this manuscript. Thank you to the president of the jury, Danièle Steer, and to Joanna Dunkley and Tomotake Matsumura for accepting to be examiners of my work.

Thanks a lot to our group at APC and the POLARBEAR Europe group — Dominic Beck, Carlo Baccigalupi, Hamza El Bouhargani, Giulio Fabbian, Aygul Jamal, Baptiste Jost, Nicoletta Krachmalnicoff, Maude Le Jeune, Clément Leloup, Julien Peloton, Davide Poletti and Giuseppe Puglisi — for all the good times we spent together, in and outside the lab, during trips and meetings, in the US or elsewhere! Thank you to all the members of the POLARBEAR/Simons Array collaboration for introducing me to both hardware and data analysis aspects of the project, and for welcoming me in Berkeley and in Chile, in particular Darcy Barron, Shawn Beckman, Yuji Chinone, Neil Goeckner-Wald, John Groh, Charlie Hill, Adrian Lee, Lindsay Lowry, Toki Suzuki, Calvin Tsai and Ben Westbrook. Thank you to Maximilian Abitbol, David Alonso, Kevin T. Crowley and Max Silva-Feaver from the Simons Observatory collaboration for our useful discussions.

I spent three great years at APC, thanks to my colleagues (in particular the Cosmology group), administrative staff and IT team. Thanks and best wishes to all the fellow and former graduate students for the good moments we shared, from the ministry canteen to ski slopes in La Thuile and the beach in Biarritz: Marc, Bastien, Pierre A., Jean-Baptiste, Ranajoy, Cyrille, Thuong, Jie, Thomas, Gabriel, Louise M., Calum, Leandro, Hugo, Guillaume, Alexandre and Tuan. Special thanks to Philippe B., Dimitri and Marion for our endless discussions and coffee breaks!

Thank you to Paola Andreani, with whom I learned the first steps of observational cosmology, and to Matt Dobbs, who taught me the basics of instrumentation and readout electronics.

Throughout all my years of study, I have had the opportunity to meet great teachers, and I would especially like to thank Mmes Cacheux, Doukhan, Lebrun and Tardiveau and M. Ravier: you taught me much more than just your academic subjects.

A huge thank you to Louise B.: from being disasters in lab work (ok, it was mostly my fault!) to whale watching in Canada and cycling in Scotland under the rain, you are never far away and I don't know how I would get along without you. Thanks a lot to Antoine P.: I love sharing passionate discussions, copious meals mostly based on homemade hummus and improbable journeys with you

(the best ones will always be to cycle across Paris by night!). Thanks a lot to Matthieu and Geoffrey, your support during this thesis was precious.

Thank you to Antoine B., Jules, Maxime, Gaëtan, Grégoire L. C., Denis, José, Gautier, Antoine S. and Dhruv: whether it is to share a good meal, go hiking, or help me debug my code, I know I can always count on you! Speaking of coding... thank you to Augustin, Camille and the rest of the team for always helping me whenever I had stupid Python/Git/Latex/Unix questions! Many thanks to my friends in the Bay Area, Louise F., Pierre L., Pierre N. and Geoffrey, for their warm welcome every time I was there. Thank you to all my friends for the good moments we shared over the years: Uriel, Gwladys and Gwendoline; Éric, Quentin and Philippe R.; Claire, Mathilde and Yann; Julie-Anne, Jiliane, Clément C., Grégoire D., Baptiste K., Louise K., Philippe L., Paul, Louis, Pierre L., Héloïse and Sonia.

Many thanks to my family, especially to my parents and my brother. I would like to dedicate this work to my parents, for their constant love, support and encouragement. I will always be grateful for everything you did for me, you have always encouraged me to pursue my dreams, and without you I would not have achieved this.

Abstract

Cosmology has known a considerable surge in the past twenty years and is now well established as a precision science. Accurate measurements of temperature anisotropies of the Cosmic Microwave Background (CMB) opened an unprecedented window on the primordial Universe. Furthermore, the existing measurements of CMB polarisation anisotropies have confirmed our understanding of early universe physics, and provided important consistency tests of the currently popular models. The next frontier in CMB science is the precise mapping of polarisation anisotropies, and the detection of a specific signature in the polarisation signal, the primordial B-modes. These observations will allow us to push further our knowledge of the Universe and its best-kept secrets, such as dark energy, dark matter and inflation.

This detection is particularly challenging, as the signal we look for is very low, and shadowed by various sources of galactic and extra-galactic contamination: polarised dust, synchrotron radiation and weak gravitational lensing - to name a few. The next generation of CMB polarisation experiments therefore needs not only to reach an unprecedented raw instrumental sensitivity, but also to be able to distinguish the signal from these contaminations. This calls for enhanced detection capabilities, new technologies, as well as novel data analysis methods.

This work focuses on understanding whether this increased complexity of CMB experiments will effectively lead to better performances, and at which cost regarding the control of systematic effects. I develop new, involved data models taking into account various instrumental parameters to ensure a better modelling of instrumental systematic effects, in the context of new generation CMB polarisation experiments - POLARBEAR/Simons Array and the Simons Observatory. To prepare for future experiments, I propose an extension of component separation forecasting framework to take into account instrumental systematic effects. I demonstrate its capabilities as a key tool for forecasting the performance of future experiments, and inform calibration strategies to achieve the required performance.

Keywords Cosmology; Cosmic Microwave Background; Instrument model; Component separation.

Résumé

La cosmologie a connu un essor considérable au cours des vingt dernières années, et a désormais acquis le statut de science de précision. Les mesures précises des anisotropies de température du fond diffus cosmologique (*Cosmic Microwave Background* - CMB) ont ouvert une fenêtre sans précédent sur l'Univers primordial, tandis que les mesures des anisotropies de polarisation du CMB ont confirmé notre compréhension de la physique de l'Univers primordial. Ces différents résultats ont notamment permis de vérifier la cohérence et de tester la validité des modèles actuels. La prochaine étape dans l'observation du CMB est la cartographie précise des anisotropies de polarisation, et en particulier la détection d'une signature spécifique dans ce même signal, les modes B primordiaux. Ces observations nous permettront de pousser toujours plus loin notre connaissance de l'Univers et de ses secrets les mieux gardés, en particulier l'énergie noire, la matière noire et l'inflation.

Cette détection est cependant particulièrement difficile, car le signal recherché est très faible, et écranté par plusieurs sources de contamination galactiques et extra-galactiques : émission polarisée de la poussière, rayonnement synchrotron ou encore effet de lentillage gravitationnel faible, pour n'en citer que quelques-unes. La prochaine génération d'expériences d'observation de la polarisation du CMB doit donc non seulement atteindre une sensibilité instrumentale brute sans précédent, mais également être capable de distinguer le signal de ces contaminations. Cela nécessite des capacités de détection améliorées, de nouvelles technologies, ainsi que de nouvelles méthodes d'analyse des données.

L'objectif du travail présenté dans cette thèse est d'évaluer, pour certains effets, si cette complexité accrue des expériences d'observation du CMB conduira effectivement à de meilleures performances, et à quel coût en ce qui concerne le contrôle des effets systématiques. Je développe de nouveaux modèles de données prenant en compte divers paramètres instrumentaux pour assurer une meilleure modélisation des effets systématiques pour la nouvelle génération d'expériences de mesure de la polarisation du CMB: POLARBEAR/Simons Array et Simons Observatory. Pour préparer ces futures expériences, je propose une extension des méthodes de séparation de composantes afin de prendre en compte les effets systématiques instrumentaux. Je démontre également les possibilités de ce nouvel outil pour prévoir les performances des futures expériences, et aider à l'établissement des stratégies de calibration afin d'atteindre les performances requises.

Mots-clefs Cosmologie; Fond diffus cosmologique; Modélisation instrumentale; Séparation de composantes.

Contents

Note on units

Throughout this manuscript, and unless otherwise specified, we adopt Planck units and therefore assume that the speed of light in vacuum c, the gravitational constant G, the Boltzmann constant k_B, and the reduced Planck constant $\hbar$ are all equal to 1.

CHAPTER 1

Cosmology

Contents

The 20th century saw the birth of modern physics. During the first decades of the century, two new theoretical framework emerged, that changed the way we do physics: quantum mechanics and general relativity. While quantum mechanics describes the fundamental constituents of matter and their interactions, general relativity aims at describing gravity, and forecasting large structures evolution.

Developed by Albert Einstein in the 1910's, the theory of general relativity was applied to Universe's modelling and evolution: this was the birth of modern

cosmology [90]. Shortly after, in the 1930s, a new model for Universe's past and evolution emerged: the Big Bang scenario.

The purpose of this chapter is to review the theoretical tools needed in cosmology. In section 1.1, I start from first principles and describe the framework of general relativity, before I take you through the timeline of the Universe in section 1.2, from the Big Bang to present time. Last but not least, I review in section 1.3 the theoretical basis of inflation theories, and their importance for cosmology.

This theoretical background is broadly based on the following resource books and lecture notes:

- *Principes de la cosmologie*, James Rich (adapted to French by Jean-Louis Basdevant), Éditions de l'École polytechnique (2011);
- *Cosmologie primordiale*, Patrick Peter & Jean-Philippe Uzan, Belin (2012);
- *Géométrie et gravitation*, lecture notes by David Langlois, École polytechnique (2012).

1.1 From general relativity to cosmology

1.1.1 The expanding Universe

Friedmann-Lemaître-Robertson-Walker metrics

Following general relativity geometric description of space-time, the Universe is described by a Riemanian manifold with a space-time metric g written as (with the signature convention $(-,+,+,+)$):

$$\mathrm{g} = g_{\mu\nu} dx^\mu dx^\nu. \tag{1.1}$$

The description of the Universe by general relativity assumes the cosmological principle: the Universe is homogeneous and isotropic, which is the basis postulate of physical cosmology. Homogeneity assures that the Universe is the same in all locations (same properties and same physics law), and isotropy that it has the same structure regardless of the observed direction. Thanks to precision measurement of the Cosmic Microwave Background (CMB) in the second half of the 20^{th} century, the cosmological principle has been confirmed within our observable horizon, but there are no ways of confirming it beyond this scale.

The space-time metric compatible with homogeneity and isotropy can be written under the generic form of:

$$\mathrm{g} = -dt^2 + a^2(t) \left[\frac{dr^2}{1-kr^2} + r^2(d\theta^2 + \sin^2\theta d\phi^2) \right], \tag{1.2}$$

where t is the time coordinate and (r, θ, ϕ) are the three spatial spherical coordinates.

These metrics form a family known as Robertson - Walker metrics. Their parameters are the curvature k, and the scale factor as a function of time $a(t)$. The curvature describes the geometry of space : $k = 0$ for flat space, $k = 1$ for spherical space, and $k = -1$ for hyperbolic space. The scale parameters measures how the distance between two regions of space evolves.

Comoving coordinates

Indeed, as it has been demonstrated by Lemaître and Hubble (see below), the Universe is expanding, and thus distances between objects vary with time, as quantified by the scale factor. In these particular conditions, coordinates and reference frame as used on Earth are not appropriate to describe the Universe at large scales. A reference frame is defined by one time coordinate, and three space coordinates. The proper time is defined as the time measured by an observer in the reference frame where they are at rest. From the metric in Eq. (1.1), the square of this proper time is written as

$$d\tau^2 = -g_{\mu\nu}dx^\mu dx^\nu. \tag{1.3}$$

In cosmology, such a coordinate system is thus not appropriate. If we consider in particular a distant object, the photons received from it were emitted before this object can receive any photons from us. The distance can therefore not be estimated by measuring the flight time of photons.

We define a new reference frame, called comoving coordinates, where each object has fixed space coordinates, independent of time, and time coordinates following Universe's expansion. A popular image describes comoving coordinates as an expandable grid, where galaxies and objects would be attached to grid intersections. If the distance between two objects is three tiles, even if the grid is expanded and the physical distance between the two objects increases, the comoving distance, i.e. the number of tiles between the two objects, remains the same.

Redshift

The expansion of the Universe thus cause distant objects to move away from each other at cosmological scales. Looking for example at distant galaxies, one can observe their cosmological redshift due to expansion. In classical physics, the redshift is due to the Doppler-Fizeau effect, which affects the wavelength of a moving object with respect to the observer. In cosmology, objects are not moving in the comoving coordinate frame, but the cosmological redshift has a similar effect on wavelength than the classic one. The cosmological redshift z is defined as:

$$1 + z \equiv \frac{\nu_e}{\nu_r}, \tag{1.4}$$

with ν_e (resp. ν_r) the emission (resp. reception) frequency.

From the FLRW metric of Eq. (1.2), the relation between redshift and the scale factor can be derived. Let us consider two photons emitted at t_e and $t_e + \delta t_e$ (for example by a galaxy), and received at t_r and $t_r + \delta t_r$ by a comoving observer. For a light wave, the geodesic equation derived from Eq. (1.2) describes a radial trajectory:

$$d\tau^2 = 0 = -dt^2 + \frac{a(t)^2 dr^2}{1 - kr^2}, \tag{1.5}$$

therefore, because the comoving path is the same for the two photons,

$$\int_0^{r_e} \frac{dr}{\sqrt{1-kr^2}} = \int_{t_e}^{t_r} \frac{dt}{a(t)} = \int_{t_e+\delta t_e}^{t_r+\delta t_r} \frac{dt}{a(t)}. \tag{1.6}$$

This leads to:

$$\int_{t_e}^{t_e+\delta t_e} \frac{dt}{a(t)} = \int_{t_r}^{t_r+\delta t_r} \frac{dt}{a(t)}. \tag{1.7}$$

For a very short period of time, the scale factor a can be assumed constant, which leads to:

$$\frac{\delta t_e}{a_e} = \frac{\delta t_r}{a_r}. \tag{1.8}$$

We apply this relation to an electromagnetic wave of frequency ν_e at emission:

$$\frac{\nu_e}{\nu_r} = \frac{a_r}{a_e}. \tag{1.9}$$

If we consider the time of reception to be the current epoch, where $a_r = a_0$, we finally derive the relation between redshift and the scale factor:

$$\frac{a_0}{a_e} = \frac{\nu_0}{\nu_r} = 1 + z. \tag{1.10}$$

This relationship is central in cosmology as it allows to probe Universe's expansion through physical redshift measurements.

Hubble-Lemaître law

In particular, it is by measuring the apparent recessing speed of distant galaxies using their cosmological redshift as defined in Eq. (1.10) that the first observational evidence of the expansion of the Universe was uncovered. Let us consider two infinitesimally small objects with constant comoving coordinates. The comoving distance between these two objects can be written as:

$$dl = \sqrt{\frac{dr^2}{1-kr^2} + r^2(d\theta^2 + \sin^2\theta d\phi^2)}. \tag{1.11}$$

This distance does not depend on time. However, the physical distance D given by the metric g depends on time through the scale factor:

$$\mathrm{D}(t) = a(t)\, dl. \tag{1.12}$$

The apparent relative speed between the two objects can therefore be defined as:

$$v = \frac{d\mathrm{D}}{dt} = \dot{a}\, dl. \tag{1.13}$$

This speed is therefore proportional to the physical distance D:

$$v = \frac{\dot{a}}{a}\mathrm{D}. \tag{1.14}$$

This relationship was first postulated and published in French in 1927 by the Belgian canon Georges Lemaître [160]. However, it is not until 1929 and its independent discovery by the American astronomer Edwin Hubble that it became widely known [131]. We introduce here the Hubble parameter:

$$H \equiv \frac{\dot{a}}{a}, \tag{1.15}$$

The Hubble-Lemaître law then reads as

$$v = H\, D. \tag{1.16}$$

This law states that the recessing speed of a galaxy, v, is proportional to its distance D through a parameter that depends on the expansion rate, the Hubble parameter H. As we detail hereafter, this parameter is of central significance in cosmology to study the local dynamics of our Universe.

1.1.2 Einstein's equations

Now that we have a metric to describe the geometry of the expanding Universe (the FLRW metric), the next step is to have an equation to relate this geometry to the matter and energy content of the Universe. This relationship is given by the Einstein field equation[1] [90]:

$$G_{\mu\nu} \equiv R_{\mu\nu} - \frac{1}{2} g_{\mu\nu} \mathcal{R} = \frac{8\pi G}{c^4} T_{\mu\nu} \tag{1.17}$$

On the left-hand side of Eq. (1.17), $G_{\mu\nu}$ is the Einstein tensor, and contains information about the geometry of the Universe:

- $R_{\mu\nu}$ is the Ricci tensor, a contraction of the Riemann curvature tensor[2];
- $\mathcal{R} \equiv g^{\mu\nu} R_{\mu\nu}$ is the Ricci scalar, contraction of the Ricci tensor.

The right-hand side of Eq. (1.17) describes the matter and energy content of the Universe:

- G is the gravitational constant. The $8\pi G$ factor assures that Einstein's equations are equivalent to Poisson equation in the limit of Newtonian mechanics;
- $T_{\mu\nu}$ is the stress-energy tensor, containing information about energy density and its flux, and momentum and its flux.

The local conservation of the energy-momentum in a curved space-time requires:

$$\nabla_\mu T^\mu_\nu = 0, \tag{1.18}$$

[1] We drop Planck units in this equation.

[2] The Riemann curvature tensor for vector fields u, v and w is defined as $R(u,v)w = \nabla_u \nabla_v w - \nabla_v \nabla_u w - \nabla_{[u,v]} w$. It expresses the curvature of a Riemannian manifold. In particular, if u and v are coordinate vector fields, their Lie bracket $[u,v]$ is zero, and the Riemann curvature measures the non-conductivity of the covariant derivative.

where ∇_μ denotes a covariant derivative, which generalises the usual derivative for a curved space-time.

Because we assume the Universe to be homogeneous and isotropic according to the cosmological principle, pressure p and energy density ρ can depend only on time. If we assume a perfect fluid at equilibrium, the energy-momentum tensor can then be written as:

$$T^\mu_\nu = \begin{pmatrix} -\rho(t) & 0 & 0 & 0 \\ 0 & p(t) & 0 & 0 \\ 0 & 0 & p(t) & 0 \\ 0 & 0 & 0 & p(t) \end{pmatrix} \tag{1.19}$$

Moreover, historically, Einstein introduced the so-called cosmological constant Λ in his general relativity equations to account for a static Universe, which was the observational paradigm at that time. Since the covariant derivative of the metric is still zero, the local energy conservation in Eq. (1.18) still stands with this addition:

$$G_{\mu\nu} + \Lambda g_{\mu\nu} = 8\pi T_{\mu\nu}. \tag{1.20}$$

As it was later observed in the late 1920s, the Universe is actually expanding, which makes the cosmological constant apparently pointless. Einstein even declared than this was his "biggest blunder". However, the observation of the accelerated expansion of the Universe in the 1990s renewed the interest in the cosmological constant, which is now interpreted as the manifestation of dark energy. Physical interpretations of the cosmological constant are discussed in section 1.1.4.

1.1.3 Friedmann-Lemaître equations

We now use Einstein's equations to combine the geometrical description of the Universe by the FLRW metric, with its matter and energy content described by the energy impulsion tensor. We first compute the Ricci tensor associated with the FLRW metric:

$$R_{\mu\nu} = a^2 \left(\frac{\ddot{a}}{a} + 2\frac{\dot{a}^2}{a^2} + 2\frac{k}{a^2} \right) g_{\mu\nu}, \tag{1.21}$$

and we can finally deduce the Friedmann - Lemaître equations from Eq. (1.19 - 1.20 - 1.21) [103]:

$$\left(\frac{\dot{a}}{a}\right)^2 + \frac{k}{a^2} = \frac{8\pi\rho}{3}, \tag{1.22}$$

$$-2\frac{\ddot{a}}{a} - \left(\frac{\dot{a}}{a}\right)^2 - \frac{k}{a^2} = 8\pi p \tag{1.23}$$

This set of equations is the basic tool for describing the expansion and evolution of the Universe on cosmological scales.

Equations of state

In particular, by combining the two Friedman-Lemaître equations, a continuity relation between pressure and energy density is obtained:

$$\dot{\rho} + 3\frac{\dot{a}}{a}(\rho + p) = 0 \tag{1.24}$$

To solve this equation, we consider a state equation of the generic form of:

$$p = w\rho, \tag{1.25}$$

where w can take the following values depending on the type of matter:

- $w = \frac{1}{3}$ for relativistic particles and radiation;
- $w = 0$ for non relativistic particles.

By integrating Eq. (1.24) between an arbitrary epoch and the current one (denoted with the subscript 0), one obtains:

$$\rho = \rho_0 \left(\frac{a}{a_0}\right)^{-3(1+w)}. \tag{1.26}$$

Together with Friedmann-Lemaître equations, the evolution of the scale factor with time is expressed as:

$$a(t) = a_0 \left(\frac{t}{t_0}\right)^{\frac{2}{3(1+w)}}. \tag{1.27}$$

Depending on the type of matter dominating the Universe, and its associated parameter w, the expansion of the Universe will thus undergo different regimes, as mentioned hereafter.

What about the cosmological constant?

The treatment of the cosmological constant in Einstein's equations is subject to many interpretations. One possible treatment is to move the cosmological constant term on the right-hand side of Eq. (1.20):

$$\begin{aligned} G_{\mu\nu} &= 8\pi \left(T_{\mu\nu} - \frac{\Lambda}{8\pi} g_{\mu\nu}\right) \\ &\equiv 8\pi \left(T_{\mu\nu}^{\text{matter}} + T_{\mu\nu}^{\text{vacuum}}\right) \end{aligned} \tag{1.28}$$

The cosmological constant would therefore be equivalent to an extra term in the energy-momentum tensor, associated with a negative pressure, or $w = -1$. This term is believed to be responsible for the accelerated expansion of the Universe, and this interpretation is discussed further in section 3.

1.1.4 The standard cosmological model

The Friedmann-Lemaître equations provide a good framework for describing the evolution of the Universe, and from this set of equations one can define several parameters that describe this evolution. In this section, I first introduce the parameters that form the so-called standard cosmological model, and then phenomenological, model-independent parameters, commonly used to describe the content and evolution of the Universe. I finally explore the content of the Universe from an observer's perspective.

The values of the cosmological parameters have been determined with high precision by CMB measurements, starting with COBE (Cosmic Background Explorer) in the 1990s, then WMAP (Wilkinson Microwave Anisotropies Probe) in the 2000s, and ultimately Planck, between 2009 and 2013. Unless otherwise specified, the values of the parameters quoted in this section are taken from the Planck 2018 data release [215].

The base ΛCDM model

From the perspective of the FLWR model, a set of key parameters has been introduced, which capture most of the evolution of the Universe. The current consensus model is called the ΛCDM model, including both the cosmological constant Λ and cold dark matter (CDM) in its description of the Universe. The minimal model requires a set of six parameters, that can be deduced from various observational probes such as CMB, supernovae and galaxy clusters. The model can also be extended with more parameters, such as the Hubble constant or the deceleration parameter, to account for more complex processes.

The six canonical parameters are:

- the physical baryon density, $\Omega_b h^2$: measures the abundance of baryons that form ordinary matter (see details hereafter);
- the physical dark matter density, $\Omega_{\mathrm{CDM}} h^2$: measures the abundance of cold dark matter, a form of matter interacting only through gravitation and not through other interactions, at least as far as we have been able to estimate (see details hereafter);
- the acoustic scale, $\theta_\star$: defined as $\theta_\star \equiv \frac{r_\star}{D}$, where $r_\star$ is the comoving sound horizon at recombination (see section 2.2), and D the comoving angular diameter distance to the last scattering surface;
- the optical depth to recombination, τ: quantifies the scattering of light beams between the observer and the last scattering surface;
- the fluctuation amplitude of the power spectrum, A_s: defines the amplitude of density fluctuations in the primordial Universe;
- the scalar spectral index, n_s: describes the shape of the power spectrum. n_s = 1 corresponds to a flat, scale invariant power spectrum.

Combined with other cosmological probes, the measurements of the CMB power spectrum by Planck provide the current best measurements of these parameters, as shown in Table 1.1.

ΛCDM parameter	Planck 2018 best fit value
$\Omega_b h^2$	0.02242 ± 0.00014
$\Omega_{\rm CDM} h^2$	0.11933 ± 0.00091
$100\ \theta_\star$	1.04101 ± 0.00029
τ	0.0561 ± 0.0071
$\ln(10^{10} A_s)$	3.047 ± 0.014
n_s	0.9665 ± 0.0038

Table 1.1 – Values of base-ΛCDM parameters [215]

Cosmological observables

In addition to the 6 basis cosmological parameters, it is common to defined additional parameters to describe the content and evolution of the Universe.

Hubble constant The Hubble parameter H introduced in section 1.1.1 quantifies the expansion rate of the Universe at a given time. Measured today, it is referred to as H_0, the Hubble constant, expressing the current expansion rate of the Universe:

$$H_0 = \frac{\dot{a}_0}{a_0}. \tag{1.29}$$

It is also useful to define the reduced Hubble constant:

$$h = \frac{H_0}{100 \mathrm{km/s/Mpc}}. \tag{1.30}$$

The value of the Hubble constant is one of the key measurements of the standard cosmological model. The latest result derived from the CMB measurements by Planck estimates its value at:

$$H_0 = 67.66 \pm 0.42\,\mathrm{km/s/Mpc}. \tag{1.31}$$

However, other measurement methods show a tension between the cosmological measurement by Planck and the estimation using local objects. This tension has been growing over the past five years, as it is summarised in Figure 1.1.

The most recent results derived from cepheids[3] observed with the Hubble Space Telescope [228] lead to:

$$H_0 = 73.24 \pm 1.74\,\mathrm{km/s/Mpc}, \tag{1.32}$$

the observation of type Ia supernovae [30] (see section 3.2.1) to:

$$H_0 = 68.1 \pm 1.27\,\mathrm{km/s/Mpc}, \tag{1.33}$$

and the analysis of time-delays in quasars to [283]:

$$H_0 = 73.3^{+1.7}_{-1.8}\,\mathrm{km/s/Mpc}. \tag{1.34}$$

There is thus an important tension on H_0 measurements, and many scenarios

[3] Cepheids are variable stars whose relationship between period and luminosity is known, which allows for distance measurements, as detailed in section 3.2.1.

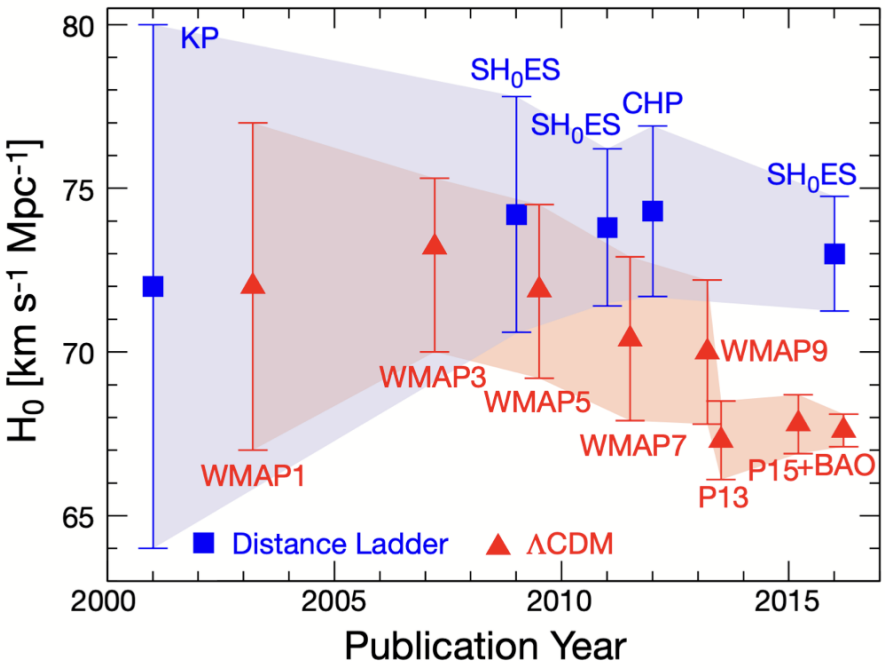

Figure 1.1 – History of H_0 measurements by two classes of method: values from astrophysical objects distance measurement in blue (cepheids, SN or quasars), and CMB-derived values in red. P13 and P15 refer to Planck data, and WMAP to the WMAP satellite, Planck's predecessor.
Credit: W. Hu

are considered to relieve it. In particular, the Hubble constant derived from CMB measurements is deduced from two other quantities: the sound horizon in the early Universe, and the angular distance diameter to the last scattering surface. The scenarios proposed to solve the tension between local and cosmological measurements are either early-time scenarios [29, 36, 221], which modify the sound horizon, or late-time scenarios [77, 78, 199, 276], which modify the dynamic of Universe expansion and therefore the angular distance diameter. The discrepancy could also arise from astrophysical biases in the determination of distances for type Ia supernovae [229].

Expected results in the coming years should help distinguish between these scenarios and solve the Hubble tension. The detection and measurement of the CMB polarisation B-modes power spectrum will help constraining the cosmology of the early Universe, in particular the sound horizon [134]. The increasing number of gravitational wave events detection will also put tighter constraints on the Hubble constant [51].

Deceleration parameter Combining the Friedmann-Lemaître equations Eq. (1.22 - 1.23), one obtains an equation describing the deceleration of the Universe expansion:

$$\frac{\ddot{a}}{a} = \frac{-4\pi G}{3}(\rho + 3p) \tag{1.35}$$

Expressed at t_0 (today), this defines the deceleration parameter q_0:

$$q_0 \equiv -\frac{1}{H_0^2}\frac{\ddot{a}_0}{a_0} \tag{1.36}$$

In the 1990's, two competing teams - one led by Saul Perlmutter and the other one by Adam Riess and Brian Schmidt - were trying to measure this deceleration parameter using type Ia supernovae observations, convinced that Universe's expansion was actually decelerating. This outcome was then considered as the only possible one, given the energy content of the Universe. However, the two teams measured negative deceleration parameters [227, 205]... which means that the expansion of the Universe is actually accelerating!

As for H_0 measurements, there is a tension between values of the deceleration parameter derived from local measurements and the ones derived from CMB observations. While Planck measures $q_0 \sim -0.55$ [215], results from type Ia supernovae leads to $q_0 = -1.08 \pm 0.29$ [46], which represents a 4.5σ discrepancy. Future H_0 measurements with new methods like gravitational waves should help alleviate this tension.

Densities The Universe is composed of several species contributing significantly to the energy and pressure density, and each of them contributes to the dynamics of the Universe, following Friedmann-Lemaître equations as described in section 1.1.3. To be able to compare the relative importance of the species, a critical energy density is introduced, which corresponds to the density of the flat Universe:

$$\rho_{\text{crit}} \equiv \frac{3H_0^2}{8\pi}, \tag{1.37}$$

and the ratio of energy density for a given species relative to this critical energy density, at the current epoch is defined as:

$$\Omega_i \equiv \frac{\rho_0^i}{\rho_{\text{crit}}} \tag{1.38}$$

This parameter is called the density parameter for a given species. Measurements of densities parameters for various species are detailed hereafter.

We rewrite the first Friedmann-Lemaître equation Eq. (1.22) to highlight the contributions of the various species to the Universe's dynamic:

$$\left(\frac{\dot{a}}{a}\right)^2 = H_0^2 \sum_i \Omega_i \left(\frac{a}{a_0}\right)^{-3(1+w_i)} - \Omega_k \left(\frac{a}{a_0}\right)^{-2}, \tag{1.39}$$

where a density term associated to the space curvature k has been introduced:

$$\Omega_k \equiv \frac{k}{a_0^2 H_0^2} \tag{1.40}$$

Except Ω_k, other densities refer to physical species, and the total density parameter is defined as:

$$\Omega_{tot} = \sum_i \Omega_i = 1 - \Omega_k. \tag{1.41}$$

Cosmic inventory

In addition to baryons and dark matter, whose density parameters are included in the standard cosmological model ΛCDM, several other species have significant densities, and their relative abundance defines the dynamic and evolution of the Universe, following equation Eq. (1.39).

Baryonic matter Baryons compose the matter for all astrophysical objects: stars, galaxies, clusters, interstellar and inter-cluster medium, etc. Baryons interact both through gravitation and electromagnetic forces, and the baryon density has been estimated at:

$$\Omega_b h^2 = 0.02237 \pm 0.00015, \tag{1.42}$$

or

$$\Omega_b = 0.04886, \tag{1.43}$$

which means that ordinary matter represents only a mere 5% of our Universe's content!

Dark matter In the 1930's, observations of the Coma cluster [288] had shown that this cluster seemed to contain more mass than what was visible. In the 1970's, further and more precise observations of galaxies and measurements of their rotation curves showed a discrepancy between observed curves and predicted ones [195, 233]. The existence of dark matter was proposed in the 1970's to explain this observation, when cosmologists concluded that a significant part of the galaxy mass does not emit light of any sort, but still interacts gravitationally. Many cold dark matter models have been developed over the years, the most popular ones can be divided in the following categories;

- WIMPs: standing for Weakly Interacting Massive Particles, WIMPs are a family of particles predicted by extension of the standard model of particle physics in the context of supersymetry. Various supersymetry models predict additional particles that would be candidates for dark matter;

- axions: proposed in 1988 to avoid CP violation in strong interactions [52, 174] and predicted by many string theory models, axions are light, cold hypothetical particles that could have been produced in the primordial Universe. They would still be present in galactic halos, and therefore explain the extra mass;

- primordial black holes: proposed in 1966 by Zel'dovich and Novikov [285], primordial black holes would originate from over-dense regions in the primordial Universe, allowing gravitational collapse with low masses compared to stellar black holes. With masses as low as 10^{-5} g - according to Hawking [121] - they are close to impossible to detect, and could account for the missing mass in galactic halos;

- baryonic dark matter: according to some theories, extra mass in galaxies could partially be explained by ordinary matter "hidden" in structures difficult to detect. Popular models include massive compact halo objects (or machos) that could be brown dwarf, white dwarf, neutron stars or black holes [49], or small clouds of primordial helium and molecular hydrogen [200, 67].

Despite this variety of dark matter models, the exact nature of dark matter remains unknown. However, the associated density can be computed from CMB observations:

$$\Omega_{\rm CDM} h^2 = 0.11933 \pm 0.00091 \tag{1.44}$$

or

$$\Omega_{\rm CDM} = 0.2607 \tag{1.45}$$

Dark energy As mentioned earlier in this chapter, the measurement of the deceleration parameter surprisingly led to the discovery of the accelerated expansion of the Universe - the deceleration parameter being in fact an acceleration parameter! Moreover, CMB observations allow to estimate the density parameter associated with this mysterious dark energy:

$$\Omega_\Lambda = 0.6889 \pm 0.0056 \tag{1.46}$$

There are several possible interpretations of the nature of dark energy. One of them is to interpret it as the cosmological constant in Einstein's equations. This interpretation is however somehow disfavoured by cosmological observations showing that to account for various energy density associated with dark energy, the equivalent cosmological constant should have changed throughout the history of the Universe - quite inconvenient for a constant...

Another possible explanation is to associate dark energy with the vacuum energy of particle physics. However, in this framework, vacuum energy has an estimated density of [183]

$$\rho_{\rm vacuum}^{\rm particle} = 10^{74}\,{\rm GeV}^4, \tag{1.47}$$

whereas the value deduced from cosmological observations is [11]

$$\rho_{\rm vacuum}^{\rm cosmology} = 10^{-47}\,{\rm GeV}^4. \tag{1.48}$$

To solve this huge discrepancy and/or the ad hoc addition of the cosmological constant in Einstein's equations, other models have been proposed, which allow the cosmological constant to be zero. They introduce new fields to explain the accelerated expansion of the Universe, and can be for example categorised in two types [236]. If these fields are not coupled or weakly coupled to matter (ordinary and dark) and photons, the framework of general relativity does not need to be modified. However, in the case of strongly coupled fields, general relativity equations have to be modified to account for this new physics.

Neutrinos Neutrinos are charge-free particles from the standard model, interacting only through weak force and gravitation. They exist in three flavours - electron, muon and tau - each of them associated with the corresponding lepton in the standard model of particle physics.

They are emitted in various nuclear and astrophysical processes, such as β-decay, nuclear fusion in stellar cores, supernovae explosion or in neutron stars. In 1998, the Super-Kamiokande collaboration measured for the first time the oscillation of atmospheric neutrinos between their three flavours, therefore establishing that neutrinos have a very small mass [104]. However, the absolute mass of each neutrino, as well as the mass hierarchy, is still unknown, and as yet to be determined. The determination of the sum of neutrino masses and the mass hierarchy can be achieved either by direct measurements in particle physics, or by indirect observations in cosmology, as detailed in section 2.6.2.

The current upper limit on neutrino masses is (with a 95 % confidence level):

$$\sum m_\nu < 0.12\,\mathrm{eV}. \tag{1.49}$$

Photons The photons of the CMB are the most abundant species in the Universe. Their emission is a black body at $T = 2.7255 \pm 0.00057$ K.

Because their temperature is very low, at the current epoch, radiation is completely sub-dominant in terms of radiation density compared to other species in the Universe. Thanks to precise measurements of the CMB temperature, their density can be estimated with a very high precision:

$$\Omega_\gamma h^2 = 5.06 \times 10^{-5}. \tag{1.50}$$

The relative abundances of all these components have varied drastically over cosmic times. These variations are the subject of the next section, which takes you through 13.8 billion years of history of the Universe.

1.2 Thermal history of the Universe

Following the observation that the Universe is expanding, and going back in time, Lemaître and Hubble both concluded that our Universe was born from an initial singularity, extremely hot and dense. Indeed, if we assume that before recombination, photons are at thermal equilibrium and their emission follows Planck's law, a temperature for the Universe can be defined:

$$T(t) = \frac{1}{a(t)} T_0, \tag{1.51}$$

with T_0 the current temperature. Since the initial singularity, the Universe has thus been cooling down during its expansion, going through various phases, dominated by different species.

1.2.1 Thermodynamics

Before going into more details of Universe's thermal history, we need to introduce a basic set of equations to describe the thermodynamics of an expanding Universe, both at equilibrium and beyond equilibrium.

When particles are at thermal equilibrium, they follow a Fermi-Dirac ($+$ at denominator) or Bose-Einstein ($-$ at denominator) distribution:

$$f(\mathbf{p}, T) = \frac{g}{8\pi^3} \frac{1}{e^{(E(\mathbf{p})-\mu)/T} \pm 1} \tag{1.52}$$

where g is the degeneracy factor that quantifies the number of degrees of freedom, μ is the chemical potential, and $E = p^2 + m^2$ is the energy.

Decoupling criteria

The key criteria that triggers decoupling from this equilibrium state is the comparison between Γ, the interaction rate, and H, the Hubble parameter measuring the expansion rate. If $\Gamma \gg H$, nuclear reactions occur more rapidly than the expansion of the Universe, which allows to maintain thermodynamic equilibrium. However, as Γ decreases with temperature, it becomes comparable to H as the Universe cools. The thermal equilibrium can not be maintained anymore, and species start to decouple.

A decoupled species is called a relic, and can usually be classified in one of the two categories:

- hot relic: if the decoupling occurs when the particle is relativistic, i.e. $T \gg m$;
- cold relic: if the decoupling occurs when the particle is not relativistic, i.e. $T \ll m$.

A good order of magnitude for the Hubble parameter in the early Universe is $H \sim T^2$, and $\Gamma \sim T^{n+3}$ for the interaction rate, with n depending on the interaction. When $\Gamma \sim H$, the interaction freezes, and the species decouple from the thermal bath. Depending on their properties, different species have different interaction rates, while the expansion the rate is the same for all species. This causes species to decouple from radiation at different times, as described hereafter.

Boltzmann equation

When leaving the thermal equilibrium, the distribution function f at equilibrium of Eq. (1.52) is not appropriate to fully describe the freezing and decoupling phenomena. The Boltzmann equation describes the evolution of the distribution function outside of equilibrium:

$$L[f] = C[f], \tag{1.53}$$

where C describes all possible collisions, and L is the Liouville operator. In the homogeneous and isotropic Universe, f depends only on energy E and time t, and the Liouville operator can be written as:

$$L[f] = E\frac{\partial f}{\partial t} - Hp^2\frac{\partial f}{\partial E}. \tag{1.54}$$

In a homogeneous, isotropic, expanding universe described by the FLRW metric, the Liouville operator for the comoving particle density n simplifies to:

$$L[n] = \frac{dn}{dt} + 3Hn, \tag{1.55}$$

where n is expressed as (following the distribution function in Eq. (1.52)):

$$n(t) = \int f(\mathbf{p},t)d^3\mathbf{p} = \frac{g}{2\pi^2}\int_m^\infty \frac{\sqrt{E^2-m^2}E}{e^{(E-\mu)/T} \pm 1}dE. \tag{1.56}$$

To express the collision term $C[n]$, let us consider a simple interaction

$$i + j \leftrightarrow k + l. \tag{1.57}$$

There are two possible sources of variation for n_i from the collision operator:

- creation with $C_i = C_{kl\to ij}$, with a rate of $\langle\sigma v\rangle n_i n_j$, where $\langle\sigma v\rangle$ is the thermally averaged cross-section;
- annihilation with $C_i = C_{ij\to kl}$, with a rate of $-\langle\sigma v\rangle \left(\frac{n_i n_j}{n_k n_l}\right)_{\text{eq}} n_k n_l$, so that $C_{kl\to ij} + C_{ij\to kl} = 0$ at equilibrium.

We equalise these interactions rates with the Liouville operator expressed as in Eq. (1.55), and obtain the the Boltzmann equation in cosmological conditions:

$$\dot{n}_i + 3Hn_i = -\langle\sigma v\rangle\left[n_i n_j - \left(\frac{n_i n_j}{n_k n_l}\right)_{\text{eq}} n_k n_l\right], \tag{1.58}$$

The equation Eq. (1.58) is the master equation describing the evolution of out-of-equilibrium species in the early Universe.

Now that we have all the tools to describe Universe's evolution, let's wander through its history!

1.2.2 Big Bang & its aftermath

Initial singularity

Originally named "primordial atom" by Lemaître, the initial singularity was nicknamed "Big Bang" by the English astronomer Fred Hoyle in 1949, who was himself in favour of a steady-state Universe. Intended as a popular image - or maybe even as a pejorative one - the name of Big Bang gained acceptance over the years and is now fully part of the vocabulary used to describe the standard cosmological model. It refers to a moment back in time when, according to the

FLRW metric describing the Universe, the distances between objects were infinitely small. This initial singularity was placed 13.8 billion years before the present epoch, based on observations of the CMB.

During the 10^{-43}s following the Big Bang, the so-called Planck time, laws of physics as we know them did not apply. The Universe, extremely dense, was then governed by the laws of quantum gravity.

The very early Universe

Before the Universe is 10^{-12}s old, the three forces of the standard model of particle physics (strong, weak and electromagnetic forces) rapidly decouple. The Universe is then composed of a quark and gluon plasma, described by the equations of quantum chromodynamics (QCD). During this epoch, called the quark epoch, particles have an energy within 100 MeV range. This scale of energy is accessible in particle accelerators down on Earth, and investigated at CERN (see section 3.4).

Between 10^{-6}s and 1s after the Big Bang, quarks bound into hadrons. The excess of matter with respect to antimatter appears at this epoch, called baryogenesis. The conditions necessary for this asymmetry to occur were postulated by the Soviet physicist Andrei Sakharov in 1967 [238]:

- matter and antimatter have different laws - this implies the C-violation and CP-violation;
- violation of the baryon number conservation in interactions - allowing to produce more baryons than anti-baryons;
- the thermal equilibrium in the early Universe is broken.

Neutrino decoupling

Neutrinos are coupled to matter and photons through weak interaction. Following the dynamics described in section 1.2.1, when the interaction rate becomes smaller than the expansion rate of the Universe, this interaction becomes ineffective and neutrinos decouple. It is estimated that this interaction occurs only 1s after the Big Bang, at an energy of 1 MeV. The decoupling of neutrinos forms a Cosmic Neutrino Background (CNB), yet to be detected. However, indirect evidence for this neutrino background is provided by phase shift in acoustic oscillations detected in the CMB [102].

Energy injection

Several processes can lead to energy release in the early Universe, slightly affecting the thermal distribution of photons [53], which otherwise follows Planck's law. In particular, the annihilation of pions reheats photons, that therefore decouple later than neutrinos because they have gained energy. Other processes include but are not limited to annihilating dark matter, dissipation of acoustic waves or decaying relic particles. They can be probed using spectral distortions in the CMB - as detailed in section 2.7.2.

1.2.3 Primordial nucleosynthesis

Primordial nucleosynthesis is the early Universe phase when light elements form, mainly deuterium and helium-4, smaller quantities of helium-3 and tritium, as well as traces of beryllium and lithium. It takes place between $t \sim 1\,\mathrm{s}$ and $t \sim 1000\,\mathrm{s}$. The term *primordial* is in opposition with *stellar* nucleosynthesis, which takes place in stellar cores and is responsible for the synthesis of heavy elements - up to iron.

Neutron-proton interaction freezing

Primordial nucleosynthesis starts shortly after neutrino decoupling, at a temperature of $0.7\,\mathrm{MeV}$ that does not allow to maintain nuclear thermodynamic equilibrium. The first interaction to freeze is the neutron-proton one:

$$n + e \longleftrightarrow p + \bar{\nu}_e. \tag{1.59}$$

Because protons are slightly lighter than neutrons, the neutron/proton ratio decreases, and then leads to the presence of free protons as final products of the interaction, while neutrons will end up mostly confined in Helium-4.

Chain reaction

The synthesis of deuterium is the first key step to spark a chain reaction that can lead to the production of other light elements. Because deuterium is easily photo-dissociated, this chain reaction can start only when the Universe is cool enough so that deuterium is stable over a sufficiently long period of time and therefore has time to react with other baryons:

$$\begin{aligned}
p + n &\rightarrow {}^2\mathrm{H} + \gamma \\
p + {}^2\mathrm{H} &\rightarrow {}^3\mathrm{He} + \gamma \\
{}^2\mathrm{H} + {}^2\mathrm{H} &\rightarrow {}^3\mathrm{He} + n \\
{}^2\mathrm{H} + {}^2\mathrm{H} &\rightarrow {}^3\mathrm{H} + p \\
{}^3\mathrm{He} + {}^2\mathrm{H} &\rightarrow {}^4\mathrm{He} + p \\
{}^3\mathrm{H} + {}^2\mathrm{H} &\rightarrow {}^4\mathrm{He} + n
\end{aligned} \tag{1.60}$$

The key parameter controlling the abundances of elements is the baryon/photon ratio. It controls how much deuterium and helium-4 can be formed, and therefore primordial abundances of all elements depend on this parameter. Figure 1.2 shows evolution of abundances versus time and temperature of the Universe from [43], and Figure 1.3 shows the final values of light element abundances as predicted by solving Boltzmann equation Eq. (1.58), as a function of the baryon/photon ratio. These predictions can be confronted with baryon density measured by CMB space probes. They show very good agreement with abundances measured by WMAP [59], and then confirmed by Planck [215].

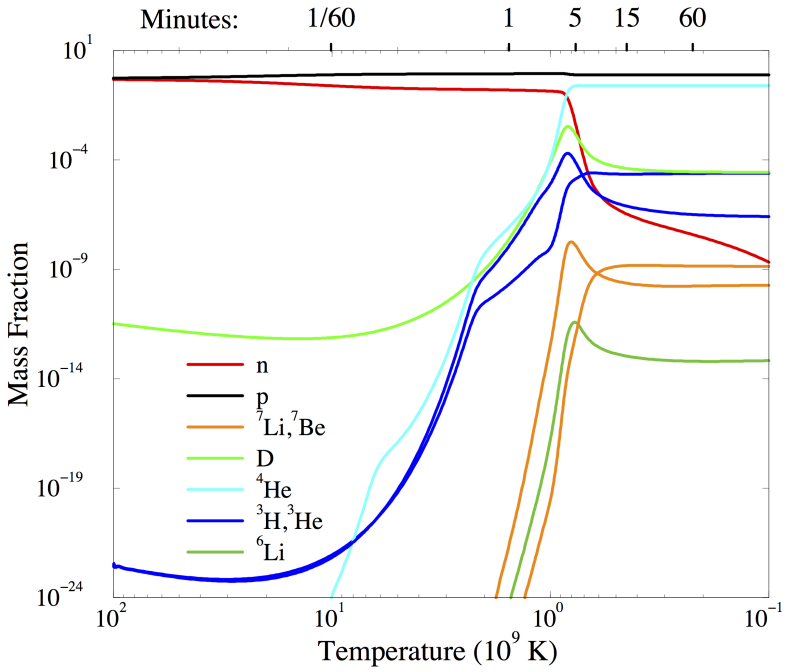

Figure 1.2 – Abundances of light elements during primordial nucleosynthesis
Credit: S. Burles et al. [43]

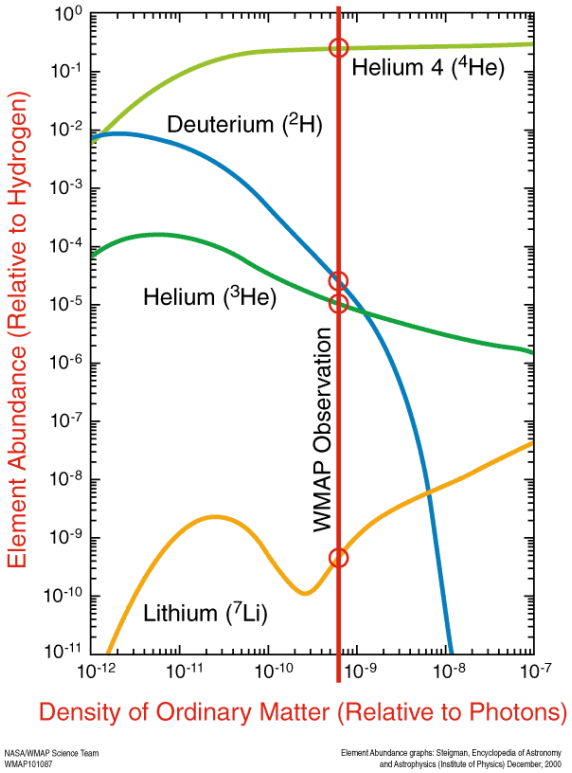

Figure 1.3 – Abundances of light elements after primordial nucleosynthesis confronted to WMAP observations
Credit: NASA/WMAP Science Team

1.2.4 Cosmic Microwave Background

Recombination

After the primordial nucleosynthesis, the expansion and cooling down of the Universe goes on. About 60 000 years after the Big Bang, the matter energy density starts to dominate the radiation one: the regime of expansion therefore changes, and the expansion rate increases. As long as the temperature is high enough (above $3\mathrm{eV} \sim 3600\mathrm{K}$), the Universe is largely ionised since the reaction

$$e^- + p \longleftrightarrow \mathrm{H} + \gamma \tag{1.61}$$

is at equilibrium.

When the temperature reaches $T \sim 3600\mathrm{K}$, the interaction described by Eq. (1.61) results in an excess of hydrogen atoms, as photons do not have enough energy to maintain the equilibrium. This is the recombination, and the Universe becomes neutral, as more atoms form: this is one of the major phase transitions in the history of the Universe.

Photon decoupling

As long as free electrons are present in the early Universe, they are coupled to photons through Compton scattering:

$$e^- + \gamma \Longleftrightarrow e^- + \gamma. \tag{1.62}$$

Like all other interactions previously mentioned, this interaction ultimately becomes inefficient, and photons decouple from the primordial plasma, following Boltzmann equation Eq. (1.58). This photon decoupling occurs 380 000 years after the Big Bang (at $z = 1100$), and from then, the Universe becomes transparent to light. The last interaction between photons and electrons is referred to as the last scattering surface, and the photons emitted at decoupling form the CMB. They are emitted with a temperature $T \sim 3000\mathrm{K}$, and, following Eq. (1.51) describing the dilution of photons energy density as the Universe is expanding, they can be detected today [215] with a temperature $T = 2.7255 \pm 0.00057$ K.

The spectrum of CMB photons has been measured by the instrument FIRAS (Far Infrared Absolute Spectrophotometer) on the COBE spacecraft, showing an almost perfect black body spectrum [175], as shown in Figure 1.4. The physics of CMB is reviewed in detail in Chapter 2.

.

1.2.5 Structure formation and evolution

After the recombination, the Universe remains matter dominated. Its energy content is estimated to be 84.5 % of dark matter and 15.5 % of ordinary matter. In the standard model, the energy density associated with dark energy is negligible at such early times. However, some models predict dark energy in the early Universe that could explain the discrepancy between Hubble constants measurements [79, 16].

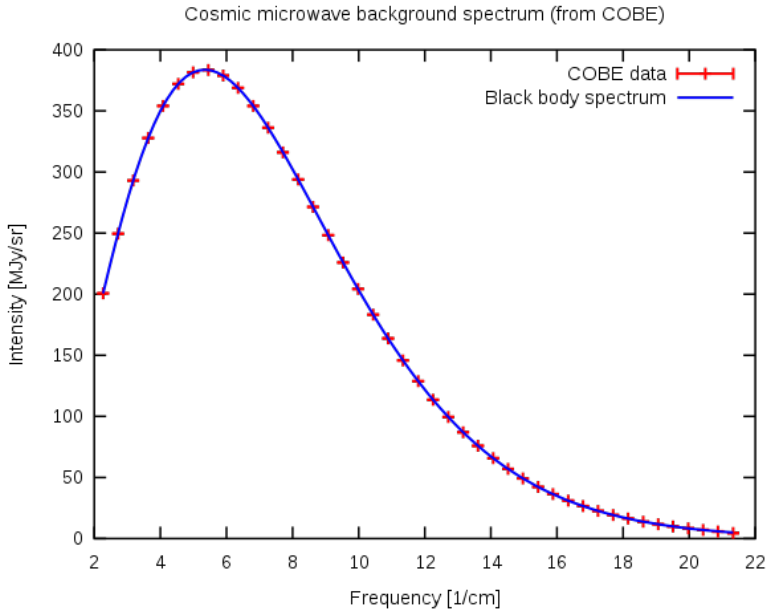

Figure 1.4 – CMB spectrum measured by FIRAS

Dark ages

Before the first stars start to form, there is almost no source of light in the Universe, apart from CMB photons cooling with the expansion, and the ones emitted by diffuse hydrogen clouds. Because of this absence of observable astrophysical objects, very little is known about this epoch, spanning from 380 000 to about 1 billion years after the Big Bang.

However, during these dark ages, dark matter slowly forms halos and filaments, gravitationally attracting ordinary matter. These matter aggregates are the host of the first stars and galaxies.

First stars and galaxies

The gravitational collapse of matter forms denser regions, ultimately collapsing into the first stars. It is estimated that the first stars have started to form only 150 million years after the Big Bang. The oldest galaxy ever detected, GN-z11, has been observed for the first time in 2016 [193], and has a redshift $z = 11.09$, corresponding to only 400 million years after the Big Bang!

Reionisation

Another major phase transition in the Universe occurs between 150 million and 1 billion years after the Big Bang ($6 < z < 20$). It consists in the ionisation of neutral hydrogen in the interstellar medium through the injection of vast quantity of energy by newly formed objects. The possible sources of reionisation are first stars, dwarf galaxies and Active Galactic Nuclei (AGN).

According to the latest Planck results [215], the redshift at which reionisation occurs (if it were an instantaneous event) is $z = 7.68 \pm 0.79$. This estimation is in good agreement with distant quasars observation [26], estimating the reionisation

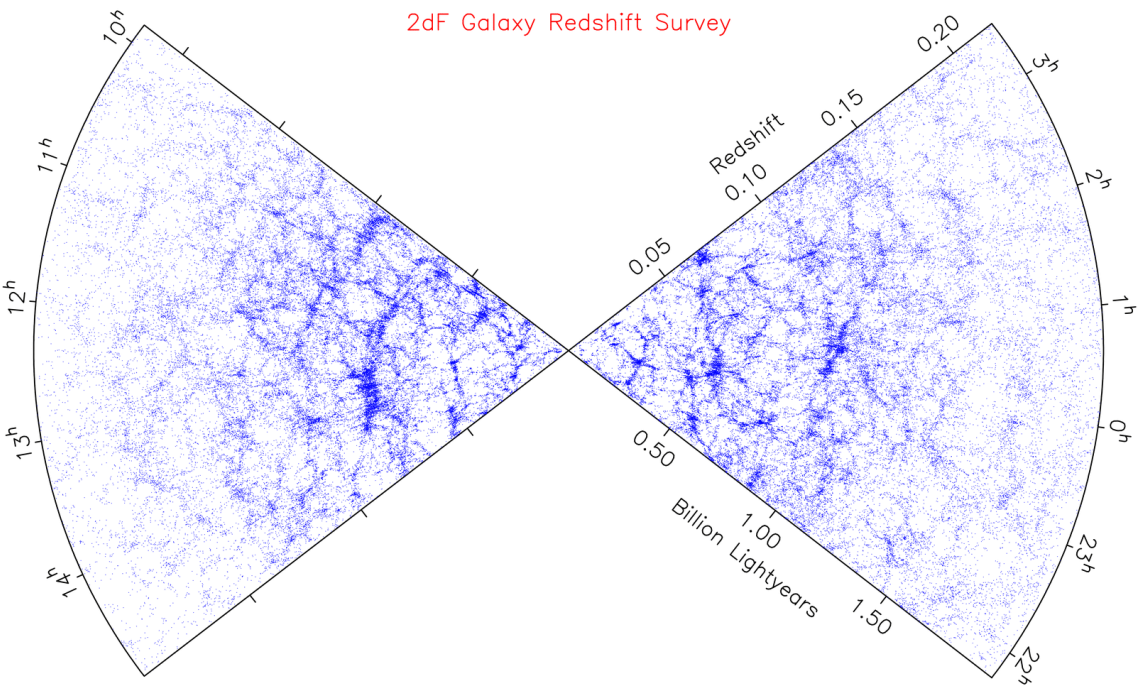

Figure 1.5 – Map of the cosmic web
Credit: The 2dF Galaxy Redshift Survey

redshift at $z \sim 6$.

However, the share of the various possible sources in the process of reionisation, as well as the redshift when most of it occurs are still active areas of research in cosmology, since very little is known about this period. In particular, observations using the 21 cm line of neutral hydrogen are a particularly promising probe to explore this epoch (see section 3.1.3).

Large scale structures

The Universe observed today in our cosmic neighbourhood (a few billion years) consist of galaxy clusters and superclusters, filaments of matter and dark matter - a complex set of structures, sometimes referred to as the cosmic web, pictured in Figure 1.5 by the 2dF Galaxy Redshift Survey[4]. Several probes can be used to map large scale structures, and I give a review of the common ones in section 3.1.

1.2.6 To infinity and beyond!

The observation that the expansion rate of the Universe is increasing prompted the (re)introduction of the cosmological constant in Einstein's equations. This constant acts like a fluid with a negative pressure, the so-called dark energy, which dominates today's Universe. The moment in cosmic history when the Universe transitions from a matter dominated era to a dark energy dominated one is estimated at 9 billion years after the Big Bang, i.e. 4.8 billion years ago.

[4] The2dFGalaxyRedshiftSurvey

What about the future? Given the current available data, the ΛCMB model is still our best framework to describe the evolution of the Universe, given how good it performs on past and current epoch. According to this model, it is therefore likely that the Universe will continue its accelerated expansion for the billions years to come, until space and matter are so diluted that the temperature of the Universe reaches the absolute zero...

The Big Bang scenario and thermal history of the Universe is a relatively simple theoretical framework, and has shown very good agreement with observations. However appealing that model may be, it is nevertheless not exempt of several flaws and unknowns. Some of the most important ones are the unknown nature of dark energy and dark matter. Many missions and experiments are on-going to tackle these issues. In particular, the European Space Agency (ESA) Euclid mission[5] and the Vera Rubin Observatory[6] (formerly LSST) aim at unravelling some of the mysteries of the dark Universe - dark energy and dark matter - by mapping galaxies and their shapes until redshift $z \sim 2$, which corresponds to looking 10 billion years back in time. A more complete review of large scale structures observation can be found in section 3.1.

1.3 Inflation

Moreover, the Big Bang scenario leaves many other unanswered questions, in particular about the primordial Universe. In this section, I review the common problems in the standard cosmological model, and present the most comprehensive theory proposed so far to solve them: the theory of inflation, which postulates a very short phase of extremely rapid expansion, fractions of second after the Big Bang.

In addition to resources already cited in introduction to this chapter, I used for this section the following references:

- *TASI Lectures on Inflation*, Daniel Baumann (2009);
- *Inflation, quantum fluctuations and cosmological perturbations*, lecture notes by David Langlois, Institut d'Astrophysique de Paris (2008) (for section 1.3.3).

1.3.1 Problems in the standard model...

Homogeneity and the horizon problem

Measurements of the CMB temperature indicate that the observable Universe is exceptionally isotropic: its temperature is the same in every observing direction[7]. This property can naturally be explained by the homogeneity of the primordial Universe: if the Universe is homogeneous at its very start, then all regions will behave the same as it evolves and expands. However, assuming the homogeneity of the Universe at very large scales does not stand a more careful look.

[5] https://www.euclid-ec.org/

[6] https://www.lsst.org/

[7] This is true up to $\frac{|\Delta T|}{T} \lesssim 10^{-5}$ as detailed in section 2.3.1 on CMB temperature anisotropies

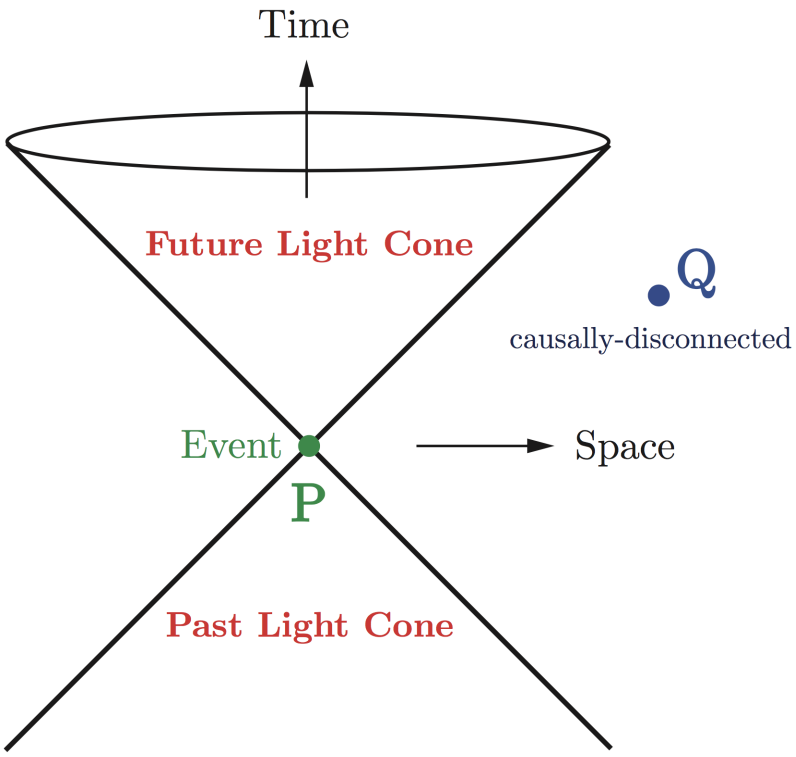

Figure 1.6 – Causality and particle horizon
Credit: D. Baumann [25]

Comoving particle horizon The comoving particle horizon $d_{\rm H}$ is defined by how far a particle can travel between its emission at $t = 0$ and a given moment in time t, taking into account the expansion of the Universe. It defines its light cone, represented in Figure 1.6, or the fraction of the Universe that is causally connected to a particle at a given time. It can be expressed as:

$$d_{\rm H} \equiv \int_0^t \frac{dt'}{a(t')} = \int_0^{a(t)} \frac{da}{Ha^2}. \tag{1.63}$$

The comoving particle horizon depends on the content of the Universe, through the equation of state and its parameters w:

$$d_{\rm H} \propto a^{\frac{1+3w}{2}} \tag{1.64}$$

which is of the same order of magnitude as the Hubble radius

$$(aH)^{-1} \propto H_0^{-1}\, a^{\frac{1+3w}{2}}. \tag{1.65}$$

(In)homogeneity Considering a matter dominated Universe ($w = 0$), one can show that the particle horizon when the CMB is emitted is much smaller than the scales where the CMB is homogeneous. It means that regions of the sky that never were in causal contact before - according to the classic Big Bang scenario - have the same properties, without any physically observable reason. A scenario to explain the homogeneity of the Universe on very large scales in the CMB is therefore needed.

Moreover, as we detail in Chapter 2, the CMB exhibits small inhomegeneities - seeds for future galaxies - that have very low amplitudes. We would therefore need a mechanism that would explain why the Universe is homogeneous at scales larger than the particle horizon... but at the same time how inhomogeneities were seeded in this very smooth Universe. Not so easy...

Flatness

The homogeneity problem is moreover not the only unanswered question in the Big Bang scenario. The curvature parameter is defined by Eq. (1.40), and Current measurements indicate that $\Omega_{tot}(a(t)) \sim 1$ [215], corresponding to an almost perfect flatness, i.e. $k = 0$. Since $\Omega_k(t)$ can only grow with time because it evolves as the Hubble radius $(aH)^{-1}$, the flatness of the Universe requires a fine tuning of Ω_{tot} in the early Universe. More precisely, at Planck time ($10^{-43}\,\mathrm{s}$ after the Big Bang), the deviation from perfect flatness has to be smaller than 10^{-61} to explain the curvature parameter that we measure today!

Although there is no theoretical or physical obstacle to this value, such a fine tuning seems unlikely. It would therefore be convenient to have a mechanism explaining the flatness observed today, without relying on the fine tuning of initial conditions.

Magnetic monopoles

Lastly, according to Maxwell's equations and classical physics, magnetic monopoles do not exists - and have never been detected. However, Grand Unified Theories (unifying electroweak and strong interactions) predict the existence of magnetic monopoles, that would therefore have existed in the early Universe, before interactions separate. Relics of these monopoles should be observable in the Universe, which is not the case.

Confronted to these accumulating arguments discrediting the Big Bang scenario in the 1970s, theorists - in particular Alexei Starobinsky, Alan Guth and Andrei Linde - proposed a theoretical framework to address them: inflation.

1.3.2 ... and solution?

Inflation is defined as an accelerated phase of expansion in the early Universe, before Planck time. The theory was initially proposed to solve for horizon, flatness and monopole problems, and it appeared only later than it also address the question of fluctuations in the early Universe.

Characteristics of inflation

Let us revisit the two[8] main problems we mentioned in the Big Bang scenario - horizon and flatness problems - in the light of inflation theories.

[8] We leave the magnetic monopole problem on the side, as it is more a high energy and particle physics problem, and it would be beyond the scope of this thesis to treat it properly.

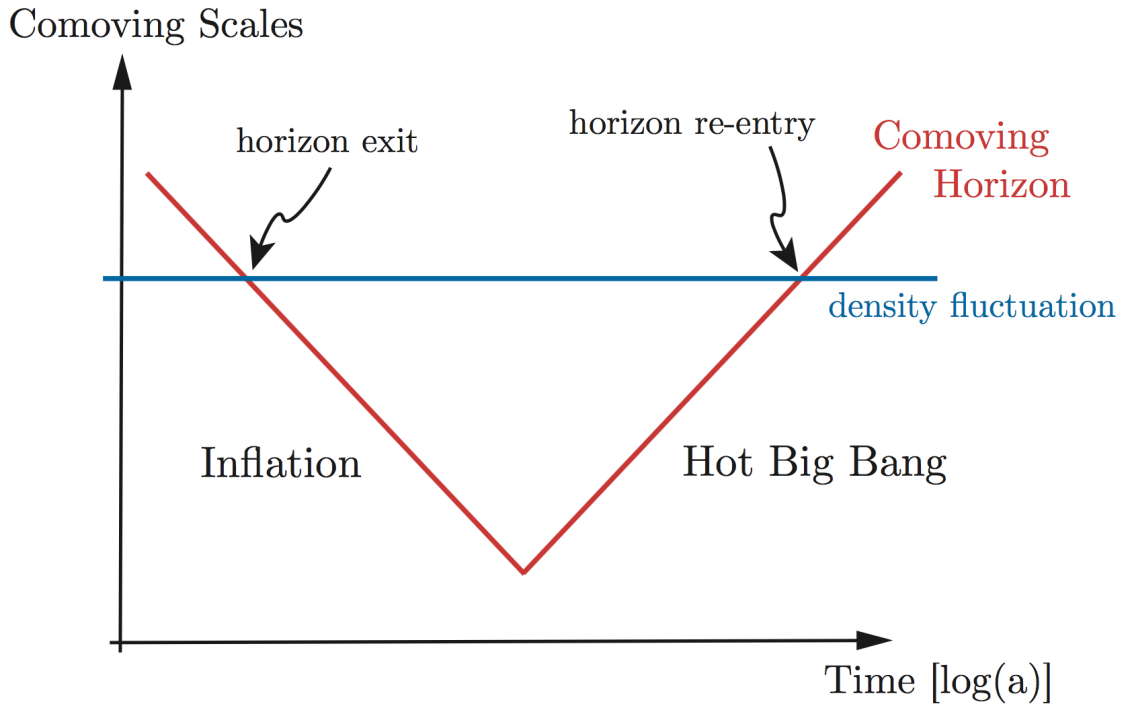

Figure 1.7 – Evolution of the Hubble radius with time
Credit: D. Baumann [25]

Horizon The initial goal of inflation theories was to solve the horizon problem. As described in the previous section, horizon problem arises from the fact that the CMB is homogeneous at scales larger than the Hubble radius at recombination. Since the Hubble radius is always *increasing* in standard cosmology, they could never have been in causal contact before. The simple idea of inflation postulates that the Hubble radius went through a *decreasing* phase in the early Universe as shown in Figure 1.7, and that it was much larger at some time before recombination, explaining the large scale homogeneity.

Flatness Going back to the definition of the curvature parameter:

$$\Omega_k = \frac{k}{(aH)^2} = 1 - \Omega_{tot}, \tag{1.66}$$

it is clear that a decreasing Hubble radius will drive flatness closer to zero. In this case, there is no need for fine tuning of initial conditions, since even a Universe far from flatness before inflation would have been driven to it during the process.

The accelerated expansion during inflation can be seen as a consequence of the decreasing Hubble radius. Indeed, we can express the derivative of the Hubble radius (expansion rate) as:

$$\frac{d}{dt}(aH)^{-1} = -\frac{\ddot{a}}{(aH)^2}. \tag{1.67}$$

A decreasing Hubble radius leads to $\ddot{a} > 0$, corresponding to an accelerated expansion, hence the name of inflation. Note that, according to the definition of the

deceleration parameter in Eq. (1.35), an accelerated expansion means $p + 3\rho < 0$, i.e. $w < 0$, as for dark energy.

Physics of inflation

The idea of the decreasing Hubble radius and accelerated expansion is seductive, but it has to be backed-up by a theoretical framework. The physics of inflation can be well described by a scalar field, called inflaton. Many models and theories exist, but I focus here on a canonical toy model of slow-roll inflation. Although simple, this model is sufficient to describe the physics of inflation and its main results.

Scalar field To describe inflation through the inflaton field, we consider a real scalar field $\phi(\mathbf{x}, t)$ associated with a potential $V(\phi)$. The energy-momentum tensor of the field can be written as:

$$T_{\mu\nu} \equiv \partial_\mu\phi\partial_\nu\phi - g_{\mu\nu}\left(\frac{1}{2}\partial^\sigma\phi\partial_\sigma\phi + V(\phi)\right) \tag{1.68}$$

To satisfy the condition of homogeneity in the Universe, we consider that ϕ depends only on time t. The energy-momentum tensor is written as in Eq. (1.19), leading to:

$$\rho_\phi = \frac{1}{2}\dot{\phi}^2 + V(\phi) \tag{1.69}$$

$$p_\phi = \frac{1}{2}\dot{\phi}^2 - V(\phi) \tag{1.70}$$

The term $V(\phi)$ is associated with potential energy, and the term $\frac{1}{2}\dot{\phi}^2$ with kinetic energy. The condition for an accelerated expansion becomes:

$$w_\phi = \frac{p_\phi}{\rho_\phi} < 0. \tag{1.71}$$

This condition can be satisfied only if the potential energy term dominates the kinetic one: this is one of the condition for inflation to happen.

The dynamics of this scalar potential can be derived by applying Friedmann equations Eq. (1.22 - 1.23) to the inflaton field:

$$\ddot{\phi} + 3H\dot{\phi} + V'(\phi) = 0 \tag{1.72}$$

$$H^2 = \frac{8\pi}{3}\left(\frac{1}{2}\dot{\phi}^2 + V(\phi)\right) \tag{1.73}$$

where $3H\dot{\phi}$ is called the Hubble friction term. Qualitatively, inflation can therefore be described by a scalar field rolling down a potential with a friction term - hence the name of slow-roll single-field inflation for this family of models

Slow-roll parameters As we just mentioned, the condition to have an accelerated expansion and fulfil the slow-roll condition, Eq. (1.71), is that the potential energy of the scalar field dominates its kinetic energy, i.e. we have:

$$\frac{\dot{\phi}^2}{2} \ll V, \ddot{\phi} \ll V'. \tag{1.74}$$

In this regime, the inflation equations Eq. (1.72 - 1.73) become

$$3H\dot{\phi} + V' = 0 \tag{1.75}$$

$$H^2 \simeq \frac{8\pi}{3}V. \tag{1.76}$$

Using these simplified equations, the slow-roll conditions Eq. (1.74) can be expressed in terms of two so-called slow-roll parameters:

$$\epsilon_V \equiv \frac{1}{16\pi}\left(\frac{V'}{V}\right)^2 \ll 1 \tag{1.77}$$

$$\eta_V \equiv \frac{1}{8\pi}\frac{V''}{V} \ll 1 \tag{1.78}$$

Number of e-folds To describe inflation theories, it is also convenient to introduce another parameter N that quantifies the number of e-folds before the end of inflation:

$$N \equiv \ln \frac{a_{\text{end}}}{a} \tag{1.79}$$

In the slow-roll approximation, N can be expressed as:

$$N(\phi) \simeq \int_{\phi}^{\phi_{\text{end}}} 8\pi \frac{V}{V'} d\phi, \tag{1.80}$$

and therefore depends of the model of inflation and its associated potential V. It is important to note that to solve the horizon problem, we need at least $N \gtrsim 60$.

In the slow-roll framework, the two slow-roll parameters and the number of e-folds are thus good benchmarks to evaluate proposed theories of inflation, and ensure that they meet the required criteria for an accelerated expansion and flatness problem.

Reheating

During inflation, all the energy density is contained in the inflaton field, with its equation of state governed by $w_\phi < 0$. After inflation ends, the temperature rises as the Universe enters the radiation dominated era with $w = \frac{1}{3}$, and the Big Bang scenario described in the previous section starts. The transition between these two phases is called reheating, but little is known about it. It likely involves the coupling of the inflaton field with fields from the standard model of particle physics, explaining the creation of elementary particles.

1.3.3 Fluctuations

The inflationary process was originally proposed to address the horizon and flatness problems. However, its mechanism also explains very well the initial conditions of the Big Bang scenario: a very smooth Universe, with small inhomegeneities.

The inflaton quantum field ϕ controls the energy density of the early Universe ρ_ϕ, and the end of inflation. Such a field has some quantum variance $\delta\phi(\mathbf{x}, t)$, and because of these fluctuations, different parts of the Universe exit inflationary phase at different times. As the inflaton field is thought to be coupled with standard model fields at reheating, the quantum variance of the inflaton field will ultimately result in different densities for different regions of the Universe.

These early density inhomogeneities seeded by inflation are unstable because of gravitational attraction: from these infinitesimal quantum fluctuations will arise large scale structures observed today. For most of the history of the Universe, large scale perturbations can be treated in the linear regime. It is only in our recent past that this approximation stops to be valid, when inhomogeneities grow into large scale structure. We will therefore limit ourselves to the linear regime in the following description.

Brief overview of cosmological perturbations theory

I first describe the classical dynamics of perturbations in the Universe, first through perturbed metric and matter, and then adding quantum fluctuations of scalar fields. Combining these two kinds of perturbations in the linear regime leads to a simple yet sufficient model to describe the birth and growth of inhomogeneities.

In this section, instead of the usual cosmic time t, we use the conformal time:

$$\eta \equiv \int \frac{dt}{a(t)}, \tag{1.81}$$

and its inverse $\mathcal{H}$, the Hubble radius.

Perturbing metric & matter Starting from a flat FLRW metric, a linear perturbation is written as:

$$\mathrm{g} = a^2 \left\{ -(1+2A)d\eta^2 \, + \, 2B_i dx^i d\eta \, + \, (\delta_{ij} + h_{ij}) dx^i dx^j \right\}, \tag{1.82}$$

where A is a scalar field, B_i is a vector field and h_{ij} is a symmetric tensor field perturbing the metric δ_{ij}. Perturbations are usually split into three categories: scalar, tensor and vector modes, coming from the decomposition of the scalar, vector and tensor fields:

- B_i can be decomposed into longitudinal and transverse parts : $B_i = \nabla_i B + \bar{B}_i$ with $\nabla_i \bar{B}^i = 0$. There are therefore one scalar mode B and two vector modes $\bar{B}^i$;
- h_{ij} can be decomposed as $h_{ij} = 2C g_{ij} + 2\nabla_i \nabla_j E + \nabla_i E_j + \nabla_j E_i + \bar{E}_{ij}$. There are therefore two scalar modes C and E, two vector modes E_i, and two tensor modes $\bar{E}^{ij}$.

Given a scalar field $\phi(\mathbf{x}, t)$, for example the inflaton field, its energy-momentum tensor perturbations can be described using the same decomposition into scalar, vector and tensor modes as for metric perturbations. To properly describe perturbations, combinations of modes coming from the field itself and from the metric have to be considered together. Note that scalar and tensor modes are the most important for cosmology. Scalar modes describe density perturbations, while tensor modes describe gravitational waves. I will not consider the case of vector modes here, since they are not relevant in the cosmological context[9].

Quantum fluctuations The action for a massless scalar field ϕ (typically the inflaton field) in a FLRW metric with exponential expansion (as during the inflation phase) is written as a function of the canonical variable $u \equiv a\phi$, where a is the scale factor:

$$S = \frac{1}{2}\int d\eta\, d^3x \left[u'^2 - \nabla u^2 + \frac{a''}{a}u^2\right] \tag{1.83}$$

Quantising the scalar field u using usual quantum field theory procedure, by expanding the associated quantum field $\hat{u}$ in Fourier space, leads to:

$$\hat{u}(\eta, \mathbf{x}) = \frac{1}{(2\pi)^{\frac{3}{2}}}\int d^3k \left\{\hat{a}_k u_k(\eta) e^{i\mathbf{k}.\mathbf{x}} + \hat{a}_k^\dagger u_k^*(\eta) e^{-i\mathbf{k}.\mathbf{x}}\right\} \tag{1.84}$$

where $\hat{a}$ (resp. $\hat{a}^\dagger$) is the annihilation (resp. creation) operator, $k = |\mathbf{k}^2|$ is the scale of the perturbation and $u_k(\eta)$ has to satisfy the equation of motion in Fourier space. This choice of $u_k(\eta)$ is equivalent to the choice of the vacuum state $|0\rangle$, and of the creation and annihilation modes.

Once a vacuum state $|0\rangle$ is chosen, one can write the power spectrum with the Legendre transform of the correlation function of the field:

$$\langle 0|\hat{\phi}(\mathbf{x_1})\hat{\phi}(\mathbf{x_2})|0\rangle = \int d^3k e^{i\mathbf{k}.(\mathbf{x_1}-\mathbf{x_2})}\frac{\mathcal{P}_\phi(k)}{4\pi k^3} \tag{1.85}$$

For the field u, this leads to:

$$\mathcal{P}_\phi(k) = \frac{k^3}{2\pi^2}\frac{|u_k^2|}{a^2}. \tag{1.86}$$

This description gives us a general theoretical framework to describe perturbations in the primordial Universe, in the specific case of the inflaton field as detailed hereafter.

Perturbations in the primordial Universe

In the previous section, frameworks to describe separately metric perturbations, matter perturbations and quantum fluctuations of a scalar field have been introduced separately. We now need to consider all these contributions together

[9] Although vector perturbations can be produced in the early Universe, they are thought to have decayed by the time of recombination when the CMB is emitted, and are therefore not relevant in the context of this thesis.

to have a realistic description of the generation of inhomogeneities in the early Universe.

Considering metric perturbations up to second order, the perturbed action is expressed as:

$$S[\bar{\phi}+\delta\phi, \bar{g}_{\mu\nu}+h_{\mu\nu}] = S^{(0)}[\bar{\phi}, \bar{g}_{\mu\nu}] + S^{(1)}[\delta\phi, h_{\mu\nu}; \bar{\phi}, \bar{g}_{\mu\nu}] + S^{(2)}[\delta\phi, h_{\mu\nu}; \bar{\phi}, \bar{g}_{\mu\nu}] \quad (1.87)$$

The first order term $S^{(1)}$ vanishes when using Friedmann-Lemaître equations of motion, so we focus on the second order term $S^{(2)}$ to quantise perturbations, as done for perturbations of a scalar field in the previous section. We emphasised earlier than the modes of interest for cosmology are scalar and tensor perturbations. Moreover, as we are in the linear regime, we can consider them separately.

Scalar perturbations We focus first on scalar perturbations, i.e. the ones arising from A, B, C and E modes of metric perturbations, as well as the scalar field perturbation $\delta\phi$. As for quantum fluctuations where we introduced u, it is possible to introduce a canonical variable

$$v \equiv a\left(\delta\phi - \frac{\phi'}{\mathcal{H}}C\right), \quad (1.88)$$

for which the action takes a very simple form, close to the one of Eq. (1.83):

$$S = \frac{1}{2}\int d\eta\, d^3x \left[v'^2 - \partial_i v\, \partial^i v + \frac{z''}{z}v^2\right] \quad (1.89)$$

with

$$z \equiv a\frac{\phi'}{\mathcal{H}}. \quad (1.90)$$

We also define the comoving curvature perturbation:

$$\mathcal{R} = -C + \frac{\phi'}{\mathcal{H}}\delta\phi. \quad (1.91)$$

By analogy with Eq. (1.86) the power spectrum of scalar perturbations can be written as:

$$\mathcal{P}_{\mathcal{R}}(k) = \frac{k^3}{2\pi^2}\frac{|v_k^2|}{a^2}. \quad (1.92)$$

In the slow-roll inflation regime, the power spectrum of scalar perturbations on scales larger than the Hubble radius can be written as a function of the inflaton potential V and the first slow-roll parameter ϵ_V defined in Eq. (1.78):

$$\mathcal{P}_{\mathcal{R}} = \frac{1}{24\pi^2}\left(\frac{V}{m_P^4\epsilon_V}\right)_{k=aH} \quad (1.93)$$

where the reduced Planck mass $m_P \equiv \frac{\hbar c}{\sqrt{8\pi G}}$ was introduced.

The power spectrum of scalar perturbations Eq. (1.92) is not strictly scale-invariant, since the amplitude of a perturbation depends on the value of H and $\dot{\phi}$

when its scale exits the Hubble radius, which can be slightly different for different scales. To quantify this scale invariance, we define the scalar spectral index n_s as:

$$n_s - 1 \equiv \frac{d \ln \mathcal{P}_\mathcal{R}(k)}{d \ln k} \tag{1.94}$$

It is also convenient to define the running of the spectral index:

$$\alpha_s \equiv \frac{dn_s}{d \ln k}. \tag{1.95}$$

We currently measure $n_s = 0.9665 \pm 0.0038$ (see Table 1.1) and $\alpha_s = -0.0041 \pm 0.0067$, which is compatible with a non strictly scale invariant power spectrum, and therefore compatible with an early phase of inflation.

Tensor perturbations Tensor perturbations of the metric h_{ij} are associated with tensor modes $\bar{E}_{ij}$, sources by primordial gravitational waves (see section 3.3.1 for a derivation of gravitational waves equation). As for scalar perturbations, the tensor power spectrum as a function of the inflation potential V can be expressed as:

$$\mathcal{P}_\mathcal{T} = \frac{2}{3\pi^2} \left(\frac{V}{m_P^4} \right)_{k=aH}, \tag{1.96}$$

and we also define the tensor spectral index:

$$\begin{aligned} n_t &\equiv \frac{d \ln \mathcal{P}_\mathcal{T}(k)}{d \ln k} \\ &\overset{\text{slow-roll}}{=} -2\epsilon_V \end{aligned} \tag{1.97}$$

Under the slow-roll approximation, the ratio of scalar and tensor modes power spectra is directly proportional to the slow-roll parameter ϵ_V:

$$r \equiv \frac{\mathcal{P}_\mathcal{T}}{\mathcal{P}_\mathcal{R}} = 16\epsilon_V = -8n_t. \tag{1.98}$$

This tensor-to-scalar ratio r is of central importance for cosmology, as this is almost the unique parameter setting the amplitude of tensor modes in the primordial Universe. As detailed in the next Chapter, the detection of primordial B-modes in the CMB would be a smoking gun for inflation theories, and would allow to measure the tensor-to-scalar ratio r as well as other inflation parameters.

The two parameters, the scalar spectral index n_s and the tensor-to-scalar ratio r, thus depend on inflationary models and their precise measurement allow to discriminate between models. The estimation of the scalar spectral index already allowed to disfavour models that predict $n_s = 1$ [216] as well as $n_s > 1$. The joint constraints on inflation models coming from n_s and r are shown in Figure 1.8.

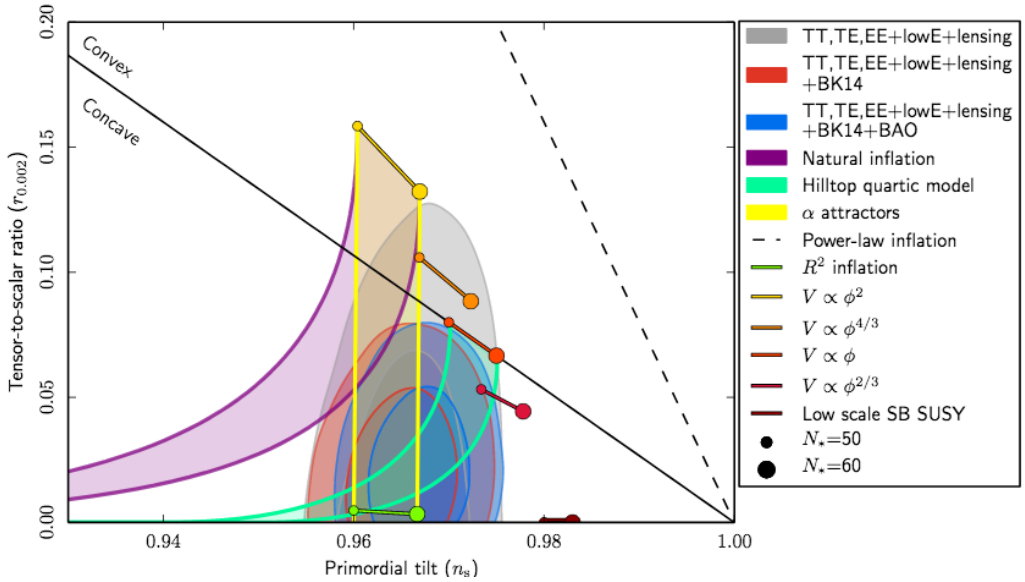

Figure 1.8 – Observational constraints on n_s and r from various data sets: TT, EE, TE, lowE and lensing refer to Planck 2018 results, BK14 to BICEP/Keck 2014 release and BAO to 6dF and SDSS surveys. The contours correspond to 95% and 68% confidence level. The observational constraints are compared to various inflationary models and their parameters (see details in [216]), where V is the potential, N_* is the number of e-folds
Credit: The Planck Collaboration [216].

Upshots

Many inflation models have been proposed, some of them much more complex than the simple slow-roll model, with sometimes several scalar fields. Other theories suggest that, if the inflaton field remains necessary to explain the accelerated expansion phase needed to solve the horizon and flatness problems, cosmological perturbations could arise from a different scalar field with other properties. A better understanding of inflationary process is therefore important not only for its cosmological implication, but also for fundamental and particle physics.

However, given the energy scale at which inflation would have occurred, there is no direct access to the inflaton field using particle accelerators - contrary to the long-hypothetical Brout-Englert-Higgs field, that was finally observed at the LHC. The best observational probes to explore the early Universe are the density and polarisation fluctuations of the CMB, imprints of perturbations of the primordial Universe, and "frozen" at the stage of recombination. The detection of tensor modes in the CMB, and the measurement of their amplitude r and spectral index n_t would therefore be not only a smoking gun for inflationary models, but would also help discriminate between models, based on their theoretical prediction of these phenomena.

CMB observations are therefore of crucial importance to understand the primordial Universe, not only for inflation, but also to measure cosmological parameters and probe density fluctuation in the early Universe, as mentioned through-

out this first chapter. The second chapter aims at giving a more detailed review of CMB physics and observations, and in particular the connection between CMB anisotropies and early Universe physics.

CHAPTER 2

The Cosmic Microwave Background

Contents

After introducing our Universe's history in the first chapter, I now aim at giving a more detailed description of the Cosmic Microwave Background (CMB) physics. The CMB is indeed one of the best probes we have to study the physics of the early Universe. Moreover, CMB observations allow us to have an insight into very high energy processes that can hardly be studied on Earth. Nevertheless, as detailed in Chapter 3, other probes exist and can be cross-correlated with CMB observations to yield a more comprehensive picture of the Universe than what can be obtained from any of those probes separately.

After a brief historical overview in section 2.1, I present in section 2.2 one of the central observables in CMB science: its anisotropies. In sections 2.3 and 2.4, I detail the physical processes sourcing primary and secondary anisotropies, as well as their observable features in section 2.5. In section 2.6, I outline how we can use the CMB to extract values of cosmological parameters, and I finally conclude this chapter by reviewing, in section 2.7, the extra CMB science that can be performed beyond anisotropies.

The content of this chapter is based on the following resource book and reviews:

- *Cosmologie primordiale*, Patrick Peter & Jean-Philippe Uzan (2012);
- *TASI Lectures on Cosmological Perturbations*, Julien Lesgourgues (2013);
- *Cosmic Microwave Background Anisotropies*, Wayne Hu & Scott Dodelson (2002);
- *The Quest for B Modes from Inflationary Gravitational Waves*, Marc Kamionkowski & Ely D. Kovetz (2016).

2.1 Cosmic Historical Background

The idea of the Cosmic Microwave Background as a relic radiation from the Big Bang was first postulated in the late 1930s by Georges Lemaître, who very poetically named it "*écho disparu de la formation des mondes*" [1]... At a time when the Big Bang scenario was still hypothetical, this theoretical insight was hardly investigated and rejected by a large part of the scientific community.

In 1948, the Soviet-American physicist George Gamow and his then PhD student Ralph Alpher published a ground breaking paper on primordial nucleosynthesis and elements abundances [10]. They demonstrated an agreement between observed abundances and the ones predicted by their model, thereby bringing more credence to the Big Bang theory. The same year, Ralph Alpher and Robert Herman made the first quantitative prediction of a background radiation, estimating the temperature of the background to be $5\mathrm{K}$. In the 1950s and early 1960s, Gamow, Alpher and Herman re-estimated several times the temperature of the background radiation, with values ranging from $6\mathrm{K}$ to $28\mathrm{K}$. The prediction of a background radiation was also made independently in the early 1960s by Robert Dicke and Jim Peebles, and Yakov Zel'dovich.

[1] This expression can be translated into English much less poetically by "faded echo of the creation of words".

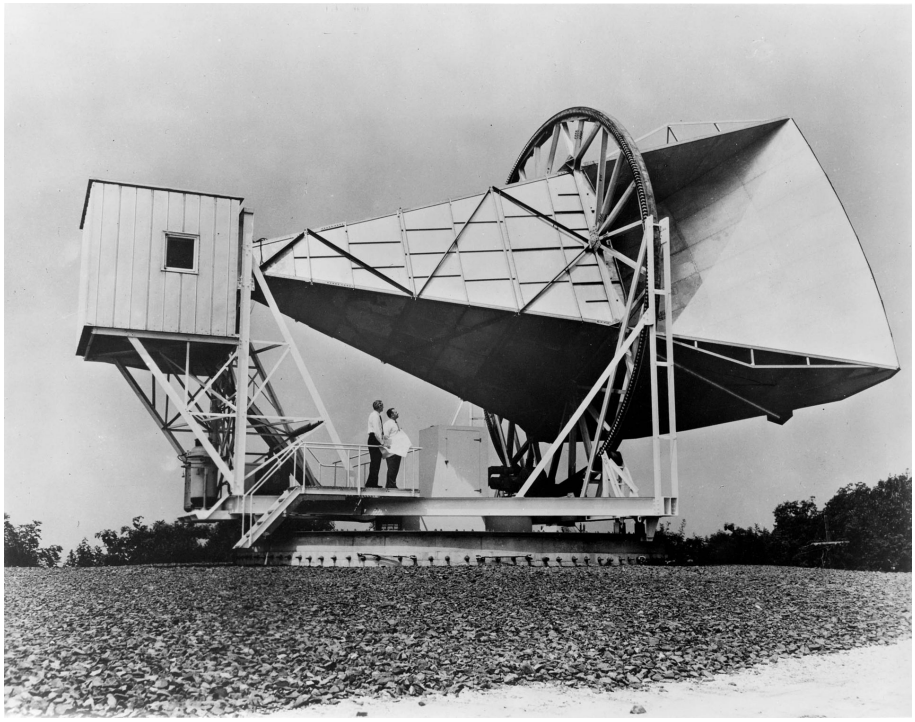

Figure 2.1 – Penzias and Wilson in 1964 with the antenna used for their historical detection
Credit: NASA

In 1964, Robert Dicke and his Princeton colleagues David Wilkinson and Peter Roll began building a Dicke radiometer aiming at detecting the Cosmic Microwave Background. However, at the same time, two researchers from the Bell Laboratory, Arno Penzias and Robert Wilson, were working on a radiometer intended for satellite communication experiments. They observed an excess of $4.2\mathrm{K}$ in their antenna temperature. After spending a year looking for an explanation to this measurement - from remnants of a nuclear experiment to bird droppings - they finally came to the conclusion, after a discussion with Robert Dicke, that they had detected the echo of the past Universe [203]. This discovery almost definitely confirmed the Big Bang scenario, allowing modern physical cosmology to start flourishing. In the following years, the theory of cosmological perturbations was further developed and applied to early Universe physics, following the first principles derived in the late 1940s by Lifshitz [166]. In the early 1970s, several cosmologists predicted the existence of CMB anisotropies, such as Zel'dovich [286], Peebles and Yu [202] or Harrison [119].

After these early discoveries and predictions, the CMB progressively became an object of central interest in cosmology, attracting more and more scientists and prompting new experiments. Throughout the review of CMB physics in this chapter, I mention historical discoveries and measurements alongside recent results.

2.2 Density fluctuations

As detailed in the first chapter, the primordial Universe can be well described by a homogeneous plasma of tightly coupled particles. This primordial plasma cools down with expansion, which causes various species to decouple from it, at times that are set by the comparison of their interaction rate Γ to the expansion rate H (see section 1.2.1). In particular, 380 000 years after the Big Bang, photons decouple, and these first photons free-stream to form the CMB. The distribution of CMB photons is thus modelled on that of matter in the early Universe, because they were tightly coupled before photons decoupling. The matter distribution in the early Universe, in particular its density fluctuation, is related to the inflation phase, which is thought to leave density fluctuations in the primordial Universe. To describe the evolution of matter inhomogeneities and understand how they relate to CMB temperature anisotropies, the size of these fluctuations (k^{-1}) has to be compared with two relevant scales:

- the Hubble radius $r_H \equiv (aH)^{-1}$ (or comoving horizon, shown in Figure 1.6), corresponding to the observable part of an expanding Universe;
- the sound horizon $r_s \equiv c_s r_H$, where c_s is the sound speed in the photon-baryon fluid.

Depending on their scale, fluctuations re-enter the Hubble radius at different times. Fluctuations larger than the Hubble radius are frozen in their initial state. For smaller scale fluctuations which progressively enter the Hubble radius, the evolution is more complex. As detailed hereafter, their evolution is governed by acoustic oscillations, hence the importance of the sound speed and its associated length, the sound horizon.

2.2.1 Kinetic approach

A complete description of the evolution of inhomogeneities in the early Universe requires a kinetic approach, using Boltzmann equation, as introduced in Eq. (1.53):

$$L[f] = C[f]. \tag{2.1}$$

In this section, we use again the conformal time η, and thus the left-hand side (Liouville operator) simplifies to:

$$L[f] = \frac{df}{d\eta}. \tag{2.2}$$

We recall that before recombination, photons are tightly coupled to baryons, that are tightly coupled to electrons. The left-hand side of the Boltzmann equation (collision term) thus corresponds to the Thompson scattering in the photon-baryon plasma. At this stage, it is therefore important to note that, as long as photons are at equilibrium with baryons and electrons, they are described by the value of the equilibrium temperature $T(\eta, \mathbf{x})$.

In these conditions, the distribution function of photons can be approximated by a Bose-Einstein distribution with a vanishing chemical potential, i.e. $\mu = 0$:

$$\bar{f}(\eta, \mathbf{x}, \mathbf{p}) \sim \frac{1}{e^{p/T(\eta,\mathbf{x})} - 1}, \tag{2.3}$$

where $\mathbf{x}$ is the position, $\mathbf{p}$ the four-momentum and $p = |\mathbf{p}|$. This distribution function can be described as an unperturbed homogeneous part $\bar{f}$, and a perturbation δf:

$$\bar{f}(\eta, \mathbf{p}) = \frac{1}{e^{p/T(\eta)} - 1} \tag{2.4}$$

$$\delta f(\eta, \mathbf{x}, \mathbf{p}) = \frac{d\bar{f}}{d\log p} \frac{\delta T(\eta, \mathbf{x})}{\bar{T}(\eta)}, \tag{2.5}$$

where we have introduced the homogeneous background temperature $\bar{T}(\eta)$. We introduce

$$\Theta(\eta, \mathbf{x}) \equiv \frac{\delta T(\eta, \mathbf{x})}{\bar{T}(\eta)}, \tag{2.6}$$

that describes temperature anisotropies. The Boltzmann equation will then leads to an equation of motion for $\Theta(\eta, \mathbf{x})$.

Although it is more comprehensive, the description of the primordial Universe and the CMB using Boltzmann equation requires many analytical and numerical calculations, that are for example developed in [202]. Hereafter, we therefore adopt a canonical simplified description based on fluid mechanics, which is well justified as the photon-baryon plasma is tightly coupled and can therefore be treated as fluid. This description allows to derive most of the important results we need to describe CMB anisotropies, and has the advantage of being more intuitive in terms of physical mechanisms.

2.2.2 Fluid mechanics description

Because of the expansion of the Universe, the temperature of the photon-baryon fluid decreases and matter starts to dominate over radiation. This leads to the gravitational collapse of matter - and consequently of photons coupled to baryonic matter. Precisely because photons also collapse with baryons, they induce a radiation pressure that counteracts the gravitational collapse. This leads to density oscillations in the primordial plasma, which resemble standard acoustic oscillations, and are therefore named as such. As temperature continues to decrease, matter and photons decouple, matter collapses further, and photons free-stream.

A perturbation starts oscillating once it enters the horizon, and stops at recombination: the phase at which it happens to be at recombination is therefore determined. Perturbations of different characteristic sizes are thus at different phases of their oscillation, generating a characteristic pattern of density fluctuations. This pattern, and in particular acoustic peaks, is encoded in the statistical properties of the spatial distribution of CMB photons, as detailed hereafter. These density fluctuations source primary anisotropies of the CMB: temperature

anisotropies arise directly from acoustic oscillations (section 2.3.1), and are also responsible for polarisation anisotropies through differential Thompson scattering (section 2.3.2).

2.3 Primary anisotropies

Primary anisotropies refer to anisotropies arising from primordial inhomogeneities in the early Universe, and present at the time of the last scattering (or recombination), as opposed to secondary anisotropies that are sourced by phenomenon happening between the last scattering surface and the observer. Prior to last scattering, primordial fluctuations (sourced e.g. by inflation) go through the phase of acoustic oscillations, which is the main driver for observable density fluctuations in the primordial Universe. However, their complete description, for temperature as for polarisation, requires to take into consideration more complex processes.

2.3.1 Temperature anisotropies

As described above, the temperature field can be decomposed into a homogeneous background $\bar{T}(\eta)$, and a superimposed small perturbation $\Theta(\eta, \mathbf{x})$. In this section, I first develop equations for a toy-model of the early Universe, considering only acoustic oscillations as the sources of anisotropies. Although simplified, this approach introduces necessary concepts and notations. I then present results for a more complex model.

Simplified approach

Temperature anisotropies can easily be described qualitatively: a denser region - with more matter and therefore more photons - appears hotter, when a less dense region appears cooler. In this approximation, the oscillation equation for the temperature field follows the one of acoustic oscillations, and can thus be written as:

$$\ddot{\Theta} + c_s^2 k^2 \Theta = 0, \tag{2.7}$$

with $1/k$ the characteristic size of the perturbation. Θ keeps oscillating until recombination, and the temperature anisotropy field spatial dependence at that time $\eta_* = \eta(\text{recombination})$ simply reads:

$$\Theta(\eta_*) \propto \cos(2\pi k s_*), \tag{2.8}$$

where $s_* \equiv \int_0^{\text{recombination}} c_s d\eta$ is the sound horizon at recombination - how far the sound can travel between $t = 0$ and the last scattering surface. Integer values of k correspond to perturbations which find themselves at maximum compression or expansion at the time of the last scattering. This quantification of acoustic oscillations is one of the key feature of CMB physics, as detailed hereafter.

Sachs-Wolfe formula

For a more comprehensive description of CMB anisotropies, more terms have to be considered in Eq. (2.7), to encompass more complex processes. In particular:

- gravitation, that (1) provides a gravitational term in the oscillator sourced by the gravitational potential Ψ, and (2) generates an Einstein effect for photons escaping a potential well. The effect of gravitation on temperature is referred to as the Sachs-Wolfe effect;
- Doppler shift, due to bulk motion of the plasma at the time of last scattering;
- line-of-sight effect of varying potentials, knows as the integrated Sachs-Wolfe (ISW) effect.

We first consider only the temperature field Θ and the gravitational term Ψ, so one can rewrite Eq. (2.8) as:

$$(\Theta + \Psi)(\eta_*) \propto \cos(2\pi k s_*), \tag{2.9}$$

$\Theta + \Psi$ is sometimes referred to as the apparent temperature field, as this equation describes quite well the competing effect of temperature and gravitation in acoustic oscillations: higher density leads to higher temperature, but at the same time a higher gravitational potential and thus a bigger Sachs-Wolfe effect that counterbalance the effect of temperature.

However, Eq. (2.9) does not take into accounts all effects previously mentioned, such as Doppler shift and ISW effect. Once all these source terms are taken into account in the equation of oscillation Eq (2.7), anisotropies of the temperature field Θ can be projected on the sphere using their multipole moments. The observed temperature anisotropy can then be expressed on the basis of spherical harmonics $Y_{\ell m}$[2] [130]:

$$\Theta(\eta_*, (\theta, \phi)) = \sum_{\ell m} Y_{\ell m}(\theta, \phi) \left[(-i)^\ell \int \frac{d^3k}{(2\pi)^3} a_\ell(\mathbf{k}) Y^*_{\ell m}(\mathbf{k}) \right], \tag{2.10}$$

where $a_\ell(\mathbf{k})$ is the so-called projected source term, that includes all the anisotropies sources discussed before. In the simplest case taking into account only temperature Θ and gravitational potential Ψ, a_ℓ can be expressed:

$$a_\ell(\mathbf{k}) = [\Theta + \Psi](\mathbf{k}, \eta_*) j_\ell(kD_*), \tag{2.11}$$

where D_* is the comoving angular diameter distance to recombination, j_ℓ the spherical Bessel function, and $k = |\mathbf{k}|$. Note that this is a projection on the sphere of plane waves, with amplitudes roughly as in Eq. (2.9).

If we now consider all possible sources of anisotropies, as listed above, the source term becomes:

$$a_\ell = \underbrace{[\Theta + \Psi](\mathbf{k}, \eta_*) j_\ell(kD_*)}_{\text{Sachs}-\text{Wolfe}} + \underbrace{v_b(\mathbf{k}, \eta_*) j'_\ell(kD_*)}_{\text{Doppler}} + \underbrace{\int_{\eta_*}^{\eta_0} d\eta (\dot{\Psi} - \dot{\Phi}) j_\ell(kD)}_{\text{Integrated Sachs}-\text{Wolfe}}, \tag{2.12}$$

[2] Spherical harmonics are defined in Appendix A.

where v_b is the velocity of the electrons responsible for the Doppler shift, and $j'_\ell(kD_*)$ denotes the space derivative of the Bessel functions. Primary temperature anisotropies are mostly sourced by the Sachs-Wolfe term. The Doppler term generates quadrupole anisotropy on the last scattering surface, which is not dominant for the temperature field, but which is still of great significance for CMB physics, as it sources polarisation anisotropies (see next section). Finally, the ISW term is dominated by effects of varying potential of the line-of-sight *after* the last scattering surface $\dot{\Phi}$, as opposed to the one in the primordial Universe $\dot{\Psi}$, i.e. *before* the last scattering surface. This effect is therefore more often classified as a secondary anisotropy term (see section 2.4.2).

Silk damping

Another effect that needs to be taken into account in the description of primordial anisotropies is the damping of acoustic oscillations by diffusion. Because of acoustic fluctuations, some regions are denser and hotter than others. However, photons continue to diffuse between over-dense and under-dense regions, which damps temperature anisotropies at scales smaller than the diffusion scale. This effect can be modelled as a multiplicative factor to be applied to the source term in Eq. (2.12) for a given scale k:

$$\mathcal{D}(k) = \int_0^{\eta_*} \dot{\tau} e^{-\left(\frac{k}{k_D(\eta)}\right)^2} d\eta, \tag{2.13}$$

where $\dot{\tau}$ is the differential optical depth for Thomson scattering and k_D is the effective diffusion scale. This scale is related to the diffusion characteristic length $\lambda_D = \frac{2\pi}{k_D}$, which estimates how far photons can travel during diffusion. In particular λ_D is inversely proportional to the fraction of ionised electrons and to the baryon number. This effect, known as Silk damping [243] is imprinted in the CMB power spectrum, as described in section 2.5.2.

2.3.2 Polarisation anisotropies

Unlike temperature anisotropies that are directly related to density fluctuations, the generation of polarisation anisotropies in the early Universe is a bit more complex. Polarisation anisotropies are indeed sourced by quadrupolar anisotropies of temperature, and their generation involves differential Thompson scattering of photons by electrons.

Mechanism

Qualitatively, the process for generating polarisation is the following: a photon with a given polarisation direction $\mathbf{p}$ scatters on an electron, and is re-emitted with a polarisation in the direction of emission $\mathbf{p}'$. Since the outgoing polarisation has to be orthogonal to the emission direction, the fraction of incoming radiation whose polarisation is parallel to the emission direction cannot scatter: the outgoing radiation is thus linearly polarised. If the primordial Universe was composed of an isotropic radiation (from a perfectly homogeneous plasma with no anisotropies), there would be no preferred direction for Thompson scattering,

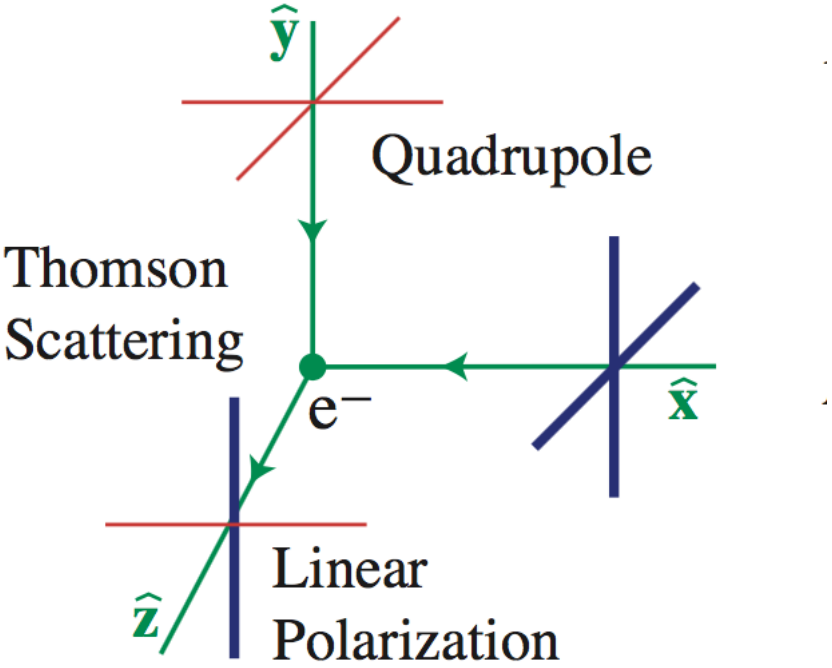

Figure 2.2 – Thomson scattering generating polarised light.
Credit: W. Hu

and thus no specific polarisation signature. Polarisation anisotropies are therefore necessarily sourced by quadrupolar anisotropies, as illustrated in Figure 2.2.

Formally, this is written in the form of a differential cross-section for Thompson scattering :

$$\frac{d\sigma}{d\Omega} = \frac{3}{8\pi}\sigma_T |\mathbf{p}'.\mathbf{p}|^2, \tag{2.14}$$

where Ω denotes a solid angle, and σ_T is the Thompson cross section.

There are two possible sources of quadrupolar temperature anisotropies that can generate polarisation anisotropies. First of all, fluid viscosity generates a quadrupole anisotropy following the velocity field v_b, which sources temperature anisotropies through Doppler shift (see Eq. (2.12). Qualitatively, as we consider the primordial plasma as a perfect fluid, the amplitude of the velocity is out of phase with the amplitude of density fluctuations: the maximum velocity is when density goes through the zero point of the oscillations, and zero velocity when the density is at its extreme, either over- or under- density. There is thus a $\pi/2$ phase shift between density and velocity fluctuations, and adapting again Eq. (2.8), one can write:

$$v_b(\eta_*) \propto \sin(ks_*). \tag{2.15}$$

This phase shift impacts the position of the polarisation power spectrum acoustic peak, as detailed in section 2.5.3.

However, acoustic oscillations are not the only source of quadrupole anisotropy in the early Universe. Primordial gravitational waves - possibly arising from inflation - would also contribute to quadrupolar anisotropies.

These two sources of polarisation anisotropies result in different polarisation patterns. To distinguish those, it is convenient to introduce canonical tools and quantities to describe polarisation: Stokes parameters, and then the so-called E and B-modes.

Stokes parameters

The four Stokes parameters are a basis to describe the polarisation state of any light:

$$\mathbf{S} \equiv \begin{pmatrix} I \\ Q \\ U \\ V \end{pmatrix}, \tag{2.16}$$

where I is the total intensity, directly related to the temperature field T, Q and U are the linearly polarised components, and V is the circularly polarised one. They can be written in the canonical Cartesian coordinate system as:

$$\begin{aligned} I &= |E_x|^2 + |E_y|^2 \\ Q &= |E_x|^2 - |E_y|^2 \\ U &= 2\mathrm{Re}(E_x E_y^*) \\ V &= -2\mathrm{Im}(E_x E_y^*), \end{aligned} \tag{2.17}$$

where E_x (resp E_y) are the two orthogonal components of the electric field. In the standard model, CMB light is not circularly polarised, so only Q and U are considered hereafter.

Although very practical, Stokes component depend on the chosen coordinate system and observing direction on the sky. For a rotation by an angle ψ, they become:

$$\begin{pmatrix} Q' \\ U' \end{pmatrix} = \begin{bmatrix} \cos(2\psi) & \sin(2\psi) \\ -\sin(2\psi) & \cos(2\psi) \end{bmatrix} \begin{pmatrix} Q \\ U \end{pmatrix}. \tag{2.18}$$

Instead of using directly Q and U, quantities invariant by rotation are defined, i.e. independent from the chosen coordinate frame.

E and B-modes

Q and U are combined into spin-2 and spin-(-2) fields that fully describe polarisation:

$${}_{\pm 2}P \equiv Q \pm iU. \tag{2.19}$$

To project this field P on the sphere, we use the spin-2 spherical harmonics basis[3]:

$${}_{\pm 2}P(\theta,\phi) = \sum_{\ell m} {}_{\pm 2}a_{\ell m}\ {}_{\pm 2}Y_{\ell m}(\theta,\phi) \tag{2.20}$$

[3] See Appendix A.

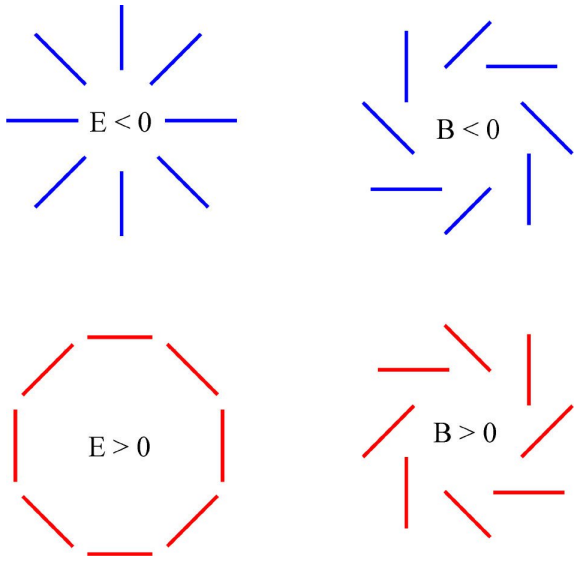

Figure 2.3 – E and B-modes typical patterns

From this, two new quantities can be defined on the sphere: a curl-free scalar field E and a gradient-free pseudo-scalar field B, as shown in Figure 2.3. Their names come from the analogy with electric and magnetic fields, that are respectively curl-free and divergence-free.

In harmonic space, the coefficients of their decomposition in spherical harmonics are:

$$\begin{aligned} a^E_{\ell m} &\equiv -\frac{1}{2}({}_2a_{\ell m} + {}_{-2}\,a_{\ell m}) \\ a^B_{\ell m} &\equiv \frac{i}{2}({}_2a_{\ell m} - {}_{-2}\,a_{\ell m}), \end{aligned} \tag{2.21}$$

where ${}_{\pm2}a_{\ell m}$ are defined in Eq. (A.5). We go one step further and define a spherical harmonic basis for spin-s fields using E and B-modes decomposition:

$$\begin{aligned} {}_s\mathbf{Y}^E_{\ell m} = {}_s\mathbf{D}^E Y_{\ell m} &\equiv \frac{1}{2}\sqrt{\frac{(\ell-s)!}{(\ell+s)!}} \begin{pmatrix} \partial^s + (-1)^s\bar{\partial}^s \\ -i(\partial^s - (-1)^s\bar{\partial}^s) \end{pmatrix} Y_{\ell m} \\ {}_s\mathbf{Y}^B_{\ell m} = {}_s\mathbf{D}^B Y_{\ell m} &\equiv \frac{1}{2}\sqrt{\frac{(\ell-s)!}{(\ell+s)!}} \begin{pmatrix} i(\partial^s - (-1)^s\bar{\partial}^s) \\ \partial^s - (-1)^s\bar{\partial}^s \end{pmatrix} Y_{\ell m}, \end{aligned} \tag{2.22}$$

where the differential operators $\mathbf{D}^E$ and $\mathbf{D}^B$ are a generalisation for arbitrary spin of the operators defined in [41].

These operators form an unique orthogonal basis on the sky, that can be used to decompose the polarisation field $\mathbf{P}$, and coefficients from Eq. (2.21) are rewritten as:

$$\begin{aligned} a^E_{\ell m} &= \int d\Omega\, \mathbf{P}\, {}_2\mathbf{Y}^{E\dagger}_{\ell m} \\ a^B_{\ell m} &= \int d\Omega\, \mathbf{P}\, {}_2\mathbf{Y}^{B\dagger}_{\ell m}. \end{aligned} \tag{2.23}$$

This decomposition is unique only in the case where full sky maps are considered. In real case, the polarisation field is measured only on a fraction of the sky because of limited instrumental and observational capabilities. This introduces some subtleties in the E and B-modes decomposition, see for example in [41, 110].

E-modes are generated through scalar density perturbation, and in particular quadrupolar temperature anisotropy. B-modes however can only be generated by tensor fluctuations arising from primordial gravitational waves[4]. The decomposition into E- and B-modes thus allows to distinguish the source of polarisation anisotropy. As primordial B-modes can only be generated by tensor modes, their detection would be a smoking gun for inflation.

2.4 Secondary anisotropies

We have focused so far on anisotropies generated before or on the last scattering surface, but we mentioned the ISW effect. Indeed, CMB photons do not travel straightforwardly from the last scattering surface to us: they are affected on the way, leading to the so-called secondary anisotropies, i.e. not originating from physics before and at the last scattering surface. They can be broadly divided into two categories: electromagnetic interactions of CMB photons with matter, and impact of gravitational fields[5].

2.4.1 Electromagnetic interactions

Interactions of CMB photons with matter occurs through two well-known scattering phenomenons: Thompson scattering, already mentioned before and which is important during reionisation, and inverse Compton scattering, which describes the interaction of the CMB with hot gas.

Reionisation

Reionisation occurs when first stars form and start emitting energy in the interstellar medium, causing neutral hydrogen atoms formed at recombination to ionise again. Reionisation depends on redshift z and position on the sky θ. However, we observe the line-of-sight integral of reionised regions, and thus an important parameter to characterise the epoch of reionisation is the optical depth to reionisation τ, the line-of-sight integral of the fraction of the free electron from reionisation for a given direction θ. CMB photons can scatter on free electrons released by reionisation, by the same basic physical processes as in the primordial Universe, which generates new - secondary - temperature and polarisation anisotropies, but with different characteristics.

[4] We do not consider here the effect of vector perturbations, because they have decayed by the time of recombination and are therefore not relevant in CMB context.

[5] This section follows the outline of *Secondary anisotropies of the CMB*, Nabila Aghanim, Subhabrata Majumdar & Joseph Silk (2007) [7].

Temperature anisotropies from reionisation can be expressed as a function of the optical depth to reionisation τ:

$$\frac{\Theta_{\text{reion.}}(\theta)}{T} = -\int dz \sigma_T e^{-\tau(\theta,z)} n_e(\theta, z) v_r(\theta, z), \tag{2.24}$$

where σ_T is the Thompson cross-section, v_r is the velocity projected along the line-of-sight and n_e the density of free electrons. Reionisation is not a uniform process, but a patchy one: some regions of the Universe are reionised before others, and regions with different n_e coexist at a given redshift. Temperature anisotropies from reionisation therefore have two contributions. The first ones come from the patchy reionisation effect: CMB light will go through regions that have undergone reionisation at different levels, i.e. they are more or less ionised and do not have the same density of free electrons. On the other hand, even fully reionised regions do not have the same electron densities (depending on the local star formation rate, galaxy density, etc.), hence creating another source of anisotropy.

Moreover, the same way temperature quadrupole anisotropy in the primordial Universe generates polarisation anisotropies, spatial and temporal density fluctuations at reionisation are responsible for secondary polarisation anisotropies due to inverse differential Thompson scattering. In particular, the E-modes signal exhibits particular features due to reionisation, that help constraining reionisation parameters as detailed in section 2.5.3.

Sunyaev-Zel'dovich effects

Contrary to reionisation which is a global effect that affects all CMB photons as they cross the reionisation epoch, Sunyaev-Zel'dovich (SZ) effects are localised, as they are due to interactions of CMB photons with galaxy clusters. More precisely, the SZ effect is caused by inverse Compton scattering between CMB photons and free electrons from hot ionised gas on the line-of-sight [250], for example from jets emitted by Active Galactic Nuclei (AGN). There are two kinds of SZ effects, reflecting two different properties of the hot ionised plasma: the random motion of thermal electrons, producing the thermal SZ effect; and the peculiar motion of electrons having a bulk motion with respect to the CMB, producing the kinetic SZ effect. The two effects lead to secondary anisotropies, and in particular the thermal effect sources localised spectral distortions in the CMB black body spectrum.

The thermal SZ is a bigger effect than the kinetic one, and the resulting anisotropy Θ_{tSZ} with respect to the CMB monopole temperature T is given by:

$$\frac{\Theta_{\text{tSZ}}}{T} = y \left[\frac{2\pi\nu}{T_e} \coth\left(\frac{\pi\nu}{T_e}\right) - 4 \right], \tag{2.25}$$

where T_e is the temperature of the electron gas, and y is the Compton-y parameter, defined as:

$$y \equiv \int_{\text{line of sight}} n_e \frac{T_e}{m_e} \sigma_T ds. \tag{2.26}$$

Thermal SZ is also predicted to produce polarisation anisotropies through differential Thompson scattering of photons in distant galaxy clusters, but this effect has not been detected yet.

As for kinetic SZ, the effect on CMB spectrum is given by:

$$\frac{\Theta_{\rm kSZ}}{T} = -v_r \tau_{\rm cluster}, \tag{2.27}$$

where $\tau_{\rm cluster}$ is the optical depth of intra-cluster medium, and v_r is the radial peculiar velocity of the scattering gas - electrons in this situation.

More than a source of anisotropies when one is interested in the CMB signal, the study of SZ effect is a powerful probe to study galaxy clusters, as detailed in section 2.7.1.

2.4.2 Gravitational fields interactions

As the Universe expands and cools down, density fluctuations evolve into large scale structures such as filaments and galaxy clusters through the gravitational collapse of matter. CMB photons travelling from the last scattering surface to the present time are therefore affected by gravitational potentials on the line-of-sight, which induce both large and small scale effects.

Large scale structures effects

The effect of varying gravitational potentials was already mentioned in the previous section, as the integrated ISW effect: large scale structures in the recent Universe generate gravitational potentials along the line-of-sight, leading to this integrated effect between the observer and the last scattering surface. At first order in perturbations of the gravitational potential, it can be treated as a linear effect: there is no coupling of modes at different scales, but the amplitude at a given scale can be modified. It is mostly visible at large angular scales, where the crossing time is long enough so the change in potential is noticeable.

CMB photons are also affected by more rapidly evolving potentials due to emerging non-linear structures, leading to second order effects. In this regime, this is called the Rees-Sciama effect [223], and it can generate temperature as well as polarisation anisotropies. In particular, it could generate secondary B-modes, hence hindering our capability to detect primordial B-modes [186]. However, the predicted amplitude of the Rees-Sciama effect is well below the amplitude of the most important source of contamination of polarisation anisotropies that cosmologists face in the search for large-scale B-modes: weak gravitational lensing, that mixes E- and B-modes.

Gravitational lensing

Weak gravitational lensing by large scale structures affects both temperature and polarisation anisotropies of the CMB. Contrary to effects previously described, lensing does not generate new anisotropies on its own, but rather modifies pre-existing anisotropies, as different regions of the sky are affected differently depending on what is on the line-of-sight. Primary anisotropies are therefore (de)magnified and shifted in harmonic space, leading to apparent secondary anisotropies.

Formally, this effect can be modelled as a vector field on the sphere, that modifies every apparent direction when looking at the sky:

$$\mathbf{n} \rightarrow \mathbf{n}' \equiv \mathbf{n} + \boldsymbol{\alpha}(\mathbf{n}). \tag{2.28}$$

At first order, since α is at the arc-minute level, it can be modelled as the gradient of a lensing potential ϕ:

$$\boldsymbol{\alpha} \equiv \nabla\phi, \tag{2.29}$$

and the lensed CMB fields are expressed as:

$$\begin{aligned} \tilde{T} &= T(\mathbf{n} + \nabla\phi(\mathbf{n})) \\ \tilde{P} &= P(\mathbf{n} + \nabla\phi(\mathbf{n})). \end{aligned} \tag{2.30}$$

Lensed harmonic coefficients for both temperature and polarisation can be expressed as a function of the lensing potential ϕ as [128]:

$$\tilde{a}^T_{\ell m} = a^T_{\ell m} + \sum_{\ell' m'} \sum_{LM} \phi_{\ell m} a^T_{\ell' m'} \left(F_{\ell m L M \ell' m'} + \frac{1}{2} \phi^*_{L' M'} G_{\ell m L M \ell' m' L' M'} \right) \tag{2.31}$$

$$\tilde{a}^E_{\ell_m} = a^E_{\ell m} + \sum_{\ell' m'} \sum_{LM} \phi_{LM} (-1)^m \, {}_2F_{\ell L \ell'} \begin{pmatrix} \ell & L & \ell' \\ m & -M & -m' \end{pmatrix} (\epsilon_{\ell L \ell'} a^E_{\ell' m'} + \beta_{\ell L \ell'} i a^B_{\ell' m'}) \tag{2.32}$$

$$\tilde{a}^B_{\ell_m} = a^B_{\ell m} + \sum_{\ell' m'} \sum_{LM} \phi_{LM} (-1)^m \, {}_2F_{\ell L \ell'} \begin{pmatrix} \ell & L & \ell' \\ m & -M & -m' \end{pmatrix} (\epsilon_{\ell L \ell'} a^B_{\ell' m'} - \beta_{\ell L \ell'} i a^E_{\ell' m'}), \tag{2.33}$$

with:

$$\epsilon_{\ell L \ell'} \equiv \frac{1 + (-1)^{\ell + L + \ell'}}{2} \tag{2.34}$$

$$\beta_{\ell L \ell'} \equiv \frac{1 - (-1)^{\ell + L + \ell'}}{2}. \tag{2.35}$$

F and G are lensing convolution kernels, whose complete definition can be found in [128], which reviews CMB lensing in harmonic space. For an extensive review of CMB lensing theory, in particular the sources of lensing and how they affect the CMB, one can refer to [163].

One of the most important consequences of CMB lensing, as already shown in Eqs. (2.32 - 2.33), is that it mixes contributions of E and B fields. This raises observational issues when seeking to detect primordial B-modes, as detailed in section 2.5.4.

When observing the CMB from Earth, we measure at once primary and secondary anisotropies, as they are both imprinted in the CMB signal. However, as we mentioned throughout this section, different physical effects generating temperature and polarisation anisotropies leave specific signatures on the CMB signal. In particular, effects can be distinguished in the harmonic domain, using the power spectrum representation.

2.5 Power spectrum

As already introduced in section 1.3.3 when describing quantum field perturbations, the power spectrum is the Legendre transform of the two-point correlation function of a field. A Gaussian field is fully described by this quantity, with no need to compute higher order statistics. In this section, CMB perturbations are assumed to be Gaussian and therefore the power spectrum is sufficient to describe them. We go beyond this assumption and look at CMB non-Gaussianity in section 2.7.3.

2.5.1 Computation

From the decomposition of CMB temperature and polarisation fields in spherical harmonics coefficients $a_{\ell m}$, their power spectrum is expressed as:

$$C_\ell^{XY} = \frac{1}{2\ell+1}\sum_m \langle a_{\ell m}^{X*} a_{\ell m}^{Y} \rangle \tag{2.36}$$

where X and Y could be either T, E or B fields. Assuming statistical isotropy of the CMB, the covariance matrices of two harmonic coefficients are diagonal in ℓ and m, and this expression can be further simplified to obtain:

$$\langle a_{\ell m}^{X*} a_{\ell m}^{Y} \rangle = \delta_{\ell\ell'}\delta_{mm'} C_\ell^{XY}. \tag{2.37}$$

The power spectrum can be computed for a single field with $X = Y$ (auto power spectrum), or for two different fields (cross power spectrum).

C_ℓ are computed by doing the average of $|a_{\ell m}^2|$ measured on an ideally infinite number of sky realisations. However, this is not possible in practice, and an estimator of C_ℓ is used instead, by replacing the mean on an infinite number of sky realisations by the mean on m modes, i.e. $m = 2\ell + 1$ modes for each ℓ:

$$\hat{C}_\ell = \langle |a_{\ell m}^2| \rangle = \frac{1}{2\ell+1}\sum_{m=-\ell}^{\ell} |a_{\ell m}^2|. \tag{2.38}$$

The variance associated with this estimator, known as cosmic variance, is expressed as:

$$\Delta\hat{C}_\ell = \sqrt{\frac{i}{2\ell+1}\hat{C}_\ell^{\,2}}, \tag{2.39}$$

with $i = 1$ for temperature power spectrum, and $i = 2$ for polarisation. For high-ℓ modes, many modes m for each ℓ can be measured, and the cosmic variance is therefore not a limitation with respect to other sources of uncertainty. However, for low ℓ corresponding to large sky regions, the cosmic variance is often a dominant source of uncertainty.

For the CMB, one scalar temperature field T and two polarisation fields Q and U are measured, from which E and B fields are then computed (see section 2.3.2). Six power spectra can therefore be computed: C_ℓ^{TT}, C_ℓ^{TE}, C_ℓ^{TB}, C_ℓ^{EE}, C_ℓ^{EB} and C_ℓ^{BB}, each of them containing different information about CMB physics. The effects described previously, both for primary and secondary anisotropies, have effects at various angular scales, and therefore generate typical patterns in the

power spectra, which I explore hereafter. I start with the temperature auto-power spectrum (section 2.5.2), then polarisation auto- and cross-power spectra (section 2.5.3), and I present effects of lensing on power spectra in a dedicated section (section 2.5.4).

2.5.2 Temperature

In the harmonic domain, CMB temperature anisotropies have an amplitude 10^5 times smaller than the average background temperature. This very low level of anisotropies shows us the remarkable homogeneity of the primordial Universe.

Characteristics

In the temperature power spectrum C_ℓ^{TT}, three main regions can be distinguished, as shown in Figure 2.4.

Sachs-Wolfe region The low ℓ regions ($\ell \lesssim 100$), corresponding to large angular scales, offers a direct snapshot of initial fluctuations since these fluctuations were larger than the Hubble radius at recombination. In this regime, the gravitational potential is constant and fluctuations are not subject to acoustic oscillations. Assuming that the power spectrum is (almost) scale invariant ($n_s \simeq 1$), the power spectrum is flat and [237]:

$$\frac{\ell(\ell+1)}{2\pi} C_\ell \approx \frac{32\pi^3}{9} A_s, \tag{2.40}$$

which corresponds to the so-called Sachs-Wolfe plateau.

At very low ℓ ($\ell \lesssim 5$), there is a small upturn in the power spectrum shape, known as the Integrated Sachs-Wolfe rise. This is due to the effect of time-varying gravitational fields at very large scales. In particular, varying dark energy equation of state could be probed through the ISW rise. Unfortunately, measurement uncertainties in this region of the spectrum are dominated by cosmic variance, which makes it difficult to constrain a specific model.

Acoustic peaks Acoustic peaks are located between $\ell \sim 100$ and $\ell \sim 1000$, with the first (and most prominent) one at $\ell \sim 200$. They are the most distinctive features of the temperature power spectrum, imprints of the acoustic oscillations in the early Universe. There is a range of acoustic peaks in the harmonic space, corresponding to harmonics of the scale defined by the sound horizon. Peaks are thus located at multipoles ℓ_n

$$\ell_n = n\pi \frac{D_*}{r_{s,*}} \tag{2.41}$$

where $r_{s,*}$ is the sound horizon at recombination and n is an integer.

From positions of the acoustic peaks, key parameters of the cosmological model can thus be determined, such as the densities of baryons, dark matter and radiation, as well as the Hubble constant. These acoustic oscillations are also imprinted in the matter field, probed by galaxy cluster distribution, as detailed in section 3.1.1.

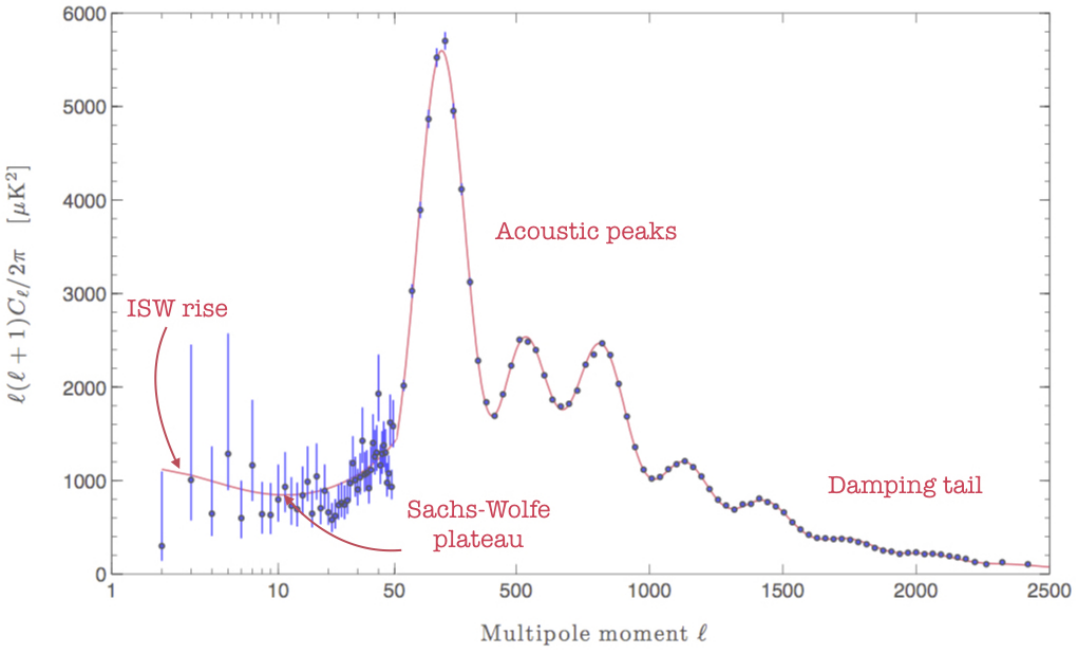

Figure 2.4 – CMB temperature power spectrum and its main regions.
Credit: Adapted from Planck Collaboration [208]

Damping tail For $\ell \gtrsim 1000$, effects of Silk damping (see section 11) dominate the acoustic oscillations, resulting in a progressive cut-off of anisotropies in the power spectrum. Another effect contributing to the damping of the power spectrum is the apparent thickness of the last scattering surface. Since decoupling is not instantaneous, a given observed mode can have contributions from physical oscillation modes that have decoupled at different moments. These contribution do not add coherently, resulting in an effective damping of oscillations, in particular at high ℓ. At very high ℓ ($\ell \gtrsim 4000$), acoustic peaks are not distinguishable anymore, as the effects of secondary anisotropies, in particular Rees-Sciama effect and point sources, become dominant.

Measurements

Although they were predicted in the 1970s (see section 2.1), CMB temperature anisotropies were measured for the first time only in 1992 by the satellite COBE on angular scales larger than 10°. In 2001, two balloon-borne experiments, BOOMERanG (Balloon Observations Of Millimetric Extragalactic Radiation ANd Geophysics) and MAXIMA (Millimeter Anisotropy eXperiment IMaging Array), detected the first acoustic peak, and secondary ones were measured by BOOMERanG as well as DASI[6] (Degree Angular Scale Interferometer). These detections were a major milestone in modern cosmology, since it proved the existence of acoustic oscillations in the early Universe, building the case for the ΛCDM model as standard cosmological model. Although they were much more sensitive than COBE, being ground-based or balloon-borne, these experiments had access to only a limited patch of the sky (less than 1%).

The full-sky measurements of COBE have then been greatly improved by the

[6] https://kicp.uchicago.edu/research/projects/dasi.html

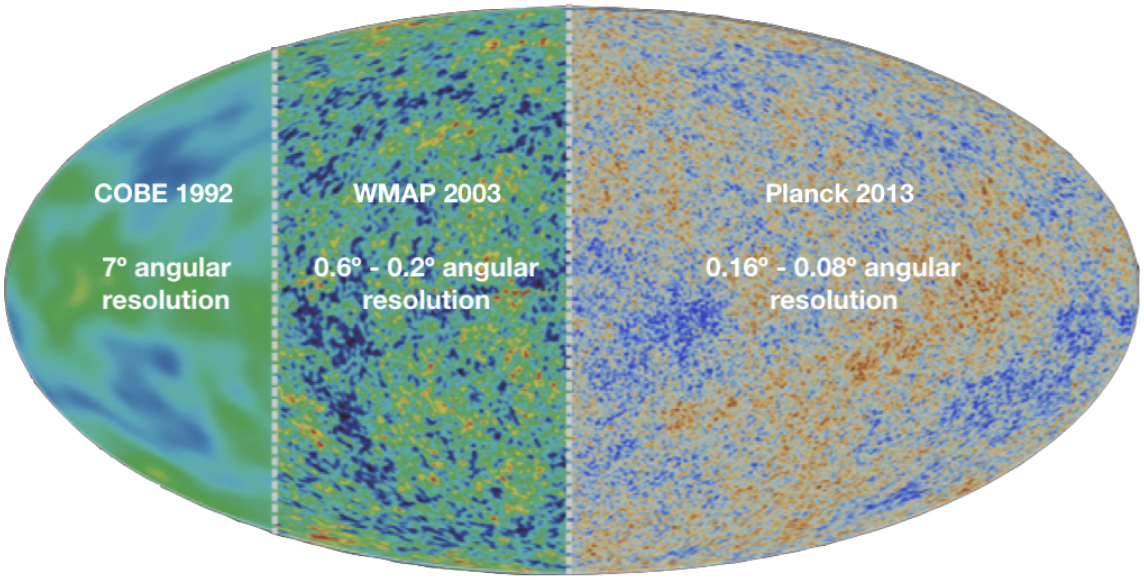

Figure 2.5 – Almost 30 years of CMB temperature anisotropies measurement, from early stages to precision cosmology
Credit: Adapted from ESA and NASA

mission WMAP (Wilkinson Microwave Anisotropies Probe), operating from 2001 to 2010, and most recently by the Planck mission, launched in 2009 and whose first results were released in 2013. The improvement of angular resolution and temperature sensitivity is illustrated in Figure 2.5. The angular resolution has been improved by a factor of 100, which provides an access to smaller angular scales in most recent data sets. This allows not only a better knowledge of the primordial Universe, but also a window into phenomena happening between the observer and the last scattering surface (see section 2.4.1). Today, temperature anisotropy measurements reach the cosmic variance limit down to scales of a few arcminutes.

2.5.3 Polarisation

Polarisation anisotropies are several order of magnitude below those of temperature, which makes them very challenging to detect: Compared to the isotropic temperature field $T = 2.7255$ K, E-modes have a relative amplitude of 10^{-6}, and cosmological B-modes are estimated to be as low as $10^{-7} - 10^{-8}$ - at most.

Characteristics

Just like the temperature ones, polarisation power spectra - observed or predicted - have distinct features, that probe the physical processes already involved in the temperature power spectrum in a complementary way, with the exception

of B-modes that have the potential to probe primordial gravitational waves in an unique way.

EE power spectrum As they arise from the same physical process as temperature anisotropies (i.e. density fluctuations in the primordial Universe), E-modes do not probe new physical processes in the primordial Universe, and their power spectrum has the same global structure as the one of temperature. Because of the phase shift between the velocity field and the density field, E-modes are out of phase with temperature modes in the harmonic domain: a peak in the temperature power spectrum corresponds to a minimum in the E-modes power spectrum, and vice-versa.

Another distinctive characteristic of the E-modes power spectrum arises not from primordial Universe physics, but from reionisation. As outlined in section 2.4.1, inverse differential Thompson scattering during reionisation leads to polarisation anisotropies. In particular, it generates the so-called reionisation bump at low ℓ, as shown in Figure 2.6: the amplitude and position of the bump probes the optical depth to reionisation τ. Note that a - degenerated - measurement of τ can be obtained thanks to the amplitude of the power spectra that scales like $A_s e^{-2\tau}$.

The position of the reionisation peak also gives information about the redshift of reionisation as:

$$\ell_{\text{reion.}} \propto \sqrt{z_{\text{reion.}}} \tag{2.42}$$

Reionisation is the only known physical process that could generate such a bump, and therefore its precise measurement is of importance to constrain the epoch of reionisation better. Unfortunately, as this is a low ℓ effect, observations are limited by cosmic variance. If measured, the primordial B-modes power spectrum C_ℓ^{BB} is expected to exhibit the same structure due to reionisation at low ℓ.

BB power spectrum We focus here on primordial B-modes, and lensing B-modes will be reviewed in more details in the next section. Following Eq. (1.98), the amplitude of the power spectrum of primordial B-modes is directly proportional to the tensor-to-scalar ratio r:

$$C_{\ell,\text{obs}}^{BB} = r\, C_{\ell,r=1}^{BB}. \tag{2.43}$$

As shown in Figure 2.7, for large angular scales, primordial B-modes have a shape similar to that of E-modes, with the reionisation bump clearly visible at low ℓ.

The current upper limit on r, set by the BICEP-2/Keck Array experiment [257] in combination with WMAP and Planck data sets, is $r < 0.06$ with a 95% confidence level[7]. Current and future experiments aim at measuring r as low as $r = 0.001$ (see Chapter 5 for more details). Ground experiments mostly target small patches of the sky and aim at measuring the primordial B-modes recombination peak, at $\ell \sim 80$ (see Figure 2.7), roughly corresponding to a one-degree wide sky patch. This would be a breakthrough in cosmology, as it would bring the first direct observational evidence for inflation. The exact position of the peak

[7] It is possible to constrain the tensor-to-scalar ratio with temperature and E-modes data only. The upper limit set by Planck is $r < 0.11$ at 95 % confidence level [217].

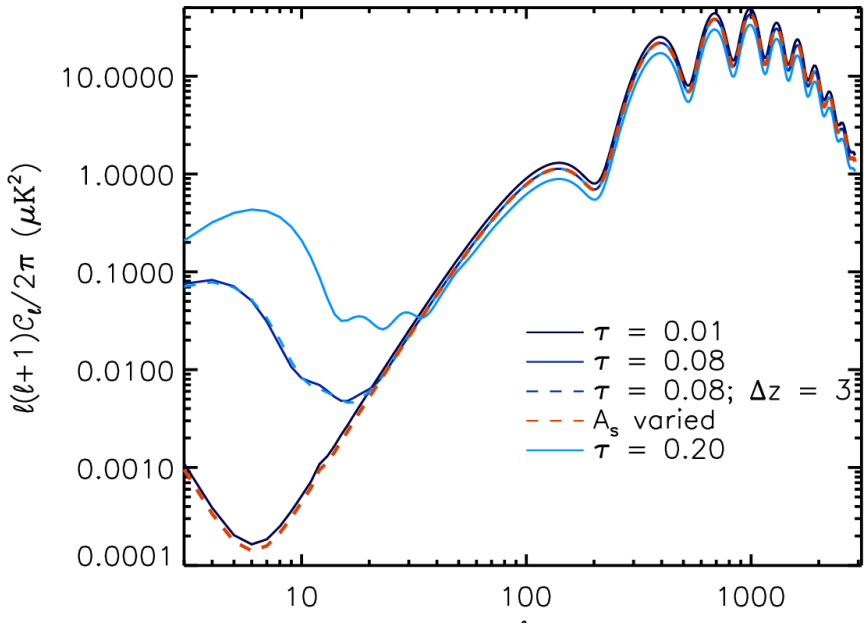

Figure 2.6 – Reionisation bump in E-modes power spectrum, for various values of τ, the optical depth to reionisation. $\Delta z = 3$ refers to an increased duration of reionisation, and A_s is the primordial amplitude of scalar perturbations (see section 1.1.4).
Credit: C. L. Reichardt [224]

would also help constraining some primordial Universe parameters (in particular the sound horizon, used to determine the Hubble constant). However, as for temperature and E-modes, the measurement of the B-modes power spectrum at large angular scales can only be achieved from space.

Cross-spectra In addition to auto spectra (C_ℓ^{TT} for temperature, and C_ℓ^{EE} and C_ℓ^{BB} for polarisation), one can compute three cross-spectra: C_ℓ^{TE}, C_ℓ^{TB} and C_ℓ^{EB}. For parity reasons, since T and E are even fields while B is odd, $C_\ell^{TB} = C_\ell^{EB} = 0$ in standard cosmology. However, we go beyond this assumption in section 2.7.4.

We recall that, roughly speaking, we have:

$$(\Theta + \Psi)(\eta_*) \propto \cos(k s_*) \tag{2.44}$$

for the effective temperature field, and:

$$v_b(\eta_*) \propto \sin(k s_*) \tag{2.45}$$

for the velocity field that sources polarisation anisotropies. The cross correlation of the two fields will then give:

$$(\Theta + \Psi) \times v_b \propto \cos(k s_*) \times \sin(k s_*) \propto \sin(2 k s_*). \tag{2.46}$$

The cross-spectrum between T and E fields, C_ℓ^{TE}, will therefore have oscillations at twice the frequency of those of temperature and E-modes (from the factor 2), in phase with E-modes acoustic peaks (from the sinus term).

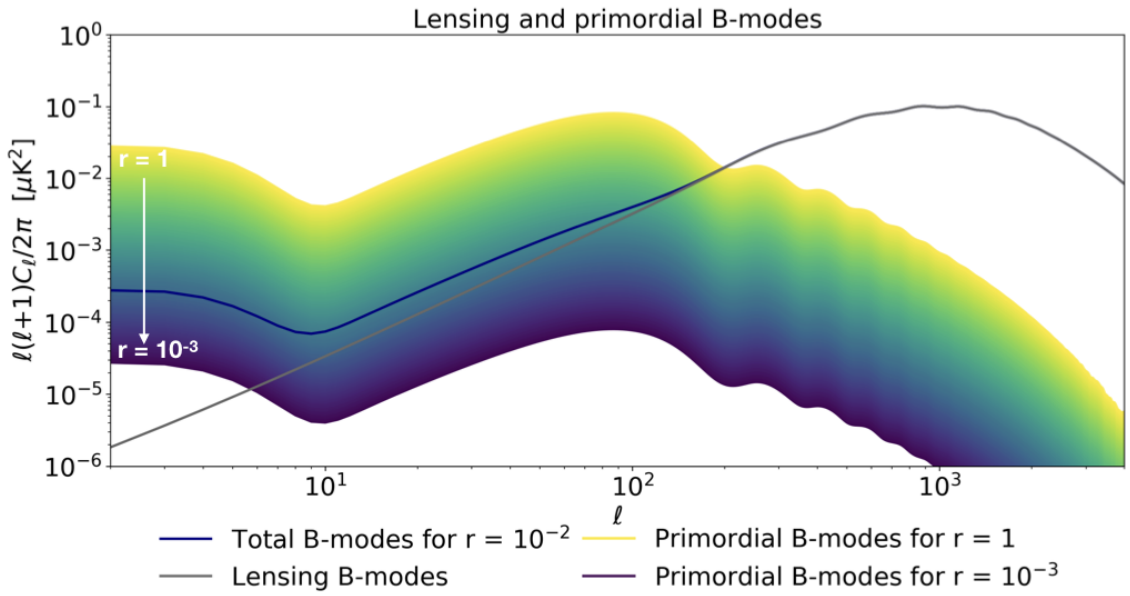

Figure 2.7 – Primordial and lensing B-modes

Finally, let us mention that all spectra (temperature and polarisation, auto and cross) are impacted at low ℓ by primordial gravitational waves from inflation - if it ever occurred. There should therefore be a small excess of power at low ℓ compared to purely scalar perturbations predictions. However, as mentioned already, our observation capabilities are limited by cosmic variance in this part of the harmonic spectrum, and the amplitude of primordial gravitational waves is not large enough to overcome this limitation. This leaves us with no other choice than detecting primordial B-modes if one wants to probe inflationary process!

Measurements

Polarisation E-modes were first detected in 2002 by the DASI experiment [152], and then by various experiments, including WMAP and Planck. Today, they are very well constrained on a wide range of angular scales, but improvements are still possible at very large and small angular scales, where the cosmic variance limit has not been reached yet. The story is more complex when it comes to B-modes. As already mentioned, B-modes are expected to have two main contributions: from lensing, the so-called lensing B-modes, which are E-modes converted to B-modes by weak gravitational lensing, and primordial B-modes arising from a hypothetical inflationary process. Lensing B-modes have first been detected in 2013 by the South Pole Telescope[8] through cross-correlations with the CIB (Cosmic Infrared Background - see section 3.1.4) [117], and this detection was confirmed in 2014 by the POLARBEAR experiment [263], this time using only the B-modes auto-spectrum. Since then, several CMB polarisation experiments have detected lensing B-modes. Most recent measurements of E- and B-modes, as well as TE and TT power spectra are shown in Figure 2.8.

Primordial B-modes, however, have not yet been detected by any experiment, although international efforts aiming at their detection and characterisation is on-

[8] https://pole.uchicago.edu/

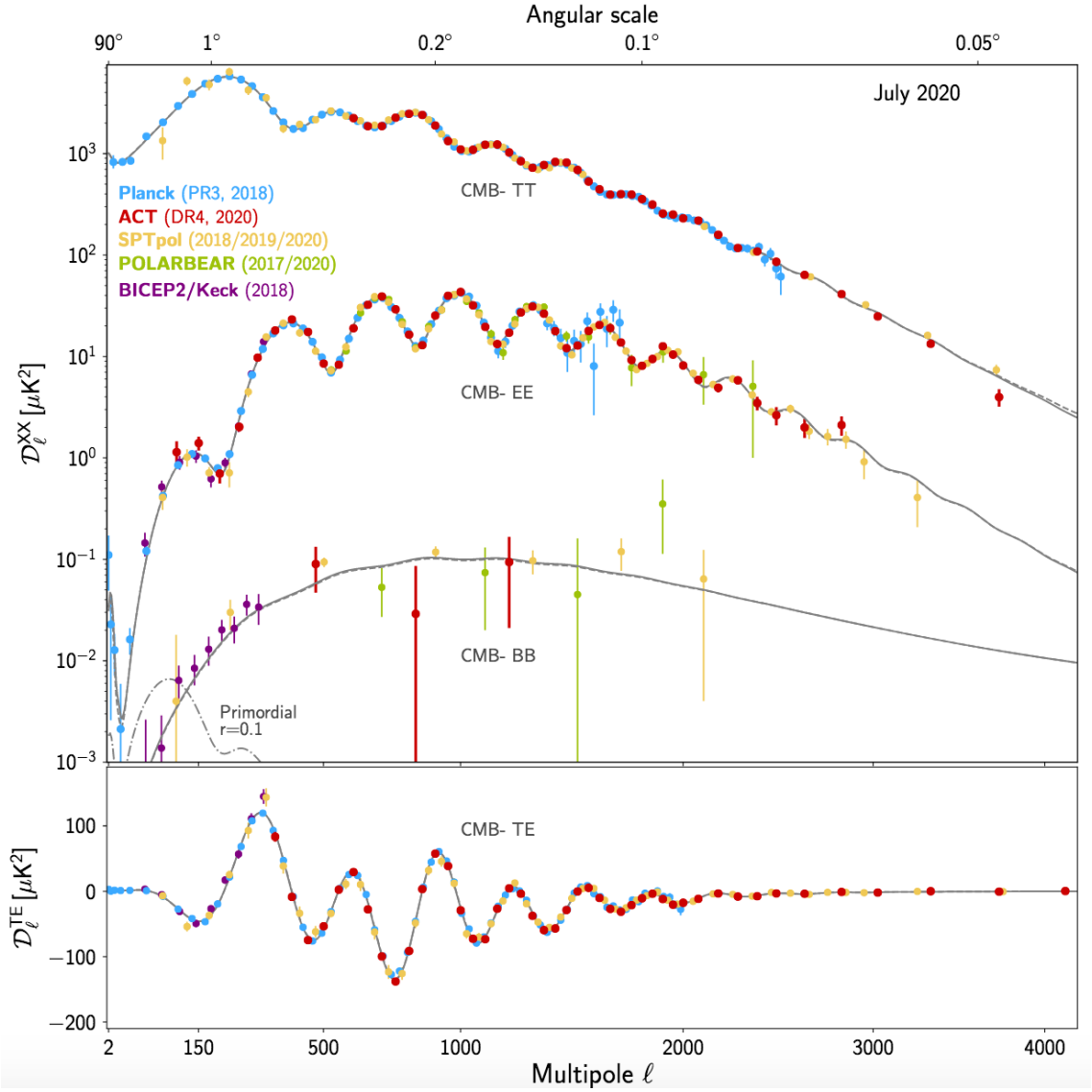

Figure 2.8 – State of the art measurements of CMB power spectra, as of July 2020. *Credit*: The ACT Collaboration [57]

going. In addition to lensing B-modes, polarised foregrounds represent a huge challenge when one tries to detect primordial B-modes. These galactic signals on the line-of-sight between the observer and the CMB can be mistaken for CMB emission and thus hinders our capability to detect primordial B-modes. This topic is reviewed in detail in Chapter 4.

2.5.4 Lensing

Weak gravitational lensing affects all CMB fields, and therefore has a detectable effect on all auto- and cross-spectra. The expression for lensed spectra can be computed using lensed $a_{\ell m}$ in Eqs. (2.31 - 2.33), and leads to [128]:

$$\tilde{C}_\ell^{TT} = [1 - \ell(\ell+1)R]\, C_\ell^{TT} + \sum_{L,\ell'} \frac{F^2_{\ell L \ell'}}{2\ell+1} C_L^{\phi\phi} C_{\ell'}^{TT} \tag{2.47}$$

$$\tilde{C}_\ell^{TE} = [1 - (\ell^2+\ell-2)R]\, C_\ell^{TE} + \sum_{L,\ell'} \frac{F_{\ell L \ell' 2} F_{\ell L \ell'}}{2\ell+1} C_L^{\phi\phi} C_{\ell'}^{TE} \tag{2.48}$$

$$\tilde{C}_\ell^{EE} = [1 - (\ell^2+\ell-4)R]\, C_\ell^{EE} + \frac{1}{2} \sum_{L,\ell'} \frac{{}_2F^2_{\ell L \ell'}}{2\ell+1} C_L^{\phi\phi} \left(\epsilon_{\ell L \ell'} C_{\ell'}^{EE} + \beta_{\ell L \ell'} C_{\ell'}^{BB}\right) \tag{2.49}$$

$$\tilde{C}_\ell^{TB} = [1 - (\ell^2+\ell-2)R]\, C_\ell^{TB} + \sum_{L,\ell'} \frac{F_{\ell L \ell' 2} F_{\ell L \ell'}}{2\ell+1} C_L^{\phi\phi} C_{\ell'}^{TB} \tag{2.50}$$

$$\tilde{C}_\ell^{EB} = [1 - (\ell^2+\ell-4)R]\, C_\ell^{EB} + \frac{1}{2} \sum_{L,\ell'} \frac{{}_2F^2_{\ell L \ell'}}{2\ell+1} C_L^{\phi\phi} \left(\epsilon_{\ell L \ell'} C_{\ell'}^{EB} - \beta_{\ell L \ell'} C_{\ell'}^{EB}\right) \tag{2.51}$$

$$\tilde{C}_\ell^{BB} = [1 - (\ell^2+\ell-4)R]\, C_\ell^{BB} + \frac{1}{2} \sum_{L,\ell'} \frac{{}_2F^2_{\ell L \ell'}}{2\ell+1} C_L^{\phi\phi} \left(\beta_{\ell L \ell'} C_{\ell'}^{EE} + \epsilon_{\ell L \ell'} C_{\ell'}^{BB}\right), \tag{2.52}$$

where $C_\ell^{\phi\phi}$ is the lensing power spectrum, F, $\epsilon_{\ell L \ell'}$, $\beta_{\ell L \ell'}$ are defined in section 2.4.2 and:

$$R \equiv \frac{1}{2} \sum_L \frac{2L+1}{4\pi} C_L^{\phi\phi}. \tag{2.53}$$

R is the total deflection angle power, which physically corresponds to the angle by which a CMB photon would be deflected before its detection, in average. For typical models, $R \sim 3 \times 10^{-7}$, corresponding to an angle of ~ 2.7 arcminutes [163].

Note that a couple of assumptions were made to derive Eq. (2.47 - 2.52), in particular the Gaussianity of the lensing field, and consequently the computation was done only at the lowest order in $C_\ell^{\phi\phi}$. This set of equations is thus only exact up to a few percent on the final spectra. The amplitude of the lensing power spectrum $C_\ell^{\phi\phi}$ can be parametrised with a single parameter A_L, with $A_L = 1$ in the fiducial ΛCDM model.

It is clear from Eq. (2.52) that lensing B-modes can be generated from unlensed E-modes (and vice versa), whereas other spectra only see their shape modified by lensing. In particular, lensing induces an excess of power below $\ell \sim 100$. It also boosts non-Gaussianity at small scales, that can hinder the detection of primordial non-Gaussianity (see section 2.7.3). Lensed and unlensed power spectra are shown in Figure 2.9. The effect of lensing is more important on B-modes: primordial E-modes have an amplitude several orders of magnitude higher than primordial B-modes, and thus the E-to-B leakage induced by lensing is much more important than the B-to-E one. This is all the more true for low values of the tensor-to-scalar ratio r, as shown in Figure 2.7: in the range of r values that are currently investigated (i.e. below $r = 0.06$ which is the current upper limit), primordial B-modes are dominated by lensing B-modes.

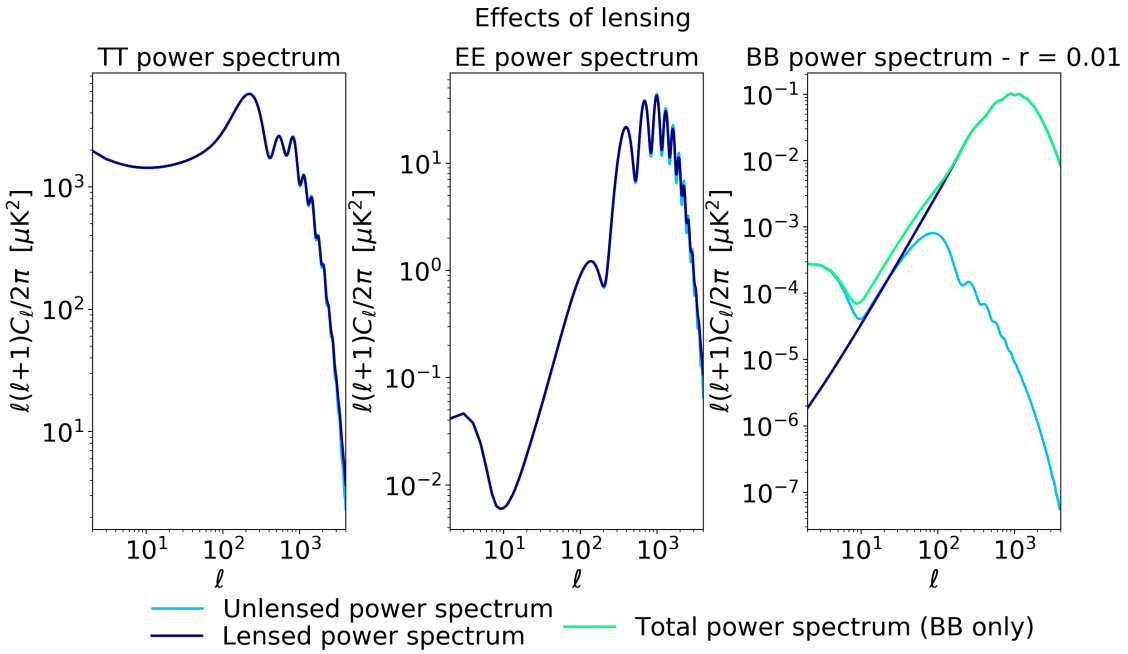

Figure 2.9 – Effects of lensing on power spectra

2.6 From observations to cosmological models

Power spectra thus have distinctive, easy-to-identify features, such as peaks position, that allow us to determine certain properties of the Universe. moreover, most of cosmological parameters - such as ΛCDM parameters - can be straightforwardly inferred from power spectra.

Another facet of power spectra analysis is the lensing analysis, in which the lensing potential is estimated, and used to constrain cosmological parameters. Once the lensing potential is estimated, the lensing effects on the CMB spectra can be potentially removed in the so-called delensing process.

2.6.1 Cosmological parameters estimation

We start with the estimation of cosmological parameters from power spectra, in particular base ΛCDM parameters introduced in section 1.1.4. Other cosmological parameters defined earlier can be derived from these base parameters, such as the Hubble constant, and the model can also be extended to allow for other parameters to vary, such as the curvature parameter which is otherwise fixed to zero in ΛCDM.

The favoured method in observational cosmology to infer values of parameters from data is the Bayesian framework, which I quickly describe hereafter. This framework is of course not limited to the estimation of cosmological parameters from power spectra, and it will be used many times in this manuscript to infer values of parameters in various cases of interest.

Elements of Bayesian statistics

Given a data set D (power spectrum, maps, or any other observable), we want to test the degree of belief of an hypothesis H, derived from theoretical model. Bayes' theorem states that this quantity, also called the posterior, is given by:

$$p(H|D) = \frac{p(D|H)p(H)}{p(D)}, \tag{2.54}$$

where $p(H)$ is the prior, i.e. what we know or assume about the model, $p(D)$ is the evidence, i.e. what we observe, and $p(D|H)$ is the likelihood, i.e. the probability of the data given the hypothesis. While standard Bayesian approaches maximise the prior, in cosmology, the determination of parameters is most often done by maximising the likelihood to determine the best-fit. For an observed data set, the probability distribution of the data is maximised as a function of the parameters, for one or several data models. One must however note that, even if parameters are inferred with a good precision as the maximum-likelihood best fit, they might not be a good description of the reality if the underlying model is a bad description of the data. It is thus very important to note that this approach provide a best-fit for parameters for a given theoretical framework, but does not asses whether the data is even compatible with the chosen framework.

This formalism also makes it possible and relatively straightforward to include constraints on parameters coming from other data sets, by including them in the prior or in the evidence. This approach is more and more put into practice in the era of multi-probe cosmology (see Chapter 3). However, one of the drawbacks is that it can be computationally expensive to characterise the posterior in a wide, multi-dimensional parameter space. In many applications, these methods can be replaced by sampling of the parameter space, by using Markov chain Monte Carlo (MCMC) to alleviate this difficulty. MCMC methods build a chain in the parameter space, so that its samples are distributed according to the posterior probability. It allows to sample preferentially areas of the parameter space where the posterior is important, without spending too much time in a subset of the parameter space which is far from the peak of the likelihood. This allows for higher convergence speed and improved performance.

Application to CMB data sets

I give here a practical example of a cosmological parameter likelihood, based on the approach used in e.g. [267], and close to the approach that we adopt in Chapter 8. We want to estimate cosmological parameters from an observed power spectrum. The observed power spectrum is usually split in several ℓ-bins, or bandpowers b, (e.g. $50 \leqslant \ell \leqslant 100$, $100 < \ell \leqslant 150$, etc.), that are chosen so that the signal has similar properties, in particular in terms of noise and foreground contaminations, that can both significantly differ at various angular scales. For each bandpower, we then form the data covariance matrix $\hat{\mathbf{C}}_b$, composed of all power spectra for all observing frequencies. Assuming a model $\mathbf{C}_b$ for the data covariance matrix, the cosmological parameter likelihood can be written as (up

to a constant):

$$-2\log\mathcal{L} \equiv \sum_b \nu_b \times \left[\mathrm{tr}(\hat{\mathbf{C}}_b\mathbf{C}_b^{-1}) - \log\det(\hat{\mathbf{C}}_b\mathbf{C}_b^{-1}) - n_{\mathrm{freq}}\right], \tag{2.55}$$

where ν_b is the number of degrees of freedom per bandpower b.

If we want to estimate for example the Hubble constant, we express the true covariance matrix $\mathbf{C}_b$ as a function of the Hubble constant following the underlying cosmological model. By minimising the likelihood Eq. (2.55) with respect to this parameter, one then finds the best-fit value for the Hubble constant, in the underlying model.

Moreover, we note that the model $\mathbf{C}_b$ should contain not only a cosmological model for the parameter of interest, but also other contributions to the signal. In particular, if the CMB map used to compute $\hat{\mathbf{C}}_b$ is derived from a data set containing foreground and instrumental contribution, the model $\mathbf{C}_b$ has to be amended for these contributions to deproject them. If not, this can lead to bias in the determination of cosmological parameter, as discussed in Chapter 8.

2.6.2 Delensing

As mentioned in the previous section, weak gravitational lensing by large scale structures modifies the shape of CMB power spectra, and mixes E- and B-modes. In the specific case of B-modes, delensing the CMB signal allows to access pristine, unlensed CMB power spectra, and thus improve constraints on cosmological parameters, in particular the tensor-to-scalar ratio. Moreover, the reconstructed lensing signal itself enables to constrain parameters relative to structure formation rate and evolution. Lensing analysis is thus a complementary analysis to the cosmological parameters estimation we just described, and can deliver information about other processes and epochs of the history of the Universe.

Reconstructing the lensing potential

The first step in lensing analysis is to reconstruct the lensing potential $C_\ell^{\phi\phi}$. To do so, one can use either CMB or non-CMB data.

Lensing reconstruction from CMB When observing the CMB, we measure the lensed signal, and the unlensed CMB signal is not a priori known. One thus has to rely on statistical information to reconstruct the lensing field from CMB data. One of the most popular method is to use quadratic estimators built from CMB temperature and polarisation measurements. I present here the basis of this method in the simplified case of full and flat sky. I follow the approach of [194], which one should refer to for detailed derivation and more complex cases.

As shown in Eq (2.47 - 2.52), lensing mixes CMB fields from different multipoles, and therefore correlates modes over a range that depends directly on the deflection angle R. We assume here that, similarly to CMB fields, the lensing field is isotropic and Eq. (2.37) is thus correct to define lensed power spectra:

$$\langle \hat{a}^{X*}_{\ell m}\hat{a}^{X'}_{\ell m}\rangle = \delta_{\ell\ell'}\delta_{mm'}\hat{C}_\ell^{XX'}, \tag{2.56}$$

Considering an ensemble of CMB fields (T,E,B) lensed by a fixed deflection field, this is however not true anymore. The multipole covariance for two fields (X,Y) is written as:

$$\langle \hat{a}^{X*}_{\ell m} \hat{a}^{Y}_{\ell m} \rangle = \delta_{\ell\ell'}\delta_{mm'} C^{XY}_{\ell} + \sum_{LM} (-1)^M \begin{pmatrix} \ell & \ell' & L \\ m & m' & -M \end{pmatrix} f^{XY}_{\ell L \ell'} \phi_{LM}, \tag{2.57}$$

with $f^{XY}_{\ell L \ell'}$ defined as:

$$f^{XY}_{\ell L \ell'} \equiv {}_{s_X}F_{\ell L \ell'} \left[\epsilon_{\ell L \ell'} \hat{C}'^{XY}_{\ell} + \beta_{\ell L \ell'} \hat{C}'^{Y\bar{X}}_{\ell} \right] + {}_{s_Y}F_{\ell' L \ell} \left[\epsilon_{\ell L \ell'} \hat{C}^{XY}_{\ell} + \beta_{\ell L \ell'} \hat{C}^{Y\bar{X}}_{\ell} \right], \tag{2.58}$$

where s_X and s_Y are the spin of the associated field (1 for temperature and 2 for polarisation), and $\bar{X}$ refers to the parity complement of X:

$$\begin{aligned} \bar{T} &= 0 \\ \bar{E} &= -B \\ \bar{B} &= E. \end{aligned} \tag{2.59}$$

For a given observed realisation of the lensing field ϕ_{LM}, we construct an estimator of the deflection as a weighed sum on multipole pairs:

$$\hat{\phi}^{XY}_{LM} \equiv \frac{A^{XY}_L}{\sqrt{L(L+1)}} \sum_{\ell m} \sum_{\ell' m'} (-1)^M \begin{pmatrix} \ell & \ell' & L \\ m & m' & -M \end{pmatrix} g^{XY}_{\ell\ell'}(L) \hat{a}^{X}_{\ell m} \hat{a}^{Y}_{\ell' m'}, \tag{2.60}$$

where $g^{XY}_{\ell\ell'}(L)$ are the weights, and A^{XY}_L is a normalisation factor. We require that the estimator is unbiased over CMB realisations for a fixed lensing field, i.e.:

$$\langle \hat{\phi}^{XY}_{LM} \rangle = \sqrt{L(L+1)} \phi_{LM}, \tag{2.61}$$

which leads to:

$$A^{XY}_L = L(L+1)(2L+1) \left[\sum_{\ell\ell'} g^{XY}_{\ell\ell'}(L) f^{XY}_{\ell L \ell'} \right]^{-1}. \tag{2.62}$$

The minimum variance estimator is then derived by minimising the variance of the estimator $\langle \phi^{XY*}_{LM} \phi^{XY}_{LM} \rangle$ with respect to the weights. One thus finds that:

$$g^{XY}_{\ell\ell'}(L) = \frac{C^{XX}_{\ell'} C^{YY}_{\ell} f^{XY*}_{\ell L \ell'} - (-1)^{\ell+L+\ell'} C^{XY}_{\ell} C^{XY}_{\ell'} f^{XY*}_{\ell' L \ell}}{C^{XX}_{\ell} C^{XX}_{\ell'} C^{YY}_{\ell} C^{YY}_{\ell'} - (C^{XY}_{\ell} C^{XY}_{\ell'})^2}. \tag{2.63}$$

Lensing reconstruction with non-CMB data Another option to estimate the lensing potential is to use external matter field tracers such as galaxy surveys or the CIB, as they probe the same underlying matter distribution (see section 3.1.1 for a more detailed review on ways to probe the matter distribution). The method used to estimate the lensing potential is similar to the one above that uses CMB data, with the notable difference that matter power spectra are used instead of CMB power spectra.

The reconstruction of the lensing potential using CMB data proves difficult to extend to small scales ($\ell \gtrsim 1000$). As temperature anisotropies are dominated by secondary anisotropies other than lensing, this requires the measurements of polarisation anisotropies at high resolution [191, 241], which depends on the beam size of the instrument and its sensitivity. The reconstruction at small scales is not an issue when using the matter power spectrum, that can probe the matter field at very high ℓ, better than CMB polarisation, and these methods are forecasted to be more efficient than internal reconstruction [173, 244]. However, they come with two main drawbacks: they potentially source additional biases, as some effects are not controlled (in particular instrumental systematics), and they do not probe high redshift sources that contribute to the CMB lensing potential.

Delensing in practice

Lensing B-modes are a major contaminant to primordial B-modes, as shown in Figures 2.7 and 2.9. This is all the more true for modern experiments targeting low values of r. The general idea of delensing is to estimate the lensing B-modes power spectrum and to subtract it from the observed B-modes spectrum so to keep only primordial B-modes. In practice, this is done by using Eq. (2.52) (or an equivalent expression derived at higher order), which requires an estimation of the lensing potential, obtained by either external or internal delensing.

Moreover, we note that lensing of E into B-modes appears as a white noise (independent of the angular scale) contaminant, equivalent to a $\simeq 5\mu\mathrm{K.arcmin}$ noise level. If the instrumental noise in polarisation is much higher than this level, delensing does not have much impact, as the instrumental noise dominates the uncertainty. The characterisation of the polarisation noise is usually achieved using E-modes measurements: since primordial B-modes are low, one can assume that the leakage from B to E-modes due to lensing is negligible. One can therefore use E-modes as a tracer for polarisation instrumental noise. This is also true for other instrumental characteristics that have to be precisely characterised using E-modes data as they could bias lensing reconstruction if not properly taken into account [249].

Some experiments, such as the Simons Observatory and LiteBIRD, do not plan on delensing to achieve baseline performance, while other experiments, such as CMB-Stage 4, assume a certain level of delensing in the science forecast (see Chapter 5). One should note that, in nearly all cases, there is something to gain if delensing is performed successfully.

Constraining the early Universe

To conclude this section on lensing and delensing, one should not forget that lensing B-modes are not only a contaminant in the search for primordial B-modes, but also a probe to study early Universe physics and structure formation, in particular the dark energy equation of state and the sum of neutrino masses [163].

Dark energy As a tracer of large scale structures and matter distribution, lensing is sensitive to the dark energy equation of state parameter (for an equation of

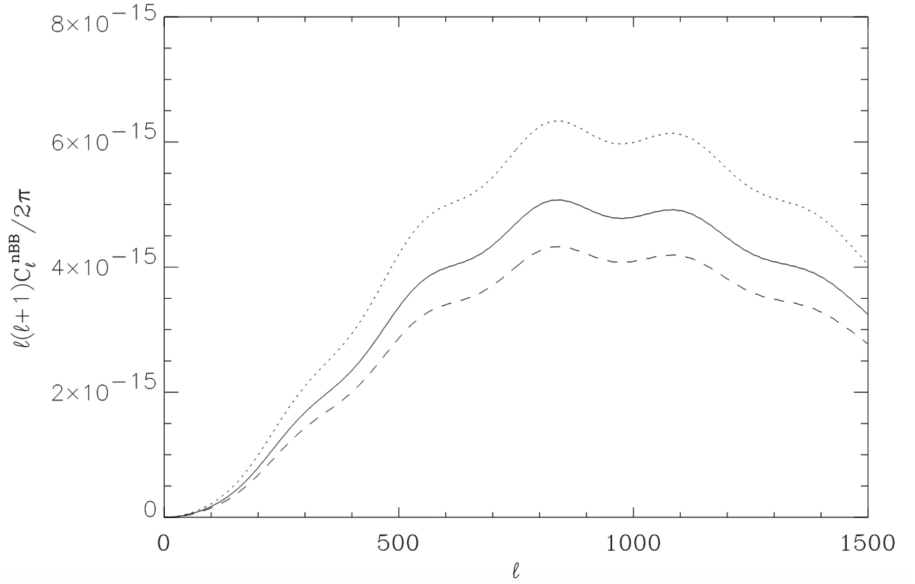

Figure 2.10 – B-modes power spectrum for various of values of w_0 and w_a (from top to bottom): $w_0 = 0.8$ and $w_a = 0.24$ (dotted line), $w_0 = 0.9$ and $w_a = 0.5$ (solid line), $w_0 = 0.965$ and $w_a = 0.665$ (dashed line).
Credit: V. Acquaviva & C. Baccigalupi [3]

state as defined in Eq. (1.25)):

$$w(a) = w_0 + w_a(1 + a), \tag{2.64}$$

where w_0 is the current value, and w_a its derivative with respect to the scale factor a. Dark matter models predict various values for these parameters, and a way to probe them is by using CMB lensing power spectra [3]. In particular, the position of the B-modes lensing peak is sensitive to these parameters, as shown in Figure 2.10.

Neutrinos Although very hard to detect because of the low interaction rate, the cosmological neutrino number density is the second highest in the Universe after CMB photons (see section 3.3.2 on the Cosmic Neutrino Background). Therefore, even if their masses are very small, they play an important role in the dynamics of the Universe. In particular, large cosmic scales are sensitive to neutrinos effects.

In the early Universe, neutrinos are fully relativistic, and therefore are part of the radiative energy content of the Universe (and not the matter one). Their contribution to the energy density can be written as

$$\rho_{\nu,\mathrm{rad}} = \rho_\gamma \left[1 + \frac{7}{8}\left(\frac{4}{11}\right)^{\frac{4}{3}} N_{\mathrm{eff}}\right], \tag{2.65}$$

where N_{eff} is the so-called effective number of relativistic species. If neutrinos decoupled instantaneously from radiation and had no flavor oscillations, N_{eff} would be equal to 3. Theoretical models, taking into account QED corrections, predict $N_{\mathrm{eff}} = 3.045$ [75]. The best currently available constraint, derived from lensing

observations by Planck combined with measurements of Baryon Acoustic Oscillations (BAO - see section 3.1.1) is [215]:

$$N_{\rm eff} = 2.99 \pm 0.17, \tag{2.66}$$

in good agreement with the predicted value.

Once neutrinos have become non relativistic at low redshift, they have to be considered as matter rather than radiation, and their density parameter can be expressed as follows:

$$\Omega_\nu h^2 = \frac{\Sigma m_\nu}{93.14\text{eV}}, \tag{2.67}$$

where the sum is taken over all three neutrino species. The effect of massive neutrinos on the (unlensed) CMB power spectrum can be detected at low ℓ because of the ISW effect (see section 2.4.2), but this is not enough to constrain neutrino masses because of cosmic variance limitations.

The lensed power spectrum is however more sensitive to these effects. Before becoming non-relativistic, neutrinos free stream regardless of primordial density fluctuations, and they suppress power in the matter power spectrum on scales below the matter-radiation equality scale. One can therefore use the CMB lensing signal to reconstruct the matter lensing potential and power spectrum, and therefore constrain the sum of neutrino masses through large scale structures formation. The best upper limit on neutrino masses comes from the combination of CMB anisotropies and lensing, Lyman-α and BAO data [197]:

$$\Sigma m_\nu < 0.09\,\text{eV}, \tag{2.68}$$

at 95 % confidence level.

These two quantities - $N_{\rm eff}$ and Σm_ν - play a key role in cosmology, and impact in particular the expansion rate as well as the CMB and matter power spectra. Neutrino physics, in particular the precise determination of their masses, is a rich and active area of research, where cosmologists and particle physicists work side by side. In particular, a value of $N_{\rm eff}$ higher than the standard model prediction could be a hint for new physics beyond the standard model, including axions [52, 174], sterile neutrinos [2], or even dark photons, which would interact with dark matter. The currently available constraints will also be improved thanks to the deployment of experiments dedicated to large scale structures formation and evolution, such as the Dark Energy Spectroscopic Instrument[9] (DESI), the Vera Rubin Observatory and the space mission Euclid.

2.7 CMB observables beyond anisotropies

Over the past 30 years, more and more observations of the CMB have accumulated, mostly measurements of its temperature and polarisation anisotropies, all of them remarkably confirming the standard cosmological model[10]. The detection of primordial B-modes would be a long awaited confirmation of inflation

[9] https://www.desi.lbl.gov/

[10] The Hubble constant measurement discrepancy is currently the main tension in the ΛCDM model, but as discussed in section 1.1.4 there are several leads to release this tension.

theories. More than that, once they are detected, measurement of their angular power spectrum over a wide range of scales would open the way for new physics, probing always further the primordial Universe.

Besides temperature and polarisation anisotropies, other characteristics of the CMB signal can be used to detect and study the hypothetical inflationary process. They are also powerful probes to learn about the Universe and physics in a broader frame. Localised spectral distortions due to the Sunyaev-Zel'dovich effects have been detected as early as 1983, but large population studies and precise measurements are only a mere ten years old, and are a promising new probe for galaxy clusters science as I detail in section 2.7.1. When it comes to larger angular scale effects, global spectral distortions (section 2.7.2) - deviation from the monopole signal on large angular scales - and primordial non-Gaussianity (section 2.7.3) have gathered the most interest in the prospect of future experiments. In particular, spectral distortions are a very rich topic, since they can be used to probe not only inflation, but also other physical processes. Finally, in section 2.7.4, I introduce cosmic birefringence, an effect predicted by various models going beyond standard physics, that would potentially affect CMB polarisation.

2.7.1 Cluster science with the Sunyaev-Zel'dovich effect

The CMB is a snapshot of the Universe 300 000 years after the Big-Bang. As I already mentioned, primary over-densities later evolved to form large scale structures observed today. Between the last scattering surface where it is emitted and its detection on Earth, CMB photons travel through 13 billion years of Universe history. Although these interactions are hindering our capabilities to detect primordial features in the CMB signal, we can also make use of them to probe physics taking place between the last scattering surface and us, and in particular to study galaxy cluster formation and properties.

Galaxy clusters

Galaxy clusters are gravitationally bound structures consisting of hundreds to thousands of galaxies. They are the biggest structures to decouple from the overall expansion of the Universe, and were long thought to be the biggest structures of the Universe, until superclusters were discovered in the 1980s. Yet, with their masses of 10^{14} - 10^{15} solar masses and radius of a few to 10 Mpc, they are amongst the most massive objects in the Universe. This is true only to a certain extent since the existence of superclusters and cosmic filaments has been confirmed (as shown in Figure 1.5, but these bigger structures are not gravitationnaly bound.

Between galaxies forming a cluster, there is diffuse hot gas, the so-called intracluster medium (ICM). The ICM accounts for $\sim$ 10 % of a typical cluster mass, while galaxies themselves host only $\sim$ 1 % of the total mass, and dark matter accounts for all the remaining mass. Galaxy clusters can be observed from the ground in visible light, but they also strongly emit in the X-ray domain, not observable from the ground. The development of high-resolution, space-based X-ray observatories such as Chandra[11] and XMM-Newton[12] have allowed to probe

[11] https://chandra.harvard.edu
[12] https://sci.esa.int/web/xmm-newton/

high energy processes such as shock waves resulting from AGN.

Imaging clusters with the CMB

Introduced in section 2.4.1, Sunyaev-Zel'dovich effects (thermal and kinetic) are the reverse Compton scattering of CMB photons by the hot ICM. The thermal SZ effect induces a localised distortion of the CMB spectrum, with a reduced intensity at low frequency and an enhanced one at high frequency. This localised effect requires high angular and spectroscopic resolutions in CMB observation to be detected: predicted in 1972, the thermal effect was detected for the first time in three galaxy clusters in 1984 [35], and the kinetic one only in 2012, both in an individual cluster [188] and in a statistical study of a wide cluster population [115]. SZ clusters have been mapped by Planck [212], and are considered as a foreground that has to be removed when one is interested in CMB anisotropies.

However, SZ effects are not just a contaminant to CMB. Thanks to new high resolution ground-based telescopes, we are now able to image SZ clusters in the radio domain with a high angular resolution, up to 20″ with NIKA[13] [5], and up to 5″ thanks to interferometry with ALMA[14] [145]. These high resolution observations, combined with X-ray observations, are a powerful probe to explore cluster science and the ICM, and in particular the distribution of matter and dark matter in galaxy clusters.

The X-ray intensity probes the electron density n_e along the line-of-sight dl:

$$I_X = \int dl\, n_e^2\, \Lambda(T_X), \tag{2.69}$$

where $\Lambda(T_X)$ is the X-ray luminosity, and the SZ intensity probes the electron temperature T_e:

$$I_{SZ} = g_\nu \frac{\sigma_T}{m_e} \int dl\, n_e\, T_e. \tag{2.70}$$

The comparison of images at the same angular resolution therefore enables studies of gas dynamics inside clusters, as shown for example in Figure 2.11. Such observations have allowed to establish that gas motion in ICM shocks is sub-sonic [273], and to reveal typical gas structures showing the dynamical state of the ICM [6]. In particular, using the two observing frequencies of NIKA2 (150 GHz and 260 GHz), the kinematic Sunyaev-Zel'dovich effect was resolved for the first time in a cluster in 2016 [4]. In particular, it revealed the dynamic inside the cluster, with sub-clusters moving away and toward us, as shown in Figure 2.12.

These structures thus probe history and evolution of cluster formation, as well as the local gravitational potential. This is of particular interest when one aims at constraining the matter and dark matter distributions. Moreover, the SZ intensity does not depend on redshift, when the X-rays scale as $(1+z)^{-4}$. At larger scales, the cross-correlation of SZ maps with cluster maps at known redshift will allow to map the gas pressure as a function of redshift, and thus help us progress in our

[13] https://ipag.osug.fr/nika2/Welcome.html
[14] https://www.almaobservatory.org/en/home/

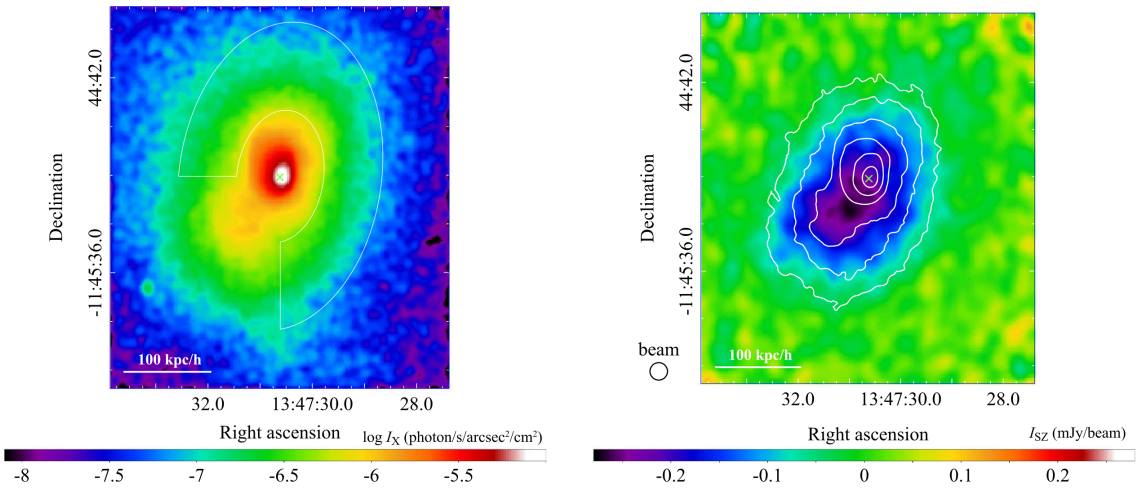

Figure 2.11 – Surface brightness of the X-ray (left) and the SZE (right) of RX J1347.5–1145. The green cross marks the position of the central AGN. *Credit*: S. Ueda et al. [273]

knowledge of large scale structure formation and evolution. To continue investigating these effects with better sensitivity, several CMB experiments such as the Simons Observatory or CMB-Stage 4 (see section 5.3.1) plan to have programs dedicated to SZ science. The Cerro Chajnantor Atacama Telescope [15] CCAT-prime, that should see first light in 2021, will also be partly dedicated to study of SZ effects.

2.7.2 Spectral distortions

As detailed in the first chapter and shown for example in Figure 1.4, the CMB spectrum follows the Planck's law up to the 10^{-5} level. However, spectral distortions are predicted by several processes, including inflation.

Typology

There are three main types of spectral distortions that can possibly be observed in the CMB. All three types are related to effects taking place before or at the time of recombination. Before recombination, the primordial plasma can be heated by high energy processes, injecting photons at a temperature greater than the background temperature. If this happens at high enough redshifts ($z > \text{few} \times 10^6$), thermalisation processes such as Compton scattering are efficient enough so that no spectral distortions are created, but the background temperature of the plasma slightly increases, as shown in Figure 2.13. If the energy release occurs at lower redshifts, two types of distortion can be distinguished depending on the redshift, known as y and μ distortions. Later, around recombination, the free-free distortion also affects the CMB spectrum at low frequency. One can refer to [54] for a comprehensive review.

[15] https://www.ccatobservatory.org/

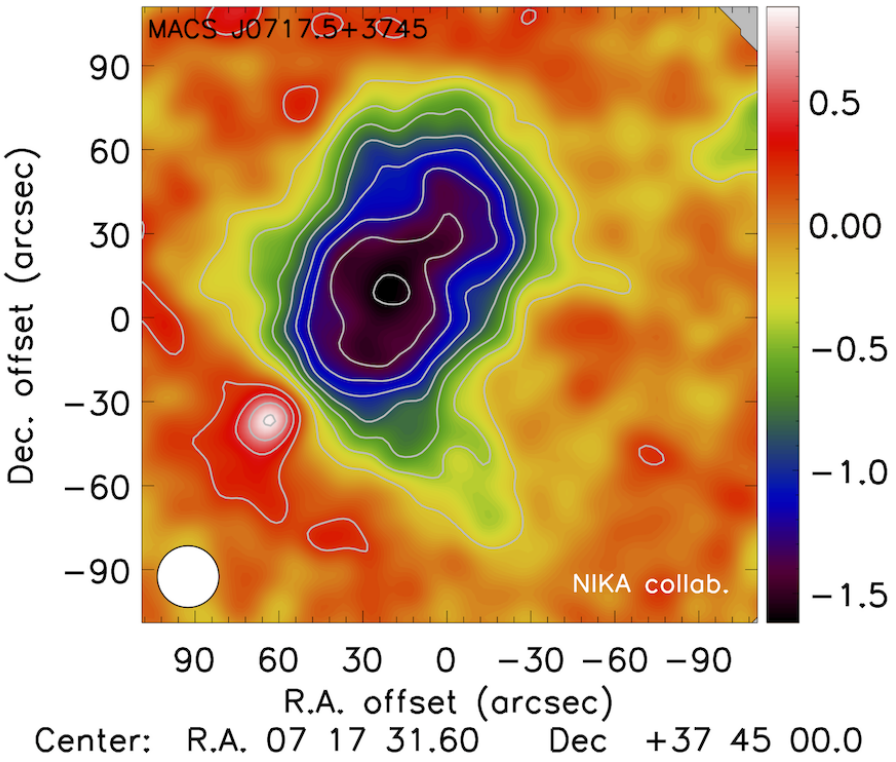

Figure 2.12 – Map of the cluster MACS J0717.5+3745 by NIKA2, showing the two sub-clusters revealed by the kinetic SZ effect.
Credit: The NIKA Collaboration, R. Adam et al. [4]

Chemical potential distortion For $10^5 < z \lesssim few \times 10^6$, if high energy photons are injected, they can not relax to the standard black body because the photon number has to be conserved. The CMB spectrum therefore takes the shape of a Bose-Einstein spectrum, with a non-zero chemical potential μ:

$$I(\nu) \propto \frac{\nu^3}{e^{(\nu-\mu)/T_\gamma} - 1}. \tag{2.71}$$

This distortion can be characterised by the dimensionless parameter

$$\tilde{\mu} \equiv \frac{\mu}{T_\gamma}. \tag{2.72}$$

Compton distortion At lower redshifts, $10^3 \lesssim z < 10^4$, Compton scattering stops to be efficient, so that full kinetic equilibrium between electrons and photons can not be achieved anymore. The CMB spectrum is therefore distorted towards higher frequencies, creating an excess of power in this region of the spectrum. This is the same process that generates Sunyaev-Zel'dovich effects, with the notable difference that in this case, the effect is isotropic and observable across the entire sky, while the SZ effect is a cluster-scale, localised effect. This Compton distortion is characterised by a Compton parameter:

$$y = \int \sigma_T n_e \frac{T_e - T_\gamma}{m_e} dl. \tag{2.73}$$

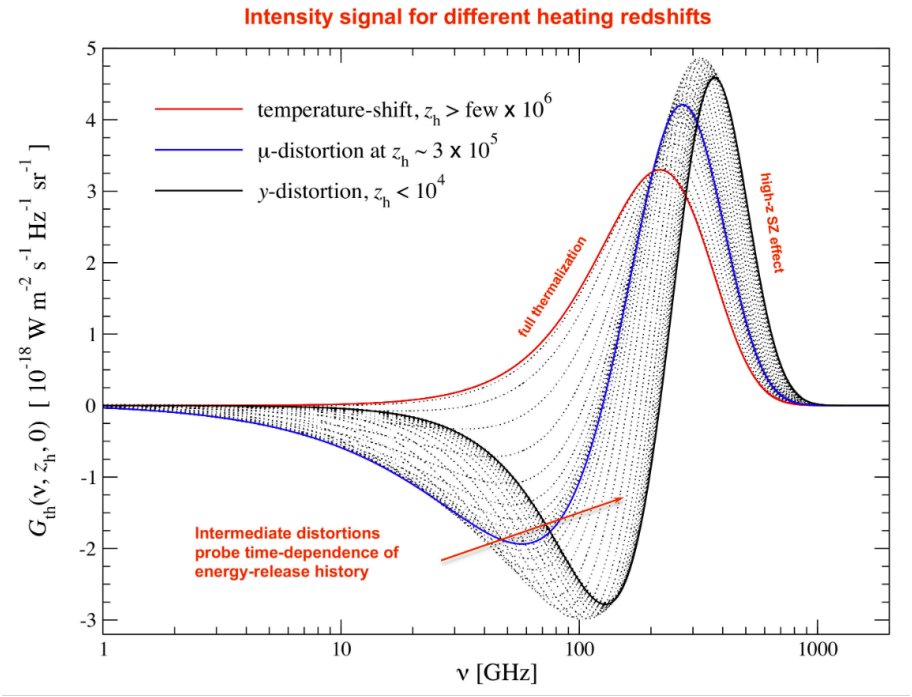

Figure 2.13 – Spectral distortions in the CMB depending on the redshift of the energy release.
Credit: J. Chluba [55]

where the integral is along the photon path, and with m_e the electron mass, n_e their density, T_e their temperature and T_γ the photon temperature.

Free-free distortion Free-free emission, or *brehmsstrahlung*, is the emission of photons by a charged particle deflected and decelerated by another charged particle. In the CMB, it is often electrons scattered by charged particles - first nuclei for example - and it therefore occurs when first nuclei have formed, at the beginning of recombination $z \sim 10^3$. The effect on the CMB can be quantified by the parameter

$$Y_{\rm ff} = \int \kappa \left(1 - \frac{T_\gamma}{T_e}\right) dl, \tag{2.74}$$

where the integral is again along the photon path and κ depends on the electron temperature and density, and the photon bath temperature.

A road to new physics?

There is wide range of topics for which studying CMB spectral distortions would help constrain a potential new physics, or rule out some models. I introduce some of them here to give an overview of the broad science which is left to do, and one can refer to the review given in the Voyage 2050 Spectral Distortions white paper [53] for more details.

Inflation Spectral distortions, and in particular μ distortion (chemical potential) are particularly sensitive to the running of the spectral index of the density

power spectrum (defined in Eq. (1.95)), i.e. its shape deviations from a scale invariant spectrum. Measuring μ distortions with a higher precision would help to constrain this parameter, and therefore set tighter constrains on inflationary slow-roll models.

Primordial non-Gaussianity Non-Gaussianity in the primordial Universe would generate coupling between short- and long-wavelength modes, enhancing spatial anisotropy in the spectral distortions. The angular cross-correlation between the temperature field and the μ distortion field would help to discriminate between single- and multi-field inflation (a more detailed review on primordial non-Gaussianity can be found in the next section).

Dark matter Annihilating and decaying particles can generate spectral distortions. In the case of dark matter, the detection of specific signatures in the spectral distortions of the CMB would allow to discriminate between several dark matter models. This is true for decays happening in the early Universe, but also in the case of secondary distortions, caused by processes happening after recombination.

Axions and axion-like particles are hypothetical particles postulated to resolve the strong CP problem, and they are natural candidates for dark matter. Several particle physics experiments are on-going to detect them directly. They are also expected to interact with photons in the presence of an external magnetic field, leading to oscillations between photons and axions. CMB photons going through cosmic and galactic magnetic fields could therefore be affected by these oscillations, leading to spatially varying spectral distortions, depending on the distribution of both dark matter and magnetic fields on the line-of-sight.

Another candidate for dark matter is primordial black holes, which could affect the CMB spectrum by dissipating some of the large density perturbations that collapse in primordial black holes, and by electromagnetic particles emitted by evaporating black holes through Hawking radiation.

Measurements

As of 2020, the best upper limits on CMB spectral distortions are the ones conducted by the spectrometer FIRAS on COBE [101], presented in Table 2.1.

More recent CMB space probes - WMAP and Planck - have indeed been focusing exclusively on temperature anisotropies and did not have a spectrometer on board. However, in the past few years, there has been proposals for a next frontier CMB experiment targeting spectral distortions, for example PIXIE [148],

Distortion type	Upper limit
Compton	$\lvert y\rvert < 1.9 \times 10^{-5}$
Chemical potential	$\lvert\tilde{\mu}\rvert < 9 \times 10^{-5}$
Free-free	$\lvert Y_{\rm ff}\rvert < 1.5 \times 10^{-5}$

Table 2.1 – Upper limits on CMB spectral distortion parameters

PRISM [12] or more recently PRISTINE[16]. None of these mission concepts have been selected so far, but they are considered in the context of Voyage 2050, ESA's next long term planning of scientific missions.

2.7.3 Primordial non-Gaussianity

So far, we have assumed that any CMB field (temperature or polarisation) is Gaussian, and can therefore be fully described by its two point correlation function, i.e. its power spectrum. However, it is predicted that the inflation process would introduce some level of non linearity in the CMB, generating second order perturbations and non-Gaussianity. The level of the predicted effects is model-dependent, and could therefore be used to further differentiate between models of inflation.

High order statistics

To probe CMB non-Gaussianity, one has to extend the power spectrum analysis presented in section 2.5 to high order statistics. The three-point correlation function, known as the bispectrum, is the lowest order statistics which vanishes for Gaussian fields. As it is computationally more tractable than higher order statistics (e.g. trispectrum), which quickly become computationally prohibitive, it is therefore favoured as a first step in the analysis. The bispectrum for three fields X, Y and Z is defined as:

$$B^{mm'm''}_{\ell\ell'\ell''} \equiv \langle a^X_{\ell m} a^Y_{\ell' m'} a^Z_{\ell'' m''} \rangle \equiv \mathcal{G}^{\ell\ell'\ell''}_{mn'm''} b^{XYZ}_{\ell\ell'\ell''}, \tag{2.75}$$

where $b^{XYZ}_{\ell\ell'\ell''}$ is the reduced bispectrum and $\mathcal{G}^{\ell\ell'\ell''}_{mn'm''}$ is known as the Gaunt integral:

$$\mathcal{G}^{\ell\ell'\ell''}_{mm'm''} \equiv \int d\Omega_s Y_{\ell m}(\mathbf{n}) d\Omega_{s'} Y_{\ell' m'}(\mathbf{n}') d\Omega_{s''} Y_{\ell'' m''}(\mathbf{n}''). \tag{2.76}$$

From the bispectrum, a non-linearity parameter $f_{\rm NL}$ can be estimated, that measures deviations from the linear spectrum in Fourier space. Given theoretical bi-spectrum templates computed with Eq. (2.75), one can compute an estimator $\hat{f}_{\rm NL}$ [181]

$$\hat{f}_{\rm NL} = \frac{1}{N} \sum_{\ell m} B^{mm'm''}_{\ell\ell'\ell''} \frac{a_{\ell m}}{C_\ell} \frac{a_{\ell' m'}}{C_{\ell'}} \frac{a_{\ell'' m''}}{C'_{\ell'}}. \tag{2.77}$$

where N is the total number of modes. A brute force implementation of this formula scales as $\ell^5_{\rm max}$, which makes it computationally challenging if not impossible to achieve in a reasonable time. Several analytical and numerical methods have therefore been developed to compute $\hat{f}_{\rm NL}$ more efficiently under some separability assumptions. Examples and useful references can be found in [219].

The generic $\hat{f}_{\rm NL}$ estimator can also be refined and broken down to several estimators probing different types of non-Gaussianity, depending on their sources. In particular, one has to distinguish primordial non-Gaussianity arising from inflation, from late non-Gaussianity induced by the ISW and Rees-Sciama effects, point-source contamination or lensing [21].

[16] https://www.ias.u-psud.fr/en/content/pristine.

We focus here on inflation-driven non-Gaussianity, where $f_{\rm NL}$ can be connected to inflation parameters.

From inflation to non-Gaussianity

Since density fluctuations in the early Universe arise from quantum fluctuations of a scalar field, their statistics is Gaussian as long as they evolve linearly. However, in the single field slow-roll inflation model, if non linear terms become dominant in the equations describing the dynamics of the scalar field Eq. (1.72 - 1.73), non linearity can induce a small level of non-Gaussianity at the second order in perturbations. Another hypothesis in the framework of single field models is to consider a characteristic scale for which the derivative of the potential varies quickly, hence introducing non-Gaussianity at this scale.

The generation of non-Gaussianity in single field inflation models is however limited. Considering more complex models, it is nevertheless possible to explain the generation of non-Gaussianity that would be easier to detect. The main models predicting an important level of non-Gaussianity are listed below, and one can refer to the review [20] for more details:

- topological defects generated in the early Universe during phase transitions;
- multi-field inflation: in this situation, the auxiliary field can be non-Gaussian and affect isocurvature fluctuations without modifying the general dynamics of inflation;
- curvaton models, where a scalar field generates curvature fluctuations at late times (when the inflaton field has decayed), and does not impact the dynamics of inflation itself.

Without diving into the details of all these models, primordial non linearity can be represented quite easily for a wide range of models by the following equation [149]

$$\Phi = \Phi_{\rm lin} + f_{\rm NL}\left(\Phi^2_{\rm lin} - \langle\Phi^2_{\rm lin}\rangle\right) + g_{\rm NL}\left(\Phi^3_{\rm lin} - \langle\Phi^2_{\rm lin}\rangle\Phi_{\rm lin}\right) + ... \tag{2.78}$$

where Φ is the large-scale gravitational potential, $\Phi_{\rm lin}$ its linear Gaussian contribution, and $f_{\rm NL}$ and $g_{\rm NL}$) are respectively the first and second order non-linearity parameter - note that the sum can in theory be indefinitely expanded.

Measurements

The most recent results on primordial non-Gaussianity were derived from Planck data, and presented in the Planck 2018 data release in a dedicated article [219]. The current results on various $f_{\rm NL}$ are consistent with the ΛCDM model (i.e. compatible with zero!), but also with expectations from single field slow roll inflation. They also put constraints on more exotic inflation models, without ruling them out. However, given the uncertainty, it is currently impossible to conclude on any favored model. Improving sensitivity on $f_{\rm NL}$ is therefore necessary to be able to produce discriminatory results on inflation models from primordial non-Gaussianity.

2.7.4 Cosmic birefringence

In optics, birefringence refers to materials having their refractive index dependent on the polarisation and the direction of propagation of light. When it comes to cosmology, cosmic birefringence describes the rotation of the polarisation angle of the CMB, turning polarisation E-modes into B-modes, and vice-versa. In particular, it generates non-zero C_ℓ^{TB} and C_ℓ^{EB} power spectra.

Mechanisms

To a large extent, one can attribute cosmic birefringence to two major mechanisms: Chern-Simons effect and Faraday rotation.

Chern-Simons effect The Chern-Simons mechanism describes the coupling between CMB photons and a generic pseudo-scalar field ϕ. This type of fields can be associated with axion-like particles, and their existence is predicted by string theory. This coupling generates a rotation of the CMB polarisation angle [50]:

$$\alpha = \frac{\Delta a \, g_{a\gamma}}{2}, \tag{2.79}$$

where Δa is the change of pseudo-scalar field over CMB photons trajectory, and $g_{a\gamma}$ is the Chern-Simons coupling coefficient. Irrespective of the absolute value of Δa, which is likely to be very small, its spatial variation can generate anisotropy in α, whose power spectrum can be expressed as [33]:

$$\sqrt{\frac{\ell(\ell+1)C_\ell^{\alpha\alpha}}{2\pi}} = \frac{H_I \, g_{a\gamma}}{4\pi}, \tag{2.80}$$

where $H_I \equiv 2\pi m_P \sqrt{A_s r/8}$ is the inflationary Hubble parameter. The measurement of this spectrum would help to determine if cosmic birefringence is correlated with primordial density perturbations, parametrised by their amplitude A_s and the tensor-to-scalar ratio r [44].

Faraday rotation Faraday rotation is the rotation of polarised light proportional to the magnetic field component that is parallel to the direction of propagation. Faraday rotation of CMB polarisation can be used to probe Primordial Magnetic Fields (PMF). PMF are weak magnetic fields of the early Universe, postulated to explain the presence of currently observed galactic magnetic fields. They would be of very low amplitude, smaller than nG (1G = 10^{-4}T), and could have affected CMB polarisation at recombination. As for Chern-Simons-induced birefringence, regardless of their amplitude, their anisotropy can be probed through the power spectrum of the polarisation angle [44]:

$$\sqrt{\frac{\ell(\ell+1)C_\ell^{\alpha\alpha}}{2\pi}} = 1.9 \times 10^{-4} \left(\frac{\nu}{150\mathrm{GHZ}}\right)^2 \left(\frac{B_{1\mathrm{Mpc}}}{1\mathrm{nG}}\right), \tag{2.81}$$

where $B_{1\mathrm{Mpc}}$ is the magnetic field averaged over 1 Mpc.

Measurements

$C_\ell^{\alpha\alpha}$ can be estimated from C_ℓ^{EE} and C_ℓ^{BB}, using a similar method to the one used for lensing reconstruction introduced in section 2.6.2. As for the lensing estimator, the unnormalized quadratic estimator for α is constructed as a combination of E and B-modes, using appropriate weights [139], different from the ones used for lensing. From the recovered value of α, the associated power spectrum $C_\ell^{\alpha\alpha}$ can be reconstructed.

The current best upper limits on cosmic birefringence are set by the Atacama Cosmology Telescope[17] (ACT) for the Chern-Simons effect [192]:

$$g_{a\gamma} \leq \frac{2 \times 10^{-2}}{H_I}, \tag{2.82}$$

and by the BICEP/Keck experiment for primordial magnetic fields [33]:

$$B_{1\mathrm{Mpc}} \leq 30\mathrm{nG}, \tag{2.83}$$

both with a 95% confidence level (2σ).

Calibration challenges In order to estimate $C_\ell^{\alpha\alpha}$ with the required precision, the polarisation angle of the instrument itself has to be very carefully calibrated. This is something which is very difficult to achieve in observing conditions, and several techniques have been proposed. A good measurement can be obtained by observing a far-field polarised source, such as Tau A (Crab nebula). However, this kind of measurement is always contingent to how well we know the polarisation of Tau A, with current precision being 0.33° [15]. A method has been proposed to estimate simultaneously miscalibrated polarisation and birefringence angles [184], but it has never been applied to real data yet. The work presented in Chapter 7 also addresses polarisation angle modelling and calibration, and can therefore be an important tool for later measurements of cosmic birefringence.

Thanks to precision measurements of CMB temperature, polarisation and lensing, as they are available to today's cosmologists, the value of most of cosmological parameters - those of the ΛCDM model and other observables such as the Hubble constant - can be accurately determined. However, many challenges still remain, in particular the detection of primordial B-modes, on which I focus in the following. Furthermore, as outlined in this last section, the CMB signal is very rich and many of its characteristics other than anisotropies and lensing can be exploited as new probes.

Nevertheless, as precise as CMB science may be, in the typical case of H_0 that I presented in section 1.1.4, the determination of this parameter using different observables (CMB, supernovae, etc.) leads to strikingly different values. This can be due to unknown systematics in one of the methods, insufficient modelling of some instrumental and/or astrophysical effects... or new physics! This particular case stresses out the fact that our understanding of the Universe can not rely on only one observable - even if it can apparently constrain many parameters as the CMB does. Moreover, the uncertainty on some parameters, such as the sum

[17] https://act.princeton.edu/

of neutrino masses, can be significantly reduced using other observables such as galaxy clustering. In the next chapter, I provide a more detailed review of multi observables cosmology, and how this is a powerful and necessary method to ensure that we have minimum biases in our Universe understanding.

CHAPTER 3

Multi-probe cosmology

Contents

The Cosmic Microwave Background is a powerful observational tool to probe the early Universe and fundamental laws of physics... but not the only one! Modern cosmology relies more and more on other objects than the CMB, for example the matter distribution, supernovae, quasars, etc. Each of these objects can provide information from various observable effects: for example, for the CMB, we have access to temperature and polarisation anisotropies, but also spectral distortion, non-Gaussianity and SZ effects, as detailed in the previous chapter. The same is true for other cosmological and astronomical objects: each of them offers a collection of observables that can be studied using different probes. All these observables and probes can be combined in various ways (cross-correlation, joint study, comparisons of independent results, etc.).

Moreover, to have a more complete and robust picture of the Universe and its laws, we have to leave the field of usual electromagnetic radiation observations, and delve into multi-messenger astrophysics and particle physics. With

multi-messenger astrophysics, one has access to new tools, to probe either the same objects as electromagnetic observations, or different ones. For example, supernovae have been observed both with neutrinos and with visible light, and are also expected to produce gravitational waves.

Describing in details observables of cosmological interest, probes available to study them, and various messengers they emit would be way beyond the scope of this chapter. Instead, I aim at reviewing a few key concepts of multi-probe cosmology: in section 3.1, I detail the large scale structures observables that can be used to probe the matter field, and in section 3.2, I focus on supernovae as a probe of cosmological expansion. I then give a brief review of other messengers used in astrophysics and cosmology in section 3.3, and I conclude this chapter with a note on particle physics for cosmology in section 3.4. None of these sections are intended to be exhaustive, so this chapter should rather be seen as an introduction to some aspects of multi-probe cosmology.

3.1 Matter distribution

Reconstructing the matter field is of crucial importance in cosmology to understand large scale structure evolution, as well as for CMB lensing analysis. We also know very little about the dark ages and reionisation, while we expect first galaxies and clusters to form during this period.

However, the matter field is much more complex to observe than, e.g., the CMB. First of all, most of the matter in the Universe is not directly observable at all, since dark matter accounts for roughly 30% on the Universe content, while ordinary matters represents only 5%. The matter field can nevertheless be observed, using different probes (galaxy clusters, hydrogen clouds, line-of-sight integrated signal, etc.), and each of them tells us something different, and complementary, about it.

Reconstructing the matter distribution is therefore not a straightforward task, and by using different probes, one can estimate it at different epochs in the history of the Universe. Observations probe mostly ordinary matter, but are also used to reconstruct the underlying dark matter field. This section details the most common probes used to study matter distribution.

3.1.1 Large scale structures

Galaxy clusters emerge from the gravitational collapse of large scale initial perturbations, around $100\,h^{-1}\mathrm{Mpc}$. On larger scales, structure evolution is linear and driven by gravity, whereas for smaller scales, dynamical effects such as hot gas start playing a role. As they are at the interface between these two scales, galaxy clusters are of particular importance for both astrophysics and cosmology [38].

Galaxy cluster science is indeed a very broad and promising topic, in particular in the coming era of large sky surveys like Euclid or the Vera Rubin Observatory. These modern surveys will measure the position and distance (through redshift) of billions of galaxies. These data catalogues are of huge importance to estimate the matter field δ and its evolution.

The latter can be synthesised as:

$$\langle \delta^2 \rangle = \sigma_8^2 D(z) P_0(k), \tag{3.1}$$

where $P_0(k)$ is the initial power spectrum of the matter field, σ_8 quantifies the amplitude of the matter power spectrum at $8h^{-1}\mathrm{Mpc}$, and $D(z)$ is the growth factor. The determination of δ and other related cosmological parameters can be achieved by several tracers, all of them relying on galaxy surveys.

Baryon Acoustic Oscillations

As detailed in the previous chapter, density fluctuations in the primordial plasma give birth to acoustic oscillations. These acoustic oscillations prior to the recombination are not only reflected in the acoustic peaks of the CMB power spectra (see section 2.5.2), but are also expected to have left imprints on the matter distribution. After recombination, over-dense and under-dense regions stay frozen, and over-densities collapse under gravity, forming the first stars and galaxies. The distribution of galaxy clusters over the sky therefore also exhibits a specific spatial pattern due to these oscillations, the so-called Baryon Acoustic Oscillations (BAO) peaks. By measuring the 3D-distribution of hundreds of galaxy clusters, it is therefore possible to infer the sound horizon at recombination. This provides a powerful consistency test to cross-check CMB observations [8].

Moreover, the galaxy distribution δ_g can be related to the matter field δ with

$$\delta_g \sim b\delta, \tag{3.2}$$

with $b = 1.83 \pm 0.06$ as measured by the Dark Energy Survey[1] (DES) collaboration [71].

BAO are also useful to study dark energy: as galaxies can be observed at multiple redshifts (unlike the CMB), they provide information on dark energy at different epochs of the Universe, i.e. at times when the dark energy density parameter was not the same as today. BAO thus provide an excellent probe for the accelerated expansion of the Universe [23], and, like the sound horizon measured in the CMB, constitute a standard-ruler. We also mentioned in section 2.6.2 the importance of BAO (combined with CMB lensing) to constrain neutrino properties.

Gravitational lensing

I have introduced the gravitational lensing of CMB photons by massive galaxy clusters in section 2.4.2. The light emitted by galaxy clusters itself is subject to the same phenomenon: light rays from distant clusters are deflected by other massive clusters on the line-of-sight. However, if lensing is an observational barrier when it comes to CMB observation, it is a powerful tool in cluster science to probe masses of galaxy clusters, and thus study baryonic and dark matter distribution. Strong gravitational lensing refers to objects that are lensed so much that several images of the background objects are created - as illustrated in Figure 3.1.

[1] https://www.darkenergysurvey.org/

However, we focus here on weak lensing, which is a more powerful tool to constraint the matter distribution. The principle is, on a large galaxy catalogue, to study galaxies that exhibit a shear in their shape, and appear slightly elongated in one direction because of lensing. Averaging over a given patch of the sky, there should be no preferred direction. However, if all galaxies are lensed by the same matter field, a locally favoured orientation will naturally arise. As for CMB polarisation, this cosmic shear can be decomposed into E and B-modes. Positive E-modes are created by over-densities, while negative ones arise from under-densities.

One drawback to this method is that nothing looks more like a lensed galaxy than... an unlensed galaxy! but whose shape has been affected by the atmosphere, or the PSF (point spread function) of the instrument. It is possible to mitigate these effects during data analysis [127] by observing a large population of stars, but techniques seeking to minimise these effects at an instrument level, such as adaptive optics, are particularly useful in this situation. Moreover, a lensed galaxy can easily be mistaken for two overlapping galaxies on the line-of-sight. With the upcoming surveys of billions of galaxies, the automatic detection of lensed galaxies therefore represents a huge challenge. This so-called deblending process has recently received a huge boost with the help of neural networks, that allow to automatically deblend galaxies and discriminate between blended and lensed galaxies [39, 226].

Redshift-space distortions

In most cases, we do not directly measure the distance to a given galaxy but rather its redshift, although distance measurements are possible using standard

Figure 3.1 – SDSS J0928+2031 lensing system, showing strong lensing of background galaxies.
Credit: ESA/Hubble & NASA, M. Gladders et al.

candles such as type Ia supernovae, as detailed in section 3.2. Using Hubble's law, one can then reconstruct the distance from redshift measurement, but the mapping between these two quantities is not straightforward: in addition to the cosmological expansion, galaxies and clusters have their own peculiar motion, which distorts the redshift-distance relation. These are the so-called redshift-space distortions (RSD), which have two contributions:

- at small scales, random motion of galaxies within their local environment, which produces a particular pattern in redshift space, elongated toward the observer and nicknamed "Finger of God";
- at large scales, global motion due to gravitational potentials also affects galaxy dynamics, which flattens the distribution on the line-of-sight [138].

Redshift-space distortions are, at first, hindering our capability to properly map galaxy positions, but they can also be used to constrain the matter distribution, using anisotropies in the measured galaxy power spectrum. In particular, one can infer the quantity $f\sigma_8$, where f is the linear growth rate $f \equiv \frac{d\ln D}{d\ln a}$, by modelling redshift-space distortion and correct for their effect on the spectrum [204]. This approach is complementary to the one provided by weak lensing measurements: while weak lensing probes integrated effects on the line-of-sight due to both metric and localised effects, RSD probes only localised effects. The growth of structures depends on redshift, and is crucial to understand the dynamics of structures and galaxy formation. In the past 15 years, the growing number of large galaxy surveys, at various redshifts, allowed to probe RSD and derive cosmological parameters from these measurements. In particular, thanks to SDSS/BOSS[2] surveys, $f\sigma_8$ has been constrained at redshift $z \sim 0.3 - 0.6$ [108, 109, 225]. These works also jointly constrain other parameters such as the Hubble and density parameters, as a function of redshift, which makes RSD a complementary probe to other measurements methods.

3.1.2 Lyman-α forest

The Lyman series is the well-known discrete spectral emission of the hydrogen atom when an electron relaxes from an excited state ($n_i \geq 2$) to the fundamental ($n_f = 1$). The Lyman-α line is the first of these transitions, with $n_i = 2$. It produces a photon at 1215.67 Å, corresponding to a frequency of 2.47×10^{15} Hz. This emission is therefore in the ultraviolet range, and is normally not observable from Earth because it is blocked by the atmosphere. However, for distant sources such as galaxies, this line is redshifted and can become observable from the ground. In cosmology, it is not this emission line which is observed, but its corresponding absorption line by neutral hydrogen clouds on the line-of-sight.

First detected in 1971 [170], the Lyman-α forest is a series of absorption lines in the emission of distant quasars. Quasars are galaxies with an active nuclei (AGN - Active Galactic Nuclei), whose emission comes from matter accreting to a massive central black hole. The light they emit travels through the intergalactic medium (IGM), and is absorbed by hydrogen generating Lyman-α absorption

[2] https://www.sdss.org/surveys/boss/

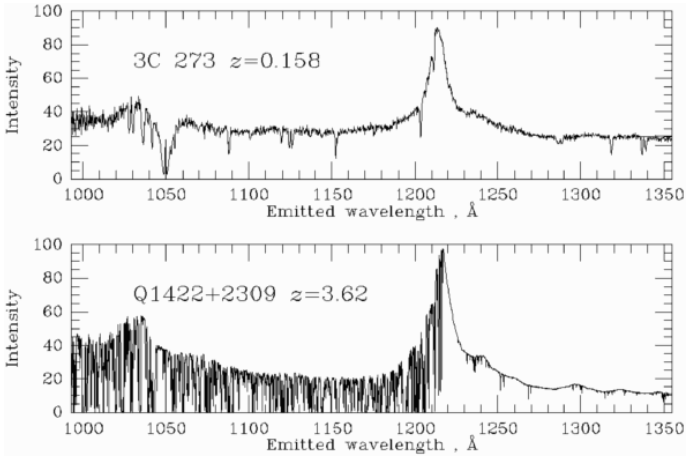

Figure 3.2 – Lyman-α forest for a close quasar (top) and a distant one (bottom)
Credit: Adapted from W. Keel

lines in its spectrum. Because this process is repeated several times at different redshifts, the spectrum of the signal finally received on Earth exhibits several lines at various frequencies: this range of absorption line is known as the Lyman-α forest. The higher the redshift, the more emission lines in the forest, as shown in Figure 3.2. The number and spectral localisation of absorption lines can thus be used to directly probe clouds of neutral hydrogen in the IGM, and determine both their spatial localisation and column density. The density of neutral hydrogen can then be used to estimate the total baryon density, thus probing the matter distribution. For a complete review of cosmology with Lyman-α observations, one can refer to [281].

3.1.3 21 cm intensity mapping

Intensity mapping refers to techniques to observe large scale structures in the Universe by measuring integrated radio emission along the line-of-sight. Intensity mapping techniques can of course be used on a wide range of frequencies, but there has been a recent growing interest in 21 cm intensity mapping for cosmology.

The 21 cm emission line originates from neutral hydrogen, and corresponds to the transition between two sub-levels of the hyperfine structure of the fundamental level of the hydrogen atom. Once redshifted, this line can be detected on Earth in a wide range of radio frequency. In particular, the frequency range of interest for cosmology lies between 50 and 200 MHz. In this frequency range, 21 cm intensity mapping can be used to probe hydrogen clouds on the line-of-sight. In particular, the epoch of reionisation when the Universe is gradually reionised (see section 1.2.5) appears as holes in the 21 cm background. With the development of giant radio experiments such as SKA[3], 21 cm intensity mapping is one of the most promising probes of the 21st century cosmology [24, 222]. However, it is important to note that such experiments have to be located in radio-quiet zones, because the signal they seek to detect is in the same band as Earth-based radio communication. Moreover, they have to deal with an important foreground

[3] https://www.skatelescope.org/

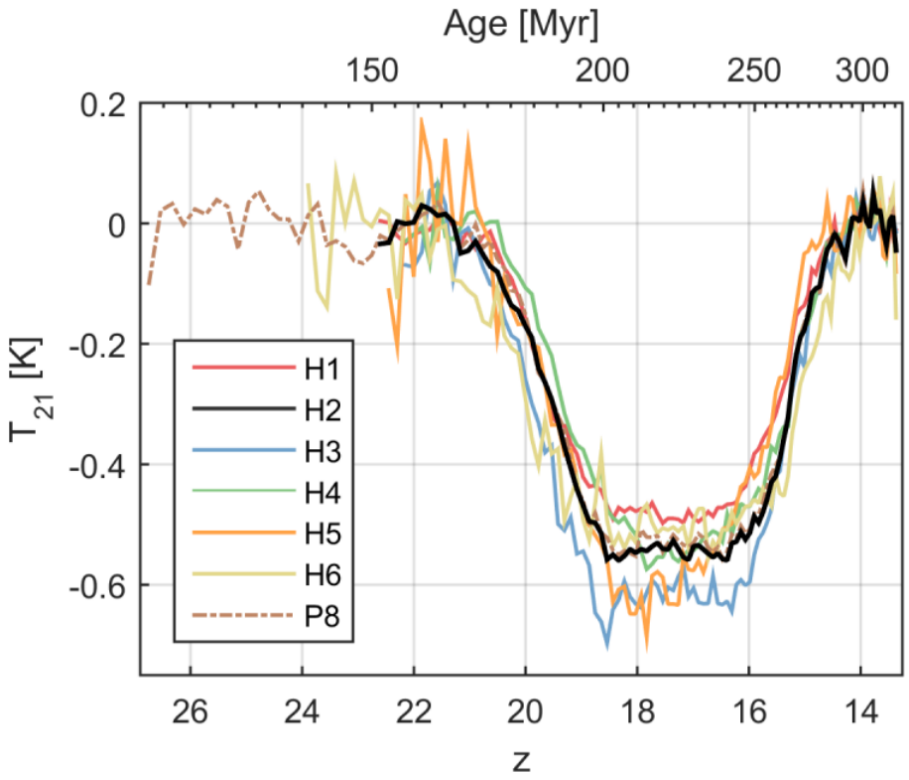

Figure 3.3 – Absorption profile detected by EDGES. The different lines correspond to various instrumental and data pipeline configuration to test for systematic effects
Credit: J. Bowman et al. [40]

contamination.

In 2018, the Experiment to Detect Global EoR Signature[4] (EDGES), located in the Australian desert, detected an absorption signal at 78 MHz at a redshift of $z \sim 17$ [40], shown in Figure 3.3. At such early stages in the Universe, neutral hydrogen is at thermal equilibrium with CMB photons, making the absorption line of hydrogen impossible to observe. When first stars appear, they emit Lyman-α photons, that are absorbed by neutral hydrogen, and then re-emitted. This process modifies the distribution of electrons in hyperfine states, and consequently lower the spin temperature of neutral hydrogen. Neutral hydrogen and CMB are not at equilibrium anymore, and the 21 cm line of hydrogen becomes observable: this phenomenon is known as the Wouthuysen–Field effect [99, 284].

However, the signal detected by EDGES has too big an amplitude to be explained by this effect, because it is highly unlikely that stars would be able to affect neutral hydrogen that much, and at such early times. The other explanation would be that primordial neutral hydrogen was already much cooler than expected, even without interaction with early stars. This cooling could result from the interaction between baryons and dark matter [18]. The EDGES signal would therefore be one of the first detections of dark matter not based on its gravitational effects. Although it still needs to be confirmed by other experiments, this detection paves the way for a very rich 21 cm cosmology era, in particular to probe early stages of our Universe's history.

[4] https://www.haystack.mit.edu/ast/arrays/Edges/

3.1.4 Cosmic Infrared Background

The Cosmic Infrared Background (CIB) is a high frequency signal (compared to CMB), peaking around 1 THz, and present in all sky directions like the CMB. Although it is not strictly speaking a foreground, it is nevertheless a contaminant to CMB observations at high frequencies. It has therefore to be carefully modelled and removed in CMB data analysis.

However, the CIB is not just an unwanted foreground! It is actually an integrated signal, carrying contributions of most of the energy released during structure formation (stars and galaxies) since the CMB decoupling. It is therefore used to constrain galaxy formation and evolution [120, 141, 209].

In particular, the anisotropies of the CIB can be mapped in the same way as CMB anisotropies. This is used to trace dust and star forming regions, and is therefore a useful probe to constrain star formation rates, at redshifts where stars are not directly observable. Understanding galaxy formation and evolution also allows us to constrain dark matter distribution. Recent measurements of CIB anisotropies by Planck [261] call for a better modelling of the CIB, since current measurements are not well understood given available theoretical models, in particular in the non-linear regime (bispectrum). The CIB is therefore a powerful probe to understand the impact of dark matter distribution on galaxy formation and evolution.

Probing the matter distribution can thus be achieved using a wide variety of probes. These measurements are expected to flourish in the coming years with the deployment and operation of several large scale surveys specifically targeting matter distribution (both baryonic and dark), as well as dark energy. Since 2019, DESI has been mapping about a third of the sky, measuring optical spectra of millions of galaxies and quasars. In 2020, the Vera Rubin Observatory should also see its first light, and start investigating in particular weak gravitational lensing and BAO as a function of redshift. These ground-based surveys will be complemented by the space mission Euclid, whose launch is expected in 2022, and that will also map gravitational lensing and BAO. These surveys, with unprecedented sky coverage and spectral precision, will enable to set better constraints on the matter distribution and dark energy, using many of the probes mentioned above (BAO, RSD, Lyman-α, lensing), as well as supernovae.

3.2 Supernovae

A supernova is a very powerful stellar explosion, of which several types exist, depending on progenitor star(s). In this work, we refer only to so-called type Ia supernovae, which are of interest for cosmology.

3.2.1 Standard candles

Determining distances is one of the greatest challenges in extragalactic astrophysics and cosmology. When observing a galaxy or a distant object, we have access to its redshift and its luminosity. Both of these quantities are however only apparent quantities: they depend on the distance between the observer and

the object... which is precisely what we are trying to determine! Cosmologists therefore have to rely on specific properties of observed objects, that allow to determine their distances (almost) unequivocally. Several so-called standard candles are often used to get a more precise determination of distances, and calibrate candles themselves.

The first standard candles ever discovered are cepheids, variable stars whose period-luminosity relation was determined by Henrietta Leavitt in the 1910s [158, 159]. They were later used by Hubble in addition to redshifts to establish his law in the late 1920s. Cepheids are still used in modern cosmology, but many other standard candles have been discovered, in particular for distant objects. The most precise ones are type Ia supernovae, used as standard candles since the early 1990s, because of their distinctive light curve[5].

Supernovae light curve

Type Ia supernovae occur in binary systems where one of the stars is a white dwarf, and the other one can be almost any other stellar object. The white dwarf accretes matter from its companion star until it reaches the limit of carbon nuclear fusion in its core. This triggers a chain reaction, consequently leading to an enormous release of energy: the star can not sustain its own gravity anymore, and unbinds. This results in a huge explosion, a shock wave and releases elements formed in the core of the star in the interstellar medium - a key element of stellar nucleosynthesis models.

Because of this very specific process that can happen only under precise conditions of mass and temperature, type Ia supernovae exhibit a distinctive light curve, shown in Figure 3.4. It is precisely because of this distinctive light curve that supernovae are used as standard candles to measure cosmological distances. The Phillips relationship [114, 206], first published in 1993, is a phenomenological relation that correlates the intrinsic magnitude in B band (blue, centred at 436 nm) with the decline of the supernovae light curve 15 days after the peak of emission in the same band $\Delta m_{15}(B)$ (see Figure 3.4):

$$M_{\max}(B) = -21.726 + 2.698\,\Delta m_{15}(B). \tag{3.3}$$

The apparent magnitude (the one measured) is defined as:

$$M_{\text{app}}(X) \equiv -2.5 \log\left(\frac{L_X}{4\pi d^2}\right), \tag{3.4}$$

where L_X is the star intrinsic luminosity in band X, and d its distance to Earth. By comparing the intrinsic magnitude as predicted by Phillips relationship, in Eq. (3.3), to the observed one, one can therefore infer the distance to a given supernova, and to its host galaxy.

3.2.2 Application to cosmology

Using type Ia supernovae as standard candles thus allows to determine distances with high precision, which has many applications to cosmology. Let us

[5] For a complete overview of known standard candles, one can refer to https://universe-review.ca/R02-07-candle.htm

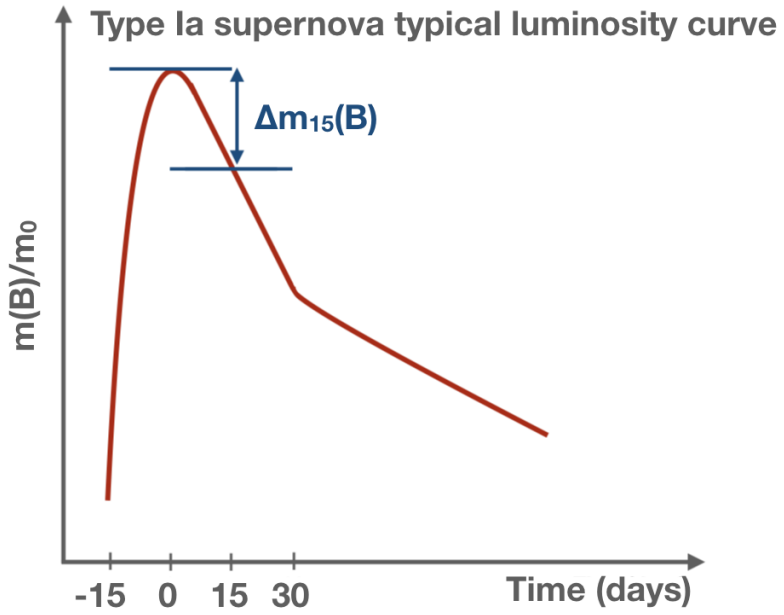

Figure 3.4 – Type Ia supernova typical magnitude curve, normalised to maximum luminosity (m_0), as a function of time. The peak is due to nickel decay, while the tail comes from cobalt emission. The difference between peak magnitude and magnitude 15 days after is used to calibrate luminosity distance using the Phillips relationship.

mention two of the most interesting ones, that allow to probe the expansion and the matter distribution of the Universe.

Hubble constant determination

The main advantage of type Ia supernovae compared to other types of standard candles is that they allow to probe distances up to a redshift of ~ 1, corresponding to 500 times further than cepheids. This is due to their high luminosity, which can be as important as the one of their host galaxy when the supernova is at its emission peak! Moreover, the method has been refined over the years, Phillips relationship has been adapted to other magnitude band, and better calibrated. This allows to reach a precision of 5% on distances - unless there are unknown systematics that would explain the discrepancy between local and cosmological H_0 measurements. Some properties of the light curve and supernovae are indeed correlated with the local star formation rate, and therefore measurements have to be corrected for these effects [229]. As star formation rates change in time, older and younger galaxies host supernovae that do not have the same properties when it comes to their light curve. If this effect is not properly modelled and taken into account, it could distort the determination of the cosmological parameters and the dark energy equation of state, as the latter derives from the deceleration parameter measurements [230]. This issue is all the more important as our capabilities to map the sky always deeper constantly improve, and thus more distant, younger galaxies are observed.

Peculiar velocities

Peculiar velocities refer to the component of a galaxy velocity not explained by Hubble's law, and therefore responsible for redshift-space distortion as explained in section 3.1.1. As outlined above, these velocities and resulting RSD depend on matter distribution and can therefore be used to probe it. Moreover, it is possible to infer directly peculiar velocities (without using RSD) by using type Ia supernovae, thanks to their distinctive light curve.

Peculiar velocities depend on the matter field as:

$$\vec{\nabla}\vec{v} = -H_0 f \delta, \tag{3.5}$$

and the difference between the observed redshift z, and the cosmological one purely due to expansion $\bar{z}$ can be written as:

$$1 + z = (1 + \bar{z}) \left(1 + \frac{v}{c}\right). \tag{3.6}$$

The observed redshift is derived using the Tully-Fisher relation [272] for the host galaxy, and the cosmological redshift of type Ia supernovae is determined thanks to the light curve (see above). The observed redshift can therefore be used to constrain peculiar velocity projected on the line-of-sight. From peculiar velocity, one can then infer the total distribution of matter, including dark matter, using Eq. (3.5). For a more complete review on type Ia supernovae and peculiar velocity, one can refer to [111].

The use of supernovae in the determination of peculiar velocities thus opens up new perspectives for the reconstruction of the matter field. As for the matter distribution, future surveys will enable further progress in distance determination with supernovae, that could help alleviate the Hubble constant tension. Moreover, distance determination will benefit from the boom of multi-messenger astrophysics, and in particular gravitational waves detection.

3.3 Multi-messenger observations

For most of astronomy and astrophysics history, observations relied on electromagnetic radiation. Until the 18$^{\text{th}}$ century (only 300 years ago!), physicists and astronomers only knew about non separated white light, until Isaac Newton discovered the decomposition of visible light in 1704. A century later, in 1800, William Herschel discovered infrared radiation, followed a year later by the discovery of ultraviolet radiation by Johann Ritter. In the 1860s, all these discoveries were unified by James Maxwell, whose famous equations predicted the existence of the entire electromagnetic spectrum. Things quickly accelerated in the last quarter of the 19$^{\text{th}}$ century and beginning of the 20$^{\text{th}}$ century, with the discovery of radio waves, X and γ-rays. The full electromagnetic spectrum is now commonly used in astrophysics to probe various phenomena, and observing the same object in several parts of the electromagnetic spectrum has become natural to today's astrophysicists.

The next frontier is the so-called multi-messenger astrophysics: observations using not only electromagnetic waves, but also the three other types of messengers that we know of: gravitational waves, neutrinos and cosmic rays. I introduce here hints of gravitational waves and neutrino astrophysics, and mention the first results obtained thanks to the few multi-messenger events already detected. i.e. when the same phenomenon is detected with two or more messengers, as well as the progress expected in the coming decades from these observations.

3.3.1 Gravitational waves

Gravitational waves were predicted by Albert Einstein as a direct consequence of his general relativity theory, as early as 1916 [89, 91]. At that time however, Einstein himself doubted their existence, arguing that they could be nothing more than a mathematical artefact due to the choice of coordinates. This interrogation was resolved at the Chapel Hill conference in 1957 [28], where the community was finally convinced that gravitational waves have a physical reality, and therefore must be detectable. It was the starting point of a long series of experiments aiming at detecting gravitational waves. Their core idea, which is still used in modern gravitational waves detector, is to detect the effect of a passing wave on a massive test object, thus modifying its size. As the displacement of the object was predicted to be of the order of $10^{-18} - 10^{-20}$m, the detection challenge was huge!

In the 1960s, the American physicist Joseph Weber proposed a system made of aluminium bars connected to piezoelectric sensors able to detect the passing of a gravitational wave. Although he claimed detection of gravitational waves in 1968, his results were doubtful because of potential faults in the data analysis, and no similar experiment was never able to reproduce them.

The first convincing evidence for gravitational waves was however indirect. In 1974, the first binary pulsar was discovered, allowing for new tests of general relativity. In particular, in 1982, results reporting a very slow decay over time of the pulsar period were published [282]. Such a phenomenon can only be explained if the binary system looses energy in a non-electromagnetic form, i.e. through gravitational waves. The first direct detection of gravitational waves occurred only in 2015 [167], almost a century after Einstein's prediction, using interferometry, as detailed hereafter.

Sources

Gravitational waves can be emitted only by sources with a varying quadrupole moment [6]. This greatly limits the type of sources that can be observed using gravitational waves. As described in section 1.3.3, primordial gravitational waves can be generated in the primordial Universe. However, we focus here on another type of sources: gravitational waves emitted by compact binary systems. This category encompasses a wide range of systems, in particular binary black holes and neutron stars mergers. For a binary system, one can relate the

[6] One can refer to Appendix B for the derivation of gravitational waves equations, as well as emission and propagation mechanisms.

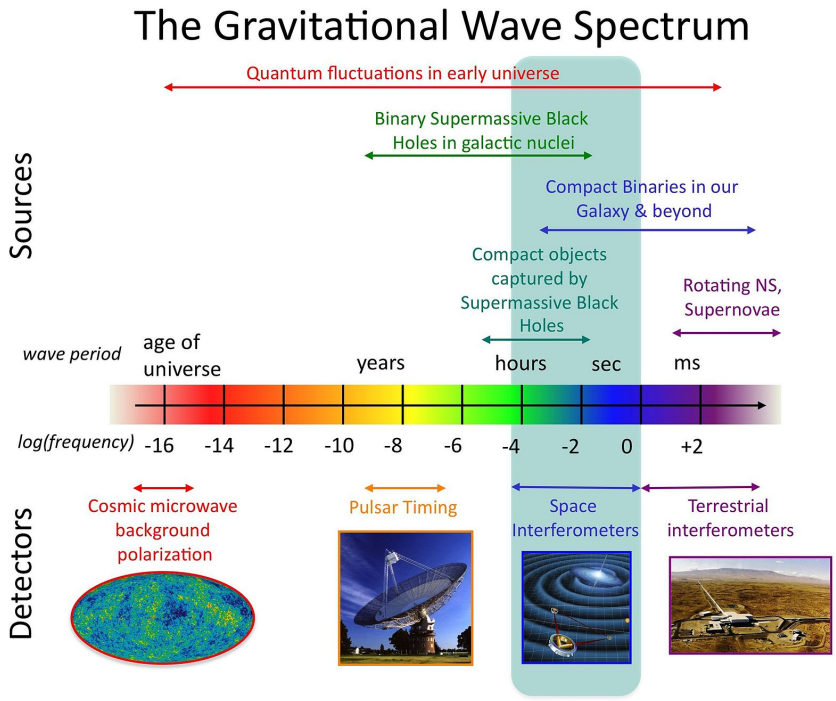

Figure 3.5 – Gravitational wave spectrum sources and detectors
Credit: NASA Goddard Space Flight Center

frequency of the gravitational wave perturbation to the properties of their binary source as[7]:

$$\omega_{\text{grav. wave}} = 2 \times \omega_{\text{binary}} = 2\sqrt{\frac{GM}{a^3}}, \tag{3.7}$$

where M is the total mass of the binary system and a its semi-major axis. Depending on the nature of astrophysical objects, the frequency of the gravitational waves thus varies, as shown in Figure 3.5.

One can also relate the amplitude of the gravitational wave h to the source location and properties:

$$h = \frac{(GM)^{5/3}}{c^4 R T^{2/3}}, \tag{3.8}$$

with R the distance to the source and T its period.

The measurement of gravitational wave parameters as permitted by modern observatories thus allows to estimate source parameters, and is a unique way to study compact objects (black holes and neutron star) in the binary systems they form.

Direct detection by interferometry

A passing gravitational wave locally modifies lengths, by stretching or distending space-time. Modern gravitational waves detectors use this effect to de-

[7] In this section, usual units are used, not Planck ones.

tect waves with a Michelson interferometer. Inspired by the historical Morley-Michelson experiment [182], the ground work for modern gravitational waves detector was laid in the 1970s, and the first detectors were completed in the early 2000s: LIGO[8] and Virgo[9].

When a wave passes through the detector, the two arms of the interferometer do not have the same length anymore, and the interference figure is modified. Detectors have to reach an exceptional sensitivity to detect gravitational waves. The length modification induced by a passing wave is indeed proportional to the amplitude of the gravitational wave h, times the initial length of the arm L. For a typical wave with an amplitude of $h = 10^{-21}$ and an arm of $L = 3\,\mathrm{km}$, the detector should be sensitive to $\Delta L \sim 10^{-18}\,\mathrm{m}$! To achieve this, the Michelson interferometers used as detectors have to be isolated from environmental noises (in particular seismic noise), and other sources of noise (technical noise and fundamental noise) have to be mitigated when possible, and otherwise carefully monitored to be accounted for during data analysis. In addition to that, gravitational wave detectors use Fabry-Pérot cavities [97] to increase the length of the optical path, without increasing physical arm length. This device allows to amplify the gravitational wave signal, and also filters some sources of noise such as laser fluctuations and radio-frequency noise.

In 2015, LIGO detected a gravitational wave for the first time [167], the merger of two black holes of around 30 and 35 solar masses. Since then, dozens of events have been recorded, an ever-increasing number as experimental sensitivity increases: LIGO and Virgo are upgraded after each observing run, and new gravitational wave experiments are built, such as KAGRA in Japan and LIGO India. In addition, after its launch scheduled for the early 2030s, the space-based interferometer LISA[10] and its one million kilometre arms will be able to detect gravitational waves with a frequency several orders of magnitude below frequencies that can be reached from the ground, and thus study the stochastic background of gravitational waves [47].

In 2017, LIGO and Virgo detected the merger of two neutron stars - or kilonova - and were able to provide a precise enough localisation of the event so that it was almost simultaneously observed in the electromagnetic spectrum, paving the way for multimessenger astrophysics [168].

Gravitational waves and the Hubble constant

For a multimessenger event, one can infer the redshift z of the gravitational wave source using the electromagnetic counterpart of the kilonova, which is not present in the case of a binary black hole merger. We recall that, in the low redshift limit:

$$H_0\, D_L = c\, z, \tag{3.9}$$

where z is the redshift and D_L the luminosity distance. As outlined in the previous section on supernovae, the determination of the luminosity distance is crucial to infer the Hubble constant... but not trivial at all! With gravitational waves, one

[8] https://www.ligo.org/
[9] https://www.virgo-gw.eu/
[10] https://www.lisamission.org/

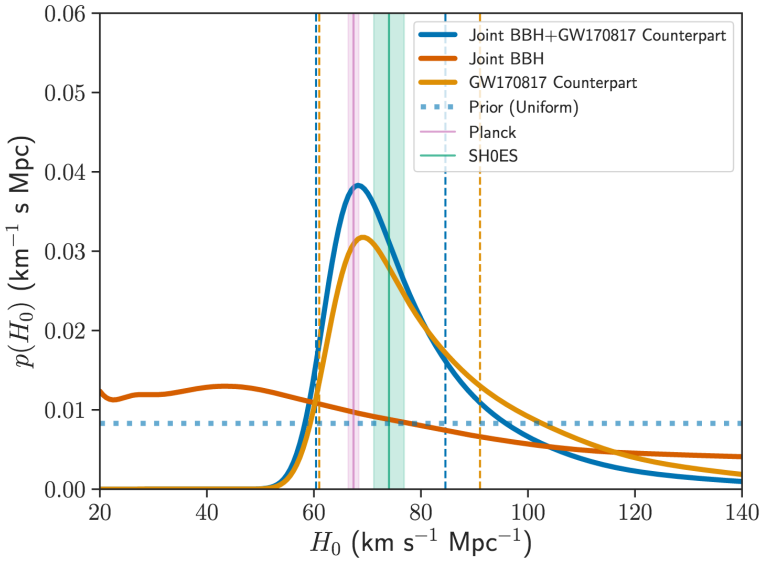

Figure 3.6 – H_0 values inferred from CMB (Planck), supernovae (SH0ES) and gravitational waves measurements.
Credit: LIGO and Virgo collaborations [260]

can estimate this luminosity distance using the properties of the detected event, in particular the distance to the source - R in Eq. (3.8) - without relying on any electromagnetic standard candles!

However, the distance between a gravitational wave source and the observer is a parameter which is degenerated with the inclination of the source with respect to the line-of-sight. This is one of the reasons why several detectors are needed for an accurate determination of gravitational waves event parameters. So far, only one multimessenger event has been identified, and therefore we lack data and statistics to estimate precisely the Hubble constant and lift the tension between CMB and standard candles measurements, as shown in Figure 3.6. In the years to come, with the increasing sensitivity of gravitational waves detectors, we expect to detect more multimessenger events and refine the Hubble constant estimation.

3.3.2 Neutrinos

Neutrinos are a great example of the interplay between particle physics and cosmology. While cosmological observations help to constrain neutrino properties (see section 2.6.2, neutrinos themselves carry a lot of valuable information about cosmological and astrophysical processes.

The Cosmic Neutrino Background

As the CMB is the relic radiation of photons decoupling from the primordial plasma, early Universe physics predicts the emission of a relic neutrino radiation, emitted at neutrino decoupling (see section 1.2.2). This Cosmic Neutrino Background (CNB) would have been emitted only one minute after the Big-Bang, and its current temperature, diluted by expansion, is estimated at $T_\nu \simeq 1.95\mathrm{K}$, cor-

responding to 56 neutrinos/cm^3. This is about ten times lower than the CMB photon density, since we measure $\sim$ 410 photons/cm^3.

This low density, together with our relatively poor neutrino detection capabilities, would correspond to only one count in 590 000 years in a neutrino detection experiment like KATRIN[11] [98]! However, assuming that our local environment is denser thanks to gravitational clustering, one can expect $\sim$ 1.7 counts/year in KATRIN. Improving instrumental sensitivity could lead up to 170 counts/year, and other similar neutrino experiments similar - for example the projects PTOLEMY [31] and Project 8 [85] - should be able to place an upper limit on the local relic neutrino density... and maybe detect it in a not so far future!

Neutrinos and CP-violation

As mentioned in section 1.2.2, CP violation is one of the Sakharov conditions for matter-antimatter asymmetry to occur. This violation is possible within the standard model of particle physics if we allow for a complex phase in the matrix describing matter - antimatter oscillations. Such a phase would lead to processes at different rates for particles and antiparticles, hence violating CP. This violation has been under investigation for many years, and small symmetry breaches between quarks and anti-quark have been detected [106]. Their amplitude is however not big enough to explain the observed matter predominance.

In the T2K[12] experiment, neutrino oscillations are scrutinised to detect a potentially different behaviour between neutrinos and their antiparticles. A beam of alternatively muon neutrinos or antineutrinos is emitted in a particle accelerator, and some of the neutrinos are detected 295 km further, by the Super-Kamiokande[13] experiment. During this short journey, some of the neutrinos oscillate, and are converted from muon (anti)neutrinos to electron ones. Very recently, results of ten years of data taking have been published [65], showing that neutrinos seem to oscillate much more than antineutrinos, a clear signature of the CP-violation (see Figure 3.7), with 3σ confidence level. These results however need to be confirmed because of low statistics, and future generation of neutrino experiments could bring more evidence for CP-violation in neutrino oscillations.

Neutrino astrophysics

Beyond the interest in neutrinos as standard model particles, progress in neutrino detection capacities in the last 30 years now allows to observe astrophysical objects through their neutrino emissions. Neutrinos are of interest for stellar physics, because they are produced in star cores, that are impossible to observe in electromagnetic radiation.

Moreover, neutrinos are emitted in high-energy astrophysical processes, such as supernovae (first and only detection in 1987) and in Active Galactic Nuclei. The first multi-messenger detection of an AGN in both electromagnetic radiation and neutrino emission was achieved in 2018 using the IceCube[14] neutrino

[11] https://www.katrin.kit.edu/
[12] https://t2k-experiment.org/
[13] http://www-sk.icrr.u-tokyo.ac.jp/sk/index-e.html
[14] https://icecube.wisc.edu/

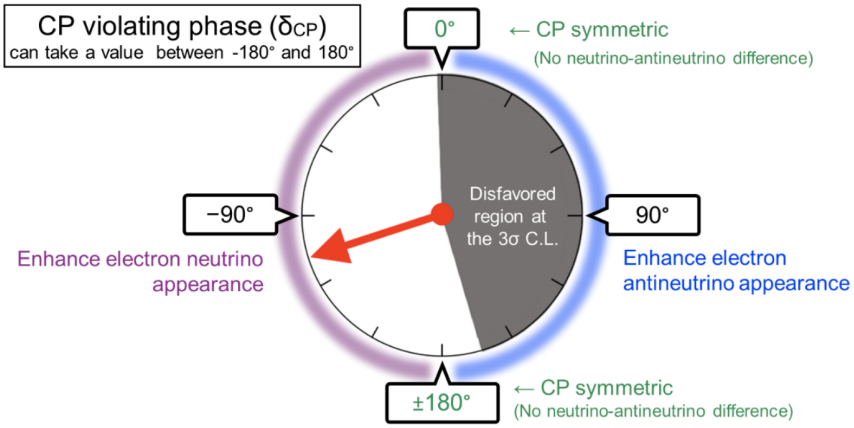

Figure 3.7 – CP-violating phase in neutrinos and antineutrinos oscillations measured by the T2K experiment.
Credit: The T2K Collaboration [65].

detector, located at the South Pole [63]. Although they are predicted to be emitted during neutron star mergers, neutrinos were however not detected during the multi-messenger gravitational event in 2017 (see previous section), likely because the neutrino jets were not aligned with Earth for this specific event. In the near future, the growing number of neutrino detection experiments being built or upgraded should result in progress in neutrino astrophysics, and help us better understand high energy processes in the Universe.

3.4 Cosmology on Earth

Cosmology is closely linked to particle physics, with research topics such as neutrinos, dark matter particles, matter/antimatter asymmetry, primordial plasma, etc. It is therefore instructive to approach these issues both from the point of view of cosmological and astrophysical observations - as I described earlier - and from the point of view of particle physics. Some of the studies carried out in the various experiments hosted at the Large Hadron Collider (LHC), as well as in other particle physics experiments, are of direct interest for cosmology.

Quark-gluon plasma

The quark-gluon plasma is a state of matter composed of free quarks and gluons, not yet bound into hadrons. It is assumed to have filled the entire Universe between 10^{-12} and 10^{-6}s, and is therefore of high interest to understand the very beginning of our cosmic history. In particular, matter and antimatter are created when quarks and gluons bound into hadrons. Understanding this phase transition in the quark-gluon plasma could therefore help us investigate the matter-antimatter asymmetry. However, as this plasma existed only before the last scattering surface, we have no chance to observe it directly in cosmological conditions. It is nevertheless possible to recreate this state of matter in specific conditions of very high density and pressure. The ALICE experiment[15] [60] stud-

[15] https://home.cern/science/experiments/alice

ies collisions of heavy ions - lead nuclei - in order to recreate locally the quark gluon plasma. This was achieved in 2011, resulting in the highest temperature ever reached on Earth: 5.5×10^{12} K! ALICE also observed that the quark-gluon plasma behaves much more like a perfect fluid with a much smaller viscosity than a gas, as it was previously expected. Asymmetric collisions of protons and lead nuclei are also investigated at CERN. They are of particular interest to be compared to lead-lead collisions, which are crucial in our understanding of QCD that rules primordial Universe.

Dark matter

Dark matter particles are being actively searched for by the ATLAS[16] and CMS[17] experiments. Their results have allowed to considerably narrowing down the potential candidates dark matter particles and model [113]. Moreover, other particle physics experiments aim at achieving a direct detection of dark matter particles through their interaction with other particles. For example, in the Xenon1T experiment, photo-multiplier tubes (PMT) record interactions producing scintillation light inside a liquid xenon target. Although no detection has been recorded so far, most recent results have allowed to put strong direct constraints on potential dark matter particle masses [270].

Matter/antimatter asymmetry

I already mentioned the contributions of neutrino physics in the search for CP violation within the standard model, that would explain for the matter/antimatter asymmetry. This violation is also investigated by the Belle II[18] experiment, that collides electron and positron, and by the LHCb[19] experiment, that studies collisions of particles containing a bottom quark. CP violation has recently been observed in charm decays [164], building the case for scenarios of the CP violation in the early Universe.

Cosmology and particle physics thus provide complementary constraints on some of the most elusive particles and phenomena in the Universe, which can only be beneficial to the progress our knowledge of the Universe.

[16] https://atlas.cern/
[17] https://home.cern/science/experiments/cms
[18] https://www.belle2.org/
[19] https://home.cern/science/experiments/lhcb

CHAPTER 4

Astrophysical foregrounds

Contents

I have already mentioned the problem of foregrounds when I described secondary anisotropies in Chapter 2. This term encompasses a wide variety of contaminants that contribute to the emission of the sky in the frequency range in which the CMB is observed, thus overshadowing its signal. Two families of foregrounds can be distinguished: diffuse foregrounds and more localised effects.

The later impacts predominantly very small angular scales, and is due to infrared and radio extragalactic sources, or Sunyaev-Zel'dovich clusters (see section 2.4.1). As these are mostly responsible for temperature anisotropies and lensing, at scales that are not of major interest for primordial B-modes, this part of the analysis is not detailed in the present work. One can refer for example to the review [157] for more details on their modelling and removal.

Our focus here is therefore more on diffuse foregrounds, that find their origin in the emission of our own Galaxy. The interstellar medium (ISM) is a complex environment, made of gas in different forms (molecular, atomic, ionised), dust of various sizes and compositions, and cosmic rays. The ISM is permeated by magnetic fields and exhibits turbulent regions, which makes its structure and dynamics difficult to study. Two phenomena are of particular interest for cosmology: dust interaction with magnetic fields that emits polarised light, and polarised synchrotron emission of cosmic rays particles spiralling around magnetic

fields. Even in the best frequency window and for the cleanest patch of the sky [154], these spurious polarisation signals are at levels comparable or higher than the one of the CMB B-modes, and could lead to a false detection of primordial B-modes. It is therefore necessary to disentangle CMB from foreground contribution if one wants to detect primordial B-modes with the highest possible level of confidence.

I first present a catalogue of diffuse foregrounds and their spatial, spectral and statistical properties in section 4.1, and then outline the principles of component separation in section 4.2.

4.1 Foreground inventory

In this first section, I give an overview of the main diffuse polarised foregrounds, in particular their frequency scaling and spectral laws. The two most important foregrounds when it comes to CMB polarisation are thermal dust and synchrotron radiation, and require a particularly careful modelling and removal. Other contaminants are also mentioned, but not described in detail since they are of less importance and are not always considered in polarisation component separation problems.

4.1.1 Thermal dust

Thermal dust emission is the most important contaminant to CMB polarisation, as it is the dominant foreground at frequencies higher than 70 GHz. To probe the structure of dust, we therefore mostly rely on high frequency channels. Typically, the best dust tracer that we currently have is the 353 GHz frequency channel from the Planck mission. At higher frequencies, CIB is not negligible anymore - and besides, high frequency channels in Planck were not sensitive to polarisation.

Dust grains are mainly made of silicate and carbon molecules, predominantly located in the galactic plane. Their sizes range from 0.005 to $0.25\,\mu\mathrm{m}$ [176]. They are not spherical, and tend to aggregate in bigger clusters, as shown in Figure 4.1, and thus behave as small electric dipoles. Most importantly, dust grains and their aggregates partially align perpendicularly to galactic magnetic fields. These aggregate absorb and re-emit starlight [74], and because of their alignment, the polarisation of the emitted light does not fully average out: dust emission is thus partially polarised.

Two important quantities measured when mapping the sky are both its polarisation fraction p and polarisation angle ψ, defined from Stokes parameters:

$$p \equiv \frac{\sqrt{Q^2 + U^2}}{I} \tag{4.1}$$

$$\psi \equiv \frac{1}{2} \arctan\left(\frac{U}{Q}\right). \tag{4.2}$$

The constraint on polarisation set by the Planck mission is $p = 19.8\% \pm 0.07$ [210]. More than the polarisation angle itself, an important quantity measured across

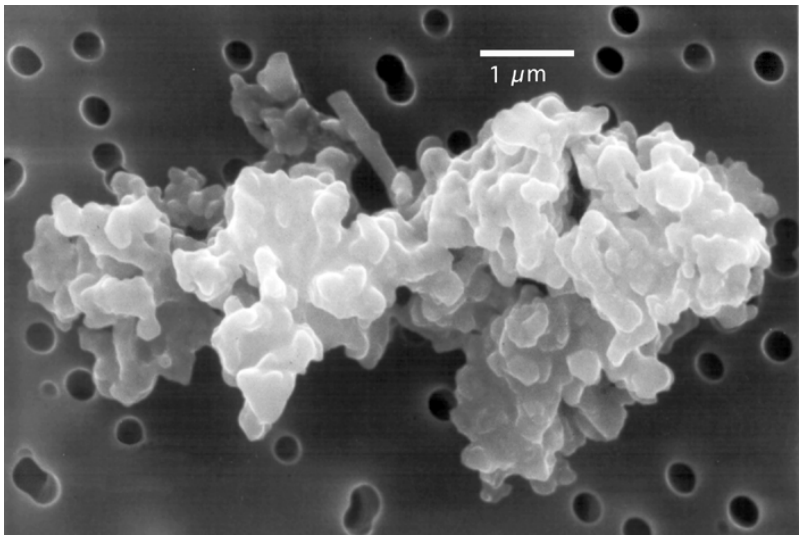

Figure 4.1 – Typical aggregate of interstellar dust grains.
Credit: D. E. Brownlee & E. K. Jessberger [135]

the sky is the polarisation angle dispersion for a given radius δ at a given sky position $\mathbf{r}$, defined as in e.g. [125, 210]:

$$\mathcal{S}(\mathbf{r},\delta) = \sqrt{\frac{1}{N}\sum_{i=1}^{N}[\psi(\mathbf{r}) - \psi(\mathbf{r}+\boldsymbol{\delta}_i)]^2}. \tag{4.3}$$

where $\boldsymbol{\delta}_i$ is a displacement vector from the central position $\mathbf{r}$. The average is taken over an annulus of radius δ containing N pixels. Measurements of S show that dust is organised in filaments, probing the structure of underlying magnetic fields, as shown in Figure 4.2. The interplay between galactic magnetic fields and foregrounds (mostly dust and synchrotron) is a very active topic of investigation in galactic science. The ultimate goal is to propose a foreground model based not only on template observations for various foregrounds, but rather on the three-dimensional structure of underlying magnetic fields.

For cosmological purposes, one of the most important results from dust measurements is the modelling of spectral emissivity: knowing dust emission at a given frequency, how can it be extrapolated at any other frequency - in particular at frequencies closer to the maximum emission of the CMB? This is particularly relevant in the context of component separation (see section 4.2).

There are two possible pitfalls in this approach. The first one is the variation of the emissivity parameters across the sky, that can source systematic errors if mis-estimated. Another drawback is frequency decorrelation, that can arise from spatial variations of emissivity parameters, or can have more complex sources such as a too simple model of dust properties. Planck results [218] show that the frequency decorrelation is not statistically significant, and poses no issues for experiments targeting to measure r above 0.01. Below this level, it is not possible to conclude given the Planck sensitivity [153].

A commonly used model for dust emission at any frequency ν is a modified

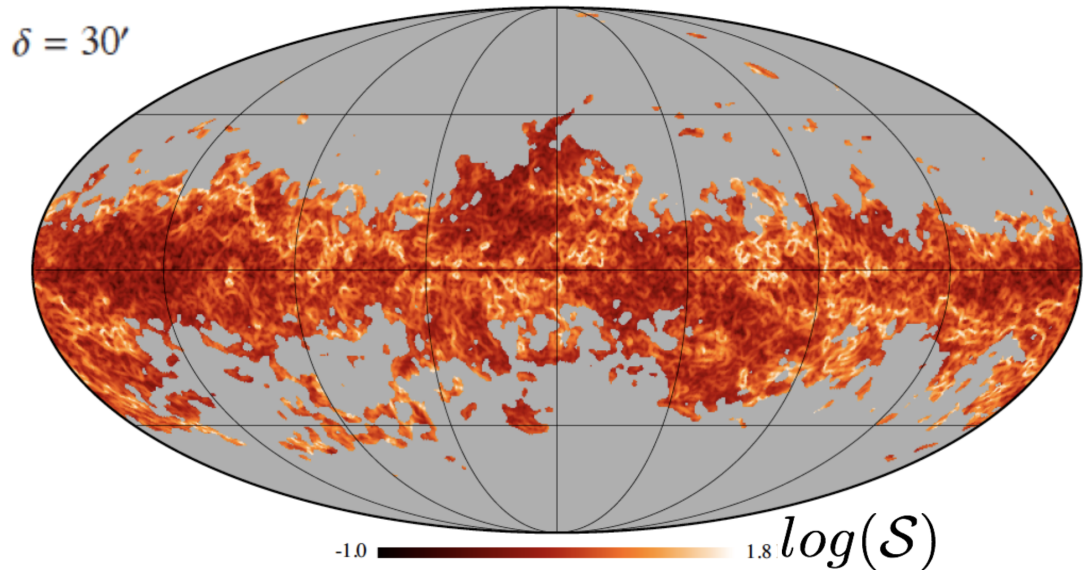

Figure 4.2 – Polarisation angle dispersion as defined in Eq. (4.3), probing underlying galactic magnetic fields
Credit: ESA and the Planck Collaboration [210]

black body spectrum (sometimes referred to as grey body):

$$A^{\rm dust}(\nu) \propto \frac{\nu^{\beta_d - 2}}{e^{\frac{h\nu}{kT_d}} - 1}, \tag{4.4}$$

where β_d is the dust spectral index and T_d is the dust temperature. The mean value across the sky of these parameters as measured by Planck are $\beta_d = 1.53 \pm 0.02$ and $T_d = 19.6\text{K} \pm 1.3\text{K}$. These values are however obtained from temperature but not polarisation data.

Moreover, in the context of ISM modelling, more refined models are developed. Some aim at reproducing more precisely the physical effects at the origin of dust polarisation by considering several dust populations with varying characteristics [86, 100], while others rather have a statistical approach, with dust population coupled to turbulent interstellar medium and galactic magnetic fields [275]. This refinement of models becomes all the more necessary in the current quest for B-modes, as one would ultimately like component separation to be informed by advanced ISM models.

4.1.2 Synchrotron radiation

Synchrotron is the second most important contaminant to CMB observations. Contrary to dust which is a high frequency contaminant, synchrotron emission is mostly present at lower frequencies, typically below 70 GHz, and is the dominant radio sky emission below 10 GHz.

In space, synchrotron radiation is typically emitted when relativistic particles (often electrons) spiral around magnetic fields, for example in pulsars or nebulae where strong magnetic field are present. In the Milky Way, magnetic fields are not very intense, with only $20 - 40\,\mu$G, but this is sufficient for cosmic ray particles to spiral around and emit synchrotron radiation.

Synchrotron emission frequency scaling can be modelled with a power-law spectrum

$$A^{\mathrm{sync}}(\nu) \propto \nu^{\beta_s}, \tag{4.5}$$

where β_s is the synchrotron spectral index. A good fit for the synchrotron spectral index is $\beta_s = -3.1$ [214], but this value can significantly vary spatially, in particular across the galactic plane (see section 4.1.4 hereafter).

4.1.3 Other foregrounds

Beside dust and synchrotron, there are other minor contaminants in the frequency range of interest for CMB observation. Since their polarisation fraction is very low, they are often not considered in component separation problems when it comes to CMB polarisation. However, they might have to be taken into account in data analysis for future experiments, in order to improve even further our sensitivity to primordial B-modes.

Free-free radiation

Free-free emission in sub-millimetre and radio domains arises from HII regions in our galaxy. It mostly depends on electron and ion densities and temperature. It is intrinsically unpolarised because of the isotropic nature of the interaction, but a fraction of emitted photons can be scattered through Thompson interaction, generating a small polarisation fraction. Since HII molecular clouds are not very dense, the polarisation fraction of free-free emission in the Milky Way is very low. Constraints from WMAP observations indicate a polarisation fraction of 3.4 % at most (with a 95% confidence level), and likely to be less than 1 % at high galactic latitudes [171].

Anomalous Microwave Emission

Anomalous Microwave Emission (AME) [81] is observed to contribute significantly between 10 GHz and 60 GHz, however its physical origin is not very well determined. It is likely emitted by very small spinning dust grain. At higher frequency (above 50 GHz), thermal fluctuations of dust grain magnetisation could also contribute to AME. It is not a very significant contaminant to CMB polarisation, since it is very weakly polarised, with a mean polarisation fraction $p \sim 1\%$, and at most 2.8% in some regions of the sky [105].

CO line

"CO line" usually refers to the first rotational emission line of the carbon monoxide (CO) molecule. CO is found in large hydrogen molecular clouds, and is therefore an excellent tracer of these star forming regions. Contrary to other foregrounds and precisely because it is an emission line, CO emission is very localised in frequency, around 115 GHz. It is therefore possible to avoid it when designing the frequency coverage of a CMB experiment, which is not the case for a foreground covering a broad frequency range. There are also other lines at higher frequencies (corresponding to other emission lines), that have to be avoided when

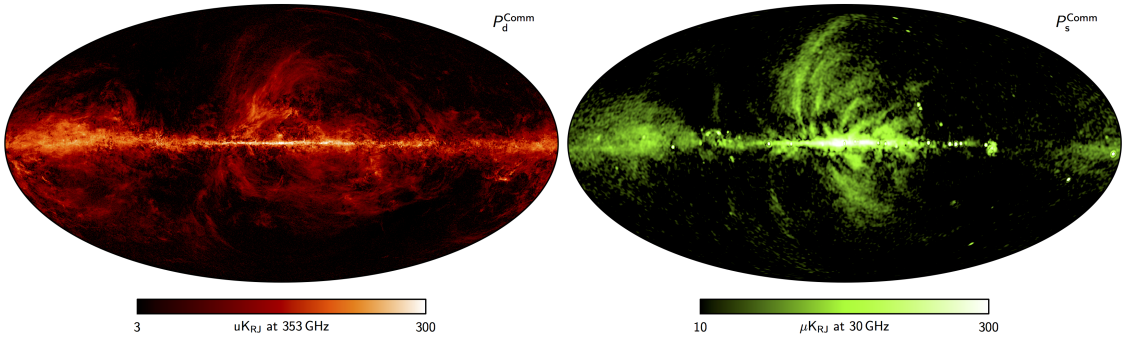

Figure 4.3 – Planck maps of dust at 353 GHz with a 5′ resolution (left) and synchrotron at 40 GHz with a 40′ resolution (right).
Credit: ESA and the Planck Collaboration

designing a space missions, since they usually have a broader frequency cover than ground experiments (as detailed in Chapter 5). However, as for AME, CO line polarisation fraction is very low, a few percent at most [68], which limits its impact on CMB polarisation measurements.

Although these last three foregrounds are weakly polarised, their signal combined with instrumental effects, such as bandpass or gain mismatch (see Chapter 5), could turn the unpolarised signal into a spurious polarisation signal. As we target lower values for the tensor-to-scalar ratio r, we may have to take this effect into account in the future.

4.1.4 Spatial and statistical properties

As mentioned in the introductory part of this chapter, diffuse foregrounds find their origin in the emission of our Galaxy. Their emissions are therefore more important in the galactic plane, as shown in Figure 4.3 for dust and synchrotron. CMB polarisation observations in the galactic plane are impossible because of this strong contamination, and when observed in full sky surveys (for example with Planck or WMAP), this region is masked in the maps before further analysis is performed. In contrast, it is possible to choose a sky patch further away from the galactic plane where foreground contamination (and in particular dust which is the main contaminant) is particularly low. This is one of the key drivers for CMB polarisation observations from the ground, which helps to compensate for the limited number of frequency bands available from the ground.

As mentioned above, spectral indices of foregrounds can significantly vary across the sky. This is particularly true for synchrotron, and requires to observe the sky at low frequency, where synchrotron emission is dominant, as this is done for example with the S-PASS experiment that surveys the sky at at 2.3 GHz [154]. In addition to this spatial effect, synchrotron is also expected to have spectral curvature, i.e. its spectral index slightly changes depending on the frequency domain. Once again, this effect has to be modelled to avoid bias in component separation [147, 146]. As for dust, in addition to varying spectral indices over the sky [213], the problem is also that we lack a precise modelling of the dust spectral emission, as the modified black-body that I introduced earlier is a rather simple

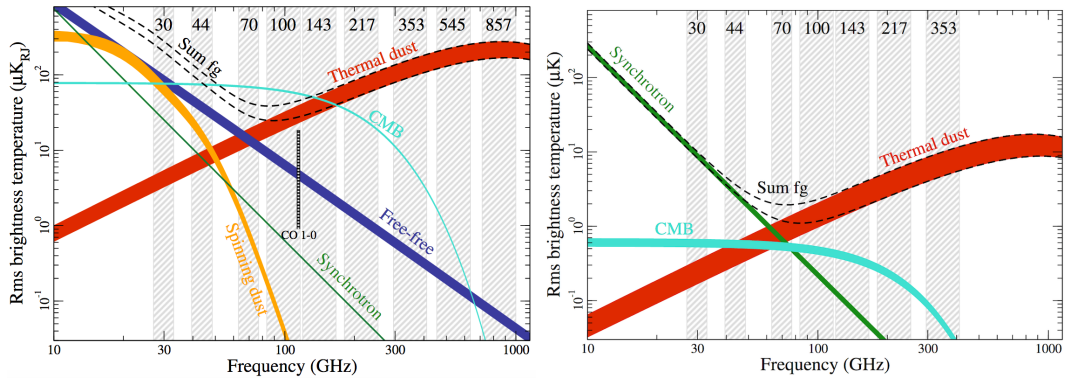

Figure 4.4 – Frequency coverage of foregrounds and CMB, in temperature (left) and polarisation (right).
Credit: ESA and the Planck Collaboration [211]

model. As mentioned at the end of section 4.1.1, a precise modelling of various properties of dust populations (such as their composition, size, etc.) might be needed in the future to better encompass the complexity of thermal dust polarised emission [124].

Finally, we need to mention a very important statistical property of foregrounds: contrary to the CMB, foregrounds are non-Gaussian, and therefore have non zero bispectrum. This is true for dust both in temperature and polarisation, but only for synchrotron temperature [69, 154, 185]. This property is used by some of the component separation techniques that I describe in the next section.

4.2 Component separation

Figure 4.4 shows the amplitude and frequency dependence of foregrounds presented in the previous section, both in temperature and polarisation. For polarisation, only the two main contaminants are shown - i.e. dust and synchrotron. Given the current upper-limits on r and the angular scales where primordial B-modes are expected to peak ($\ell \sim 80$), B-modes are always dominated by the total foreground contribution, whatever the frequency. This poses both technical challenges in terms of frequency coverage of CMB experiments as detailed in the next chapter, and data analysis challenges as detailed hereafter.

4.2.1 Challenges for B-modes measurements

As we target lower and lower B-modes amplitude, corresponding to lower tensor-to-scalar ratio r, foregrounds quickly become dominant over the CMB power spectrum, as shown in Figure 4.5. As a result of this, CMB B-modes can be mistaken with dust polarisation. This is what happened with the BICEP/Keck experiment[1] in 2014, whose team announced the measurement of $r = 0.2^{+0.07}_{-0.05}$ [32]. This detection - which would have been groundbreaking if confirmed - was essentially due to dust polarisation dominating CMB emission. Although dust

[1] http://bicepkeck.org/

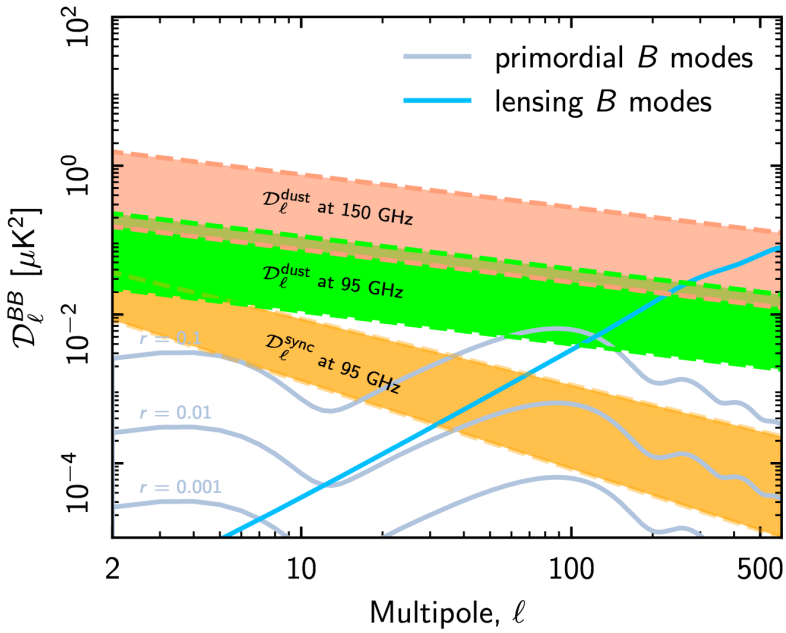

Figure 4.5 – Power spectra of foregrounds at different frequencies, compared to lensing and primordial B-modes, for different values of r.
Credit: ESA and the Planck Collaboration [218]

models provided by Planck were used to check for potential foreground contamination, the data relevant to the sky area targeted by BICEP was not available to the BICEP team. This emphasises the importance of self-consistent, internal data sets for component separation. The result was then amended a year later, with a co-analysis of BICEP/Keck data using new Planck dust maps [34]. This led to a new upper limit on r ($r < 0.06$ with a 95% confidence level), but any hint of the detection was thus removed.

Component separation is therefore a crucial issue in the current data analysis effort for CMB experiments. It calls for multi-frequency experiments, to measure maps of the sky at both lower and higher frequencie than CMB channels, where foregrounds dominate the sky emission. All major CMB polarisation experiments now cover a wide frequency range to alleviate this issue - experiment design and operations are detailed in Chapter 5, and in particular in section 5.2.3 for the design of frequency coverage.

4.2.2 Overview of methods

Once multi-frequency data sets are gathered, component separation techniques are required to separate the multi-component sky signal into its CMB and foregrounds contribution. The idea common to all methods is to separate the (almost) Gaussian black body signal of the CMB, from other signals. Although it looks simple, this process nevertheless faces many challenges. There is therefore a wide range of component separation techniques [2], in map or harmonic domain, that can be used on the same data set to validate results.

[2] A more extensive catalogue of methods and their variations can be found at `https://lambda.gsfc.nasa.gov/toolbox/tb_comp_separation.cfm`, on which this review is partially based.

In the most general way, the data model for component separation problems is written as:

$$\mathbf{m} = \mathbf{A}\mathbf{s} + \mathbf{n}, \tag{4.6}$$

where $\mathbf{s}$ is the sky signal of the individual components (CMB and foregrounds), $\mathbf{n}$ is the noise and $\mathbf{A}$ is the so-called mixing matrix. This matrix models the mixing of sky components, as a function of frequency. The challenge of component separation is to reconstruct $\mathbf{s}$ from the observed signal $\mathbf{m}$, without having a full knowledge of $\mathbf{A}$. To achieve this, some methods rely on parametric modelling of the mixing matrix $\mathbf{A}$ (the so-called parametric methods), whereas others rely more on the specific properties of CMB and foreground signals, such as their (non-)Gaussianity and/or spectral distribution, without explicitly reconstructing the mixing matrix. I give here an overview of the three main categories of component separation methods: template removal, blind and semi-blind methods, and parametric methods.

Template fitting

Template removal or template fitting methods are the most intuitive ones: high (resp. low) frequency channels are used to build a dust (resp. synchrotron) template. They are then scaled in frequency using fitted spectral laws, and subtracted from frequency channels of interest for the CMB. The general data model, Eq. (4.6), can be written so that CMB channels are formally separated from foreground channels:

$$\mathbf{m}(\nu) = \mathrm{CMB}(\nu) + \sum_i a_i \mathbf{f}_i(\nu) + \mathbf{n}(\nu), \tag{4.7}$$

where $\mathbf{f}_i$ are the individual foreground signals, and a_i are the template fitting coefficients, that correspond to elements of the mixing matrix $\mathbf{A}$ introduced in Eq. (4.6). These coefficients are most often scaling laws of actual physical components, but can also be arbitrary. To remove foregrounds, template fitting methods form a linear combination of all single frequency maps modelled as in Eq. (4.7), and estimate the CMB signal by setting all the foreground terms to zero [133]. This allows to reconstruct a cleaned CMB map, but not to estimate scaling laws and/or foreground maps, as parametric methods do.

The first template fitting methods that were developed assumed fixed fitted foreground parameters over the whole sky or very large pixels, which could lead to biases on the recovered value or r [142]. However, most recent methods allow to deal with spatially varying spectral indices. For example, the "Delta-map method", proposed in [133], takes advantage of the fact that modern experiments have redundant dust and synchrotron channels (at least 2). One can thus constrain two parameters per foreground - sky-averaged value and first order variation.

Although it is most commonly applied in map domain, template fitting can also be adapted to the wavelet space [116], and to some extent to the harmonic domain. Indeed, in the context of Planck data analysis, one of the methods developed for component separation was hybrid between template fitting and Independent Component Analysis (see below). In the Spectral Matching Independent

Component Analysis (SMICA)[3] [48], foregrounds are modelled arbitrary in terms of power spectra, amplitude and correlation between components. It is a method quite different from other template fitting approaches in the sense that the variance is parametrised, not a linear combination of maps or power spectra as it is most often the case in component separation techniques. The data model in the harmonic domain reads as [132]:

$$\boldsymbol{\mathcal{C}}_\ell(\theta) = aa^\dagger \boldsymbol{\mathcal{C}}_\ell^{CMB} + \mathbf{F}\mathbf{P}_\ell\mathbf{F}^\dagger + \mathbf{N}_\ell, \tag{4.8}$$

where a describes the spectrum of the CMB at each frequency, $\mathbf{F}\mathbf{P}_\ell\mathbf{F}^\dagger$ is the foreground covariance and $\mathbf{N}_\ell$ the noise. The model $\boldsymbol{\mathcal{C}}_\ell(\theta)$ is fitted to the data by minimising:

$$\hat{\theta} = \arg\min_\theta \sum_\ell (2\ell+1)[\mathrm{tr}(\hat{\boldsymbol{\mathcal{C}}}_\ell \boldsymbol{\mathcal{C}}_\ell^{-1}(\theta)) + \log\det(\boldsymbol{\mathcal{C}}_\ell(\theta))]. \tag{4.9}$$

Here, $\hat{\boldsymbol{\mathcal{C}}}_\ell$ contains an estimate of all auto and cross-spectra of input data computed from spherical harmonic coefficients of the observed maps $a_{\ell m}$ as in Eq. (2.38).

Blind and semi-blind methods

Blind and semi-blind methods assume little to no prior information on foregrounds, and are therefore often used in the first instance when analysing a data set. To give a very general description, only the spectral distribution of the CMB is known (black body), and the sky signal is modelled as a sum of non-Gaussian contributions. Blind and semi-blind methods identify the least non-Gaussian one, which is then assumed to be the CMB.

Internal Linear Combination Internal Linear Combination (ILC) methods are a class of blind methods able to extract a component of known emission law, typically CMB, while assuming very little about other emissions. In these methods, no prior information on foregrounds, such as spectral emission laws, or external data sets are required, and no precise properties about instrumental noise are needed. For these reasons, it was one of the first methods to be used in component separation problem for multi-frequency data sets, in particular for the WMAP mission [27]. Here, I adopt the approach of [93, 279] to describe briefly the method.

As for template fitting, the idea behind ILC is that CMB emission is frequency independent, or equivalently that the CMB follows a perfectly known black body spectrum, and thus that CMB emission is independent of the observing frequency (its mixing matrix element are all equal to one). The data model resembles that of template fitting

$$\mathbf{m}(\nu) = \mathrm{CMB}(\nu) + \mathbf{f}(\nu) + \mathbf{n}(\nu), \tag{4.10}$$

[3] SMICA imposes independence between signals, hence the name, but because it assumes foreground models (even arbitrary), it is most often classified as a harmonic domain template fitting method.

with the notable difference that the foreground term $\mathbf{f}$ is not modelled as a sum of several components, but is just considered as such. We then form a linear combination of data (foregrounds and noise) for all n_f frequency bands:

$$\mathbf{m} = \mathrm{CMB} + \sum_{i=1}^{n_f} w_i(\mathbf{f}(\nu_i) + \mathbf{n}(\nu_i)) \tag{4.11}$$

with $\sum_f w_f = 1$. Under this assumption, weights w_f can be chosen to minimise the data variance, which also minimise residuals in the cleaned CMB maps:

$$\mathrm{Var}(\mathbf{m}) = \mathrm{Var}(\mathrm{CMB}) + \mathrm{Var}\left(\sum_{i=1}^{n_f} w_i(\mathbf{f}(\nu_i) + \mathbf{n}(\nu_i))\right). \tag{4.12}$$

The weights minimising Eq. (4.12) are given by

$$w_i = \frac{\sum_{j=1}^{f} C_{ij}^{-1}}{\sum_{jk} C_{jk}^{-1}}, \tag{4.13}$$

where the data covariance matrix $\mathbf{C}_{ij}$ is defined as

$$\mathbf{C}_{ij} \equiv \frac{1}{N} \sum_{N} \left(\mathbf{m}_i(n) - \bar{\mathbf{m}}_i\right)\left(\mathbf{m}_j(n) - \bar{\mathbf{m}}_j\right), \tag{4.14}$$

with $\bar{\mathbf{m}}$ the average of $\mathbf{m}$ over the relevant data set (map, power spectrum, etc.).

Until now, the domain in which the data objects are defined was indeed intentionally left not specified. The standard ILC approach is a map-based method: in this case, CMB, $\mathbf{f}$ and $\mathbf{m}$ are maps, N in Eq. (4.14) is the total number of pixels, and n the index of an individual pixel. The method can be applied several times on several sky patches to take into account foreground variation over the sky. However, the method can also be extended in other domains than the map domain, without losing in generality. In the context of CMB data analysis, ILC methods have been developed in the harmonic [256], wavelet [76] and spin-wavelet [234] domains.

Independent Component Analysis Independent Component Analysis (ICA) techniques are another popular class of blind or semi-blind methods, depending on their variations and implementation. The underlying idea of ICA is to assume that the CMB is independent of all other components, and that it is the least non-Gaussian component of all relevant to the problem. The data model is the same generic data model Eq. (4.6), and the solution for component separation is to find a linear transformation $\mathbf{W}$ such as $\mathbf{W}$s has independent components. In this case, for a single component i we have (neglecting the noise here for more clarity):

$$\mathbf{y}_i = \mathbf{W}_i^t \mathbf{m} = \mathbf{W}_i^t \mathbf{A} \mathbf{s}. \tag{4.15}$$

In the most general case, $\mathbf{y}_i$ is a linear combination of the sources $\mathbf{s}$, since $\mathbf{W}$ and $\mathbf{A}$ are linear. According to the central limit theorem, the distribution of $\mathbf{y}_i$ is likely to be more Gaussian than any of the components, even if elements of the sum are non-Gaussian. In ICA methods, the matrix $\mathbf{W}$ is chosen so that the

non-Gaussianity of components $\mathbf{y}_i$ is maximised, and the left over component is the CMB. One of the requirements for ICA is therefore to find a function to evaluate the non-Gaussianity of a distribution, and to maximise it. The most popular implementation of ICA in map domain is FastICA [172], that uses negentropy to measure non-Gaussianity. Like ILC, ICA methods can be applied both in space domain or in harmonic domain.

Parametric methods

Parametric methods rely on the estimation of components spectral parameters. Observations are modelled using their respective spectral laws, and parameters of the model are then fitted to the data. Parametric methods therefore naturally allow to reconstruct not only the CMB signal, but also the foreground signal, as foreground physical parameters are explicitly estimated. They can however lead to systematic biases in the results, if the model used for a component does not match the true component emission. The data model is again as in Eq. (4.6), but one has to note that the mixing matrix $\mathbf{A}$ is explicitly parametrised by foreground emissivity parameters:

$$\mathbf{m}(\nu) = \sum_{\text{comp.}} \mathbf{A}^{\text{comp.}}(\beta_{\text{comp.}}, \nu)\mathbf{s}_{\text{comp.}} + \mathbf{n}(\nu), \tag{4.16}$$

where components $\mathbf{s}_{\text{comp.}}$ are typically CMB, dust and synchrotron. $A(\beta_{\text{comp.}}, \nu)$ is a mixing matrix built using spectral laws and component parameters $\beta_{\text{comp.}}$, estimated in the component separation process.

The most popular implementation of a parametric method is COMMANDER [94], which adopts a Bayesian approach based on Monte-Carlo sampling using Gibbs sampling to sample the posterior distribution. Given the data d, the algorithm estimates jointly the signal map s and foreground parameters, and the CMB power spectrum C_ℓ, by computing the joint distribution of parameters $P(s, A(\beta_{\text{comp.}}), C_\ell|d)$. However, COMMANDER relies on intensive Monte-Carlo sampling, that can be a limitation in the case of high-dimensional problems and large data sets, as this is more and more the case in CMB experiments.

xForecast In this work, I have been working in the xForecast framework [95, 96, 246], which is an implementation of a two-step parametric component separation method, and turns it into a forecasting machinery. The two steps are:

- the mixing matrix $\mathbf{A}^{\text{comp.}}$ is reconstructed by fitting for foregrounds parameters $\beta_{\text{comp.}}$ from a multi-frequency data set;
- cleaned, single frequency foreground and CMB maps are reconstructed using the fitted parameters.

The forecasting capability of xForecast is based on extending the standard component separation formalism to allow it to deal with objects, such as likelihoods, averaged over an ensemble of potential data sets. This allows to reduce significantly the computation time, without loosing accuracy. The single

frequency data model is the same as Eq. (4.16), and for a multi-frequency data set we write:

$$\mathbf{m} = \hat{\mathbf{d}} + \mathbf{n} \equiv \hat{\mathbf{A}}\,\hat{\mathbf{s}} + \mathbf{n}, \tag{4.17}$$

where $\hat{\mathbf{d}}$ is the noiseless data, $\hat{\mathbf{A}}$ is the true mixing matrix, $\hat{\mathbf{s}}$ the sky signal and $\mathbf{n}$ the noise. Following for example [247], we write the spectral likelihood as:

$$\mathcal{S} = -(\mathbf{A}^t\,\mathbf{N}^{-1}\,\mathbf{m})^t\,(\mathbf{A}^t\,\mathbf{N}^{-1}\,\mathbf{A})^{-1}\mathbf{A}^t\,\mathbf{N}^{-1}\mathbf{m}. \tag{4.18}$$

The maximisation of this likelihood allows to determine the foreground parameters $\beta_{\rm comp}$. This procedure can be repeated for any input data, in particular for various noise realisations. However, in a forecasting approach, instead of averaging simulations over various noise realisations, we analytically average likelihoods, and write an ensemble average likelihood [246]:

$$\langle\mathcal{S}\rangle_{\rm CMB\,+\,noise} = -{\rm tr}\sum_p\{(\mathbf{N}^{-1}\,-\,\mathbf{P})\,(\langle\hat{\mathbf{d}}\,\hat{\mathbf{d}}^t\rangle_{\rm CMB\,+\,noise}\,+\,\mathbf{N})\}, \tag{4.19}$$

with $\mathbf{P}$ the projection operator defined as:

$$\mathbf{P} \equiv \mathbf{N}^{-1}\,-\,\mathbf{N}^{-1}\,\mathbf{A}(\mathbf{A}^t\,\mathbf{N}^{-1}\,\mathbf{A})^{-1}\,\mathbf{A}^t\,\mathbf{N}^{-1}. \tag{4.20}$$

The component separation procedure is achieved by minimising $\langle\mathcal{S}\rangle$ from Eq. (4.19) with respect to foreground parameters, in particular spectral indices for dust and synchrotron and dust temperature.

In this section, I gave an overview of the most common component separation techniques, outlining their principles without going into the details of actual implementation, which, as always, represents a much greater amount of work! In particular, one has to take into account various effects, such as instrumental noise, map resolution, missing data, instrumental effects, etc. During my thesis, I have been working on extending parametric component separation methods to include a more accurate instrument model, as detailed in Chapter 8.

CHAPTER 5

CMB polarisation experiments

Contents

After mentioning in the previous chapters former experiments that have measured CMB temperature and polarisation fields, I now focus on the most recent development of CMB polarisation experiments. The new generation of CMB polarisation experiments is specifically designed to target low amplitude primordial gravitational waves, taking into account contamination by lensing and foregrounds. This sets some specific constraints on instrumental design, that are detailed in this chapter. I focus in particular on POLARBEAR/Simons Array and Simons Observatory experiments, as I am a member of these collaborations.

In section 5.1, I start with the basic principles of CMB detection, common to many experiments, and I then highlight the main recent technological developments for the next generation observatories in section 5.2. In section 5.3, I present in more details some of these experiments and the scientific results that are expected.

5.1 Typical architecture

Although there are design differences due to different science goals (e.g. lensing B-modes, primordial B-modes, Sunyaev-Zel'dovich effects, etc.), most of CMB polarisation experiments share the same common architecture, broadly speaking a telescope, a cryogenic receiver and a data acquisition chain, whose designs are often similar.

5.1.1 Telescope

The design of the telescope is chosen depending on the targeted field-of-view and angular resolution. As a rule of thumb, a smaller aperture means a wider field-of-view but a lower angular resolution, which is appropriate to look for large scale, primordial B-modes. Wider apertures correspond to a smaller field-of-view, but with a sharp angular resolution, favouring observation of more localised effects such as Sunyaev-Zel'dovich effects, or lensing B-modes.

Without going into detail, let us mention here two of the most common optical design for CMB experiments

- refracting telescope: used to achieve a large field-of-view and relatively lower angular resolution. Refracting telescopes are used for example in the BICEP and Keck Array experiments [258], and are the planned design for the Simons Observatory Small Aperture Telescopes (SATs) [268] and the High Frequency Telescope (HFT) of the space mission LiteBIRD [242];

- crossed Dragone design: off-axis telescope design, which has two main advantages when it comes to CMB polarisation observations: the polarisation state of the incoming light is preserved along the optics chain, and the off-axis nature of the design limits some systematic effects, in particular in the millimetre and sub-millimetre range. A crossed Dragone design is suitable for observations at relatively small angular scales. The three telescopes of the Simons Array [251] are crossed Dragone, and it is is also the planned design for the Simons Observatory Large Aperture Telescope (LAT) and the Low Frequency Telescope (LFT) of LiteBIRD.

Combining these two types of telescopes in future experiments such as CMB-S4 (see section 5.2.3) will therefore allow to access both large and small angular scales, and greatly improve constraints on primordial B-modes [19].

The design of the optics chain of the telescope also includes a number of lenses and optical elements aiming at minimising stray light and systematic effects. Another crucial element of the optics chain is the polarisation modulator. In many current and future experiments, the polarisation modulator is a continuously rotating half-wave plate (HWP), whose design and characteristics are detailed hereafter and in section 7.1.1.

5.1.2 Receiver

Located at the end of the optics chain (telescope and optics tube), the receiver is the core and one of the most complex part of the experiment. It is composed of

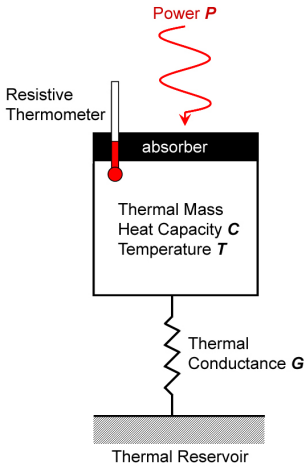

Figure 5.1 – Schematic of a bolometer
Credit: D.F. Santavicca

the focal plane, populated by detectors, a cryogenic cooler and a data acquisition system.

Detectors

Most of modern CMB polarisation experiments use transition-edge sensors (TES) bolometers[1]. Bolometers are incoherent detectors designed to measure the power of incident electromagnetic radiation. The resistance of a bolometer depends on its temperature through a dimensionless parameter α:

$$\alpha \equiv \frac{d\log(R)}{d\log(T)} \tag{5.1}$$

Bolometers are made of three main parts shown in Figure 5.1:

- an absorber, whose temperature - and thus resistance - increases when it receives power from a radiation;
- a thermal reservoir, to dissipate the power absorbed by the absorber;
- a thermal link, that couples the absorber and the thermal bath.

Transition-edge sensor (TES) bolometers are cryogenic bolometers, where the absorber is made of a superconducting material, biased so it is maintained midway in its superconducting transition. This requires sub-K temperature, typically 250 mK. When a radiation hits a TES bolometer, it oscillates between normal and superconducting state, making the change in resistance particularly important and therefore easier to measure. Current generation of TES detectors are photon-noise limited: to improve instrumental sensitivity, one therefore needs to control systematic effects better, choose a low background environment, and, most importantly, increase the number of detectors. The latter is the main driver for the deployment of arrays of thousands of detectors.

[1] Other technologies exist, in particular Kinetic Inductance Detectors (KID). Some experiments such as NIKA or CCAT deploy or plan to deploy KIDs arrays for cosmology [45, 56, 255].

In operation, TES bolometers are coupled with an antenna (see hereafter) that dissipates the sky signal (CMB photons) in the bolometer. Under certain operating conditions (voltage-biased mode), this generates a current through the bolometer, which allows to measure the sky signal. Measuring this current with high precision and without affecting the circuit containing the bolometer requires a device with high gain, low input noise and low input impedance. Moreover, collecting data from thousands of cryogenic detectors at the same time without affecting them is challenging. These technical questions are addressed in section 5.2.

Reconstructing polarisation

Before the signal is detected by the bolometer, the optical, polarised signal is amplified and converted to an electric, intensity-only signal. Most of CMB experiments achieve this by using feedhorns antennas, whereas POLARBEAR/Simons Array and some of Simons Observatory telescopes use or plan on using specifically designed lenslet-coupled antennas as amplification devices. The lenslets or horns are used to boost the gain of the antenna. The lenslet-antenna system also impacts the beam of the instrument. Once the signal has been converted to an electric signal, it dissipates power in the bolometer and thus modifies its state. This electric signal conveys all information through its intensity, and therefore the polarisation information have to be reconstructed. There are two methods to do so: pair difference or polarisation modulation.

Pair differencing On the focal plane, detectors are paired to form a pixel. Detectors are orthogonal to each other within a pixel, making them sensitive to orthogonal direction of the incoming light. The antenna being polarised, it is therefore possible to reconstruct polarisation by differentiating signals received by the detectors pair by pair, as shown in Figure 5.2. Moreover, the focal plane is populated with two types of pixels, Q and U, each of them sensitive to a different polarisation state. This is necessary if one wants to be able to reconstruct the polarised sky signal in sky coordinates.

This pair difference polarisation reconstruction scheme is intuitive, and in theory allows for the removal of most of atmospheric contribution, that cancels out in the difference. However, if there is a slight difference between detectors properties of the same pair (e.g. gain or bandpass), this can lead to a systematic bias, in particular intensity-to-polarisation (I-to-P) leakage. The performance of detector arrays can thus be limited by correlated noise, in particular atmospheric noise. This noise, that scales like $1/f$, is therefore an important contaminant at low frequency, and hinders our capability to detect large scale B-modes, precisely because these require integrating the signal over a long period of time.

Polarisation modulation An alternative to pair differencing is to modulate the polarisation of the incoming light as a function of time. It is important to ensure that each sky pixel is observed under different angles so that the polarisation signal can be reconstructed by demodulating the time-dependant signal of the detectors (see Chapter 7). This polarisation modulation can be achieved by the

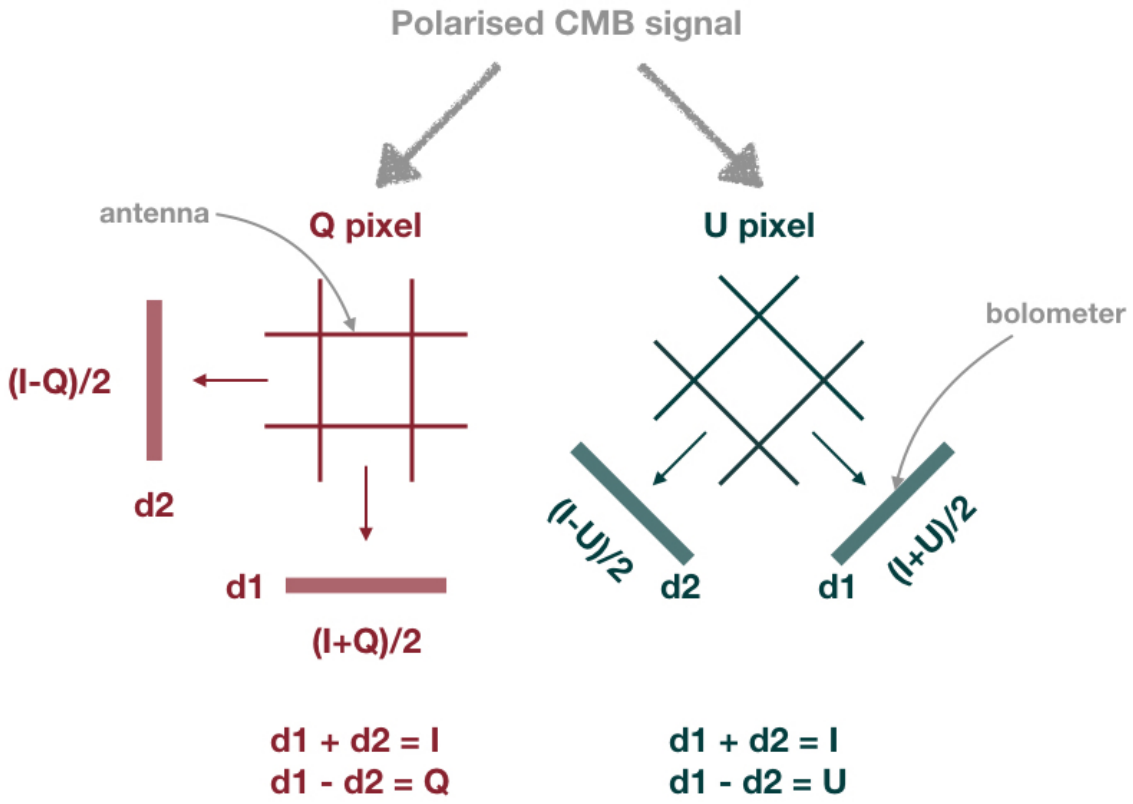

Figure 5.2 – Reconstructing intensity and polarisation from Q and U pixels

scanning strategy: in this case, the orientation of the telescope's polarised detectors with respect to the sky changes with time, which provides various attack angles. This strategy was adopted for example by Planck. Another solution is to add a mobile polarisation modulator in the optics chain of the instrument, that rapidly modulates incoming light[2]. Technical solutions include variable-delay polarisation modulator, as deployed in CLASS[3] [118], but one of the most common solution in CMB polarisation experiments is to deploy a continuously rotating half-wave plate (HWP). A HWP is made of bi-refringent material, such as sapphire, and introduces a phase shift of π between two incoming and outgoing polarisation states. For a rotating HWP with a time-dependent angle $\varphi_t = \omega t$ (with ω the rotation speed), a simplified data model can be written as (see section 7.1.1 for the derivation of this equation and a more detailed expression):

$$d = I + Q \times \cos(4\varphi_t) + U \times \sin(4\varphi_t), \tag{5.2}$$

The polarisation of the incoming signal can thus be reconstructed by demodulating the $4\varphi_t$ modulated signal from the bolometers. By doing so, one can effectively measure the polarisation signal at a frequency where the detector sensitivity is dominated by white noise and not $1/f$ noise: a HWP therefore effectively mitigates atmospheric noise [155, 231, 254]. Moreover, it allows a single detector to be sensitive to both polarisation states as shown in Eq. (5.2), which solves the issue of detector properties mismatch in the pair difference scheme. Experiments

[2] This does not change the fact that one needs a carefully designed scanning strategy to correctly sample the sky, but it does alleviate certain constraints on the scanning strategy.

[3] https://sites.krieger.jhu.edu/class/

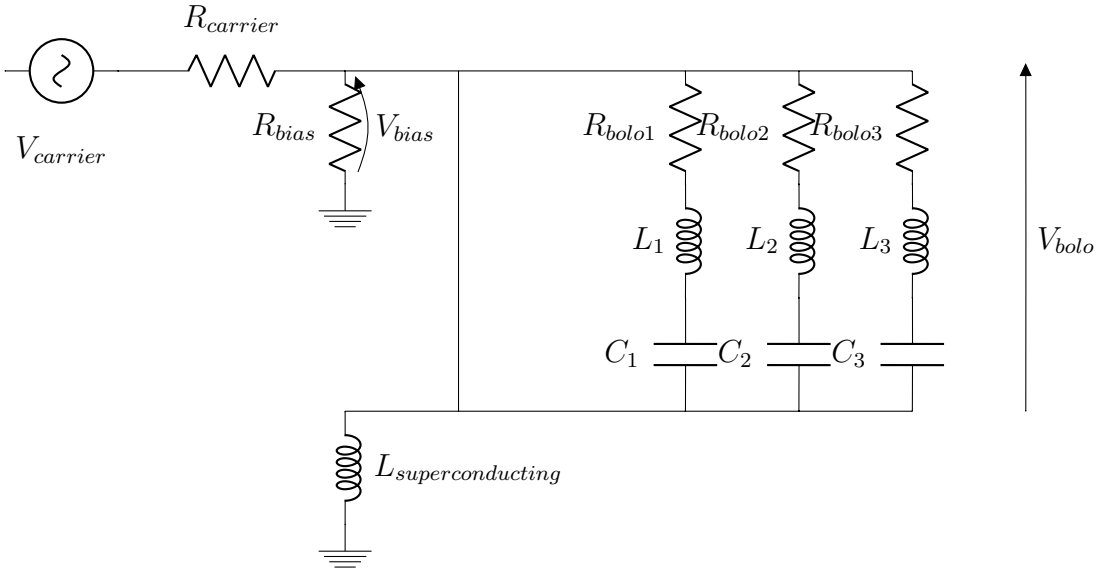

Figure 5.3 – Schematic of DfMUX readout system. Bolometers, modelled as resistors, are connected in series with a coil L and a capacitor C creating parallel RLC circuits.

deploying a HWP such as POLARBEAR/Simons Array and the Simons Observatory actually have both technologies, detector pairs for pair differencing, as well as a HWP for demodulation. This redundancy allows for internal consistency checks and better control of systematic effects.

HWPs therefore are crucial elements for some of the current and future CMB polarisation experiments, both ground- and space-based. However, introducing a new element in an instrument also necessarily introduces potential systematic effects. It is therefore needed to carefully model the HWP for efficient calibration and data analysis, as detailed in section 7.1.

Readout

Readout technologies are advanced electronic systems allowing to multiplex and read a constantly increasing number of cryogenic detectors operating simultaneously, without affecting their signal or heating them. Readout systems can vary between experiments, but one of the most popular scheme is Digital Frequency Multiplexing (nicknamed DfMUX) [83].

In order to minimise the number of wires, TES bolometers are grouped, and each bolometer is mounted in series with an inductance and a capacitance, different for each bolometer (see figure 5.3). This creates RLC resonators with different resonance frequencies. The same carrier signal with different frequency components - a frequency comb - can therefore be used to read several bolometers at the same time, which limits the number of wires, and simplifies the readout electronics. This frequency combs give its name to this readout scheme.

For TES bolometers, the current flowing through the bolometer that we want to measure, I_{bolo}, is sent through a superconducting coil, which has the required low input impedance for the measurement. This coil produces a magnetic field, which changes as I_{bolo} changes. A Superconducting QUantum Interference De-

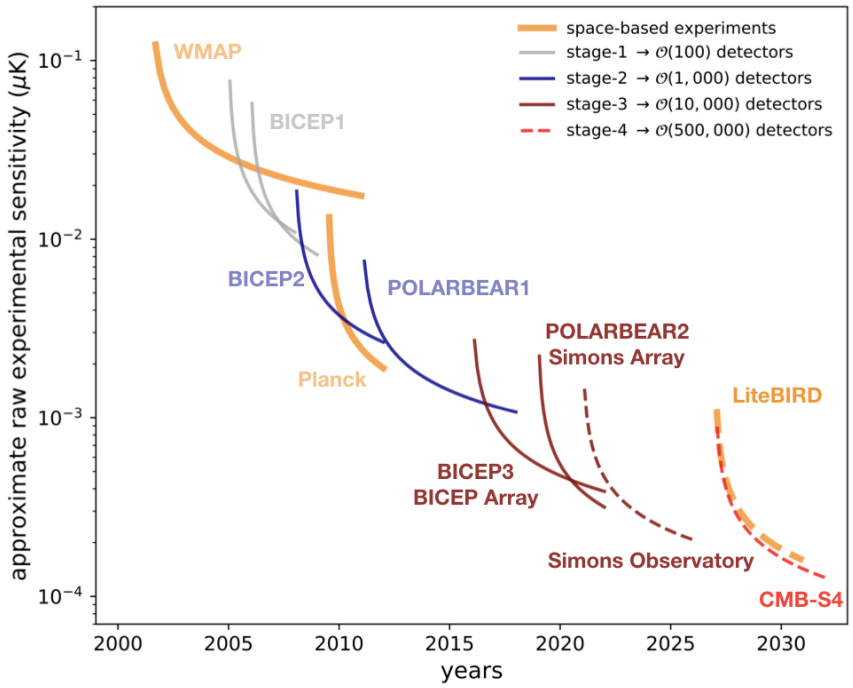

Figure 5.4 – Evolution of raw sensitivity of selected past, current and future CMB experiments
Credit: CMB Stage-4 [61], adapted by J. Errard & C. Vergès

vice (SQUID) [58] is then used to convert this magnetic flux into a voltage, easier to measure. The signal is then handled by a complex electronic system, based on FPGA hardware implementation.

I have summarised the main elements of modern CMB polarisation experiments. Many of them were deployed for the first time in CMB polarisation experiments only in the past 15 years. Although technological progress has been huge since the first anisotropy measurements in the 1990s, and allowed to map temperature anisotropies and E-modes with a very high precision, the required sensitivity to detect primordial B-modes has yet to be reached!

5.2 Toward the next-generation experiments

Detecting signals at a lower and lower amplitude indeed requires sensitivity of CMB polarisation experiments to be increased by several orders of magnitude. This sensitivity is measured in μK for raw experimental sensitivity, and in μK.arcmin for on-sky sensitivity on a fictional $1' \times 1'$ pixel. A convenient classification for CMB polarisation experiments is their stage, corresponding to the order of magnitude of the number of detectors they have, which is a good figure of merit for their sensitivity. Figure 5.4 summarises stages and raw experimental sensitivity progress over the past 20 years. It also presents the forecasted sensitivity of several incoming experiments.

In addition to increasing the number of detectors, new technological developments, combined with novel data analysis techniques, have allowed to push detection limits always further, putting progressively tighter constraints on the

primordial B-modes amplitude. To keep incrasing this sensitivity in the near future, we have a to take up many technical challenges, outlined in section 5.2.1, as well as data analysis challenges, presented in section 5.2.2. Another important aspect of CMB polarisation observations is the synergy between ground- and space-based experiments, whose principles are outlined in section 5.2.3.

5.2.1 Technical challenges

The first leverage to improve the sensitivity and performance of CMB polarisation experiments is the deployment of many thousands of detectors. Another crucial point, as described in Chapter 4, is the acquisition of multi-frequency data sets to enable component separation, which is the case for most of the current and next-generation experiments. Moreover, the determination of the polarisation state of the incoming signal has to be improved. These requirements call for new technological developments.

Readout

When it comes to readout, the larger the detector arrays, the harder to cool it down to sub-Kelvin temperatures, because of their own size, and of the increasing number of wires needed to readout bolometers, which creates thermal leaks. It becomes therefore necessary to increase the multiplexing factor, i.e. the number of bolometers that are read out together, in order to limit the number of wires and sources of noise. Readout noise is indeed one of the main concerns when it comes to readout performance, since we target lower and lower cosmological signals.

In the standard DfMUX implementation, SQUIDs are located at 4K, on a different cryogenic plate than the detectors, that are at sub-Kelvin temperatures. This is a source of readout noise, and it can limit performances of the instrument. In the context of future experiments, in particular CMB-Stage 4, one of the considered options is to move the SQUIDs to sub-Kelvin temperatures. Improving performances of SQUIDs and better understanding their noise is also a strong requirement for future arrays. Moreover, readout technologies tend to correlate signals detected by different detectors, a phenomenon called crosstalk. It depends on the readout system parameters as well as the layout of the focal plane, and in particular it tends to increase when multiplexing factors increase. It is therefore necessary to either mitigate this effect by deploying new technological solutions, or carefully model and account for it in data analysis and performance forecasting, as detailed in section 6.3.2.

A possible alternative to mitigate crosstalk at hardware level could be to use microwave SQUID multiplexers [84], where detectors with different frequencies couple to a common transmission line. Each resonator is then associated with a different SQUID. This implementation allows a much higher multiplexing factor than the usual DfMUX scheme ($\sim$ 1000 detectors versus at most a few hundreds), without increasing crosstalk and noise. Such systems are currently under development for potential deployment [122], and are considered for the Simons Observatory (see section 5.3.1).

However, all these improvements are still based on SQUIDs as amplifiers. Such components are non-linear and very sensitive, and thus require careful

tuning and operation, which can become tricky during instrument operation. For these reasons, a SQUID-less implementation of DfMUX using a transformer-coupled amplifier is also being developed [235].

Multi-frequency data sets

Although it is possible to achieve component separation using external data sets, as this was done in the past - Planck full sky maps are widely used for component separation in the context of ground experiments - upcoming experiments aim at acquiring multi-frequency data sets, which allows to have consistent instrumental characteristic (noise, beams, gains, etc.) over frequency channels, which limits systematic effects. More frequency channels therefore mean more telescopes and more detectors. Beside cost issues, this poses several technical challenges.

Multichroic focal planes In order to reduce the number of telescopes and focal planes, a convenient solution is to build multichroic focal planes, sensitive to several frequencies. It also allows to increase mapping speeds, as the sky is mapped in two (or more) frequencies at the same time. Depending on the experiments, the focal plane can either be divided in several areas corresponding to different frequencies (this is usually the case for space missions, like Planck or LiteBIRD[4]), or host multichroic pixels. For dichroic pixels, detectors are grouped by four, i.e. two pairs of detectors sensitive to two different frequencies. These four-detector pixels are coupled to the amplification system (lenslet-antenna or horn), as well as a micro-strip filter that defines the bandpass. Since micro-strip filters are associated directly to one detector, it makes it possible to have several frequency channel on the same focal plane, and even in the same pixel. However, if filters are detector-specific, antennas are not. The lenslet-antenna system for a given pixel thus has to encompass two different frequencies, and therefore has to be relatively broadband. The same remark still applies for the HWP - the situation can even be more extreme for the HWP if the focal plane is split into different frequency areas (more than two) as this will the case for LiteBIRD [150].

Sinuous antennas Some of the previous CMB experiments (such as POLARBEAR-1) used crossed double slot dipole antennas, that are limited in bandwidth and are therefore not suited for dichroic pixels. Sinuous antennas [87] are linearly polarised, broadband antennas whose parameters can be finely tuned to achieve the required characteristics.

Like most of broadband components, some of their characteristics slightly depends on frequency. In particular, sinuous antenna polarisation axis exhibit a small rotation, known as polarisation angle wobble. This variation of the polarisation angle has to be calibrated and modelled in the data analysis process, otherwise it could introduce systematic effects.

[4] Note that LiteBIRD will also have trichroic pixels, in addition to focal planes separated in different frequency areas.

Broadband half-wave plate The HWP is a crucial element to modulate, and then reconstruct, the polarisation of the incoming radiation. It is a complex optical element, which, in the most general case, introduces a phase shift δ between input and output polarisation components. This phase depends on observation frequency and HWP physical parameters, where the later can be tuned to ensure a good performance of the HWP. In the case of a multi-frequency focal plane, a broadband HWP has to be deployed. As detailed in section 7.1.1, this introduces an effective frequency-dependent polarisation angle, as do sinuous antennas.

Calibration challenges The calibration of the global polarisation angle of the instrument across frequencies is therefore crucial to achieve science goals. However, although it is possible to measure polarisation angles of various parts of the instrument in the lab before their integration and deployment. Calibration campaigns are also carried out once the instrument is fully integrated, but the measurement of the global polarisation angles is a challenging procedure to achieve in observing conditions. A miscalibrated polarisation angle can lead to E to B leakage, and therefore bias the estimation of r. This is also a crucial measurement for birefringence (see section 2.7.4).

In addition to the development of better polarisation angle calibration strategies, we propose in Chapter 7 a model of polarisation angle systematic associated with HWP and sinuous antennas for data analysis purposes. We use this model to address the issue of component separation in Chapter 8.

5.2.2 Data analysis challenges

Another consequence of the increasing number of detectors is the increased volume of time-domain data. Typical Stage 3 and Stage 4 CMB polarisation experiments will produce data sets of thousands of billions of time samples, which have to be calibrated and turned into maps of as many as millions of pixels. This requires the use of state-of-the-art computing techniques and computational platforms, in particular massively-parallel computing on huge clusters. To be efficient, this calls for not only better algorithms, but also their efficient implementation to take advantage of the always growing computational capabilities.

In particular, in CMB data analysis, there are two families of linear problems that require massively parallel computing: Wiener-filtering and map-making equation.

The Wiener-filtering problem applies to equations of the form:

$$\mathbf{m} = \mathbf{s} + \mathbf{n}, \tag{5.3}$$

where $\mathbf{m}$ is a sky map, $\mathbf{s}$ a noiseless map and $\mathbf{n}$ a noise realisation. The minimum variance estimate of the noiseless sky signal, i.e. its Wiener filter, can be written as:

$$\mathbf{s}_{\mathrm{WF}} = (\mathbf{S^{-1}} + \mathbf{N^{-1}})^{-1}\mathbf{N^{-1}}\mathbf{m}, \tag{5.4}$$

where $\mathbf{N}$ is the noise covariance matrix $\mathbf{N} \equiv \langle \mathbf{n}\mathbf{n}^{\mathbf{t}} \rangle$. To compute the Wiener filter of the measured map, one needs to invert the system matrix $(\mathbf{S^{-1}} + \mathbf{N^{-1}})$, which

quickly becomes computationally impossible in the case of millions of pixels. The problem can however be rewritten as a linear system:

$$(\mathbf{S^{-1}} + \mathbf{N^{-1}})\mathbf{s}_{\mathrm{WF}} = \mathbf{N^{-1}}\mathbf{m}, \tag{5.5}$$

that can be solved iteratively.

The map-making problem is quite similar. The data model is written as:

$$\mathbf{d} = \mathbf{P}\mathbf{s} + \mathbf{n}, \tag{5.6}$$

where $\mathbf{P}$ is the pointing matrix of the telescope. The estimator for the sky signal becomes:

$$\hat{\mathbf{s}} = (\mathbf{P^t N^{-1} P})^{-1}\mathbf{P^t N^{-1}}\mathbf{d}, \tag{5.7}$$

As the pointing matrix $\mathbf{P}$ is typically a huge sparse matrix, the system matrix $(\mathbf{P^t N^{-1} P})$ can thus not be easily numerically inverted. The solution is then to use iterative solvers to solve:

$$(\mathbf{P^t N^{-1} P})\hat{\mathbf{s}} = \mathbf{P^t N^{-1}}\mathbf{d}. \tag{5.8}$$

Reconstructed maps $\hat{\mathbf{s}}$ can then be used to compute power spectra and perform science analysis.

For maps of millions of pixels as modern CMB polarisation experiments produce, these procedures require high-performance computing to handle such data sets. Performance of linear solvers and conjugate gradient techniques in the case of CMB data analysis are therefore an active field of research[5], and some novel methods are described for example in [201].

Moreover, as we look always deeper into the CMB signal, this calls for more advanced and complex data models, needed to ensure sufficient precision. In particular, as will be elaborated on in the following chapters, more involved data models are required to take into account the complexity of modern CMB polarisation experiments and ensure a good control of potential systematic effects. Some of these new models, such as the ones developed in Chapter 7, require to amend usual map-making techniques. This calls for an end-to-end procedure for data processing, which takes into account a wide range of instrumental and systematic effects as early as possible in the data processing chain.

5.2.3 From ground to space

Observing CMB from the ground or from space has different constraints and limitations, and either approach is therefore better suited for somewhat different science goals. Both approaches are highly complementary and should ideally be pursued concurrently. I briefly discuss the pros and cons of both approaches below.

[5] See for example the website of the interdisciplinary project B3DCMB http://b3dcmb.in2p3.fr/

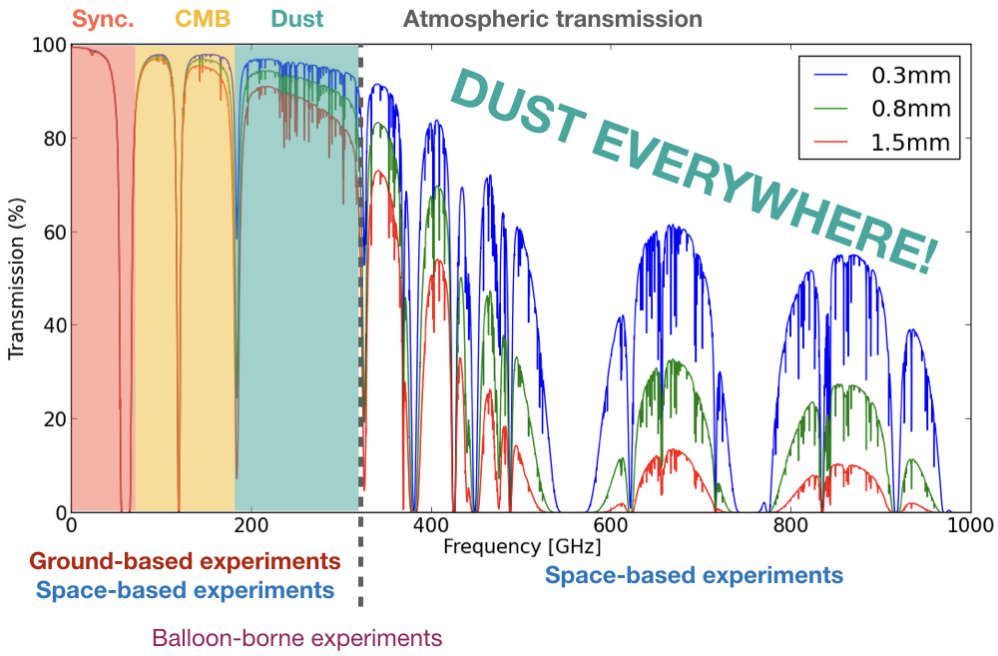

Figure 5.5 – Atmospheric transmission and foreground coverage from ground and space

Ground

Frequencies of interests for CMB observations are between 30 and 450 GHz, covering of course the peak of CMB emission but also foreground emissions to achieve component separation. Observing all these frequencies from the ground is not possible because of the limited atmospheric transmission: as shown in Figure 5.5, only a few bands below 300 GHz are available from the ground, within which ground-based polarisation experiments focus. Moreover, atmospheric transmission depends on several factors, in particular the amount of precipitable water vapour (PWV) in the atmosphere. This quantity depends on climate, weather, time of the year, etc. and therefore has to be closely monitored to correct for variations during observation time. On that basis, a band centred at 90 GHz is the best choice from the ground: it is where the CMB is the most dominant with respect to all other contaminants, including foregrounds and atmospheric water vapour and oxygen emissions.

To lower the impact of PWV, CMB experiments are mostly located in the driest places on Earth, such as the Altiplano in Chile or the South Pole. This minimises the impact of atmosphere on observations, but does not suppress it. The ground itself can also affect thermal loading, that appears as scan-synchronous signal (SSS), that one needs to model and remove from the data.

Moreover, from an Earth-based observatory, sky visibility is limited, i.e. it is not possible to observe 100% of the sky. This could be overcome by deploying experiments at several locations on Earth, but as mentioned below, only a few very specific places meet the required criteria for observations, most of them located in the southern hemisphere: Chile and South Pole, as well as South Africa and

Australia for experiments targeting the radio emission of the sky below 10 GHz. A couple of CMB experiments are located in the northern hemisphere in Spain: NIKA in the Sierra Nevada mountains, which has a 6.5 arcmin field-of-view and a 12 arsec angular resolution and is not designed for primordial B-modes search but rather for cluster science; and QUIJOTE in Canary Islands, which surveys the radio sky between 10 and 40 GHZ. It is only very recently that a CMB polarisation experiment targeting primordial B-modes (i.e. with a broad frequency and sky coverage) has been proposed for deployment in the northern hemisphere, the Ali CMB Polarisation Telescope [165], in Tibet.

However, even with these limitations, CMB ground observations are essential. First of all, it is a lot more easier and less expensive to deploy any experiment on the ground than in space! Moreover, it can be repaired and upgraded, which is not the case in space[6]. Ground based experiments are therefore essentials to validate new technologies that could be sent to space later on. This validation step on the ground is usually required by space agencies before approving a new mission design. Moreover, even from the ground, we have access to a sufficiently broad range of frequencies (see Figure 5.5) so that component separation is in principle possible by using only data obtained from the ground. This has not been achieved yet, but is expected in the coming years with the new generation of experiments.

Another very important aspect for ground-based experiment is their size. It is indeed possible to deploy huge telescopes with thousands of detectors: although there are technical challenges to do so, the size of the telescope itself is not limited by the rocket payload size, not to mention the price of a space mission... Ground-based observatories therefore tend to deploy preferentially highly sensitive focal planes, that mostly target relatively high angular scales with a sharp angular resolution.

Space

The main advantage of space based experiments is to have access to the entire sky, with a broader frequency coverage than from the ground (see Figure 5.5). Space missions are therefore essential to produce high fidelity maps of polarised foregrounds, and in particular dust because it is more difficult to access high frequencies than low frequencies from the ground. Moreover, because of more stable conditions, observation efficiency from space is much higher than from the ground.

However, these missions are much more challenging from a technical point of view. They require the validation of technologies for use in an extreme environment, their robustness to endure vibrations at launch and continuing performances for many years without external intervention. For these reasons, technologies used in space mission are usually relatively older, tried-and-tested, which can be a limiting factor compared to ground observatories. Space experiments are also limited in size and weight, and usually have a much smaller number of detectors than ground experiments - a few tens for the first generation of space missions, to a few thousand at most for the most recent proposals. This relatively

[6] Unless your experiment is the Hubble Space Telescope...

low number of detectors is compensated by their better sensitivity given lower background.

These limitations make space mission more suitable for a large scale, broad-band survey, with a relatively low angular resolution. In this respect, they are necessary to map B-modes on the largest scales in the near future, for example with the LiteBIRD mission, whose launch is scheduled in the late 2020s (see section 5.3.2).

Balloons

We can not conclude this section on ground and space without mentioning balloon-borne experiments. They offer a trade-off between the two other options. Their development is less expensive than a space mission, they can in theory be flown several times after upgrading the focal plane, and they obviously avoid atmospheric absorption and ground pick-up by flying in the high atmosphere - typically above 40 km. However, because of their reduced size and time of observation (typically a month of operation at most), they can only scan a small fraction of the sky and are therefore more suitable for small scale surveys. Moreover, balloon flights are very sensitive to weather conditions, and it can be very challenging to communicate with the experiment during the flight due to limited space on the gondola, that limits transmitter power. Although some major discoveries for CMB science were made with balloon-borne experiments (in particular BOOMERanG and MAXIMA mentioned in section 2.1), they are less favoured today because of the technical difficulties just mentioned. As the limit for primordial B-modes amplitude is pushed always lower, it becomes clear that their detection can be achieved only in very well controlled environment, which would be very difficult to guarantee in a balloon gondola.

Ground, balloon-borne and space experiments therefore have their respective advantages, and are suited for specific, complementary purposes. In the quest for such an elusive goal as primordial B-modes, it is important that all of those are tried!

5.3 Selective experimental landscape

Since the beginning of this manuscript, I have mentioned several experiments and I am sure you are eagerly waiting for a more complete picture!

5.3.1 Ground-based experiments

As advertised in the introductory part of this chapter, I detail here the experiments that I am a member of - except for CMB-Stage 4 which is a natural extension of these projects.

POLARBEAR/Simons Array

I start with a quick overview of the POLARBEAR/Simons Array projects, as more details can be found in Chapter 6.

POLARBEAR-1 The POLARBEAR experiment is located on the Chajnantor plateau in Chile, 5200m above sea level. The first instrument, POLARBEAR-1, was deployed in 2012, and observed until 2017. POLARBEAR-1 was a single frequency experiment (150 GHz) with a relatively high, 3.5' angular resolution, targeting both lensing B-modes and primordial B-modes.

Simons Array Simons Array is the second stage of the POLARBEAR experiment. In the long run, it will be composed of three telescopes observing in 4 frequency bands: 95 GHz & 150 GHz for the first two telescopes, and 220 GHz & 280 GHz on the third one. New technologies for antennas and HWP will be deployed to accommodate dual frequency pixels, and the total number of detectors will be about 20 times larger than in POLARBEAR-1.

Once fully deployed, Simons Array will reach $\sigma(r = 0.1) = 0.006$, and $\sigma(\Sigma m_\nu) = 40\,\mathrm{meV}$ thanks to cross-correlation with other data sets such as DESI. The sky region observed by Simons Array should indeed overlap with several other surveys in various wavelengths, opening up opportunities for several cross-correlation studies with existing or future surveys. Simons Array is also a technical test-bed for new technologies such as cryogenic broadband HWP and sinuous antennas, that will be deployed within the Simons Observatory and LiteBIRD.

Simons Observatory

Instrument The Simons Observatory [269] is a broad international collaboration established in 2016, aiming at building a new CMB observatory in Chile, next to Simons Array and ACT. It will consist in four Small Aperture Telescopes (SATs) and one Large Aperture Telescopes (LAT).

SATs are 42cm refractive telescopes, and will observe the sky in six frequency frequency bands: one telescope at low frequency (LF, 30/40 GHz), two at mid-frequency (MF, 90/150 GHz) where the CMB signal is stronger, and one at ultra-high frequency (UHF, 220/280 GHZ). This configuration will allow to achieve internal component separation, as SATs target large scale primordial B-modes, for which foreground contamination is most worrying. The LAT is a 6m crossed Dragone telescope, which will contain up to 13 optics tubes, each of them 38 cm wide. The LAT will also have a broad frequency coverage, and a high angular resolution, allowing for high accuracy lensing reconstruction, mapping of a large number of SZ clusters, and internal delensing within the Simons Observatory.

Science goals Thanks to its 5 telescopes operating in 6 frequency bands and at different angular scales, the Simons Observatory will be an unprecedented window on our Universe [269]. It will probe the evolution of the Universe at many different epochs, from inflation with the observation of large scale B-modes to galaxy evolution and cluster dynamics, including reionisation and dark energy. To achieve these broad goals, Simons Observatory telescopes will have an unprecedented sensitivity to both large scale primordial B-modes - down to $\sigma(r = 0) = 2 - 3 \times 10^{-3}$ without delensing - and small scale temperature and E-modes anisotropies. It will also probe many other effects on the CMB such as Sunyaev-Zel'dovich effects (both thermal and kinetic) and, of course, lensing.

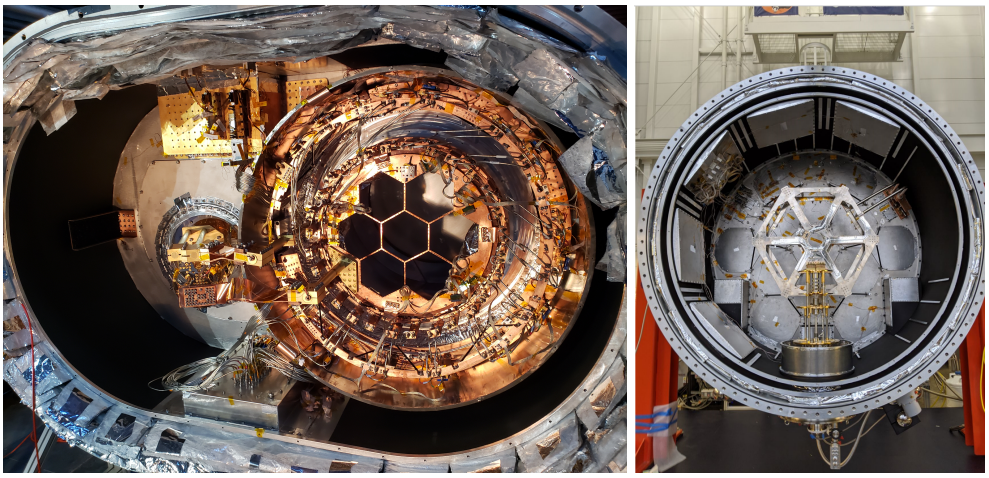

Figure 5.6 – Cryostats of one of the SATs (left) and LAT (right)
Credit: N. Galitzki & M. Devlin

CMB-Stage 4

The CMB-Stage 4[7] experiment will be the first experiment deploying more than 500 000 detectors, and will reach an unprecedented sensitivity from the ground (see Figure 5.4). It will also be the first experiment to be composed of telescopes at several observing sites: Chajnantor plateau in Chile (currently hosting Simons Array, ACT, CLASS and soon Simons Observatory and CCAT), the South Pole (currently hosting BICEP/Keck Array and SPT-3G), and potentially other sites in the Northern hemisphere. All these experiments are joining their forces into a huge international effort to detect and characterise primordial B-modes from the ground, and will also observe lensing, E-modes and clusters.

CMB-S4 targets the observation of B-modes up to cosmic variance limitation for modes accessible from the ground, with a sensitivity on r as low as $\sigma(r = 0) \simeq 5 \times 10^{-4}$ after 90 % delensing [259]. Besides primordial B-modes, CMB-S4, combined with other incoming surveys such as DESI or the Vera Rubin Observatory, will also investigate the burning issues of cold dark matter and dark energy. CMB-S4 project's ambitious science goals call for the development of new technologies for optics (both telescope and receiver), detectors and readout [62]. To this respect, the modelling and control of systematic effects will be of crucial importance for a successful project. Some of the methods I developed will therefore become all the more necessary when it comes to experiments with higher sensitivity.

5.3.2 LiteBIRD: looking for B-modes from space

In the past, only four space missions have been dedicated to CMB observations: RELIKT-1[8], COBE, WMAP and Planck. Recently, several designs have been

[7] https://cmb-s4.org/

[8] RELIKT-1 was a CMB experiment on-board the Prognoz 9 satellite, launched by the USSR in 1983. In their first results, they announced only upper limits on CMB large scale anisotropies, but after re-analysing the data ten years later, they announced the measurements of large scale temperature anisotropies in 1992 [248]. Their results were however overshadowed by those of COBE, published the same year...

proposed to continue CMB observations from space, in particular to target CMB spectral distortions (see section 2.7.2). However, the only CMB mission that have been selected - so far - is the Japanese-led mission LiteBIRD[9] [64]. According to the current planning, LiteBIRD would be launched in 2028, and last 3 years.

The satellite will map the sky 50 times deeper than Planck in polarisation, thanks to 4736 cryogenic detectors, distributed over 15 frequency bands from 40 to 402 GHz (in the current design). LiteBIRD's technology will be very similar to current ground-based technologies, notably the ones of Simons Array and Simons Observatory. In particular, readout and HWP technologies will be demonstrated on the ground, allowing for a better systematic model and control for LiteBIRD.

LiteBIRD will perform full sky observations and therefore have access to angular scales impossible to observe from the ground, with $\ell \lesssim 30$. In return, its map-depth and angular resolution are lower compared to most recent ground-based experiments. This illustrates very well the synergy between space and ground mentioned in section 5.2.3. LiteBIRD and its broad frequency coverage will provide foreground maps for ground-based experiments, and benefit from high-resolution data of ground observations to achieve delensing.

Throughout this chapter, I have emphasised the importance of controlling systematic effects, in particular for the new generation of experiments. I have introduced some of the effects I will focus on in the following chapters: crosstalk and readout systematic effects in Chapter 6, and HWP and sinuous antennas effects in Chapters 7 in 8.

[9] http://litebird.jp/eng

CHAPTER 6

POLARBEAR & Simons Array

Contents

As I presented in section 5.3.1, the POLARBEAR/Simons Array project consists in a series of experiments located in the Atacama desert in Chile. Because of its exceptional atmospheric conditions, the site hosts two other CMB polarisation experiments, ACT and CLASS, and the radio-interferometer ALMA is also located nearby. In the coming years, more experiments will be installed on the same site, in particular Simons Observatory, CCAT-prime and CMB-Stage 4.

POLARBEAR/Simons Array is dedicated to the measurement of CMB polarisation, in particular lensing and primordial B-modes. I joined the collaboration at the beginning of my PhD, and was therefore associated with the work completed over the last three years. In this chapter, I detail in section 6.1 the design, operation and science results of POLARBEAR-1. In section 6.2, I highlight my contributions to the deployment of one of the Simons Array telescopes, and in section 6.3, I outline the analysis and removal of systematic effects in general, as well as the crosstalk modelling work that I have conducted within the POLARBEAR/Simons Array collaboration and in a broader context.

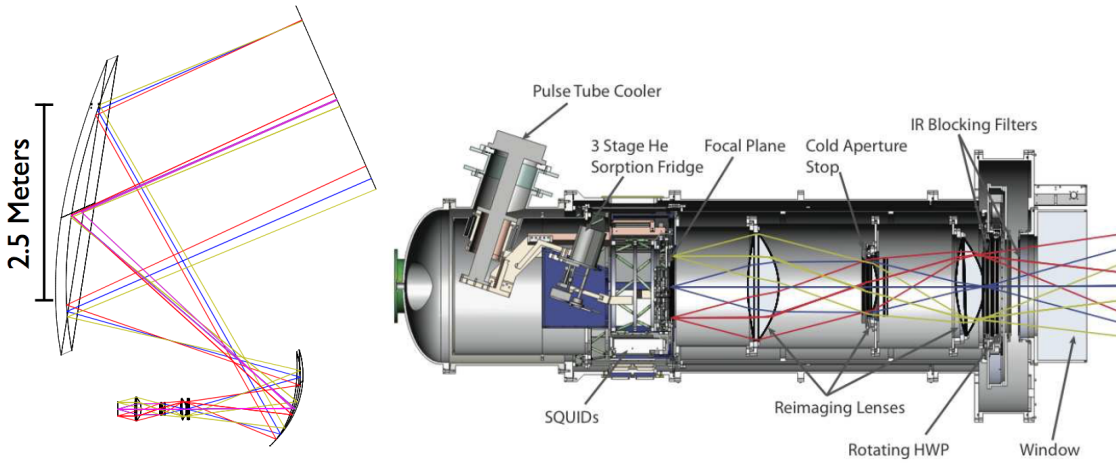

Figure 6.1 – Optical design of the POLARBEAR-1 experiment, showing the global ray tracing through the mirror and optics tube (left), and a zoom on the receiver (right)
Credit: The POLARBEAR Collaboration [143]

6.1 POLARBEAR-1

POLARBEAR-1 was the first stage of the POLARBEAR experiment, and was deployed in 2012 on the Huan Tran Telescope (HTT) in Chile, after integration tests in California.

6.1.1 Instrument

All POLARBEAR telescopes are off-axis crossed Dragone telescopes, with a 2.5 m primary mirror, and 2.4°-wide field of view. After the secondary mirror, the collected light is directed towards a cold optics tube (cooled at 80K). The focus created by the telescope mirrors is re-imaged by lenses on a flat focal plane. The optics tube also contains several filters to ensure a good performance of the instrument by limiting stray light and cross-polarisation. The optics chain of the telescope is shown in Figure 6.1.

The first instrument, POLARBEAR-1 [13, 143], had 637 pixels, each of them made of 2 TES bolometers sensitive to orthogonal polarisation directions, i.e. a total of 1274 detectors. Depending on the relative orientation of the antenna with respect to detectors inside a pixel (see Figure 5.2), half of the pixels are sensitive to Q polarisation, the other half to U polarisation. In a given pixel, as the two detectors are orthogonal, one is sensitive to +Q (or +U), and the other to -Q (or -U). The entire focal plane is cooled at 250 mK using Pulse Tube Coolers (PTC) and Helium-3 fridges (see Figure 6.1). On top of each detector are micro-strip filters defining the bandpass - POLARBEAR-1 was a single frequency experiment observing at 150 GHz. Detector beams were Gaussian beams defined by the optics chain of the telescope, including a cold aperture stop and lenslet-coupled double slots dipole antennas on each detector pair, with a full width at half maximum (FWHM) of 3.5' at 150 GHz.

The instrument operated between 2012 and 2017. An ambient temperature continuously rotating HWP was added in the prime focus in 2014. POLARBEAR-

1 was thus one of the first CMB experiments to deploy a continuously rotating HWP for polarisation modulation. This allows for a better control of instrumental systematic effects, as detailed in section 7.1.1. We successfully demonstrated the operation and polarisation reconstruction with the HWP [254].

Observing runs of POLARBEAR-1 were divided in 3 seasons of observations, corresponding to different scanning strategies. During the first two seasons, in 2012-2013 and 2013-2014, three small sky patches were observed. They are $3° \times 3°$ wide, and have been chosen because they are low in foreground contamination, and at least one of them is visible from Chile at anytime. After 2014 and the commissioning of the continuously rotating HWP, a large patch of 670 square-degrees was observed, to target more specifically large-scale B-modes.

6.1.2 Scanning strategy

The scanning strategy for any CMB polarisation experiment has to be carefully optimised to maximise the observing time as well as minimise systematic effects. For POLARBEAR-1, the scanning strategy consisted in series of Constant Elevation Scans (CES): for each CES, the position of the telescope is fixed in elevation, and it scans back and forth in azimuth (azimuth and elevation are illustrated in Figure 6.2). The nominal scan speed is $0.75°/s$ for small patch observations, and $0.4°/s$ for large patch. Change in azimuth direction at the scan endpoints, referred to as turnaround, defines a subscan. Each CES lasts for about 15 minutes (for small patch observations), and there are about 200 subscans per CES. After 15 minutes of continuous observations, the sky patch has moved with respect to the telescope, and the elevation and azimuth are adjusted to perform another CES, on the same patch or on another one. The cycle of CES is based on the fridge cycle: periodically (it can be every 24, 36 or 48 hours depending of the type of observations), the Helium-3 in the cryogenic fridge needs to be recycled. This interrupts data taking and the focal plane slightly heats up, so detector properties can be modified, in particular gains. Before beginning a new cycle of CES after the fridge has been cycled, one therefore has to perform a calibration run. In addition, every 5 CES, a calibration run is performed because atmospheric loading changes when changing elevation.

As patches are scanned with different elevations at each CES, this provides data with different attack angles on the sky: this is crucial to minimise the effects of noise correlation in the map-making, and properly reconstruct the polarisation signal. The addition of the continuously rotating HWP also provides varying attack angles. Moreover, this allows to mitigate some instrumental and ground pick-up systematics that generate spurious polarisation signals. The CMB signal is indeed fixed in sky coordinates, whereas the signal coming from the ground is not, as shown in Figure 6.3. Having scans at different elevations helps mitigating some systematics coming from the ground, as they can be averaged down, but this is true only up to some level of contamination as some modes of the ground signal are degenerated with the sky signal [220].

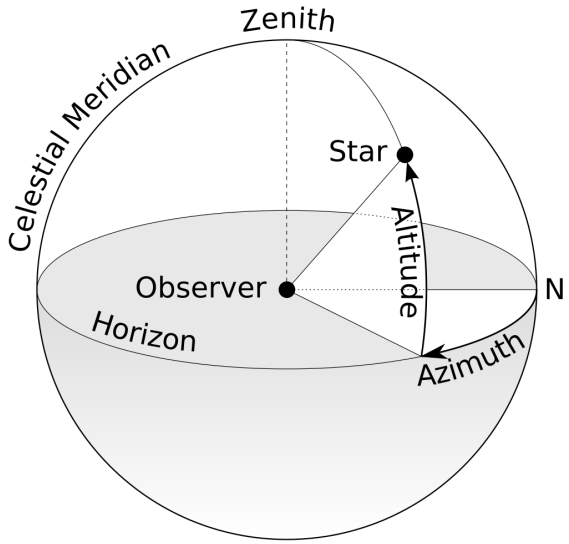

Figure 6.2 – Definition of azimuth and elevation (altitude) angles

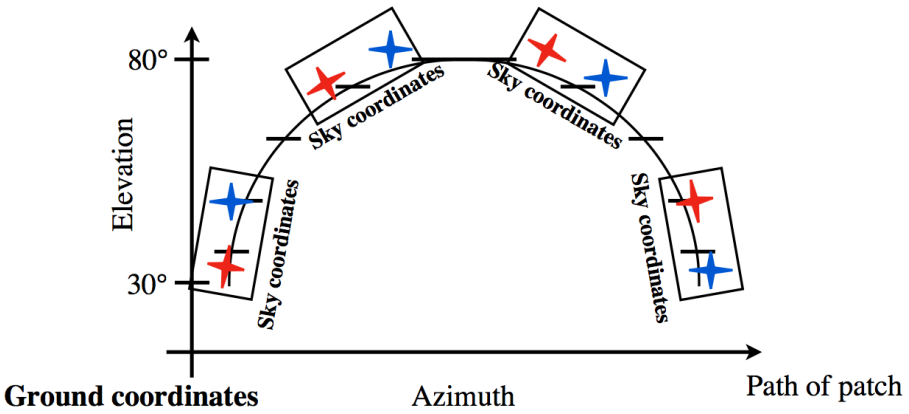

Figure 6.3 – Relative orientation of sky and ground signal. The red crosses represent the CMB signal which is fixed in sky coordinates, but not with respect to the telescope's frame. The blue crosses represent spurious contamination from the ground which is fixed with respect to the telescope.
Credit: J. Peloton

6.1.3 Data analysis

The data analysis process takes raw data from their acquisition by the telescope, and processes them so that it is usable to perform science analysis - lensing reconstruction, power-spectrum, etc. I give here an overview of the main steps. More details can be found in the POLARBEAR science papers such as [263, 264, 266, 267]. I follow here in particular the steps of the large patch data analysis [267], but the process for small patches was quite similar. The main difference was that the HWP was not present in the first two seasons of observations: this changes the polarisation reconstruction and the relative importance of systematics, but the main steps of the analysis remain similar.

Calibration

Before processing the data, one first needs to perform a number of calibration steps, that are crucial to ensure removal of some systematics and that data can be used to derive reliable science results. The main steps of calibration are:

- HWP angle: when the HWP is deployed, one needs to reconstruct the HWP angle using the encoder located on the HWP, and match it with the detector time-stamps;

- pointing: performed using raster scans over radio sources, planets and Tau A, that are usually done before each CES. The final uncertainty on pointing is predicted to be lower than 50″;

- beam: calibrated using planet maps, mostly Jupiter and Saturn. As planets are smaller than the beam size, they appear as a point source for the telescope. The image of a planet by the telescope therefore allows to characterise the PSF of the telescope and measure its FWHM. POLARBEAR's FWHM is $3.5' \pm 0.1'$ [264];

- detector gains: calibrated using a chopped thermal source which is observed every four CES. Measurements are then matched with Jupiter observation, and the overall amplitude is scaled using E-modes data from Planck;

- polarisation angle: the determination of the polarisation angle of the instrument is crucial to ensure a proper reconstruction of the CMB polarised signal. The standard calibrator for CMB observations is the Crab nebula remnant, known as Tau A [14]. Combining observations of Tau A and HWP polarisation angle measurements, we can reconstruct individual detector relative polarisation angles. This allows to calibrate the polarisation angle with a global uncertainty smaller than 0.5°[262]. The overall polarisation angle of the telescope is finally calibrated by setting $C_\ell^{EB} = 0$ - but as outlined is section 2.7.4, this does not allow to search for isotropic cosmic birefringence, and new calibration methods therefore have to be investigated for future experiments.

Data analysis

The data analysis process itself is composed of several steps. One of the challenges is to properly remove the HWP synchronous signal as well as noise from various sources, without affecting cosmological data too much. Data selection described hereafter is therefore a crucial step: on the one hand, if too much data is discarded because of high noise level, one risks lacking data and sufficient statistics for science analysis; on the other hand, one risks claiming false results if noise or other spurious sources of contamination are still present.

Data model Once calibrated, the raw time-ordered data (TOD) of the detectors can be modelled as [267]:

$$\mathbf{d}_m(t) = \mathbf{I}(t) + \epsilon\{[\mathbf{Q}(t) + i\mathbf{U}(t)]e^{-i(4\chi+2\theta_{\rm det})}\} + \mathcal{A}(\chi, t) + \mathcal{N}_m, \tag{6.1}$$

where ϵ is the polarisation efficiency of the detectors, χ the HWP angle, $\theta_{\rm det}$ the individual detector angle, $\mathcal{A}$ the varying contamination signal coming from the HWP (HWP synchronous signal - see next paragraph), and $\mathcal{N}$ the noise. We also define

$$m(\chi) \equiv e^{-i4\chi}, \tag{6.2}$$

that describes the polarisation modulation of the HWP. We already wrote a simplified data model of HWP modulated data in Eq. (5.2), but we express it here more explicitly because we need a precise modelling of the modulated signal so we can demodulate it and reconstruct the polarisation signal.

HWP filtering and demodulation The first step is to remove the HWP synchronous signal $\mathcal{A}(\chi, t)$. This signal refers to spurious signals, that can be either generated by the HWP because of its non-idealities (cross-polarisation, differential transmission and emissivity along axes, reflections, etc.), or result from the modulation by the HWP of other instrumental spurious signals. They typically appear as harmonics of the HWP rotation frequency f, mostly at $2f$, but higher harmonics are also present [232]. The most worrying component of the HWP synchronous signal is the $4f$ component, because this is the frequency at which the sky signal is modulated. Leakage or unpolarised signal to this component thus generates intensity to polarisation leakage, that has to be taken into account in the data analysis. However, in current CMB polarisation experiments, this signal remain low enough so that it is not a major contaminant [155]. For POLARBEAR data analysis, we use the time-dependent reconstructed HWP angle χ to estimate the signal using the model proposed in [155], and then to iteratively demodulate the signal as in [136].

One can then reconstruct the polarisation signal by multiplying the data by twice the conjugate of the HWP modulation $2m^\star(\chi)$, and apply a low-pass filter to recover the demodulated polarisation signal as:

$$\mathbf{d}_d(t) = \epsilon[(\mathbf{Q}(t) + i\mathbf{U}(t)]e^{-i2\theta_{\rm det}} + \mathcal{N}_d. \tag{6.3}$$

Noise model The demodulated noise $\mathcal{N}_d$ is complex, and its real and imaginary parts have twice the variance of the modulated detector noise $\mathcal{N}_m$ due to the factor 2 used in the HWP demodulation. The noise is modelled as two components: a white noise component, and a low-frequency noise component scaling as $1/f^2$. The model is common to all detectors, and is assumed to be uncorrelated between detectors. This model is then used in the data selection process (see below).

Data selection Before finally producing sky maps, data is flagged and selected at the subscan level, so that poor quality data is excluded from science analysis. In particular, one has to remove data when the noise level is too high, when detector properties change during a scan - as the tuning of detectors and readout is extremely sensitive, this is likely to happen - or when a fast event occurs, typically a cosmic ray glitch (single event effects). One also excludes data taken during turnaround of the telescope at the end and beginning of each subscan. As the telescope is accelerating then decelerating, this does not ensure a proper sampling of the sky, and is likely to cause glitches.

Four steps of data selection are then performed, with increasingly strict criteria at each step:

- glitches: removal of glitches and sharp temporal spikes in the TOD;
- noise selection: if a detector has too high a component for either white noise or low frequency noise, or if it is too far from the model, data from this detector is discarded;
- common mode selection: a common mode timestream is computed, and observations with properties too far from this common mode (in particular in terms of noise) are discarded;
- individual detector selection: individual maps for each detector are produced, and a χ^2 map is computed by comparing fluctuations in the data to the expectation from the detector noise weights. Maps with high χ^2 are rejected.

Map-making Once TOD have been demodulated and selected, the map-making step consists in reconstructing a sky map from individual detector timestreams and their position on the sky every time data is recorded (pointing matrix). Although it is a formally simple problem, it quickly becomes computationally expensive because of the huge size of data sets in modern CMB polarisation experiments as we introduced in section 5.2.2. There are two ways to approach the map-making problem: one can either pre-whiten the noise before doing map-making, or marginalise over noise templates during the map-making process.

The first approach consists in assuming that noise has effectively been removed at TOD level during data processing, even if this is not exactly true, and thus the data model can simply be written as:

$$\mathbf{d} = \mathbf{P}\mathbf{s}, \tag{6.4}$$

where $\mathbf{d}$ is the demodulated TOD as in Eq. (6.3), $\mathbf{s}$ is the true sky signal, and $\mathbf{P}$ is the pointing matrix.

We want to estimate the sky signal $\hat{\mathbf{s}}$:

$$\hat{\mathbf{s}} = (\mathbf{P^t P})^{-1} \mathbf{P^t d}. \tag{6.5}$$

The system matrix $(\mathbf{P^t P})^{-1}$ is block-diagonal and its inversion does not pose any specific computation issue. Although more simple, this methods however relies on the fact that noise could be correctly modelled and filtered at TOD level, which is a strong assumption. In particular, one does not need to model the noise too precisely, as long as the appropriate filter can be found, so that the noise is effectively white after filtering. However, in practice, this method obviously ignores any poorly constrained modes that can not be correctly filtered, and that have to be accounted for in latter analysis [220].

The second approach, not used in the context of the POLARBEAR data analysis is to include noise in the data model, as described in section 5.2.2.

6.1.4 Science results

Using small patch maps, POLARBEAR-1 was in 2014 the first CMB experiment to measure polarisation lensing based only on polarised CMB measurements [263], and also directly measure the B-modes power spectrum at sub-degree scales [262] as shown in Figure 6.4. For the second season of observations [264], a second data analysis pipeline was added, and we measured the lensing amplitude defined in section 2.5.4:

$$A_L = 0.60^{+0.26}_{-0.24}(\text{stat.})^{+0.00}_{-0.04}(\text{inst.}) \pm 0.14(\text{foreground}) \pm 0.04(\text{multi.}) \tag{6.6}$$

We rejected the hypothesis of no B-mode with a 3.1σ significance. These measurements are shown in Figure 6.4, alongside with those of other experiments in the field.

During the course of my PhD, several results were published by the POLARBEAR collaboration, to which I have contributed. In particular, I was part of the effort to estimate systematic errors due to readout crosstalk in the large patch data, as detailed in section 6.3.

Using POLARBEAR data alone, we achieved B-modes delensing on small angular scales [266], demonstrating for the first time the ability for an experiment like POLARBEAR to achieve internal delensing using polarisation data only. As mentioned in section 2.6.2, internal delensing is a necessary tool to achieve high precision measurements of primordial B-modes, and this results therefore validates the method for future surveys.

We also published results of large-patch B-modes analysis [267], aiming at setting upper limits on the tensor-to-scalar ratio r. Our results are consistent with the ΛCDM model, and using cross-correlation with Planck high frequency maps, we show that our low-ℓ B-modes power spectrum is consistent with thermal dust emission. We placed an upper limit or the tensor-to-scalar ratio $r < 0.90$ with a 95% confidence level. This is an important step towards the development of

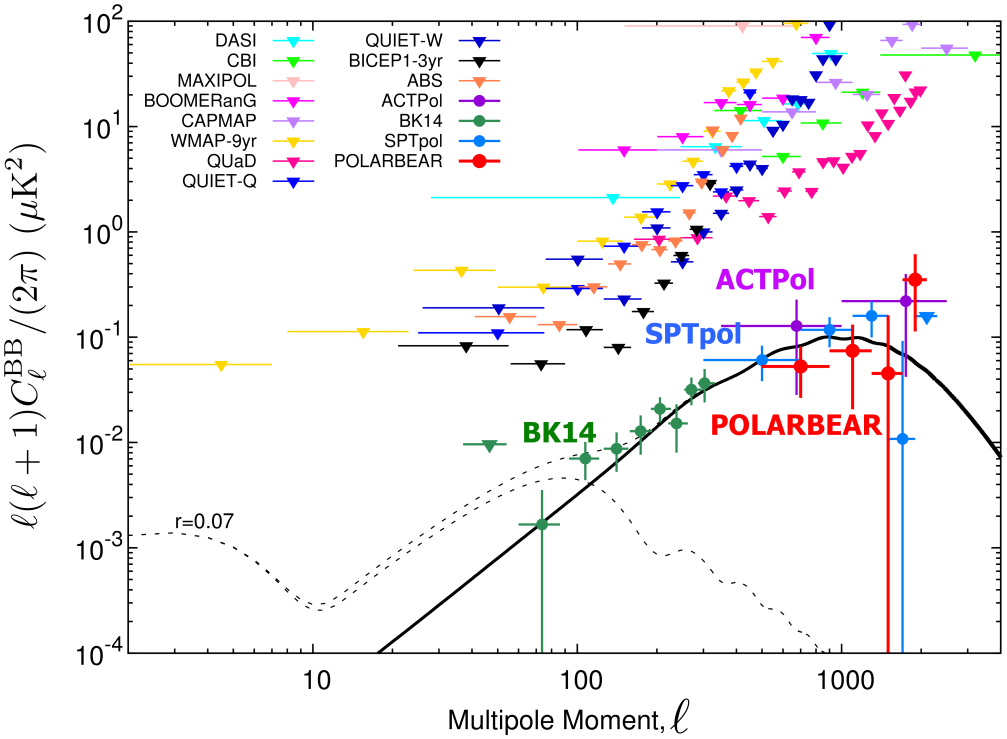

Figure 6.4 – B-modes angular power spectrum experimental measurements
Credit: Y. Chinone

Simons Array and Simons Observatory, as it validates technology (in particular the HWP) and data analysis methods.

Moreover, we completed and published two cross-correlation analysis of POLARBEAR small patch data with other experiments:

- first measurement of cross-correlation between the lensing potential, reconstructed from CMB polarisation data in one of the POLARBEAR-1 small patches, and the cosmic shear field from galaxy shapes, using data from Subaru Hyper Suprime-Cam (HSC) survey. We measured the lensing amplitude of the cross-correlation power spectrum, and estimated $A_L = 1.70 \pm 0.48$, with a 3.5σ rejection of the no-lensing null-hypothesis [190];

- cross-correlation between the CMB lensing convergence reconstructed from measurements of the CMB polarisation, and bright infrared galaxies selected in the Herschel-ATLAS survey. The wide ATLAS survey overlaps with two small patches observed by POLARBEAR-1, and we reject the no-lensing hypothesis with a significance of 4.8σ [265].

Such work emphasises the importance of developing multi-probe cosmology as described in Chapter 3, and to take into account other planned surveys and their sky coverage to allow for these cross-correlation studies between CMB and other probes, in particular galaxies surveys.

Figure 6.5 – POLARBEAR/Simons Array site in Chile in 2019. The central telescope is the Huan Tran Telescope, that hosted the original POLARBEAR-1 instrument.

6.2 Simons Array

As outlined in section 5.3.1, after 5 years of operation, POLARBEAR-1 is now being upgraded as part of the Simons Array [251], which is composed of three similar telescopes, shown in Figure 6.5.

6.2.1 Instrument

The telescope that hosted the POLARBEAR-1 instrument for 5 years has been decommissioned, and will be refurbished with a new high frequency instrument to become POLARBEAR-2c in the coming years. Two additional telescopes have been built, POLARBEAR-2a and 2b. All three telescopes are planned to have dichroic focal planes, and host an increased number of detectors compared to POLARBEAR-1, with 7588 detectors per focal plane - instead of 1274 - paired in 3794 pixels.

As in POLARBEAR-1, half of detectors are sensitive to Q polarisation while the other half are sensitive to U. However, each pixel hosts not only 2, but 4 detectors: 2 per polarisation orientation and per frequency band. Technologies for bandpasses are similar to POLARBEAR-1 as they are defined individually on each detector, but to accommodate dual frequency pixels, Simons Array will deploy dichroic technologies for antennas and HWP. All telescopes thus have an achromatic HWP as polarisation modulator, and those of POLARBEAR-2b and 2c will be cooled at 80K, the first time such a technology is developed. Moreover,

Simons Array is one of the first CMB experiment (after SPT-3G) to deploy sinuous antennas to focus the signal in two frequency bands, and their behaviour in operation will be crucial to assess the performances of future surveys (in particular Simons Observatory).

6.2.2 Deployment

POLARBEAR-2a's deployment started in 2018 in Chile and the instrument achieved first light in January 2019. Calibration tests and runs have been performed but the deployment is not yet fully completed, as some elements of the instrument have not yet been commissioned. In particular, the ambient temperature HWP has not yet been installed on the telescope, although first integration tests have been completed. In November 2019, I took part in deployment activities to prepare for the HWP installation on the telescope. In particular, I integrated all the necessary components for the HWP control and operation, and tested control and data acquisition protocols.

When operating the HWP, one of the challenges is the precise recording of the HWP position and angle, so that it is possible to demodulate detector timestreams (see section 6.1.3 on POLARBEAR-1 data analysis). To do so, the angular position of the HWP is read using an optical encoder tape on the HWP itself. An optical head reads the encoder tape, and one can then reconstruct the position of the HWP. However, a recording of the HWP position without anytime reference frame is useless, as one needs to be able to relate the HWP position to the detector timestreams at any time. To do so, we use IRIG (Inter-Range Instrumentation Group) time codes, a standard format to transfer timing information between different instruments operating together. The IRIG signal is therefore shared and distributed over all site equipment, and is used as a common time reference. Finally, one also has to be able to communicate with the motor operating the HWP through the site network. All these communications and recording operations are handled through an Arduino card, which has to be correctly wired and programmed so that communication with the HWP is possible. A schematic of a proposed implementation is shown in Figure 6.6.

I also tested simplified data acquisition protocols to record HWP angular data while operating the HWP. To do so, we operate the HWP through a motor controller and record data at the same time. A typical control script is composed as shown in Algorithm 1. Each of the steps of the algorithm are handled through specific `python` scripts to communicate with the Arduino card through the site network. The Arduino card then distributes instructions to the various elements of the system, in particular the HWP motor and encoder, and transmits recorded data back to the control computer (and error messages when appropriate).

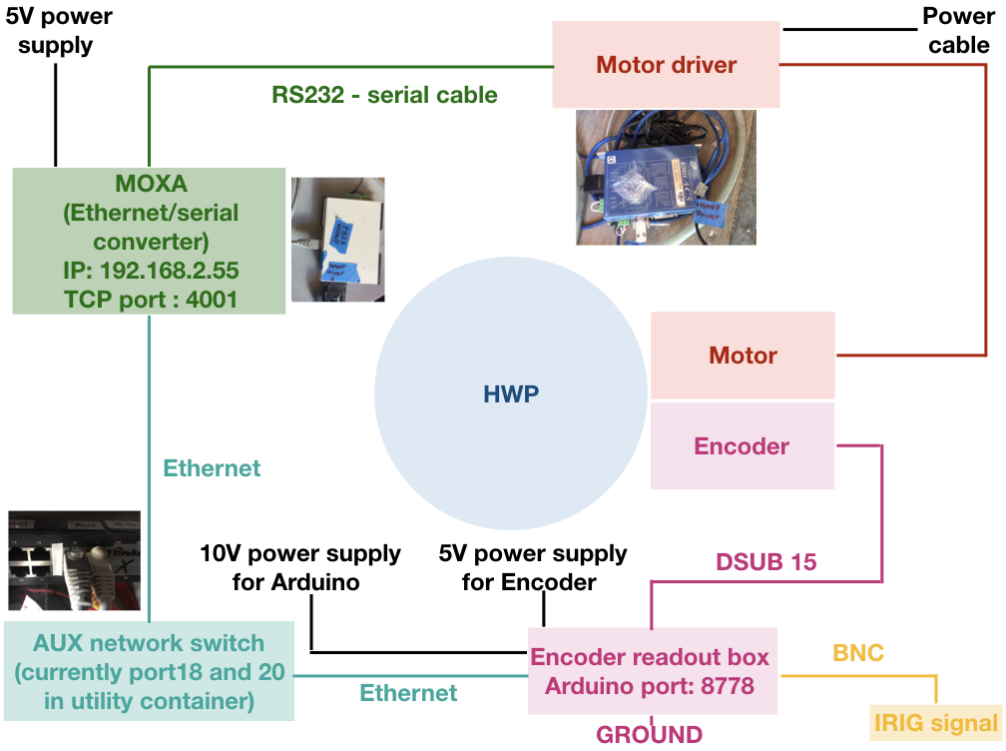

Figure 6.6 – Schematic view of HWP communication and control hardware for POLARBEAR-2a

Algorithm 1 HWP operation test

1: Record HWP encoder data and IRIG time stamps for 120s
2: Wait 10s
3: Start HWP motor rotation
4: Wait 30s
5: Stop HWP motor rotation
6: Wait 20s
7: Start HWP motor rotation
8: Wait 30s
9: Stop HWP motor rotation

Raw HWP encoder and IRIG data are recorded in a single `pickle`[1] file. We then extract data from the file and check that we are able to match the recorded angles with time, and that the recording is correct (no missing data). The position angle of the HWP has to be known with a precision of at least 0.1°to allow for primordial and lensing B-modes signal measurement [253]. Moreover, to avoid jitter noise in the HWP angle reconstruction, the sampling rate of the encoder has to be much higher than the detector sampling rate at 100Hz [126][2].

An example of angle recording is shown in Figure 6.7. Although preliminary, these tests have confirmed the capability of the electronic device I integrated

[1] `https://docs.python.org/3/library/pickle.html`

[2] The detector sampling rate must also be much higher than the bolometer time constant. For POLARBEAR, the bolometer time constant is typically 1-3 ms [143], hence the 10 ms (100 Hz) sampling rate.

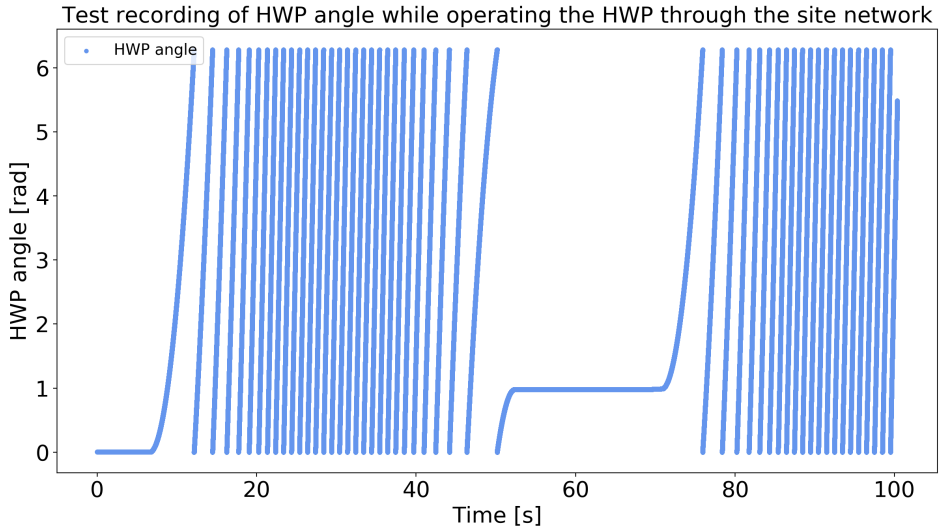

Figure 6.7 – Recording of HWP rotation angle during operation. The effective sampling rate is 21 kHz, much higher than the detector sampling rate as requested. The angular resolution is 0.017°, which also meets the requirement

to handle network communication and data recording for the HWP, and ensure proper HWP commissioning and future operation.

6.3 Systematic effects

The analysis of systematic effects is a crucial step in data analysis, to ensure that science results are not contaminated by spurious signals, coming from the instrument or from the ground.

Some of the systematic effects are known from the beginning of operations as they arise from specific parts of the instrument that have been studied on a test bench prior to integration and deployment. In such cases, one can develop a model for systematic effects and try to mitigate them in the data or during calibration phases. Other systematics, such as ground pick-up and far side-lobe contaminations, appear only when the telescope is operating and are harder to take into account. All residual systematics after calibration and mitigation thus have to be accounted for as a systematic error budget on the final results. The assessment of the relative importance of systematics is also of great importance to prepare for future experiments.

In this section, I first present the main steps of a typical systematic analysis, and I then focus on readout systematics and various techniques that I have helped to develop to better mitigate them.

6.3.1 Methods

When it comes to systematics estimation and mitigation, two important and complementary processes are usually implemented in the data analysis framework: null tests and estimation of residual systematics impacts. Although meth-

ods described here are more general, I use the example of the POLARBEAR-1 large patch analysis [267], in which I took part.

Null tests

To check for systematics, we start by performing internal consistency tests on data. The data is split in halves, and we perform a series of null tests: as the CMB is stationary, the difference between two halves should be null if all sources of contamination have been correctly removed. Depending on the contamination source, there will be a particular data split that increases power in the null map. To ensure that data is correctly cleaned, one therefore designs a series of splits and performs corresponding null tests. Splits are designed according to a wide range of criteria: chronological, CES types, subscan directions, detector and pixel properties (Q/U, gain, position in the focal plane, orientation, etc.), HWP signal amplitude, and environment (PWV, position of Sun and Moon).

Null tests are performed at the power spectrum level, and the null power spectrum is computed as:

$$\hat{C}_\ell^{\rm null} \equiv \hat{C}_\ell^{A} + \hat{C}_\ell^{B} - 2 \times \hat{C}_\ell^{AB}, \tag{6.7}$$

where A and B are the two data halves and $\hat{C}_\ell^{AB}$ is their cross-spectrum. The spectra are computed using the same filters and pipeline as described in section 6.1.

For each ℓ-bin of 50 ℓ ($50 \leqslant \ell \leqslant 100$, $100 < \ell \leqslant 150$, etc.) in each null spectrum we compute:

$$\chi^2 \equiv \frac{\hat{C}^{\rm null}}{\sigma(\hat{C}^{\rm null})}, \tag{6.8}$$

where $\sigma(\hat{C}^{\rm null})$ is the standard deviation of the null spectra as estimated using Monte-Carlo simulations of the noise. We then require than the probability-to-exceed (PTE) derived for this χ^2 test to be greater than 5% for some combinations of the tests (details for the large patch analysis can be found in [267]). The important point here is that we ensure that data pass the designed null tests, before we actually look at the final EE and BB spectra (blind analysis). This ensures that the final results can be trusted and are in principle not subjected to analysis bias.

Estimation of systematic errors

Null tests are an important consistency check, but they are limited by the statistical uncertainty of the splits produced from at most half of the data. They therefore ideally need to be backed up by an ab initio analysis, where all (known) systematics are modelled, and their effects on the final science products carefully estimated using the pipeline as used for the actual data analysis. To do so, we use a simulation pipeline to scan a realisation of the sky, and then add a modelled systematic effect. This model can come from measurements derived from instrumental calibration (as this is the case for crosstalk, as detailed hereafter), or be derived from a theoretical model when no estimation on the field is possible. Modified simulated data (with systematic effects included) is then processed through the same analysis pipeline as the one used for real data. We estimate the

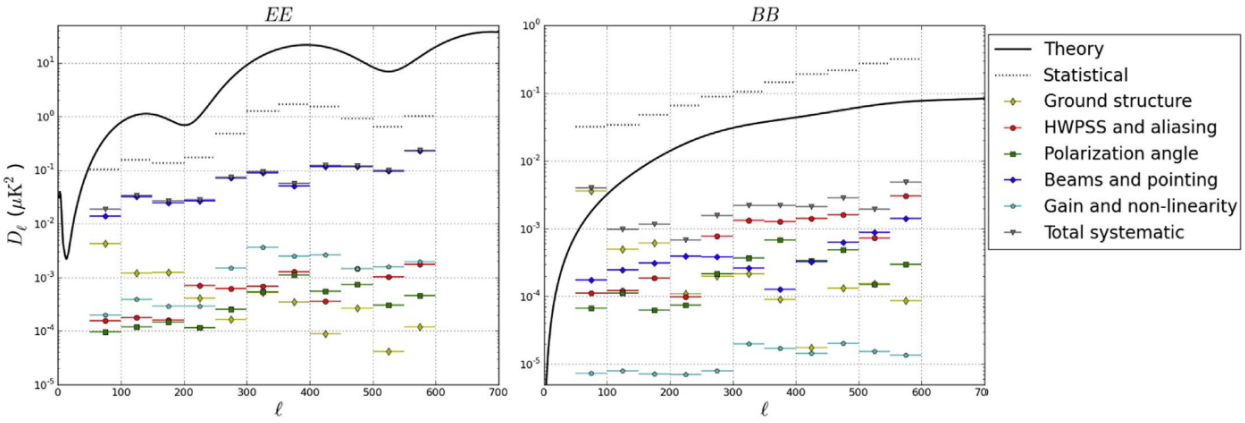

Figure 6.8 – Individual and total estimated contributions of systematic effects in POLARBEAR-1 large patch data. The most important source of contamination in E-modes comes from the beam and pointing calibration, which includes in particular detector crosstalk. In BB, the dominant source of systematics is the ground pick-up signal.
Credit: N. Goeckner-Wald and the POLARBEAR Collaboration [267]

power spectrum of the simulated map, and subtract the power spectrum obtained from a reference simulation without systematic effects. This gives an estimate of the contamination power spectrum associated with each systematic effect. All such power spectra are then simply added together, to form a total estimation of systematic contamination. Systematic contributions to POLARBEAR-1's large patch power spectra are shown in Figure 6.8.

It is therefore important to develop a framework for systematics modelling, so that their effects are correctly taken into account. This is what we propose in the next section for crosstalk, which is one of the dominant sources of contamination for E-modes [267], and and also contributes to uncertainties for B-modes.

6.3.2 Detailed example: readout crosstalk

Crosstalk is a spurious signal due to coupling between two (or more) nominally independent detectors. This coupling can occur at several levels in the detection chain: in the optical domain (beam side-lobe leakage) or, most importantly, in the electronic domain. Readout crosstalk, on which we focus in this work, is due to the specific architecture of the multiplexed readout system: as detailed in section 5.1.2, modern CMB polarisation experiments have ever increasing multiplexing factors, and new readout architectures aim at minimising crosstalk. However, even with mitigation techniques at hardware level as currently deployed, a residual level of crosstalk is always present, and must be either accounted for in the systematic errors budget, or mitigated during data analysis. If not, readout crosstalk mainly has two effects [72]: in the pair differencing scheme, it induces temperature-to-polarisation (T-to-P) leakage; and in a demodulation scheme (using e.g. a HWP), it mixes temperature or polarisation of one detector, with the corresponding signal (temperature or polarisation) in another one. This is another advantage of using a HWP, as polarisation-to-polarisation leakage is of lesser amplitude than T-to-P leakage, because the amplitude of the

temperature signal is much higher than the one of polarisation.

Finally, readout crosstalk can also induce beam miscalibration, in particular for the polarisation beam [70], by generating negative side-lobes outside of the main beam (see hereafter). This effect also has to be carefully modelled and/or corrected for in the systematic analysis: in POLARBEAR large patch analysis, it turned out to be the largest source of systematic in the E-modes power spectrum. The development of methods as we propose hereafter would allow to correct for crosstalk at TOD level, and therefore limit beam miscalibration.

Model

As a test case for crosstalk modelling, we consider the readout architecture deployed in POLARBEAR/Simons Array, the DfMUX architecture [83] shown in Figure 5.3. This architecture will also be used in LiteBIRD, and an improved version allowing for a higher multiplexing factor [84, 122] will be deployed in Simons Observatory. If the model dependence to hardware parameters we describe here is specific to DfMUX, methods we develop for mitigation can be extended to other readout architectures.

Sources In DfMUX, there are three main sources of readout crosstalk inside a given SQUID[3]:

- cross-coupling of coils between channels;
- bias carrier leakage due to the shift of the Lorentzian tail;
- stray inductance of wiring in the readout circuit.

The first term scales as the difference between resonant frequencies of two physically neighbouring channels. It can thus be mitigated at the hardware level, by ensuring that two physically neighbouring channels have sufficiently different resonant frequencies so that this term becomes negligible compared to the other two terms.

To model the crosstalk contribution to channel j (timestream d_j) from channel i (timestream d_i), I use the model developed in [83]:

$$d_{j,\mathrm{crosstalk}} = -d_i \times \left[\left(\frac{R}{4\pi f_i \delta_{ij}} \right)^2 + \frac{L_{\mathrm{stray}}}{2 L_i \delta_{ij}} \right], \tag{6.9}$$

where f_i is the readout resonant frequency of channel i, δ_{ij} is the resonant frequency spacing between channels i and j, R and L are the resistance and inductance of the resonant readout circuit (see Figure 5.3), and L_{stray} is the stray inductance of the wiring.

For a channel j if we take into account crosstalk terms coming from all other channels, we model the crosstalked timestream as

$$d_{j,\mathrm{tot}} = d_j - \sum_{i \neq j} d_i \times \left(\left(\frac{R}{4\pi f_i \delta_{ij}} \right)^2 + \frac{f_i L_{\mathrm{stray}}}{2 L_i \delta_{ij}} \right). \tag{6.10}$$

[3] We neglect here inter-SQUID crosstalk and these terms are negligible compared to intra-SQUID crosstalk [83].

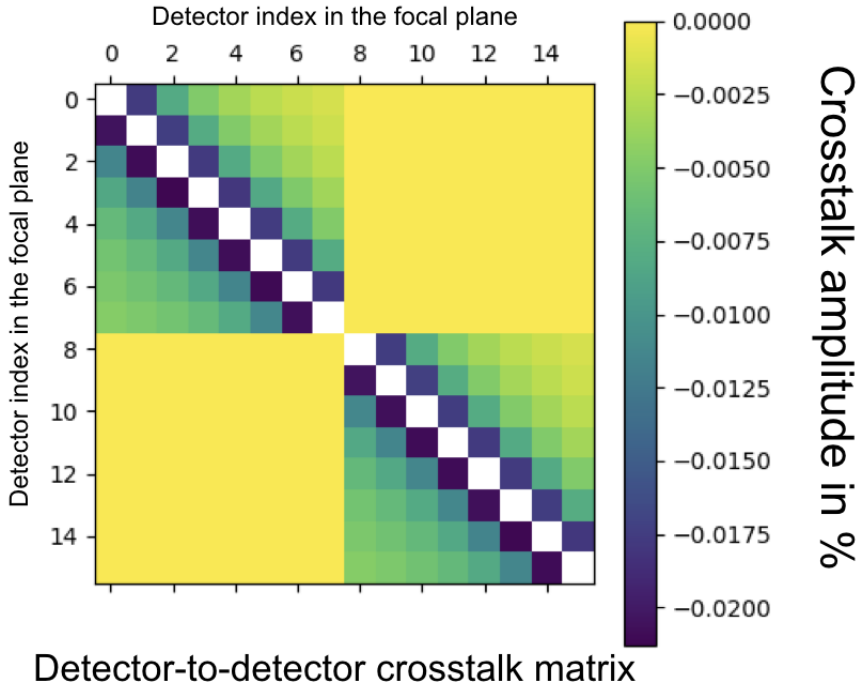

Figure 6.9 – Crosstalk mixing matrix computed using Eqs. (6.11 - 6.12) for a multiplexing factor of 8. Inter-SQUID crosstalk is set to zero.

The effect of crosstalk on a TOD is thus a mixing of TODs from different detectors, which results in a detector-to-detector leakage. This effect is small, typically less than 1% in DfMUX and even less in microwave-multiplexing, as detector arrays are designed to minimise it.

Coupling matrix formalism For a complete detector array (entire focal plane), we propose to model TOD mixing induced by crosstalk using a detector-detector mixing matrix $\mathbf{\Lambda}$ with:

$$\lambda_{ij} = -\sum_{i \neq j} \left(\frac{R}{4\pi f_i \delta_{ij}} \right)^2 + \frac{f_i L_{\text{stray}}}{2 L_i \delta_{ij}}. \tag{6.11}$$

To ensure power conservation, we further impose that

$$\lambda_{ii} = \sqrt{1 - \sum_{i \neq j} \lambda_{ij}^2}. \tag{6.12}$$

An example of a simulated crosstalk mixing matrix is shown in Figure 6.9.

We can thus write our data model as:

$$\mathbf{d} = \mathbf{\Lambda}(\mathbf{s} + \mathbf{n}), \tag{6.13}$$

where $\mathbf{s}$ is the sky signal without crosstalk and $\mathbf{n}$ is the noise. We point out here that noise is also affected by crosstalk, since it is assumed to primarily come from the environment and not from the data acquisition chain, and thus correlated detector noise is generated.

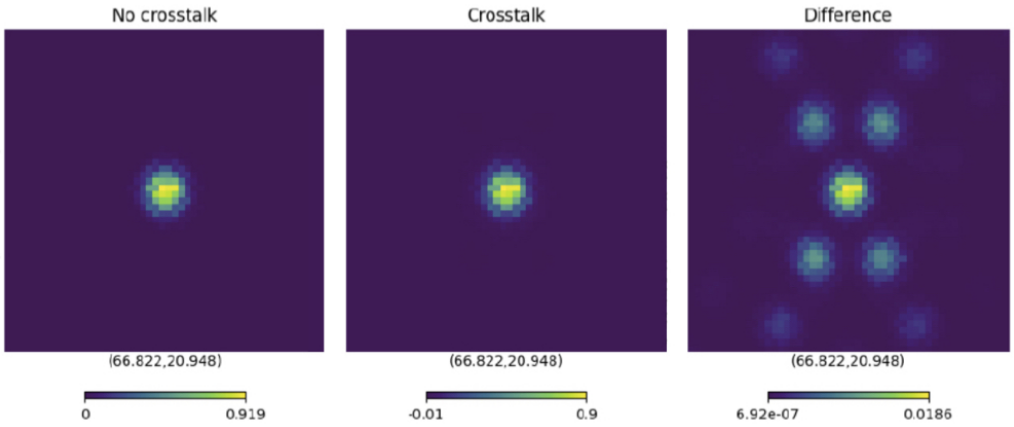

Figure 6.10 – Simulated individual detector map with crosstalk when observing Jupiter. This map is obtained from a single time-domain simulation assuming constant elevation raster scan, hence the X-shaped cross due to scan direction.

Application to planet observations As described in section 6.1.3, detectors are calibrated using planet observations, typically Jupiter, Saturn and Venus. As part of the calibration process, in particular to measure detector beam properties, individual planet maps for each detector are produced. As planets can be well approximated by point-sources for the detectors, their image through the beam allows to characterise it (the time response of the readout is small enough to have negligible impact on the effect).

I propose to use these individual detector beam maps not only to calibrate beams, but also to estimate detector-to-detector leakage. If there were no crosstalk, a given individual detector beam map would contain only the image of the planet by the detector in question. However, because of crosstalk, we expect that the detector channel also receives a negative side-lobe image of the planet from neighbouring detectors, as shown in Figure 6.10. I developed methods to take advantage of this effect to constrain the crosstalk amplitude, and propose two applications of this formalism in the following sections, in the context of POLARBEAR data analysis.

Estimation for POLARBEAR-1

In the context of crosstalk estimation for POLARBEAR-1's large patch analysis, we propose to reconstruct the crosstalk mixing matrix in map domain, by measuring the amplitude of leaked signals in individual detector beam maps. We transpose the TOD data model to map domain, and we model an individual detector beam map as:

$$b_{j,\mathrm{obs.}} = b_{\mathrm{model}} + \sum_{i \neq j} \lambda_{ij} b_{j,\mathrm{model}}. \tag{6.14}$$

Here we do not assume any specific model for λ_{ij}, as we only aim at reconstructing a phenomenological crosstalk matrix. For the beam model b_{model}, we use the co-added beam map of the instrument obtained from all individual detector beam maps and shown in Figure 6.11. We assume that, in this co-added map, crosstalk contributions from all detectors average down, and that it is thus a crosstalk-free

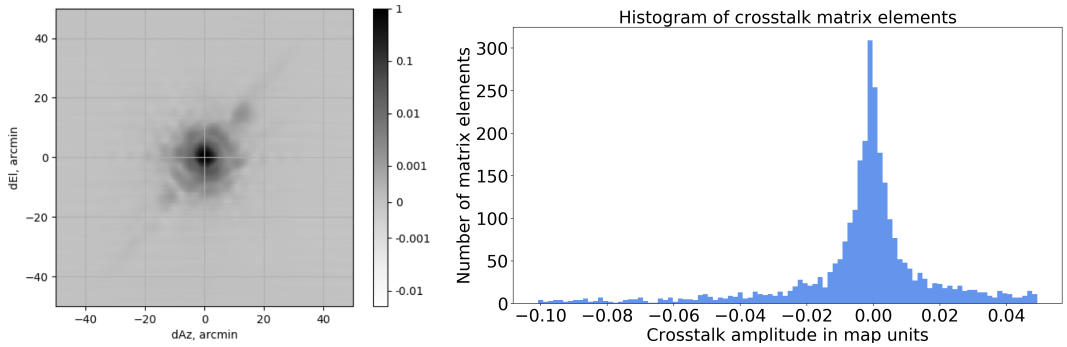

Figure 6.11 – Co-added beam map of POLARBEAR-1 (left) and histogram of recovered amplitudes of detector-detector crosstalk (right).

map. Moreover, we assume in this approach that crosstalk is linear and constant in our data sets. We discuss these assumptions hereafter.

We take each individual detector map, subtract the co-added beam and then fit for residual beam patterns of amplitude λ_{ij} using a matched filter. We assume that we know beam offsets for all detectors, so that we can identify the detector that causes crosstalk thanks to its position on the focal plane. We can thus reconstruct the crosstalk matrix in map space. We note here that, formally, this is not the same matrix as the one we introduced above. However, it can be used as a good approximation of crosstalk amplitude in the system. An histogram of recovered amplitudes is shown in Figure 6.11. To assess the reliability of the procedure, we generate a fake data set of beam maps with known amplitude of the contamination signal, and run them through the same pipeline. We check that we recover the correct crosstalk amplitude distribution, which validates our approach.

The reconstructed crosstalk matrix was then used to assess the residual level of crosstalk in POLARBEAR-1's large patch data analysis [267].

Parametric simulation

Building on the crosstalk coupling matrix model, I developed a framework to generate an accurate crosstalk matrix given realistic focal plane layouts. The goal of this framework is to be a building block for novel methods to mitigate crosstalk effects at TOD level, in particular in the context of Simons Array data analysis.

Framework We set up the amplitude of crosstalk in the crosstalk mixing matrix $\mathbf{\Lambda}$ using realistic instrumental parameters for frequency spacing and component values. Given typical values of instrumental parameters ($R \sim 1\Omega$, $L/L_{stray} \sim 150$), the dominant source of crosstalk is the first term in Eq. (6.10), and its amplitude is at most 2 % for the nearest neighbour case. We therefore propose a simplified approach with one free parameter p (leakage percentage), and we scale the amplitude of the off-diagonal terms of Λ according to frequency scheduling:

$$\begin{cases} \lambda_{ij,max} = p \\ \lambda_{ij} \propto \frac{p}{(\delta_{ij})^2} \end{cases} \tag{6.15}$$

where we recall that δ_{ij} is the difference between readout frequencies of channels i and j. We then produce simulated data of planet observations using the `s4cmb`[4] simulation framework, modified to accommodate the parametric crosstalk model we propose. Moreover, we have added options in `s4cmb` to handle the focal plane architecture of CMB polarisation experiments, so that each detector is associated with its resonant frequency in the readout system. This allows to simulate a realistic detector-detector crosstalk mixing matrix $\mathbf{\Lambda}$, and apply it to simulated data following the data model proposed in Eq. (6.13). We can for instance simulate individual detector maps of Jupiter, as shown in Figure 6.10.

As a way to constrain the crosstalk amplitude, we are interested in reconstructing the mixing matrix $\mathbf{\Lambda}$ from observations. We assume that the distribution of resonant frequencies in the focal plane is known. We then write the data likelihood to estimate p as:

$$\chi^2 = -2\log\mathcal{L} \equiv \sum_{t_s,t_s'} \left[(\mathbf{d}-\mathbf{\Lambda s})^t\,\mathbf{C}^{-1}\,(\mathbf{d}-\mathbf{\Lambda s}) + \log\left(\det(\mathbf{C})\right)\right], \tag{6.16}$$

where the sum is on time samples t_s. Since there are no correlations in time, we can simplify this expression as:

$$\begin{aligned}\chi^2 &= \mathrm{tr}\left[(\mathbf{d}-\mathbf{\Lambda s})^t\,\mathbf{C}^{-1}\,(\mathbf{d}-\mathbf{\Lambda s})\right] + n_{t_s}\,\log\left(\det(\mathbf{C})\right),\\ &= \sum_{t_s} (\mathbf{d}-\mathbf{\Lambda s})\Big|_{t_s}^{t}\,\mathbf{C}^{-1}\,(\mathbf{d}-\mathbf{\Lambda s})\Big|_{t_s} + n_{ts}\,\log\left(\det(\mathbf{C})\right),\end{aligned} \tag{6.17}$$

where $(\mathbf{d}-\mathbf{\Lambda s})\Big|_{t_s}$ denotes a t-th column of $(\mathbf{d}-\mathbf{\Lambda s})$, n_{t_s} is the number of time samples and $\mathbf{C}$ is a $n_{\rm det}\times n_{\rm det}$ matrix expressed as:

$$\mathbf{C} \equiv \langle(\mathbf{\Lambda n})(\mathbf{\Lambda n})^t\rangle = \langle\mathbf{\Lambda n n}^t\mathbf{\Lambda}^t\rangle = \mathbf{\Lambda}\langle\mathbf{n n}^t\rangle\mathbf{\Lambda}^t \equiv \mathbf{\Lambda N \Lambda}^t \tag{6.18}$$

Finally, we can express Eq. (6.16) as:

$$\chi^2 = \sum_{t_s,dd'} (\mathbf{d}-\mathbf{\Lambda s})\Big|_{t_s,d}^{t}\,(\mathbf{\Lambda N\Lambda}^t)^{-1}\Big|_{dd'}\,(\mathbf{d}-\mathbf{\Lambda s})\Big|_{t_s,d'} + n_{t_s}\,\log\left(\det(\mathbf{\Lambda N\Lambda}^t)\right) \tag{6.19}$$

By minimising Eq. (6.19) with respect to p, one can therefore reconstruct the crosstalk matrix from planet observations, and use it to correct for crosstalk, i.e:

$$\mathbf{d}_{\rm corrected} = \mathbf{\Lambda}^{-1}\mathbf{d}_{\rm observed}. \tag{6.20}$$

Proof of concept To demonstrate the proposed framework, we test it on a small data set consisting of ten detectors, $p=-1.5$ and a beam size of 3.5′. We consider the noise to be uniform on all detectors with:

$$\sigma_{\rm det} = \sigma_{\rm array}\times\sqrt{\rm ndet}, \tag{6.21}$$

[4] `s4cmb` is a simulation framework intended to test rapidly the impact of selected systematic effects for CMB polarisation experiments. It was originally developed by Julien Peloton, and modifications to the code that support this work can be found here: https://github.com/ClaraVerges/s4cmb/tree/instrument_model

where $\sigma_{\rm array} = 2.3 \times 10^{-3}\,\mu{\rm K}_{\rm CMB}$ is the array noise level, with a map resolution of $1.7'$. With these parameters, the signal-to-noise ratio is high ($\sim 10^5$), but this is coherent with a Jupiter observation at 150 GHz ($T_{\rm Jupiter} \sim 150{\rm K}$) with a typical CMB experiment.

We minimise Eq. (6.19) over 1000 noise realisations. We fit a Gaussian distribution to the histogram of recovered p values and find:

$$\begin{aligned} \mu &= -1.5 \\ \sigma_{\rm G} &= 6.635 \times 10^{-4}, \end{aligned} \tag{6.22}$$

which shows that we can correctly recover the crosstalk amplitude parameter p, as shown in Figure 6.12.

We also introduce the Hessian matrix:

$$\mathcal{H} \equiv \frac{\partial^2 \mathcal{L}}{\partial p^2}, \tag{6.23}$$

and the Fisher matrix:

$$\mathcal{F} \equiv \frac{1}{2}\,{\rm tr}\left[n_{t_s} \times \left((\mathbf{\Lambda N \Lambda}^T)^{-1} \frac{\partial (\mathbf{\Lambda N \Lambda}^T)}{\partial p} (\mathbf{\Lambda N \Lambda}^T)^{-1} \frac{\partial (\mathbf{\Lambda N \Lambda}^T)}{\partial p} \right) + 2 \times \left(\frac{\partial \mathbf{\Lambda}}{\partial p}\, s\, s^T \frac{\partial \mathbf{\Lambda}}{\partial p}^T \right) \right]. \tag{6.24}$$

We define $\sigma_{\rm H} = \frac{1}{\sqrt{\mathcal{H}}}$, which is the curvature of the likelihood $\mathcal{L}$ at its peak, and $\sigma_{\rm F} = \frac{1}{\sqrt{\mathcal{F}}}$, which gives us a lower bound on the the width of the distribution of recovered p for several noise realisations.

We estimate (see also Figure6.12);

$$\sigma_{\mathcal{H}} = 7.300 \times 10^{-4} \tag{6.25}$$

$$\sigma_{\mathcal{F}} = 6.802 \times 10^{-4} \tag{6.26}$$

which is in good agreement with the Gaussian we fit to the histogram[5].

We therefore demonstrate the capability of the proposed framework to reconstruct the crosstalk mixing matrix from single planet maps, in a simplistic case. This method could thus be extended in the context of more complex crosstalk models and instrumental configurations.

[5] The width estimated with Fisher is higher than the fitted width σ, but the result is consistent given the uncertainty on σ.

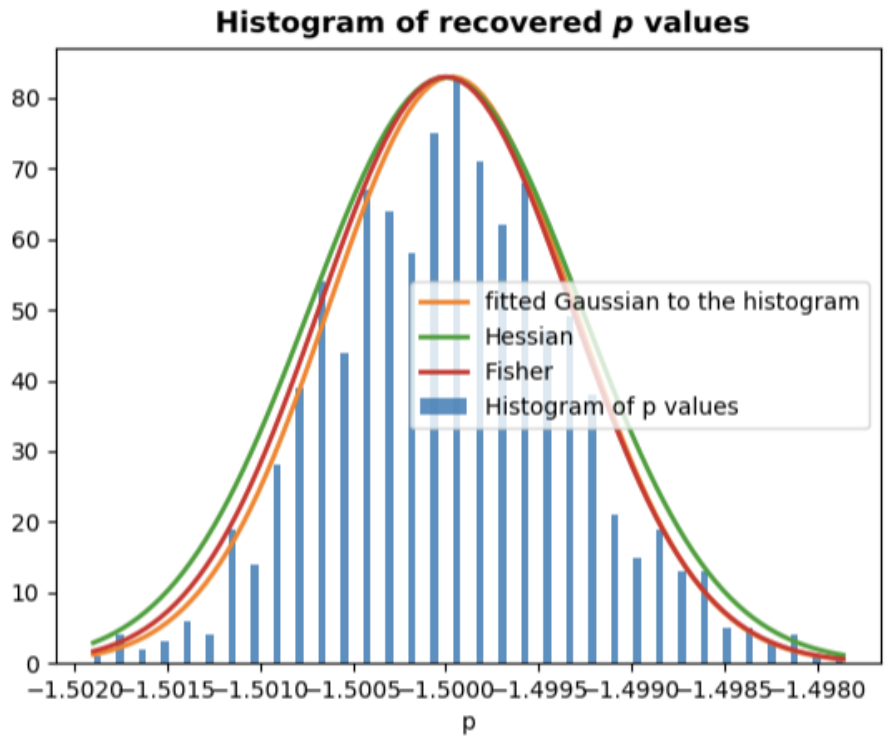

Figure 6.12 – Histogram of recovered value of the crosstalk amplitude p for thousand noise realisations. We overplot the Gaussian fit, as well as Fisher and Hessian predictions.

Perspectives

In the case of POLARBEAR-1 data analysis, we performed the crosstalk analysis after observations ended, and therefore had to make assumptions on crosstalk linearity and time stability. Moreover, we only used the reconstructed matrix as an estimation of the crosstalk amplitude in the final data set, but did not correct for it, as the effect turned out to be small enough. To go one step further, we could use the invert of the crosstalk matrix and apply it to the data set as proposed in Eq. (6.20), an operation that would effectively suppress crosstalk contribution. This was done for SPTPol data analysis [123], and we consider doing the same procedure for Simons Array. Moreover, to be more consistent with the time-domain crosstalk model that we know better, one could estimate the crosstalk matrix in time domain, as we propose in the previous section. This would allow for a better control of instrumental systematic effects

Moreover, future CMB polarisation experiments such as Simons Array and Simons Observatory will deploy dichroic focal planes. In terms of focal plane and readout architecture, it means that detectors sensitive to different sky frequencies will be in the same pixel, and thus readout together. This could source inter-band crosstalk, an effect that has never been studied or modelled for on-sky observations. The framework we propose, once interfaced with realistic hardware maps as I have started to develop during my thesis, would allow to simulate this effect and assess its impact on science analysis. This would extend the work done to study detector arrays effects in the context of Simons Observatory, in which I participated [72].

The drawback of the approach described in this section is that it considers each instrumental systematic effect individually, and they are only added up at the power spectrum level, as shown in Figure 6.8. With the increasing complexity of CMB polarisation experiments, this approach might not be sufficient to account for all potential systematic effects. In particular, interplay of some effects can not be easily modelled at the power spectrum level - we mentioned interplay between beams and crosstalk for example. Other approaches to systematics contamination mitigation therefore have to be envisaged. In particular, the method we propose to simulate crosstalk would allow to correct for readout crosstalk, and potentially some beam effects, at the map level, so that crosstalk would not have to be considered in the final systematic analysis.

In addition to crosstalk, we also propose to model optics chain systematic effects. In the following chapters, we aim at proposing a more involved data model taking into account complexity and interplay of several optics chain elements (HWP, sinuous antenna, bandpass), and associated systematic effects.

CHAPTER 7

Optics chain systematic effects

Contents

As detailed in Chapter 5, the deployment of multichroic focal planes for the new generation of CMB polarisation experiments requires technological developments, such as broadband half-wave plate (HWP) and antennas. I outlined in section 5.2 that such complexity of new projects calls for a thorough modelling of the instrument, and an accurate characterisation of hardware parameters. In this context, it is crucial to develop efficient tools for processing next generation CMB polarisation data sets, to ensure that these experiments achieve the required performance.

CMB data analysis is a complex process, composed of many steps. One of them is map-making, that reconstructs single frequency intensity and polarisation maps from time-domain data. It is typically followed by another important step, component separation, whose goal is to separate the CMB emission from galactic foregrounds, starting from noisy frequency maps obtained from map-making. While many component separation methods have been proposed, in this work we focus on a pixel-based parametric component separation technique, which we extend to account for instrumental systematic effects. As many of those can be modelled reliably only in time domain, we first consider their impact on the map-making procedure and on the maps.

Amongst systematic effects, the knowledge of the polarisation angle of the instrumental polariser with respect to the sky coordinates is one of the key is-

sues for polarisation-sensitive experiments [15]. To demonstrate the framework, I therefore address one of the issues raised by the deployment of achromatic elements (HWP, sinuous antenna): their frequency-dependent polarisation angle. I develop a new, involved data model which is suited to be used as a forecasting tool (as I demonstrate in Chapter 8), and can be straightforwardly adapted to any actual component separation code.

I derive the generalised data model in section 7.1, and present the consequent parametric component separation formalism in section 7.2.

The work detailed in this chapter and the following is published in: Clara Vergès, Josquin Errard, and Radek Stompor, *Framework for analysis of next generation, polarised CMB data sets in the presence of galactic foregrounds and systematic effects* [277].

7.1 Optics chain modelling

To model the optics chain of the instrument, we use Mueller matrix modelling. In this framework, the incoming light is represented by its four Stokes parameters:

$$\mathbf{S} = \begin{pmatrix} \mathrm{I} \\ \mathrm{Q} \\ \mathrm{U} \\ \mathrm{V} \end{pmatrix}. \tag{7.1}$$

Mueller matrices [66] are (4×4) operators acting on Stokes vectors:

$$\mathbf{M} = \begin{pmatrix} \boldsymbol{\mu}_{11} & \boldsymbol{\mu}_{12} & \boldsymbol{\mu}_{13} & \boldsymbol{\mu}_{14} \\ \boldsymbol{\mu}_{21} & \boldsymbol{\mu}_{22} & \boldsymbol{\mu}_{23} & \boldsymbol{\mu}_{24} \\ \boldsymbol{\mu}_{31} & \boldsymbol{\mu}_{32} & \boldsymbol{\mu}_{33} & \boldsymbol{\mu}_{34} \\ \boldsymbol{\mu}_{41} & \boldsymbol{\mu}_{42} & \boldsymbol{\mu}_{43} & \boldsymbol{\mu}_{44} \end{pmatrix} \tag{7.2}$$

They are commonly used to model polarising elements in general, and HWP for CMB experiments in particular [239, 150]. An optical system composed of polarised elements can be modelled as the product of Mueller matrices of its individual elements:

$$\mathbf{M}_{\mathrm{tot}} \equiv \prod_{\mathrm{elements}} \mathbf{M}_{\mathrm{element}} \tag{7.3}$$

Since we are interested in the parametrisation of Mueller matrices, we adopt an approach based on the modelling of individual elements of the optics chain, assuming idealised models for each of the steps. However, we emphasise that Mueller matrices can also be directly measured using calibration sources, and therefore the framework we develop here can be adapted to take into account direct measurements and/or more advanced models.

7.1.1 Half-wave plate

As outlined in section 5.2.1, deploying a continuously rotating HWP has many advantages, in particular to control noise and systematics [253]:

- it modulates the polarised sky signal at frequencies higher than the $1/f$ noise component of the atmosphere, mitigating the noise correlations present in the time-domain data. More generally, the high frequency modulation introduced by the HWP mitigates all low frequency sources of contamination, such as long time noise drifts;
- the optical modulation mitigates beams, bandpass and gain systematics, because one can in principle reconstruct polarised sky maps for each detector separately. This limits the impact of detector properties mismatch in a detector pair;
- the sky polarisation vector is sampled at a higher frequency, which means that for every pixel on the sky, we have more independent measurements of the same pixels. This effect, known as cross-linking, limits systematics. This is important in the case of a space mission, whose scanning strategy is particularly constrained: a satellite can not spin too fast without loosing its orientation with respect to the stars.

However, introducing a new element in the optics chain of the instrument unavoidably introduces new instrumental systematic effects. To benefit from HWP advantages without loosing too much because of new systematics, we therefore need to carefully model HWP-induced effects.

Single layer HWP

A single-layer half-wave plate (HWP) is a retarder made of bi-refringent material that introduces a phase shift between two input and output polarisation components. When parameters of the HWP (see below) are tuned for a given frequency, this phase shift is exactly equal to π. In this simplest case, the Mueller matrix of the HWP is written as:

$$\mathbf{M}_{\rm mono} \equiv \begin{pmatrix} 1 & 0 & 0 & 0 \\ 0 & 1 & 0 & 0 \\ 0 & 0 & -1 & 0 \\ 0 & 0 & 0 & 1 \end{pmatrix}. \tag{7.4}$$

In more generic cases where the light is poly-chromatic, an HWP introduces a phase δ between polarisation components, which depends on frequency. The general Mueller matrix for a single-layer HWP can be written as:

$$\mathbf{M}_{\rm layer} \equiv \begin{pmatrix} 1 & 0 & 0 & 0 \\ 0 & 1 & 0 & 0 \\ 0 & 0 & \cos\delta & -\sin\delta \\ 0 & 0 & \sin\delta & \cos\delta \end{pmatrix}, \tag{7.5}$$

where the phase shift δ is given by:

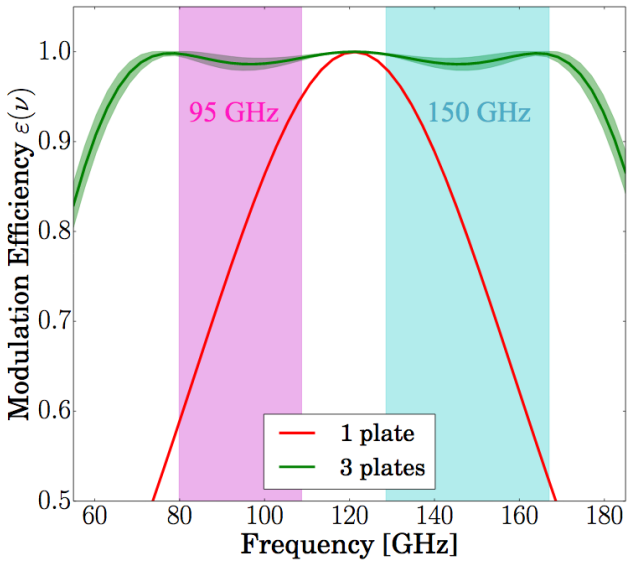

Figure 7.1 – Efficiency of a single layer HWP vs. 3 layer HWP for a broadband use. The efficiency ϵ_ν is defined as $\epsilon_\nu \equiv P_{\rm out}/P_{\rm in}$, and $P \equiv \sqrt{Q^2+U^2}$ is the total polarisation power.
Credit: C. Hill et al. [126]

$$\delta \equiv \frac{2\pi\theta_{\rm hwp}\,|n_o - n_e|\nu}{c}, \tag{7.6}$$

where c refers to the usual speed of light in vacuum. Through Eq. (7.6) defining δ, coefficients of the HWP Mueller matrix depend on the thickness of the bi-refringent layer $\theta_{\rm hwp}$, on optical indices of the ordinary and extraordinary axes of bi-refringent material n_o and n_e, and on the frequency of observation ν. For a single layer, monochromatic HWP, the thickness of the plate is optimised with respect to the observation frequency ν_0 so that δ is equal to π, and we find ourselves in the simplest case described by Eq. (7.4).

Broadband HWP

However, in the case of a multi-frequency focal plane hosting detectors that have different frequency bands, a single layer HWP can obviously not be optimised for all frequencies at the same time. Moreover, optimising a single layer HWP for an intermediate frequency in between the two bands would decrease the performance of the HWP, as shown in Figure 7.1.

In order to make HWP usable on a broader range of frequency, the trick consists in stacking several bi-refringent plates together, with anti-reflective coating between layers. Thickness and orientations of plates have to be carefully tuned to ensure good performances of the HWP [126, 151, 179]. An example of a 3-layer HWP in a configuration often used in CMB polarisation experiments is shown on Figure 7.2.

Each layer can be modelled as in Eq. (7.5). In this work, we neglect reflections at the interface between two stacked layers, as well as effects of non-orthogonal

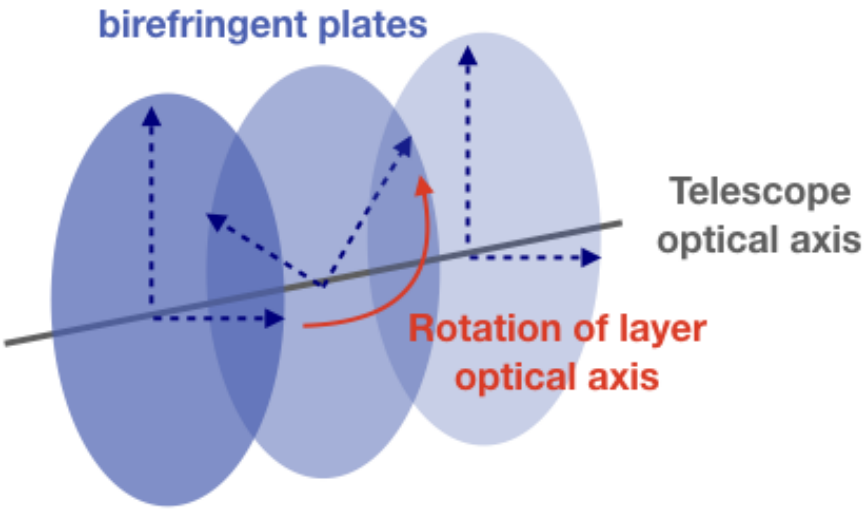

Figure 7.2 – Schematic of a typical 3-layer HWP, showing the rotation of the central layer with respect to the instrument reference frame.

incidence angles. We thus model an achromatic HWP as a stack of layers, each layer being rotated with respect to the reference frame of the instrument by an angle α_i:

$$\mathbf{M}_{\rm HWP} = \prod_{i=n_{\rm layers}} \mathbf{R}(-2\alpha_i)\mathbf{M}_{\rm layer,i}\mathbf{R}(2\alpha_i) \tag{7.7}$$

where $\mathbf{R}$ is a standard rotation matrix:

$$\mathbf{R}(\varphi) \equiv \begin{pmatrix} 1 & 0 & 0 & 0 \\ 0 & \cos\varphi & -\sin\varphi & 0 \\ 0 & \sin\varphi & \cos\varphi & 0 \\ 0 & 0 & 0 & 1 \end{pmatrix}. \tag{7.8}$$

However, as we detail in section 7.2 hereafter, this stacking of layers in a broadband HWP results in a frequency dependent polarisation angle, that we need to take into account.

7.1.2 Sinuous antennas

Description

After the HWP, the modulated sky signal is detected by pairs of detectors, coupled to antennas. As bolometers measure total power, antennas convert the polarised signal to an electric signal, and the polarised signal is reconstructed using the time-dependent modulation induced by HWP rotation (see section 5.1.2). As outlined in section 5.2, several future CMB experiments will deploy a new antenna technology, sinuous antennas, that are sensitive over a broad frequency range, and are therefore usable for multichroic focal planes.

However, their polarisation angle depends on frequency, an effect which is known as wobble angle. A good model for the polarisation angle variation as a

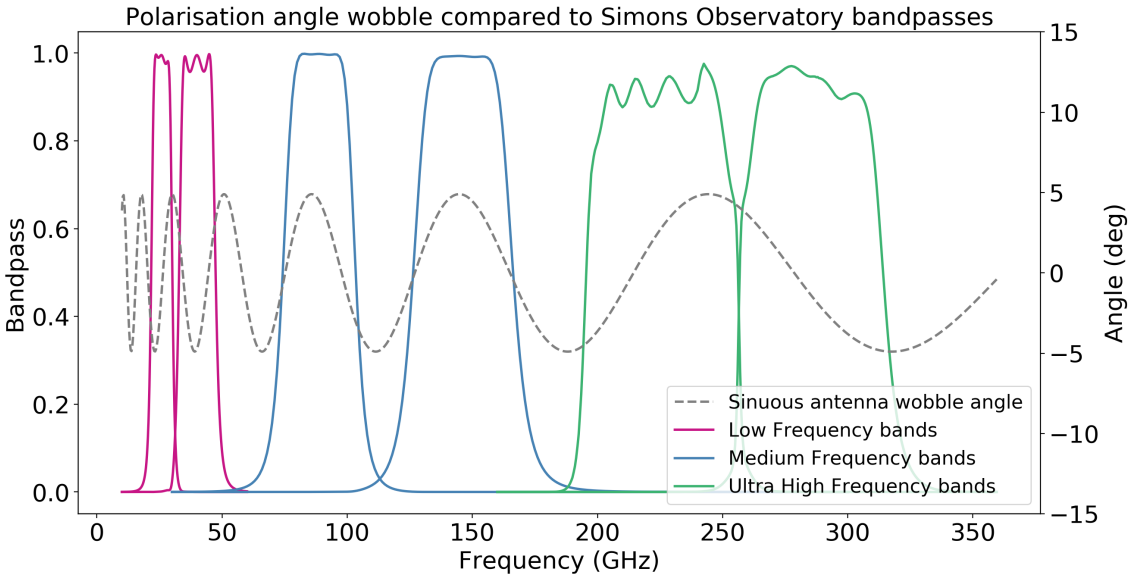

Figure 7.3 – Polarisation angle wobble due to sinuous antennas, compared to Simons Observatory design bandpasses [269].

function of frequency is given by [252]:

$$\eta_\nu = 4.9 \sin\left[12 \log\left(\frac{\nu}{1\,\mathrm{GHz}}\right) + 4.7\right] \text{ rad.} \tag{7.9}$$

Compared to a typical bandwidth of 30 % of the band-centre, the polarisation angle can therefore significantly vary across a given bandpass, as this is illustrated in Figure 7.3 for Simons Observatory bandpasses.

Mueller matrix model

A sinuous antenna can be modelled as a classic double-slot antenna (equivalent to a grid), rotated by a frequency-dependent angle η_ν (see Figure 7.4).

The grid can be modelled as

$$\mathbf{M}_{\text{grid}} \equiv \begin{pmatrix} \frac{1}{2}(p_x^2 + p_y^2) & \frac{1}{2}(p_x^2 - p_y^2) & 0 & 0 \\ \frac{1}{2}(p_x^2 - p_y^2) & \frac{1}{2}(p_x^2 + p_y^2) & 0 & 0 \\ 0 & 0 & p_x p_y & 0 \\ 0 & 0 & 0 & p_x p_y \end{pmatrix}, \tag{7.10}$$

where p_x (resp. p_y) is the efficiency along the x (resp. y) axis in the reference frame of the focal plane.

In our model, we consider a perfect grid aligned along the x direction so we have:

$$\begin{aligned} p_x &= 1 \\ p_y &= 0, \end{aligned} \tag{7.11}$$

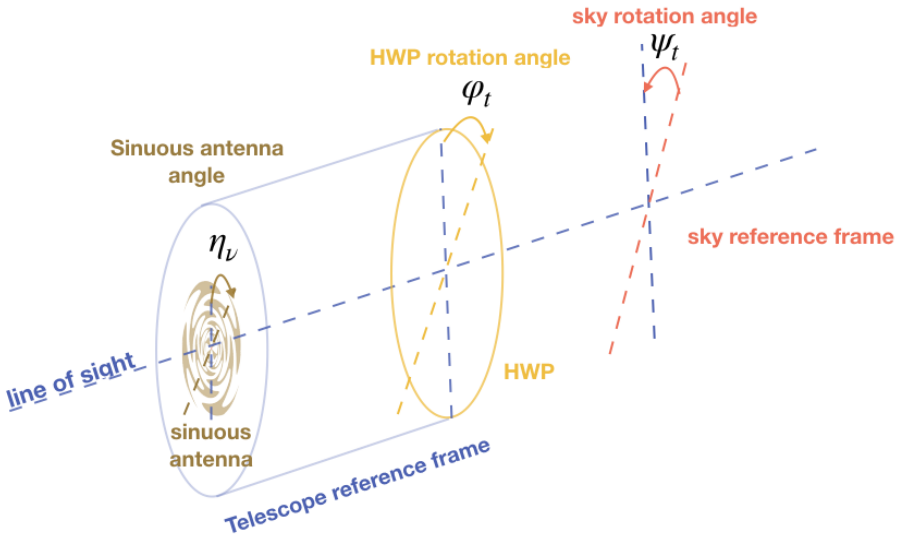

Figure 7.4 – Illustration of the sky rotation angle, ψ_t, defined as the angle between the sky reference frame and the telescope reference frame; and of the HWP rotation angle, φ_t, and sinuous antenna angle, η_ν, both assumed to be measured with respect to the telescope reference frame.

and the Mueller matrix of the grid becomes

$$\mathbf{M}_{\rm grid} = \frac{1}{2}\begin{pmatrix} 1 & 1 & 0 & 0 \\ 1 & 1 & 0 & 0 \\ 0 & 0 & 0 & 0 \\ 0 & 0 & 0 & 0 \end{pmatrix}. \tag{7.12}$$

We finally write the Mueller matrix of a sinuous antenna as:

$$\mathbf{M}_{\rm antenna} = \mathbf{R}(-2\eta_\nu)\mathbf{M}_{\rm grid}\mathbf{R}(2\eta_\nu) \tag{7.13}$$

with η_ν defined in Eq. (7.9).

Full optics chain

As we are primarily interested in the rotation of the polarisation angle with frequency, we do not include other elements than the HWP and sinuous antenna in our model. However, thanks to the generality of Mueller matrices, the proposed framework can easily be extended to account for other optical elements.

During scientific operations, the HWP continuously spins around its axis, introducing an extra rotation angle φ_t with respect to the reference frame of the instrument (see Fig. 7.4):

$$\mathbf{M}_{\rm rotating\ HWP} = \mathbf{R}(-2\varphi_t)\mathbf{M}_{\rm HWP}\mathbf{R}(2\varphi_t) \tag{7.14}$$

Thanks to this rotation, intensity and polarisation signals have different time modulations, as detailed in section 7.2 hereafter.

Including sinuous antenna, the Mueller matrix of the full optics system can thus be written as:

$$\mathbf{M}_{\rm optics} = \mathbf{M}_{\rm antenna}\mathbf{R}(-2\varphi_t)\mathbf{M}_{\rm HWP}\mathbf{R}(2\varphi_t) \tag{7.15}$$

Moreover, during observations, the telescope scans the sky in celestial coordinates and therefore its orientation with respect to the sky is not constant. We therefore introduce ψ_t, the time-dependent rotation angle describing the position of the instrument with respect to sky coordinates (see Figure 7.4). This angle modulates the time-ordered data of the instrument, in addition to the HWP modulation:

$$\mathbf{M}_{\rm tot} = \mathbf{M}_{\rm optics}\mathbf{R}(2\psi_t). \tag{7.16}$$

The matrix $\mathbf{M}_{\rm tot}$ is the transfer function of the optical system in the Stokes parameters domain, applied to the incoming light represented by the four Stokes parameters, Eq. 7.1.

In what follows, we assume that circular polarisation of the incident light vanishes and therefore the Stokes parameter V of the incident light is taken to be zero throughout. It is indeed not expected that CMB light is circularly polarised in the standard model of cosmology, and other possible sources of circular polarisation (atmospheric or foreground) are expected to be negligible [92, 196].

However, circular polarisation could be generated through a wide range of non-standard processes: interactions with dark matter and sterile neutrinos [37], inflation [9], cosmic birefringence [187], new interactions [22], early stars [144] - to cite only a few! Apart from these cosmological sources, V polarisation can also be generated from instrumental polarisation. Moreover, in the case of HWP, V polarisation will inevitably be converted to linear polarisation because of the intrinsic nature of the HWP that mixes U and V polarisation (see Eq. (7.5)). This is a potential contaminant to linear polarisation measurements because of circular-to-linear polarisation leakage, but can also be used to set upper limits on the circular polarisation level of the CMB signal [189]. In this context, the formalism we propose can be extended to model V polarisation, which should ideally be done to tackle the potential impact of spurious V polarisation generated by the instrument.

7.2 Time-domain data model

Now that we have a Mueller matrix model of the instrument, we simulate a realistic data set taking into account instrumental parameters as mentioned in the previous section. We model a data set $\mathbf{m}$ as

$$\mathbf{m} \equiv \mathbf{MS} + \mathbf{n}, \tag{7.17}$$

where M is the Mueller matrix of the full optics chain, S the Stokes vector limited to I, Q and U, and $\mathbf{n}$ is a noise realisation. As the antenna detects only the total power, corresponding to the first line $\mathbf{M}_{0\rm i}$ of the transfer function matrix, we can

write a generic data model as:

$$\mathbf{m}_t(\nu) = \mathbf{M}_{00}(\nu)\,\mathrm{I}(\gamma_t,\nu) + \mathbf{M}_{01}(\nu,\varphi_t,\psi_t)\,\mathrm{Q}(\gamma_t,\nu) + \mathbf{M}_{02}(\nu,\varphi_t,\psi_t)\,\mathrm{U}(\gamma_t,\nu) + \mathbf{n}_t, \tag{7.18}$$

where we have introduced γ_t the pointing direction of the instrument at time t. Each of the elements $\mathbf{M}_{0\mathrm{i}}$ can be written as a sum of harmonic functions of φ_t:

$$\mathbf{M}_{0i}(\nu,\varphi_t,\psi_t) = \sum_{k=0,4} \mathbf{C}_{0i;\,k}(\nu)\,\cos(k\varphi_t + 2\psi_t) + \sum_{k=0,4} \mathbf{S}_{0i;\,k}(\nu)\,\sin(k\varphi_t + 2\psi_t), \tag{7.19}$$

where we have introduced $\mathbf{C}_{0i;\,k}(\nu)$ (resp. $\mathbf{S}_{0i;\,k}(\nu)$), the coefficients of the cosine (resp. sine) modulated terms, which are linear combinations of elements of the Mueller matrices of the optics system. They therefore depend explicitly on instrumental parameters, as well as on the observational frequency ν. For a multi-layer HWP, they are in general all non-zero. In the next section, we detail the expressions of $\mathbf{M}_{0\mathrm{i}}(\nu)$ and $\{\mathbf{C}_{0i;\,k}(\nu),\ \mathbf{S}_{0i;\,k}(\nu)\ \}$ coefficients depending on optics chain elements.

7.2.1 Instrumental framework

As described in the previous section, we consider two crucial elements of the optics of the telescope in our model: the continuously rotating HWP and the sinuous antennas.

Simple case

We start with a very simple configuration: a monochromatic single layer rotating HWP with grid antennas. In this case, the Mueller matrix of the optics system is:

$$\mathbf{M}_{\text{single layer}} = \mathbf{M}_{\text{grid}}\mathbf{R}(-2\varphi_t)\mathbf{M}_{\text{mono}}\mathbf{R}(2\varphi_t). \tag{7.20}$$

with $\mathbf{M}_{\text{mono}}$ defined in Eq. (7.4). In this configuration, we have:

$$\begin{aligned}
\mathbf{M}_{00} &= 1 \\
\mathbf{C}_{01,4} &= \mathbf{S}_{02,4} = 1 \\
\mathbf{C}_{01,0} &= \mathbf{S}_{02,0} = 0 \\
\mathbf{S}_{01,0} &= \mathbf{S}_{01,4} = 0 \\
\mathbf{C}_{02,0} &= \mathbf{C}_{02,4} = 0
\end{aligned} \tag{7.21}$$

We can thus simplify Eq. (7.19) to:

$$\mathbf{d}_t = \mathrm{I} + [\cos(4\varphi_t + 2\psi_t) \times \mathrm{Q} + \sin(4\varphi_t + 2\psi_t) \times \mathrm{U}] + \mathbf{n}_t \tag{7.22}$$

where we kept only $k = 4$ in the sum. As outlined above, the signal detected by the antenna is a total power signal, but with different time modulations for I, Q,

and U. In practice, in the map-making procedure, the polarisation signal can be reconstructed by demodulating the time-domain signal recorded by the detectors according to HWP modulation: cosine $4\varphi_t$ modulated signal corresponds to Q, and sine $4\varphi_t$ modulated signal corresponds to U.

However, this one-to-one correspondence is not true anymore in the case of complex optics system including a multi-layer HWP [88, 137, 253]. One has to take into account Q and U mixing induced by the HWP and sinuous antennas.

More realistic configuration

We now consider a more complex optics system with a multi-layer HWP and sinuous antennas, whose Mueller matrix M is defined by Eq. (7.15). When the timestream is demodulated, one can only differentiate terms corresponding to their HWP modulation order, cosine or sine. With a multi-layer HWP, it is clear from Eq. (7.18 - 7.19) that cosine (resp. sine) modulated terms are not a pure Q (resp. pure U) signal as it was the case for the data model in Eq. (7.22) describing a single layer monochromatic HWP.

One thus has two options to define a data model:

- group elements of the signal by their *polarisation state*, i.e. Q or U, irrespective of their HWP modulation;
- group elements of the signal by their *HWP modulation* order, i.e. cosine or sine.

Instrumental polarisation angle approach The first approach is the one which is usually adopted in CMB data analysis [17, 178]. It requires to introduce an instrumental polarisation angle, to account for the mixing of Q and U. Following the data model in the form of Eq. (7.22), one can write:

$$\mathbf{d}_t = \mathrm{I} + \sum_{k=0,4} [\cos(k\varphi_t + 2\psi_t + \phi_{\text{inst.}}) \times \mathrm{Q} + \sin(k\varphi_t + 2\psi_t + \phi_{\text{inst.}}) \times \mathrm{U}] + \mathbf{n}_t, \quad (7.23)$$

where $\phi_{\text{inst.}}$ describes Q and U mixing due to instrumental polarisation, including HWP phase, sinuous antenna wobble angle and any other instrumental contribution. Using this data model has many advantages, in particular it allows to keep previously validated data analysis methods, such as map-making, that rely on the separation of Q and U using HWP demodulation.

However, it also has several drawbacks. First of all, it requires the introduction of a global instrument polarisation angle $\phi_{\text{inst.}}$, which is not a well defined instrumental parameter, but rather a composite of several distinct instrumental effects and signal parameters. As outlined in section 2.7.4, the calibration of the global polarisation angle of an instrument is a complex process, and therefore it is not clear how this angle could be carefully calibrated. Moreover, we have mentioned before that HWP and sinuous antennas effects depend on the observing frequency. The instrumental polarisation angle $\phi_{\text{inst.}}$ therefore also depends on frequency, and can vary significantly over a bandpass. This effect is shown in Figure 7.3 for the sinuous antenna wobble angle alone. Defining a single angle

per bandpass is therefore a simplification, as one should include the polarisation angle at each integration step in the data model. Last but not least, the global polarisation angle also depends on the spectral emission of the source [178]. Consequently, a polarisation angle calibrated on the ground with a FTS (Fourier Transform Spectrometer) [177] or with an astrophysical source such as Tau-A [15] will likely be different from the actual one, which in turn will be different for each frequency band. This is particularly worrisome in the case of polarised foregrounds whose spectral distribution is not precisely known.

We therefore resort to the alternative data model, which does not rely on introducing such a global polarisation angle, but rather models individual optical elements based on their hardware parameters.

Alternative data model To do so, we adopt the second approach based on HWP modulation order. Combining Eq. (7.18) and (7.19), we group modulated terms of the sky signal given their time dependence, and not given their polarisation state (Q or U). We thus rewrite the data model by grouping together terms having the same time-dependent modulation:

$$\begin{aligned}\mathbf{m}_t(\nu) \equiv\, & \mathbf{n}_t \,+\, \mathbf{M}_{00}(\nu)\,\mathrm{I}(\gamma_t,\nu) \\ & +\,[\,\mathbf{C}_{01;\,0}(\nu)\,\mathrm{Q}(\gamma_t,\nu) \,+\, \mathbf{C}_{02;\,0}(\nu)\,\mathrm{U}(\gamma_t,\nu)\,]\,\times\cos 2\psi_t \\ & +\,[\,\mathbf{S}_{01;\,0}(\nu)\,\mathrm{Q}(\gamma_t,\nu) \,+\, \mathbf{S}_{02;\,0}(\nu)\,\mathrm{U}(\gamma_t,\nu)\,]\,\times\sin 2\psi_t \\ & +\,[\,\mathbf{C}_{01;\,4}(\nu)\,\mathrm{Q}(\gamma_t,\nu) \,+\, \mathbf{C}_{02;\,4}(\nu)\,\mathrm{U}(\gamma_t,\nu)\,]\,\times\,\cos(4\varphi_t+2\psi_t) \\ & +\,[\,\mathbf{S}_{01;\,4}(\nu)\,\mathrm{Q}(\gamma_t,\nu) \,+\, \mathbf{S}_{02;\,4}(\nu)\,\mathrm{U}(\gamma_t,\nu)\,]\,\times\,\sin(4\varphi_t+2\psi_t). \end{aligned} \tag{7.24}$$

This expression highlights the fact that in the case of a multi-layer HWP, the Q (resp. U) Stokes parameter of the sky signal is not simply modulated at $\cos(4\varphi_t + 2\psi_t)$ (resp. $\sin(4\varphi_t + 2\psi_t)$). Instead, and in contrast to the case of the simple polarised data model in Eq. (7.22), the terms modulated in this way are composed of a mixture of these two Stokes parameters. We refer to these signals hereafter as mixed-Stokes single frequency maps. We also note the presence of two additional terms which are modulated by the sky angle only. Their corresponding sky signals constitute two additional, independent combinations of the Stokes Q and U parameters. The coefficients $\mathbf{C}_{0\mathrm{i};\,\mathrm{k}}$ and $\mathbf{S}_{0\mathrm{i};\,\mathrm{k}}$, which define the mixed-Stokes frequency maps thus depend on instrumental parameters. Their explicit expressions as a function of the HWP Mueller matrix elements $\boldsymbol{\mu}_{ij}$ are given by (we note that $\boldsymbol{\mu}_{0\mathrm{i}}$ and $\boldsymbol{\mu}_{\mathrm{i}0}$ elements are zero by design of the HWP):

$$\mathbf{C}_{01;\,0}(\nu) = \frac{1}{2}\left(\boldsymbol{\mu}_{11} + \boldsymbol{\mu}_{22}\right)\cos\left(2\eta_\nu\right) \tag{7.25}$$

$$\mathbf{C}_{01;\,4}(\nu) = \frac{1}{2}[\left(\boldsymbol{\mu}_{11} - \boldsymbol{\mu}_{22}\right)\cos\left(2\eta_\nu\right) - \left(\boldsymbol{\mu}_{12} + \boldsymbol{\mu}_{21}\right)\sin\left(2\eta_\nu\right)] \tag{7.26}$$

$$\mathbf{S}_{01;\,0}(\nu) = -\frac{1}{2}\left(\boldsymbol{\mu}_{11} + \boldsymbol{\mu}_{22}\right)\sin\left(2\eta_\nu\right) \tag{7.27}$$

$$\mathbf{S}_{01;\,4}(\nu) = \frac{1}{2}[\left(\boldsymbol{\mu}_{12} + \boldsymbol{\mu}_{21}\right)\cos(2\eta_\nu) + \left(\boldsymbol{\mu}_{11} - \boldsymbol{\mu}_{22}\right)\sin\left(2\eta_\nu\right)] \tag{7.28}$$

$$\mathbf{C}_{02;\,0}(\nu) = -\frac{1}{2}\left(\boldsymbol{\mu}_{11} + \boldsymbol{\mu}_{22}\right)\sin\left(2\eta_\nu\right) \tag{7.29}$$

$$\mathbf{C}_{02;\,4}(\nu) = \frac{1}{2}[\left(\boldsymbol{\mu}_{12} + \boldsymbol{\mu}_{21}\right)\cos\left(2\eta_\nu\right) + \left(\boldsymbol{\mu}_{11} - \boldsymbol{\mu}_{22}\right)\sin\left(2\eta_\nu\right)] \tag{7.30}$$

$$\mathbf{S}_{02;\,0}(\nu) = -\frac{1}{2}\left(\boldsymbol{\mu}_{11} + \boldsymbol{\mu}_{22}\right)\cos\left(2\eta_\nu\right) \tag{7.31}$$

$$\mathbf{S}_{02;\,4}(\nu) = -\frac{1}{2}[\left(\boldsymbol{\mu}_{11} - \boldsymbol{\mu}_{22}\right)\cos\left(2\eta_\nu\right) - \left(\boldsymbol{\mu}_{12} + \boldsymbol{\mu}_{21}\right)\sin\left(2\eta_\nu\right)] \tag{7.32}$$

As mentioned earlier, the map-making procedure enables an estimation of terms with different time dependence, assuming that these dependencies are such that they are linearly independent when limited to observations of a single sky pixel for every such pixel. If these conditions are met, the map-making procedure applied to the data model in Eq. (7.24) would recover, for each frequency channel, a map of total intensity accompanied by four maps composed of different linear combinations of Stokes Q and U parameters, the mixed-Stokes single frequency maps that we introduced above. These could and should be considered as inputs to the next data processing stages, and specifically component separation.

An important consequence of the more involved data model in Eq. (7.24) is that solving the complete map-making problem will in general require sufficient redundancy in observations of every sky pixel, with a number of different HWP as well as sky rotation angles. This can have important consequences for scan designs of future CMB experiments.

In our case, we will however assume the case of a perfectly uniform sky coverage, both in terms of the number of observations of each pixel, as well as distributions of the HWP and sky angles, i.e. a perfect cross-linking. Mathematically,

we therefore assume for all observations t of a pixel p that it holds:

$$\sum_{t\in p}\cos^2(4\varphi_t+2\psi_t) \;=\; \sum_{t\in p}\sin^2(4\varphi_t+2\psi_t) \;=\; \frac{1}{2}\,n_{\rm hits}(p), \tag{7.33}$$

$$\sum_{t\in p}\cos^2(2\psi_t) \;=\; \sum_{t\in p}\sin^2(2\psi_t) \;=\; \frac{1}{2}\,n_{\rm hits}(p), \tag{7.34}$$

$$\sum_{t\in p}\cos(4\varphi_t+2\psi_t)\,\sin(4\varphi_t+2\psi_t) \;=\; 0 \tag{7.35}$$

$$\sum_{t\in p}\cos(4\varphi_t+2\psi_t) \;=\; \sum_{t\in p}\sin(4\varphi_t+2\psi_t) \;=\; 0 \tag{7.36}$$

$$\sum_{t\in p}\cos(2\psi_t) \;=\; \sum_{t\in p}\sin(2\psi_t) \;=\sum_{t\in p}\cos(2\psi_t)\,\sin(2\psi_t) \;=\; 0 \tag{7.37}$$

$$\sum_{t\in p}\sin(4\varphi_t+2\psi_t)\,\sin(2\psi_t) \;=\; \sum_{t\in p}\cos(4\varphi_t+2\psi_t)\,\cos(2\psi_t) \;=0 \tag{7.38}$$

$$\sum_{t\in p}\cos(4\varphi_t+2\psi_t)\,\sin(2\psi_t) \;=\; \sum_{t\in p}\sin(4\varphi_t+2\psi_t)\,\cos(2\psi_t) \;=\; 0, \tag{7.39}$$

where $n_{\rm hits}(p)$ is the number of observations of each pixel p, and we assume the same for all observed pixels p, i.e. $n_{\rm hits} = n_{\rm hits}(p)$.

With these assumptions, the map-making problem for the data model in Eq. (7.24) is not only solvable, but results in estimates of the five sky signals which have mutually uncorrelated noise. In the case of white noise in the time-domain, the RMS of the noise in the four mixed-Stokes maps and in total intensity is the same as in the standard case, i.e.:

$$\sigma_{RMS}({\rm pol.}) \;=\; \sigma_{RMS}({\rm int.})\times\sqrt{2} \;\propto\; \sqrt{\frac{2}{n_{\rm hits}}} \tag{7.40}$$

We use these estimates as reflecting the noise levels in our mixed-Stokes maps in the following.

We denote the four mixed-Stokes signals as $\boldsymbol{\mathcal{C}}_0$, $\boldsymbol{\mathcal{S}}_0$, $\boldsymbol{\mathcal{C}}_4$, $\boldsymbol{\mathcal{S}}_4$, and introduce an effective intensity signal, $\boldsymbol{\mathcal{I}}(\gamma_t,\nu) \equiv \mathrm{M}_{00}\mathrm{I}(\gamma_t,\nu)$. We can thus re-express the data model, Eq. (7.24), as:

$$\begin{aligned}\mathbf{m}_t(\nu) \equiv\; & \boldsymbol{\mathcal{I}}(\gamma_t,\nu)\\ & + \boldsymbol{\mathcal{C}}_0(\gamma_t,\nu)\cos(2\psi_t) + \boldsymbol{\mathcal{S}}_0(\gamma_t,\nu)\sin(2\psi_t)\\ & + \boldsymbol{\mathcal{C}}_4(\gamma_t,\nu)\cos(4\varphi_t+2\psi_t) + \boldsymbol{\mathcal{S}}_4(\gamma_t,\nu)\sin(4\varphi_t+2\psi_t)\\ & + \mathbf{n}_t.\end{aligned} \tag{7.41}$$

These mixed Stokes components are related to the standard Stokes components, via a linear transformation given by Eq. (7.24), and that we can reformulate in

matrix form as:

$$\begin{pmatrix} \boldsymbol{\mathcal{I}}(\gamma_t,\nu) \\ \boldsymbol{\mathcal{C}}_0(\gamma_t,\nu) \\ \boldsymbol{\mathcal{S}}_0(\gamma_t,\nu) \\ \boldsymbol{\mathcal{C}}_4(\gamma_t,\nu) \\ \boldsymbol{\mathcal{S}}_4(\gamma_t,\nu) \end{pmatrix} = \underbrace{\begin{bmatrix} \mathbf{M}_{00}(\nu) & 0 & 0 \\ 0 & \mathbf{C}_{01;0}(\nu) & \mathbf{C}_{02;0}(\nu) \\ 0 & \mathbf{S}_{01;0}(\nu) & \mathbf{S}_{02;0}(\nu) \\ 0 & \mathbf{C}_{01;4}(\nu) & \mathbf{C}_{02;4}(\nu) \\ 0 & \mathbf{S}_{01;4}(\nu) & \mathbf{S}_{02;4}(\nu) \end{bmatrix}}_{\equiv \mathbf{M}(\nu)} \times \begin{pmatrix} \mathrm{I}(\gamma_t,\nu) \\ \mathrm{Q}(\gamma_t,\nu) \\ \mathrm{U}(\gamma_t,\nu) \end{pmatrix}, \tag{7.42}$$

where the transformation matrix, $\mathbf{M}(\nu)$, depends on instrumental parameters. We conclude that the map-making procedure could produce estimates of pure Q and U Stokes parameters only if the true values of the relevant instrumental parameters were known for all frequencies, or the observations were monochromatic. None of these two assumptions is actually fulfilled in the current CMB experiments.

This generalisation of the usual Stokes components avoids the introduction of an effective instrumental polarisation angle, and the subsequent data model accurately reflects the dependence on instrumental parameters. As we develop in the following sections, such a formalism allows to take into account the interplay of frequency-dependent effects with astrophysical foreground emission laws (section 7.2.2), and bandpasses (section 7.2.1). In particular, it allows to perform component separation without assuming anything about the polarisation angle of the instrument, as we demonstrate in Chapter 8.

Bandpasses

Bandpasses of the instrument are defined by micro-strip filters, as described in section 5.2.1. Depending on the instrument design, they can be located between lenses or between lenses and detector plane. The bandpass integration therefore occurs after the HWP and the sinuous antennas in the optics chain, which causes an interplay between bandpass and instrumental frequency-dependent effects.

To get a more realistic data model, we integrate mixed Stokes components as defined in Eq. (7.42), so that the bandpass integration takes into account the frequency-dependent sky signal as well as frequency dependent instrumental effects included in $\mathbf{M}(\nu)$:

$$\bar{\mathbf{X}}(\nu_c) \;\equiv\; \frac{\int d\nu\, \mathcal{B}(\nu,\nu_c)\, \mathbf{X}(\nu)\, k(\nu)}{\int d\nu\, \mathcal{B}(\nu)\, k(\nu)}, \tag{7.43}$$

where k is a conversion factor which reconciles the units used for the data, $\mathbf{X}$, and the bandpasses, $\mathcal{B}$.

We can then rewrite the data model in Eq. (7.41) using the bandpass averaged objects as:

$$\begin{aligned} \bar{\mathbf{m}}_t(\nu_c) \equiv\; & \bar{\boldsymbol{\mathcal{I}}}(\gamma_t,\nu_c) \\ & + \bar{\boldsymbol{\mathcal{C}}}_0(\gamma_t,\nu_c)\cos(2\psi_t) + \bar{\boldsymbol{\mathcal{S}}}_0(\gamma_t,\nu_c)\sin(2\psi_t) \\ & + \bar{\boldsymbol{\mathcal{C}}}_4(\gamma_t,\nu_c)\cos(4\varphi_t+2\psi_t) + \bar{\boldsymbol{\mathcal{S}}}_4(\gamma_t,\nu_c)\sin(4\varphi_t+2\psi_t) \\ & + \bar{\mathbf{n}}_t. \end{aligned} \tag{7.44}$$

The map-making codes can be used assuming this data model in the same way as in the monochromatic case however they will now produce bandpass-averaged maps of mixed-Stokes and effective total intensity. Note that we did not assume any specific shape, nor variability between detectors, for the bandpass. As we detail in the next chapter, when performing component separation, we will need to chose a parametrisation for bandpasses, which could lead to some bias if it is not a good description of the instrument (see 8.1.1 and 8.2.3).

We further note that going from these maps to the maps of pure Stokes parameters for each frequency band is not possible once the bandpasses are explicitly included. This is because the integration over the bandpasses does not preserve the matrix form of Eq. (7.42) as the pure Stokes signals, $\mathbf{s}(\nu)$, are integrated over the frequency together with the corresponding elements of the matrix $\mathbf{M}(\nu)$. Consequently, the mixed-Stokes maps are the only available objects at the end of the map-making even if the instrumental parameters were perfectly known. As we discuss in the following, this however does not prevent us from recovering pure Stokes parameters maps of components of a different physical origin.

7.2.2 Multi-component data model

The sky signal that we have so far simply described with its three Stokes components (I,Q,U) actually requires a more complex model, as we need to take into account both CMB signal and polarised galactic foregrounds. The two most important foregrounds are thermal dust polarised emission and synchrotron radiation as detailed in Chapter 4. Separating the multi-components observations into signals of the sky components is the goal of component separation procedures. These are typically performed in the pixel domain and use maps produced on the map-making step as inputs. In this section, we therefore extend the data model of the mixed Stokes maps, Eq. (7.44), to model the complexity of the multi-component sky.

Sky components

We adopt the framework of parametric component separation introduced in section 4.2. We model foregrounds by a template at a reference frequency ν_0, scaled to the observation frequency ν using foreground emission models. The effective signal as measured at each frequency is a mixture of these three major sky components (CMB, dust and synchrotron), which can be described by a mixing matrix $\mathbf{A}$ defined in Eq. (4.16), containing the scaling laws for each sky component at each frequency. Scaling laws of foregrounds are expressed in $\mu\mathrm{K}_{\mathrm{RJ}}$, and the one of CMB in $\mu\mathrm{K}_{\mathrm{CMB}}$.

The scaling laws we assume in this work are fairly standard, e.g., [246], and are given by:

- synchrotron: power-law emission characterised by its spectral index β_s:

$$\mathbf{A}^{\mathrm{sync}}(\nu, \nu_0) = \left(\frac{\nu}{\nu_0}\right)^{\beta_s} \tag{7.45}$$

- dust: modified black body emission characterised by its spectral index β_d and temperature T_d:

$$\mathbf{A}^{\rm dust}(\nu,\nu_0) = \left(\frac{\nu}{\nu_0}\right)^{\beta_d+1} \frac{e^{\frac{h\nu_0}{kT_d}}-1}{e^{\frac{h\nu}{kT_d}}-1} \tag{7.46}$$

- CMB: known black body spectrum, with $T_{\rm CMB} = 2.7255\,K.$, leading to the assumption that $\mathbf{A}^{\rm CMB}(\nu,\nu_0) = 1$ in $\mu{\rm K}_{\rm CMB}$ units.

For a given observed frequency ν, the sky signal can be modelled as:

$$\begin{pmatrix} {\rm I}(\nu) \\ {\rm Q}(\nu) \\ {\rm U}(\nu) \end{pmatrix} = \sum_{\substack{\rm comp={\rm CMB} \\ \rm dust,sync}} \mathbf{A}^{\rm comp}(\nu,\nu_0) \begin{pmatrix} {\rm I}_{\rm comp}(\nu_0) \\ {\rm Q}_{\rm comp}(\nu_0) \\ {\rm U}_{\rm comp}(\nu_0) \end{pmatrix} \tag{7.47}$$

Scaling laws as presented here are in $\mu{\rm K}_{\rm RJ}$, but for simplicity, we generate maps at all frequencies and for all components in $\mu{\rm K}_{\rm CMB}$ units, as are the recovered maps of the CMB and foreground signal. A conversion factor is then taken into account so that units are handled consistently throughout the process.

Multi-component sky model

To derive a complete multi-component sky model, we first generalise Eq. (7.42) to account for all three sky components:

$$\underbrace{\begin{pmatrix} \mathcal{I}(\gamma_t,\nu) \\ \mathcal{C}_0(\gamma_t,\nu) \\ \mathcal{S}_0(\gamma_t,\nu) \\ \mathcal{C}_4(\gamma_t,\nu) \\ \mathcal{S}_4(\gamma_t,\nu) \end{pmatrix}}_{\equiv\ \mathbf{s}(\gamma_t,\nu)} \equiv \sum_{\substack{\rm comp={\rm CMB} \\ \rm dust,sync}} \underbrace{\begin{bmatrix} \mathbf{M}_{00;\,\cos_0}(\nu) & 0 & 0 \\ 0 & \mathbf{C}_{01;\,0}(\nu) & \mathbf{C}_{02;\,0}(\nu) \\ 0 & \mathbf{S}_{01;\,0}(\nu) & \mathbf{S}_{02;\,0}(\nu) \\ 0 & \mathbf{C}_{01;\,4}(\nu) & \mathbf{C}_{02;\,4}(\nu) \\ 0 & \mathbf{S}_{01;\,4}(\nu) & \mathbf{S}_{02;\,4}(\nu) \end{bmatrix} \mathbf{A}^{\rm comp}(\nu,\nu_0)}_{\equiv\ \boldsymbol{\mathcal{A}}(\nu)} \begin{pmatrix} {\rm I}_{\rm comp}(\gamma_t,\nu_0) \\ {\rm Q}_{\rm comp}(\gamma_t,\nu_0) \\ {\rm U}_{\rm comp}(\gamma_t,\nu_0) \end{pmatrix}. \tag{7.48}$$

We then integrate both sides of this equation over the bandpasses using Eq. (7.43), and define component-specific, bandpass integrated matrices, $\bar{\boldsymbol{\mathcal{A}}}^{\rm comp}$, as:

$$\bar{\boldsymbol{\mathcal{A}}}^{\rm comp}(\nu_c,\nu_0) \equiv \frac{\int d\nu\, \mathbf{M}(\nu)\, \mathcal{B}(\nu,\nu_c)\, \mathbf{A}^{\rm comp}(\nu,\nu_0)\, k(\nu)}{\int d\nu\, \mathcal{B}(\nu)\, k(\nu)}, \tag{7.49}$$

where we assumed that the bandpass centre frequency is ν_c.

For a bandpass centred at ν_c, we can now write our full multi-component, bandpass integrated data model as:

$$\begin{aligned} \bar{\mathbf{s}}(\gamma_t,\nu_c,\nu_0) &= \underbrace{\begin{bmatrix} \bar{\boldsymbol{\mathcal{A}}}^{\rm cmb}(\nu_c,\nu_0) & \bar{\boldsymbol{\mathcal{A}}}^{\rm dust}(\nu_c,\nu_0) & \bar{\boldsymbol{\mathcal{A}}}^{\rm sync}(\nu_c,\nu_0) \end{bmatrix}}_{\equiv\ \bar{\boldsymbol{\mathcal{A}}}(\nu_c,\nu_0)} \underbrace{\begin{pmatrix} \mathbf{s}_{\rm cmb}(\gamma_t,\nu_0) \\ \mathbf{s}_{\rm dust}(\gamma_t,\nu_0) \\ \mathbf{s}_{\rm sync}(\gamma_t,\nu_0) \end{pmatrix}}_{\equiv\ \mathbf{c}(\gamma_t,\nu_0)} \\ &= \bar{\boldsymbol{\mathcal{A}}}(\nu_c,\nu_0)\, \mathbf{c}(\gamma_t,\nu_0). \end{aligned} \tag{7.50}$$

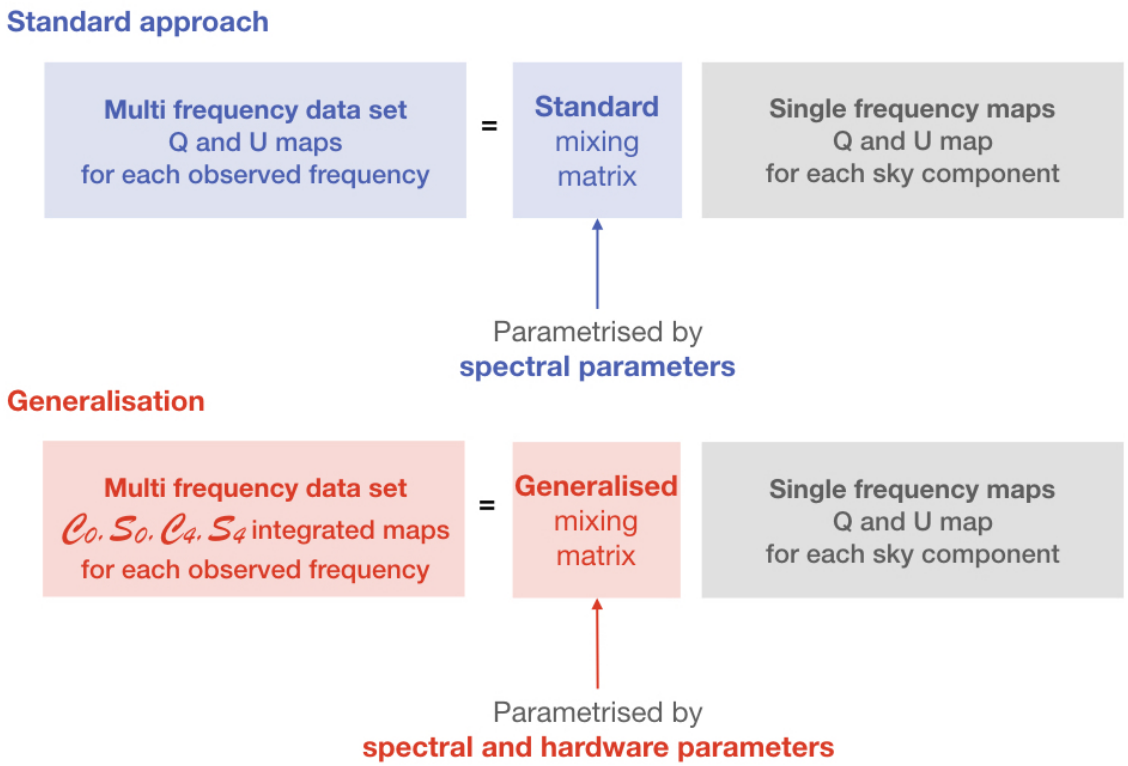

Figure 7.5 – Data model with generalised mixing matrix. The top panel corresponds to Eq. (7.47), and the bottom panel to Eq. (7.50).

The mixed Stokes maps that we define are therefore parametrised by both foregrounds spectral parameters and instrumental parameters, including bandpass parameters. This is one of the most distinctive feature of the model we propose compared to previous approaches: by design, it takes into account the interplay of bandpass integration with both instrument frequency-dependent instrumental effects and frequency-dependent sky signal.

7.2.3 Generalised mixing matrix

By writing the multi-component, integrated data model of Eq. (7.50), we generalised the standard component mixing matrix $\mathbf{A}$ by including instrument and bandpass effects. With this generalised mixing matrix, $\bar{\boldsymbol{\mathcal{M}}}(\nu_c, \nu_0)$, we can simulate multi-frequency and multi-component polarised data sets of effective Stokes components, from single frequency, single component Q and U maps. For each bandpass, $\bar{\boldsymbol{\mathcal{M}}}$ is parametrised not only by spectral parameters as in the standard approach, but also by hardware parameters, as summarised in Figure 7.5.

As mentioned earlier, each of the mixed Stokes components has a specific time-dependent modulation: $\boldsymbol{\mathcal{C}}_0$ (resp. $\boldsymbol{\mathcal{S}}_0$) is modulated only by the sky at $\cos(2\psi_t)$ (resp. $\sin(2\psi_t)$), and $\boldsymbol{\mathcal{C}}_4$ (resp. $\boldsymbol{\mathcal{S}}_4$) is modulated by the sky and the HWP at $\cos(4\varphi_t + 2\psi_t)$ (resp. $\sin(4\varphi_t + 2\psi_t)$). Consequently, the output of map-making (that separates component based on their time-dependent modulation) will not be pure Q and U maps, but a mixing of those. Thanks to the generalisation of the mixing matrix we propose, we can take this effect into account in the component

separation process, without making prior assumptions on hardware parameters to separate Q and U, as this was necessary with the effective instrumental polarisation angle that we described above. In the next chapter, we use this new, involved data model, in the context of parametric component separation methods to propose a generalisation of those based on this generalised mixing matrix.

CHAPTER 8

Generalised component separation

Contents

With the data model I developed in the previous Chapter, I extend a previously validated parametric component separation forecasting framework in order to include the extra-parametrisation with instrument parameters introduced in section 7.2.3. The framework I propose performs component separation on mixed Stokes maps that are the natural output of HWP demodulation, without reconstructing Q and U maps for each frequency band, and simultaneously estimates the foreground and instrumental parameters to the extent it is possible.

I detail the extended component separation framework and its most distinctive features in section 8.1, and demonstrate its capabilities for a typical new generation CMB experiment in section 8.2.

8.1 Component separation framework

As outlined in section 4.2, the framework of parametric component separation has been validated and used both for forecasting and data analysis [94, 95,

96, 246, 247]. In this work, we follow the formalism of [246], and we adapt the procedure to account for mixed Stokes components and instrumental parameters (HWP, sinuous antenna, bandpasses), using the data model developed in the previous chapter.

In section 8.1.1, we first simulate a data set using the data model developed in the previous chapter. We then perform component separation and estimation of foreground and hardware parameters on these mixed maps in section 8.1.2. With the estimated parameters, we reconstruct the sky signals and estimate residuals in section 8.1.3 and noise after component separation in section refnoise . From these, we can finally estimate cosmological parameters in section 8.1.5.

8.1.1 Data model

We consider a typical Stage 3 multi-frequency CMB polarisation experiment, similar to SO. We simulate mixed Stokes maps $\{\mathcal{C}_0, \mathcal{S}_0, \mathcal{C}_4, \mathcal{S}_4\}$ for each frequency band, using foreground templates and taking into account optical effects and bandpass integration as in Eq. (7.50). We also include a realisation of homogeneous noise with a sensitivity corresponding to a typical Stage 3 experiment (see section 8.1.4)

Collecting together all frequency maps, we can write our data model for an entire multi frequency data set:

$$\bar{\mathbf{m}} = \bar{\mathbf{s}} + \bar{\mathbf{n}} \equiv \bar{\boldsymbol{\mathcal{A}}}\,\mathbf{c} + \bar{\mathbf{n}}, \tag{8.1}$$

Here the combined data vector $\bar{\mathbf{m}}$ includes all the bandpass-integrated mixed-Stokes maps, $\bar{\boldsymbol{\mathcal{C}}}_0$, $\bar{\boldsymbol{\mathcal{C}}}_4$, $\bar{\boldsymbol{\mathcal{S}}}_0$, $\bar{\boldsymbol{\mathcal{S}}}_0$, as measured for all frequency bands which are all concatenated in a single data vector. From now on we focus only on polarisation and exclude total intensity from our consideration. $\bar{\mathbf{s}}$ is the noiseless signal in the recovered mixed-Stokes maps, and $\bar{\boldsymbol{\mathcal{A}}}$ is a generalised mixing matrix. The latter is composed of single channel matrices, $\bar{\boldsymbol{\mathcal{A}}}(\nu_c, \nu_0)$, defined in Eq. (7.50), put on top of each other. $\bar{\mathbf{n}}$ denotes the actual noise present in all the mixed-Stokes maps as derived by the map-making procedure.

To improve readability, as we always integrate over bandpasses, we drop the bar that indicates bandpass integration in the following.

For a given pixel p, we have:

$$\mathbf{m}_p = \mathbf{s}_p + \mathbf{n}_p \equiv \boldsymbol{\mathcal{A}}_p(\beta_f, \beta_h)\ \mathbf{c}_p + \mathbf{n}_p \tag{8.2}$$

where β_f refers to foreground spectral parameters and β_h to hardware parameters.

Whereas β_f parameters apply to a given component (dust or synchrotron) and can vary between sky pixels, β_h are however considered as global parameters, applied to all pixels and all sky components - including CMB. We therefore take into account this extra parametrisation of the CMB in the extension of the forecasting framework. There is also an extra distinction to be made between HWP parameters and bandpass parameters: the former are assumed to apply to the two frequency bands (by design of the HWP), whereas the latter apply to only one frequency band. This will have a great importance when estimating the mixing matrix parameters.

For simplicity, we hereafter assume that the foreground parameters β_f that we fit for are pixel-independent (one set of β_f for the entire observed sky). The generalisation of the proposed formalism for pixel-dependent foreground parameters would be straightforward following the steps already outlined in [246]. We also note that the proposed formalism can be extended to allow for the variability of some of the detector properties across the detector arrays, thus permitting to study their impact on the experiment performance. As such arrays are envisaged for the future generation of the CMB experiments, this feature of the framework appears to us as very timely. We leave the detailed investigation of such issues to future work, and in the following we give an example of the impact of a mismatch between the model used for generating the data and the one assumed, in the case of bandpasses. In practice, the mismatch could arise as a difference between effective bandpass parameters resulting from averaging data of many detectors and a single set of idealised parameters assumed in the reconstruction.

8.1.2 Parameter estimation

The generalised data model though more involved than the standard model for multi-frequency sky maps retains all the essential features of the latter and can therefore be used in a component separation procedure. In this work, we apply it in the context of performance forecasting for future experiments, in a similar approach to the one developed in [96, 246, 95]. We discuss below essential ingredients of the method, in particular we emphasise the new features due to the specificity of the new data model.

Spectral likelihood

In this section we use the spectral likelihood introduced in section 4.2, and extend the formalism of e.g. [246] to account for instrumental parameters in addition to foregrounds parameters. For the data model Eq. (8.2), we thus define an effective spectral likelihood, that can be maximised to determine not only foreground spectral parameters, but also instrumental parameters included in the generalised mixing matrix. To achieve this, we replace the standard mixing matrix $\mathbf{A}$ by the generalised mixing matrix $\boldsymbol{\mathcal{A}}$ in the ensemble average spectral likelihood Eq. (4.18), and write the generalised spectral likelihood as:

$$\mathcal{S} = -\sum_p (\boldsymbol{\mathcal{A}}_p^t \, \mathbf{N}_p^{-1} \, \mathbf{m}_p)^t \, (\boldsymbol{\mathcal{A}}_p^t \, \mathbf{N}_p^{-1} \, \boldsymbol{\mathcal{A}}_p)^{-1} \boldsymbol{\mathcal{A}}_p^t \, \mathbf{N}_p^{-1} \mathbf{m}_p \tag{8.3}$$

where $\mathbf{N}$ is the noise covariance matrix. While ideally instrumental parameters are known with sufficient precision from a calibration campaign, this is hardly the case for most of the parameters of interest. Here, we therefore aim at determining both these sets of parameters, i.e., β_f and β_h, from the available data set via the maximisation of the spectral likelihood. Because of inherent degeneracies, this may not be always possible and some external information may be required or beneficial. We discuss a relevant extension in Sect. 8.1.2. This procedure can be applied to any specific input data set, thus providing a basis for actual data processing framework. However, in the context of performance forecasting we

are interested in quantities averaged over statistical ensembles {CMB + noise} of the possible input data sets.

Ensemble average likelihood The maximisation of the likelihood will allow us to determine the foreground parameters β_f and instrumental parameters β_h. This procedure can be repeated for any input data, in particular various noise realisations. However, instead of averaging data over various noise realisations, we average the likelihoods, and write an ensemble average likelihood as in [246, 247]:

$$\langle \mathcal{S} \rangle = -\operatorname{tr} \sum_p \{ (\mathbf{N}_p^{-1} - \mathbf{P}_p) (\langle \mathbf{s}_p \, \mathbf{s}_p^t \rangle + \mathbf{N}_p) \} \tag{8.4}$$

where $\mathbf{s}$ is the noiseless sky signal defined in Eq. (8.2), and we have introduced the projection operator $\mathbf{P}_p$:

$$\mathbf{P}_p \equiv \mathbf{N}_p^{-1} - \mathbf{N}_p^{-1} \, \boldsymbol{\mathcal{A}_p} ({\boldsymbol{\mathcal{A}_p}}^t \, \mathbf{N}_p^{-1} \, \boldsymbol{\mathcal{A}})_p^{-1} \, \boldsymbol{\mathcal{A}}_p^t \, \mathbf{N}_p^{-1}. \tag{8.5}$$

Data covariance matrix In the noiseless data covariance matrix $\langle \mathbf{s}_p \, \mathbf{s}_p^t \rangle$, we have to explicitly account for the CMB contribution due to the extra parametrisation we introduced in 8.1.1. We split $\boldsymbol{\mathcal{A}}_p$ and $\mathbf{s}_p$ into CMB and foreground parts:

$$\mathbf{s}_p \equiv \begin{bmatrix} \mathbf{s}_p^{\rm cmb} \\ \mathbf{s}_p^{\rm fg} \end{bmatrix} \tag{8.6}$$

$$\boldsymbol{\mathcal{A}} = \left[\boldsymbol{\mathcal{A}}_p^{\rm cmb}, \boldsymbol{\mathcal{A}}_p^{\rm fg} \right] \tag{8.7}$$

We thus split the data covariance matrix into its CMB and foreground contributions:

$$\langle \mathbf{s}_p \mathbf{s}_p^t \rangle = \boldsymbol{\mathcal{A}}_p^{\rm cmb} \langle \mathbf{s}_p^{\rm cmb} \mathbf{s}_p^{{\rm cmb},t} \rangle \boldsymbol{\mathcal{A}}_p^{{\rm cmb},t} + \boldsymbol{\mathcal{A}}_p^{\rm fg} \mathbf{s}_p^{\rm fg} \mathbf{s}_p^{{\rm fg},t} \boldsymbol{\mathcal{A}}_p^{{\rm fg},t}, \tag{8.8}$$

therefore assuming the uncorrelation, on average, of the CMB signal and astrophysical foregrounds. The foreground contribution (second term) is easy to compute as we consider foregrounds as templates, and thus there is no variability in their realisation. In contrast, the CMB contribution (first term) has to be estimated numerically and, as it is not diagonal, this poses implementation and performance issues.

However, if we assume that neither the mixing matrices, $\boldsymbol{\mathcal{A}}_{\mathbf{p}}$, nor the noise, $\mathbf{N}_{\mathbf{p}}$, are pixel-dependent and that the noise is white, we do not need the full multi-pixel covariance matrix for the CMB but only its single pixel version. Considering the two polarisation states Q and U,

$$\mathbf{s}_p^{\rm cmb} \equiv [\mathbf{s}_{p,Q}^{\rm cmb}, \mathbf{s}_{p,U}^{\rm cmb}], \tag{8.9}$$

the single-pixel covariance of the CMB signal $\hat{\mathbf{S}}^{\rm cmb} \equiv \langle \mathbf{s}_p^{\rm cmb} \mathbf{s}_p^{{\rm cmb},t} \rangle$ is given by:

$$\hat{\mathbf{S}}^{\rm cmb} \equiv \begin{bmatrix} \sigma_{QQ}^2 & \sigma_{QU}^2 \\ \sigma_{UQ}^2 & \sigma_{UU}^2 \end{bmatrix}, \tag{8.10}$$

which can be either calculated from the angular spectra of the CMB signals or from simulated CMB maps.

We can write the total ensemble average likelihood explicitly as:

$$\mathcal{S} = -\operatorname{tr}\left\{n_{\rm pix}\,(\mathbf{N}^{-1}-\mathbf{P})(\mathbf{F}+\mathbf{N}+\boldsymbol{\mathcal{A}}^{\rm cmb}\hat{\mathbf{S}}^{\rm cmb}\boldsymbol{\mathcal{A}}^{{\rm cmb},t})\right\}, \tag{8.11}$$

where

$$\mathbf{F} \equiv \frac{1}{n_{\rm pix}}\boldsymbol{\mathcal{A}}^{\rm fg}\sum_{\mathbf{p}}\hat{\mathbf{s}}^{\rm fg}_{\rm p}\mathbf{s}^{{\rm fg},t}_{\rm p}\boldsymbol{\mathcal{A}}^{{\rm fg},t}. \tag{8.12}$$

The total ensemble average likelihood therefore takes into account averages over noise realisations through the noise covariance matrix $\mathbf{N}^{-1}$, and over CMB realisations through the single-pixel, CMB covariance matrix $\hat{\mathbf{S}}^{\rm cmb}$. In what follows, we use Eq. (8.11) for the spectral likelihood, and therefore keep the assumption that $\boldsymbol{\mathcal{A}}$ and $\mathbf{N}$ are sky pixel independent.

Priors on instrumental parameters As mentioned earlier, we expect that not all instrumental parameters can be constrained using the actual CMB data with sufficient precision. We would therefore need to introduce calibration priors on some instrumental parameters to break degeneracies in the system and/or to ensure a tolerable level of residuals. Where appropriate, we add Gaussian priors to the ensemble average spectral likelihood as:

$$\mathcal{S}' = \mathcal{S} + \sum_{\beta_h}\frac{1}{2\sigma^2_{\beta_h}}(\beta_h-\tilde{\beta}_h)^2, \tag{8.13}$$

where $\mathcal{S}$ is the likelihood of Eq. (8.11) and σ_{β_h} is the calibration error on parameter β_h. We assume the calibration measurements to be unbiased with a 1σ error given by σ_{β_h}. The best fit value will typically be different from the true value of the parameter, denoted with $\tilde{\beta}_h$, but their difference should be within the estimated uncertainty from it, σ_{β_h}. Our prior in Eq. (8.13) is assumed to be averaged over an ensemble of calibration procedures. Consequently, it is centred at the true value of the parameter and its uncertainty is larger by a factor of 2 (in quadrature) than that of a single calibration result.

Errors on recovered parameters

Statistical errors In this approach, the maximum-likelihood values obtained by minimising Eq. (8.13) are average values, and we compute the matrix of second derivatives at the peak of the likelihood - the Hessian matrix $\mathcal{H}$:

$$\mathcal{H}_{\beta\beta'} \equiv \left\langle \frac{\partial^2\mathcal{S}'}{\partial\beta\,\partial\beta'}\Big|_{\rm peak}\right\rangle, \tag{8.14}$$

where we do not assume that the peak of the likelihood corresponds to the true values of parameters $(\tilde{\beta}_f, \tilde{\beta}_h)$. The Hessian measures the curvature of the likelihood at its peak, and is directly related to the uncertainty due to instrumental noise:

$$\boldsymbol{\Sigma} \simeq \mathcal{H}^{-1} \tag{8.15}$$

This statistical error matrix $\mathbf{\Sigma}$ can be computed analytically following Eq. (A5) in [246]:

$$\begin{aligned}\left\langle \frac{\partial^2 \mathcal{S}'}{\partial\beta\,\partial\beta'} \right\rangle = \sum_p \mathrm{tr}\Big\{ \Big[&\mathbf{P}_p\, \boldsymbol{\mathcal{A}}_{p,\beta'} \left(\boldsymbol{\mathcal{A}}_p^t \mathbf{N}_p^{-1} \boldsymbol{\mathcal{A}}_p\right)^{-1} \boldsymbol{\mathcal{A}}_{p,\beta}^t \mathbf{P}_p + \mathbf{N}_p^{-1} \boldsymbol{\mathcal{A}}_p \left(\boldsymbol{\mathcal{A}}_p^t \mathbf{N}_p^{-1} \boldsymbol{\mathcal{A}}_p\right)^{-1} \boldsymbol{\mathcal{A}}_{p,\beta\beta'}^t \mathbf{P}_p \\ &- \mathbf{N}_p^{-1} \boldsymbol{\mathcal{A}}_p (\boldsymbol{\mathcal{A}}_p^t \mathbf{N}_p^{-1} \boldsymbol{\mathcal{A}}_p)^{-1} \boldsymbol{\mathcal{A}}_{p,\beta'}^t \mathbf{N}_p^{-1} \boldsymbol{\mathcal{A}}_p (\boldsymbol{\mathcal{A}}_p^t \mathbf{N}_p^{-1} \boldsymbol{\mathcal{A}}_p)^{-1} \boldsymbol{\mathcal{A}}_{p,\beta}^t \mathbf{P}_p \\ &- \mathbf{N}_p^{-1} \boldsymbol{\mathcal{A}}_p (\boldsymbol{\mathcal{A}}_p^t \mathbf{N}_p^{-1} \boldsymbol{\mathcal{A}}_p)^{-1} \boldsymbol{\mathcal{A}}_{p,\beta}^t \mathbf{N}_p^{-1} \boldsymbol{\mathcal{A}}_p (\boldsymbol{\mathcal{A}}_p^t \mathbf{N}_p^{-1} \boldsymbol{\mathcal{A}}_p)^{-1} \boldsymbol{\mathcal{A}}_{p,\beta'}^t \mathbf{P}_p \\ &- \mathbf{N}_p^{-1} \boldsymbol{\mathcal{A}}_p (\boldsymbol{\mathcal{A}}_p^t \mathbf{N}_p^{-1} \boldsymbol{\mathcal{A}}_p)^{-1} \boldsymbol{\mathcal{A}}_{p,\beta}^t \mathbf{N}_p^{-1} \boldsymbol{\mathcal{A}}_{p,\beta'} (\boldsymbol{\mathcal{A}}_p^t \mathbf{N}_p^{-1} \boldsymbol{\mathcal{A}}_p)^{-1} \boldsymbol{\mathcal{A}}_p^t \mathbf{P}_p \Big] \langle \mathbf{s}_p \mathbf{s}_p^t \rangle \\ &+ \mathrm{transpose} \Big\}\end{aligned} \tag{8.16}$$

where we have introduced the first and second derivatives of the mixing matrix:

$$\begin{aligned}\boldsymbol{\mathcal{A}}_{p,\beta} &\equiv \frac{\partial \boldsymbol{\mathcal{A}}_p}{\partial\beta} \\ \boldsymbol{\mathcal{A}}_{p,\beta\beta'} &\equiv \frac{\partial^2 \boldsymbol{\mathcal{A}}_p}{\partial\beta\partial\beta'}\end{aligned} \tag{8.17}$$

If the assumed mixing matrix $\boldsymbol{\mathcal{A}}(\beta_f, \beta_h)$ corresponds to the true one, $\hat{\boldsymbol{\mathcal{A}}}$, for a given set of parameters (β_f, β_h) obtained from the minimisation of the spectral likelihood, $\mathbf{\Sigma}$ will be the only source of foreground residuals, by sourcing statistical residuals in the cleaned CMB map. This will increase the error on estimated cosmological parameters, without biasing estimated values [95].

Systematic errors However, if the assumed and true mixing matrices do not match, systematic residuals will be present in the cleaned CMB maps, biasing the estimated values of cosmological parameters [246]. In particular, if we assume two models, a "true" one to simulate a mock data set, and a different one to estimate parameters in the spectral likelihood, the recovered values of instrumental parameters will be biased. This sources systematic residuals in the recovered CMB maps, and eventually biases the derived cosmological parameters.

In the next section, we derive the expression of both systematic and statistical residuals for the generalised mixing matrix.

8.1.3 Residuals

Given a set of (β_f, β_h) parameters, we can compute the corresponding mixing matrix $\boldsymbol{\mathcal{A}}$ (the same for every pixel given our assumption), and estimate the noiseless sky signal [245]:

$$\hat{\mathbf{c}}_p = \left(\boldsymbol{\mathcal{A}}^t\, \mathbf{N}^{-1}\, \boldsymbol{\mathcal{A}}\right)^{-1} \boldsymbol{\mathcal{A}}^t \mathbf{N}^{-1}\, \mathbf{s}_p \equiv \mathbf{W}(\beta_f, \beta_h)\, \mathbf{s}_p, \tag{8.18}$$

where we recall that $\mathbf{s}$ is the noiseless sky signal. The noiseless residuals are defined as the difference between the reconstructed map and the true signal:

$$\mathbf{r}_p \equiv \hat{\mathbf{c}}_p \;-\; \mathbf{c}_p = \mathbf{W}(\beta_f, \beta_h)\, \mathbf{s}_p \;-\; \mathbf{c}_p \tag{8.19}$$

We consider two main contributions to the residuals: (1) statistical residuals, if parameters are not exactly the true ones because of statistical fluctuations; and (2) systematic residuals, if the foreground or instrument models are wrong, or if there is a systematic bias in the priors (miscalibration).

In parametric component separation techniques on which this framework is based [96, 246], in the absence of calibration errors, the only residuals in the CMB map are of foregrounds origin, since all CMB signal stays in the CMB channel. However, whenever the parametrisation of the CMB component is introduced, some of the CMB signal can also leak to the recovered foreground maps and thus disappear from CMB maps, leading therefore to extra residuals terms.

Rewriting Eq. (8.19) only for the CMB channel, we have:

$$\mathbf{r}_p^{\rm CMB}(\beta_f,\beta_h) = \underbrace{\mathbf{W}^0(\beta_f,\beta_h)\mathbf{F}_p}_{\text{Foregrounds residuals}} + \underbrace{\mathbf{W}^0(\beta_f,\beta_h)\mathbf{C}_p - \mathbf{c}_p^{\rm cmb}}_{\text{CMB contribution}} \tag{8.20}$$

where index 0 denotes the CMB part of the $\mathbf{W}$ operator and $\mathbf{F}_p$ (resp. $\mathbf{C}_p$) is the total foreground (resp. CMB) contribution to each frequency, gathering contributions from all mixed Stokes parameters ($\boldsymbol{\mathcal{C}}_0, \boldsymbol{\mathcal{S}}_0, \boldsymbol{\mathcal{C}}_4, \boldsymbol{\mathcal{S}}_4$) defined in Eq. (7.44).

We perform a Taylor expansion of Eq. (8.20) around the estimated best fit values for β, denoted $\hat{\beta}$:

$$\begin{aligned}\mathbf{r}_p(\beta) \simeq\ & \mathbf{W}_p^0(\hat{\beta})(\mathbf{F}_p+\mathbf{C}_p)\\ &+\sum_\beta \delta\beta \frac{\partial \mathbf{W}_p^0}{\partial\beta}\bigg|_{\hat{\beta}}(\mathbf{F}_p+\mathbf{C}_p)\\ &+\sum_{\beta,\beta'} \delta\beta\,\delta\beta' \frac{\partial^2 \mathbf{W}_p^0}{\partial\beta\,\partial\beta'}\bigg|_{\hat{\beta}}(\mathbf{F}_p+\mathbf{C}_p)\\ &-\mathbf{s}_p^{\rm cmb}\end{aligned} \tag{8.21}$$

We introduce new quantities in pixel-domain:

$$\begin{aligned}\mathbf{y}_p &\equiv \mathbf{W}_p^0(\hat{\beta})(\mathbf{F}_p+\mathbf{C}_p) - \hat{\mathbf{s}}_p^{\rm cmb}\\ \mathbf{Y}^{(1)}_{p,\beta} &\equiv \sum_\beta \frac{\partial \mathbf{W}_p^0}{\partial\beta}\bigg|_{\hat{\beta}}(\mathbf{F}_p+\mathbf{C}_p)\\ \mathbf{Y}^{(2)}_{p,\beta\beta'} &\equiv \sum_{\beta,\beta'} \frac{\partial^2 \mathbf{W}_p^0}{\partial\beta\,\partial\beta'}\bigg|_{\hat{\beta}}(\mathbf{F}_p+\mathbf{C}_p),\end{aligned} \tag{8.22}$$

so that we can rewrite Eq. (8.21) as:

$$\mathbf{r}_p(\beta) = \mathbf{y}_p + \sum_\beta \delta\beta\,\mathbf{Y}^{(1)}_{p,\beta} + \sum_{\beta,\beta'} \delta\beta\,\delta\beta'\,\mathbf{Y}^{(2)}_{p,\beta\beta'} \tag{8.23}$$

We assume that we fit for one value of β for all considered pixels, thus we can rewrite the same equation in the harmonic domain and express the total level of foreground residuals as:

$$\begin{aligned}\mathcal{C}_\ell^{\rm res} \simeq \otimes_\ell\left(\mathbf{y},\mathbf{y}\right) \,+\, \otimes_\ell(\mathbf{y},\mathbf{z}) \,+\, \otimes_\ell(\mathbf{z},\mathbf{y}) \\ +\, {\rm tr}[\mathbf{\Sigma}\otimes_\ell\left(\mathbf{Y}^{(1)}\,,\mathbf{Y}^{(1)}\right)]\end{aligned} \tag{8.24}$$

where the symbol $\otimes$ denotes the cross-spectrum of two quantities, and $\mathbf{z}$ is defined as:

$$\mathbf{z} \equiv {\rm tr}[\mathbf{Y}^{(2)}\mathbf{\Sigma}]. \tag{8.25}$$

As outlined previously, residuals are composed of two main contributions, statistical and systematic residuals, as well as a cross-term:

$$\mathcal{C}_\ell^{\rm syst.} \equiv \otimes_\ell\left(\mathbf{y},\mathbf{y}\right) \tag{8.26}$$

$$\mathcal{C}_\ell^{\rm stat.} \equiv {\rm tr}[\mathbf{\Sigma}\otimes_\ell\left(\mathbf{Y}^{(1)}\,,\mathbf{Y}^{(1)}\right)]. \tag{8.27}$$

$$\mathcal{C}_\ell^{\rm cross} \equiv \otimes_\ell\left(\mathbf{y},\mathbf{z}\right) \,+\, \otimes_\ell(\mathbf{z},\mathbf{y}). \tag{8.28}$$

In Eq. (8.28), note that the two terms are identical. It is also important to note that the derivatives of the various quantities over β refer to derivatives with respect to spectral and hardware parameters. This is necessary if we want to correctly take into account the extra terms in our model.

Moreover, concerning the CMB contribution to the residuals, we can further simplify its expression by taking into account the fact that the CMB mixing matrix $\boldsymbol{\mathcal{A}}$ - and therefore the $\mathbf{W}$ operator - does not depend on the sky pixel. We can rewrite the CMB contribution of Eq. (8.20) as:

$$\begin{aligned}\mathbf{W}^0\mathbf{C} \,-\, \mathbf{c}_{\rm cmb} &= \mathbf{W}^0\,\boldsymbol{\mathcal{A}}^{\rm cmb}\,\mathbf{c}_{\rm cmb} \,-\, \mathbf{c}_{\rm cmb} \\ &= (\mathbf{W}^0\,\boldsymbol{\mathcal{A}}^{\rm cmb} \,-1)\,\mathbf{c}_{\rm cmb}.\end{aligned} \tag{8.29}$$

This simplifies the estimation of the CMB contribution in the residuals, that can be computed using the simplified procedure described in Appendix D of [246].

8.1.4 Noise

We make the assumption that the noise is homogeneous, and under the assumption already used before that we have the same β_f for the entire sky patch that we are studying (single scaling law), the noise power spectrum in the cleaned CMB map can be expressed as in Eq. (32) of [246]:

$$\mathcal{C}_\ell^{\rm noise} = [(\boldsymbol{\mathcal{A}}^t\,\mathbf{N}_\ell^{-1}\,\boldsymbol{\mathcal{A}})^{-1}]_{\rm CMB\,X\,CMB} \tag{8.30}$$

with $\mathbf{N}_\ell$ describing the noise spectra of a single frequency map, taking their resolution into account:

$$\mathbf{N}_\ell^{ij} \equiv (w_i)^{-1}\exp\left(\ell\,(\ell+1)\,\frac{{\rm FWHM}_i^2}{8\,\log 2}\right)\delta_i^j \tag{8.31}$$

where i,j are indices of frequency bands, $(w_i)^{-1}$ is the sensitivity of band i, and ${\rm FWHM}_i$ the full width at half maximum of its beam.

8.1.5 Cosmological likelihood

Generic expression

We write the cosmological parameter likelihood, averaged over instrumental noise and CMB signal realisations as:

$$\langle S^{\rm cos} \rangle \equiv {\rm tr}\, \mathbf{C}^{-1}\mathbf{E} \,+\, \ln\det \mathbf{C} \tag{8.32}$$

where $\mathbf{C}$ is the assumed multi-pixel covariance of the cleaned CMB signal, and $\mathbf{E}$ is the multi-pixel correlation matrix of the CMB map retrieved with the component separation procedure as outlined earlier. Consequently, $\mathbf{E}$ takes into account the presence of the residuals, Eqs. (8.26), (8.27), and (8.28), and all which can be computed semi-analytically given the actual model of the data.

The assumed covariance $\mathbf{C}$ expresses the state of our knowledge about the data. In the following we will consider two cases. In the first case, the assumed covariance is that of the CMB signal only, thus ignoring entirely the effects of the component separation. We have therefore:

$$\mathbf{C} = \mathbf{C}^{\mathbf{cmb}}. \tag{8.33}$$

In the second case we assume that the statistical errors can be modelled on some level. Specifically, we assume that:

$$\mathbf{C} = \mathbf{C}^{\mathbf{cmb}} + \mathbf{C}^{\mathbf{stat.}}, \tag{8.34}$$

where $\mathbf{C}^{\mathbf{stat.}}$ is the covariance matrix of the statistical residuals $C_\ell^{\rm stat.}$ defined in Eq. (8.27). We note that sufficient information allowing for effective modelling of the statistical residuals may be indeed available either internally, in some self-consistent statistical approaches, e.g., [247], or using some external data, e.g., [207]. Hereafter, we refer to this second case as the deprojection case.

Implementation

Our implementation of the cosmological likelihood is based on the one proposed in Appendix C of [246]. The cosmological likelihood Eq. (8.32) is split into three terms:

$$\langle S^{\rm cos} \rangle = {\rm tr}\, \mathbf{C}^{-1}\hat{\mathbf{C}} \,+\, {\rm tr}\, \mathbf{C}^{-1}(\mathbf{E} - \hat{\mathbf{C}}) \,+\, \ln\det \mathbf{C}, \tag{8.35}$$

where $\mathbf{E}$ is the true (observed) signal covariance matrix. Note that when there are no systematic residuals (our main case in this work, except when we consider bandpass variation), the second term of the sum actually vanishes. As outlined in section 8.1.5, we consider two cases for the assumed signal covariance matrix: the no deprojection case, where $\mathbf{C} = \mathbf{C}^{\mathbf{cmb}}$; and the deprojection case, where $\mathbf{C} = \mathbf{C}^{\mathbf{cmb}} + \mathbf{C}^{\mathbf{stat.}}$.

No deprojection case In the no deprojection case, the three terms of the cosmological likelihood are written as:

$$\mathrm{tr}\,\mathbf{C}^{-1}\hat{\mathbf{C}} = \sum_\ell \left[\frac{(2\ell+1)}{C_\ell}\left(\hat{C}_\ell + \mathrm{tr}[\mathbf{\Sigma}\otimes_\ell(\tilde{\mathbf{Y}}^{(1)},\tilde{\mathbf{Y}}^{(1)})]\right)\right] \tag{8.36}$$

$$\mathrm{tr}\,\mathbf{C}^{-1}(\mathbf{E}-\hat{\mathbf{C}}) = \sum_\ell \left[\frac{(2\ell+1)}{C_\ell}\left(\otimes_\ell(\tilde{\mathbf{y}},\tilde{\mathbf{y}}) + \otimes_\ell(\tilde{\mathbf{z}},\tilde{\mathbf{y}}) + \otimes_\ell(\tilde{\mathbf{y}},\tilde{\mathbf{z}})\right)\right] \tag{8.37}$$

$$\ln\det\mathbf{C} = \ln\det\mathbf{C}^{\mathbf{cmb}} \tag{8.38}$$

Deprojection case In the deprojection case, we consider that we have a model for the statistical residuals, that we include in the modelled covariance matrix $\mathbf{C}$. The three terms of the cosmological likelihood then reads as (note that this case corresponds to previous implementation of the formalism, and thus the following equations are exactly equations (C9), (C10) and (C12) of [246]):

$$\begin{aligned}\mathrm{tr}\,\mathbf{C}^{-1}\hat{\mathbf{C}} = \sum_\ell \Bigg[&(2\ell+1)\frac{\hat{C}_\ell}{C_\ell}\left(1 - C_\ell^{-1}\,\mathrm{tr}[\mathbf{U}\otimes_\ell(\tilde{\mathbf{Y}}^{(1)},\tilde{\mathbf{Y}}^{(1)})]\right)\\ &+\frac{(2\ell+1)}{C_\ell}\,\mathrm{tr}[\mathbf{\Sigma}\otimes_\ell(\tilde{\mathbf{Y}}^{(1)},\tilde{\mathbf{Y}}^{(1)})]\Bigg]\\ &-\sum_{\ell,\ell'}\frac{(2\ell+1)}{C_\ell}\frac{(2\ell'+1)}{C'_\ell}\,\mathrm{tr}[\mathbf{U}\otimes_{\ell'}(\tilde{\mathbf{Y}}^{(1)},\tilde{\mathbf{Y}}^{(1)})\mathbf{\Sigma}\otimes_\ell(\tilde{\mathbf{Y}}^{(1)},\tilde{\mathbf{Y}}^{(1)})]\end{aligned} \tag{8.39}$$

$$\begin{aligned}\mathrm{tr}\,\mathbf{C}^{-1}(\mathbf{E}-\hat{\mathbf{C}}) = \sum_\ell &\left[\frac{2\ell+1}{C_\ell}\left(\otimes_\ell(\tilde{\mathbf{y}},\tilde{\mathbf{y}}) + \otimes_\ell(\tilde{\mathbf{z}},\tilde{\mathbf{y}}) + \otimes_\ell(\tilde{\mathbf{y}},\tilde{\mathbf{z}})\right)\right]\\ &-\sum_{\ell,\ell'}\frac{(2\ell+1)}{C_\ell}\frac{(2\ell'+1)}{C'_\ell}\,\mathrm{tr}\Big[\mathbf{U}\Big(\otimes_{\ell'}(\tilde{\mathbf{Y}}^{(1)},\tilde{\mathbf{y}})\otimes_\ell(\tilde{\mathbf{y}},\tilde{\mathbf{Y}}^{(1)})\\ &+\otimes_{\ell'}(\tilde{\mathbf{Y}}^{(1)},\tilde{\mathbf{y}})\otimes_\ell(\tilde{\mathbf{z}},\tilde{\mathbf{Y}}^{(\mathbf{1})}) + \otimes_{\ell'}(\tilde{\mathbf{Y}}^{(1)},\tilde{\mathbf{z}})\otimes_\ell(\tilde{\mathbf{y}},\tilde{\mathbf{Y}}^{(\mathbf{1})})\Big)\Big]\end{aligned} \tag{8.40}$$

$$\ln\det\mathbf{C} = \ln\frac{\det\mathbf{C}^{\mathbf{cmb}}}{\det\mathbf{U}}, \tag{8.41}$$

where we have introduced $\mathbf{U}$ as defined in Eq. (C1) in [246]:

$$\mathbf{U} \equiv \left(\mathbf{\Sigma}^{-1} + \tilde{\mathbf{Y}}^{(1)\dagger}\mathbf{C}^{\mathbf{cmb}}\tilde{\mathbf{Y}}^{(1)}\right)^{-1} \tag{8.42}$$

8.2 Results

Now that we have fully described the formalism we propose, we use it in a realistic instrumental configuration and parametrisation, presented in section 8.2.1. We consider various sets of parameters and discuss uncertainties and degeneracies on parameters in these various cases in section 8.2.2. Once we have assessed degeneracies in the system and introduced the necessary priors, we finally estimate foreground residuals and forecast their impact on the determination of the tensor-to-scalar ratio r, as described in section 8.2.3. The overview of this procedure is summarised on Figure 8.1. Finally, we discuss our results and their implications for calibration and data analysis in section 8.2.4.

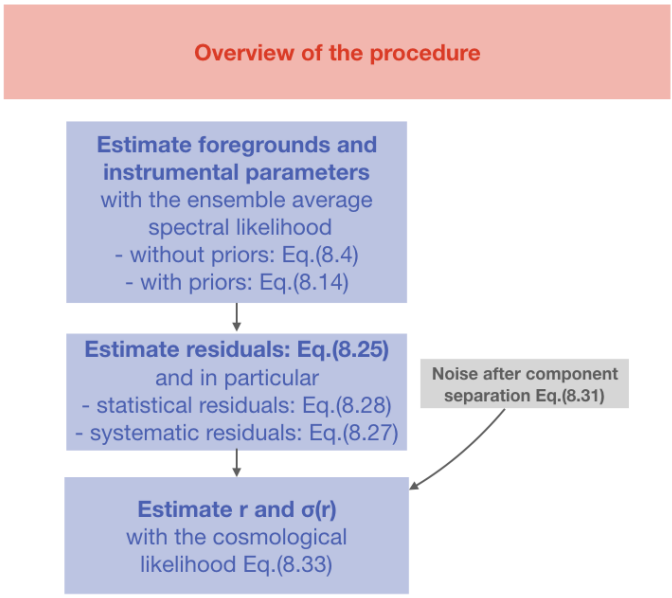

Figure 8.1 – Overview of the mains steps of the procedure we follow in this section. We apply these steps in several instrumental configurations and for various values of cosmological parameters, and discuss results and implications.

8.2.1 Configuration

The framework presented here is very flexible and could be adapted to a broad range of experiment designs. We demonstrate it in the case of a typical, ground-based, Stage 3 CMB polarisation experiment. The configuration and parameters we use are motivated by the publicly available Simons Observatory design [269]. However, some additional simplifications and assumptions are made whenever necessary to highlight some of the features of the proposed formalism. We emphasise that forecasting the performances of any particular experiment is not our goal at this stage, and we use this setup merely for demonstrative purposes, leaving applications to specific experiments to future work.

Telescopes and frequency bands

As outlined many times in this manuscript, to enable component separation, modern CMB polarisation experiments typically deploy several instruments to trace foregrounds at different frequencies, so that we can disentangle them from the CMB signal. In most of ground-based experiments, these frequency bands are grouped by two on the same focal plane, hence the use of an achromatic HWP that has to accommodate two different observing frequencies in the same optics tube. Following the Simons Observatory configuration [269], we consider three telescopes, whose frequency coverage is as follows:

- Low Frequency (LF) telescope: frequency bands centred at 27 and 39 GHz;
- Mid Frequency (MF) telescope: frequency bands centred at 93 and 145 GHz;
- Ultra-High Frequency (UHF) telescope: frequency bands centred at 225 and 280 GHz.

We model input noise covariance matrices in the pixel domain as

$$\mathbf{N}_p^{ii} = w_i^{-1}, \tag{8.43}$$

with w_i^{-1} the sensitivity of the corresponding frequency band i. We use the publicly available sensitivity calculator[1] to compute realistic instrumental sensitivities corresponding to the frequency coverage.

HWP

HWP design For each telescope (LF, MF, UHF), we consider a typical 3-layer achromatic HWP, and that only the central layer is rotated with respect to the reference frame of the instrument, i.e. $\alpha_1 = \alpha_3 = 0$, as for example in [126]. This typical choice of angle is driven by the maximisation of transmitted power and is known as Pancharatnam design [198].

The Mueller matrix of the HWP that we consider can be written as:

$$\mathbf{M}_{\rm HWP} = \mathbf{M}_{\rm layer}\mathbf{R}(-2\alpha_2)\mathbf{M}_{\rm layer}\mathbf{R}(2\alpha_2)\mathbf{M}_{\rm layer}, \tag{8.44}$$

with $\mathbf{M}_{\rm layer}$ defined as in Eq. (7.5). The Mueller matrix of a single layer is parametrised by δ (Eq. (7.6)). As already pointed out in section 7.1.1, once the bi-refringent material is chosen, δ depends on the observing frequency and thickness of each layer $\theta_{\rm hwp}$. For a given HWP, we assume all layers to be identical, and parametrise $\mathbf{M}_{\rm layer}$ with only one thickness $\theta_{\rm hwp}$.

Based on existing optimised parameters [180] and proposed designs [269, 239, 126], we choose the following nominal values for HWP parameters:

- $\theta_{\rm hwp}({\rm LF}) = 14.36$ mm
- $\theta_{\rm hwp}({\rm MF}) = 3.8$ mm
- $\theta_{\rm hwp}({\rm UHF}) = 1.86$ mm
- $\alpha_2 = 58°$

We note here that $\theta_{\rm hwp}$ is different for each telescope since the thickness is adapted to the frequency range of observations, when α_2 is in principle the same. However, to account for possible fabrication and/or calibration differences between HWP, we let α_2 vary independently for each of the telescopes when fitting for parameters (although they have the same nominal value).

Mueller matrix coefficients In Eqs. (7.25 - 7.32), we expressed the coefficients of the full optics chain Mueller matrix, as a function of HWP Mueller matrix coefficients $\boldsymbol{\mu}_{ij}$. These coefficients can be computed from Eq. (7.7) for any HWP configuration. We give here the full analytical expression of these coefficients in the instrumental configuration described above. We consider two hardware parameters per HWP:

- α_2: central layer rotation angle;

[1] `SO_Noise_Calculator_Public.py` available in the supplementary material of `https://simonsobservatory.org/publications.php`

- $\theta_{\rm hwp}$: thickness of one layer.

For clarity reasons, we express coefficients $\boldsymbol{\mu}_{ij}$ as a function of δ, defined as in Eq. (7.6), but we emphasise that the physical parameter that sets HWP behaviour is really $\theta_{\rm hwp}$. We can then express the HWP Mueller matrix coefficients as:

$$\begin{aligned}
\boldsymbol{\mu}_{11} &= \cos^2(2\alpha_2) + \cos(\delta)\,\sin^2(2\alpha_2) \\
\boldsymbol{\mu}_{12} &= \boldsymbol{\mu}_{21} = \sin(2\alpha_2)\,\cos(2\alpha_2)\left[\cos^2(\delta) - \cos(\delta)\right] - \sin^2(\delta)\,\sin(2\alpha_2) \\
\boldsymbol{\mu}_{22} &= \cos^2(\delta)\,\sin^2(2\alpha_2) + \cos^3(\delta)\,\cos^2(2\alpha_2) \\
&\quad - \left[2\sin^2(\delta)\,\cos(\delta)\,\cos(2\alpha_2) + \sin^2(\delta)\,\cos(\delta)\right]
\end{aligned} \tag{8.45}$$

Although we choose a specific instrumental configuration here, we emphasise that the proposed framework can easily be adapted to another HWP configuration by taking the corresponding $\boldsymbol{\mu}_{ij}$, for example for an HWP with more than 3 layers, as proposed for the LiteBIRD mission which will have 9 layers on its low-frequency telescope [150], or even by including a Mueller matrix modelled as measured in a laboratory, as it was done in e.g. [239].

Bandpasses

We parametrise each bandpass by two parameters: its centre ν_0 and its half-width $\Delta\nu$. We use nominal 30% bandwidths, so we have $\Delta\nu = 0.15 \times \nu_0$. We use this relation to fix bandwidths in the data model, but allow ν_0 and $\Delta\nu$ to vary independently in the fit.

We model the bandpass as top-hat function with smoothed edges as shown in Figure 8.2. The analytic expression of the bandpass $\mathcal{B}(\nu)$ as a function of ν_0 and $\Delta\nu$ is

$$\mathcal{B}(\nu) = \exp\left[-\left(\frac{|\nu - \nu_0|}{\Delta\nu}\right)^{20}\right]. \tag{8.46}$$

Realistic parametric modelling of bandpasses can be complex because true bandpasses are never as regular as the one shown in Figure 8.2. The proposed model has the advantage of being simple and fully analytic, and thus allows us to efficiently explore the impact of the two main bandpass characteristics: its centre and width.

In addition, we model a slowly varying bandpass for our data as:

$$\mathcal{B}'(\nu) = \mathcal{B}(\nu) \times \left[1 - a \times \sin\left(b \times 2\pi\nu\right)\right], \tag{8.47}$$

where $\mathcal{B}(\nu)$ is the bandpass defined in Eq. (8.46), and a and b are respectively the amplitude and frequency of the variation, as shown in Figure 8.2.

In section 8.2.3, we use such a model to generate input data, but we keep the simple model of Eq. (8.46) when computing the mixing matrix for the data likelihood. As pointed out in section 8.1.3, introducing a mismatch between the data and its model will result in systematic residuals in reconstructed maps. In particular, we explore the impact of various a and b values on systematic residual levels and cosmological parameters.

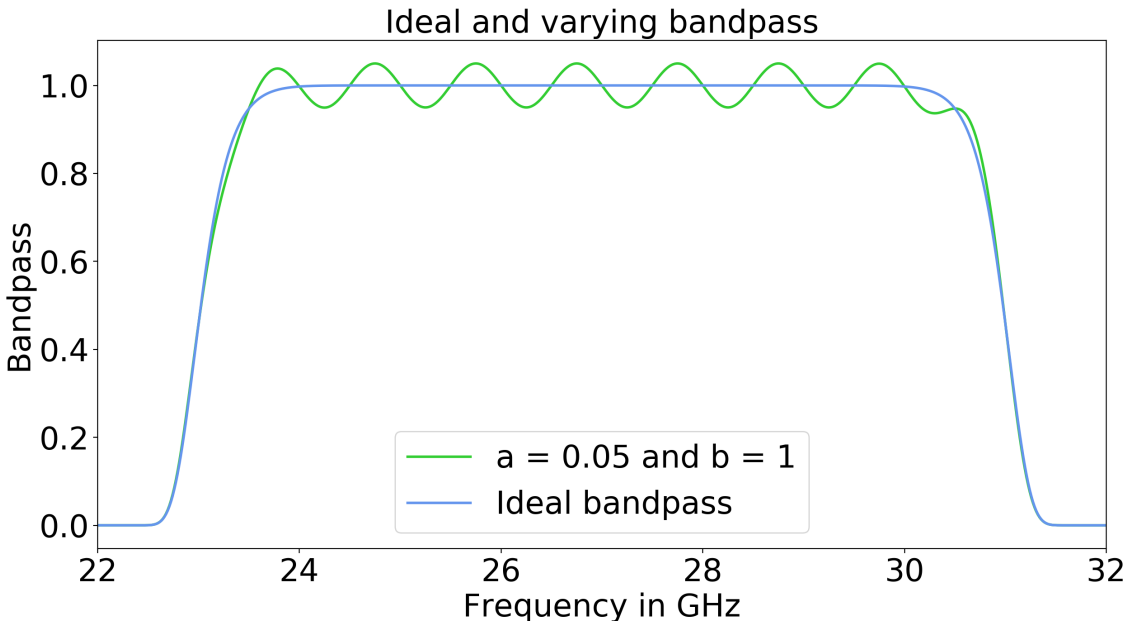

Figure 8.2 – Ideal bandpass (blue), defined in Eq. (8.46), and varying bandpass (green), defined in Eq. (8.47). We first use the ideal bandpass in both data and model, and then we introduce a varying bandpass in data only, to study the impact of this mismatch on systematic residuals.

		LF		MF		UHF	
		LF1	LF2	MF1	MF2	UHF1	UHF2
HWP	α_2	58°		58°		58°	
	$\theta_{\rm hwp}$	14.36 mm		3.8 mm		1.86 mm	
Bandpass (GHz)	ν_0	27	39	93	145	225	280
	$\Delta\nu$	4.05	5.85	13.95	21.75	33.75	42.0

Table 8.1 – Nominal values of instrumental parameters

Summary of instrumental parameters

Table 8.1 summarises all the parameters that we consider in this model, and their nominal values. We recall here that all parameters are independent and can vary when we minimise the likelihood of Eq. (8.13).

In this work, we do not study the impact of varying sinuous antennas parameters. They can easily be included in our framework as we presented in section 7.1.2, but we limit ourselves here to HWP and bandpass parameters. Similarly, although beam modelling and beam systematics could also be investigated within this framework, we leave this for future work and do not assume any beam smoothing of input maps. Note that beam smoothing is taken into account in the harmonic domain when we estimate the noise after component separation in Eq. (8.31). Again, beam sizes that we adopt here correspond roughly to the Simons Observatory ones [269].

Noise parameters

We take noise into account through the noise covariance matrix in the ensemble average spectral likelihood. In this approach, we therefore do not include a noise realisation in input maps. We consider only white noise, and take the following map sensitivities:

	LF1	LF2	MF1	MF2	UHF1	UHF2
Sensitivity in μK.arcmin	49.9	30.9	3.81	4.81	9.13	23.4

Table 8.2 – Map white noise levels

The noise covariance matrix is computed from these map levels as in Eq. (8.43), taking into account the map resolution.

Map parameters

To compute the RMS of the CMB signal covariance, we compute the fiducial CMB power spectra with `CAMB`[2] using Planck 2018 cosmological parameters [215]. We then simulate 100 realisations of the sky with the `synfast` function of the `healpy` package [287], and compute $\hat{\mathbf{S}}^{\rm cmb}$ as defined in Eq. (8.10).

We use the `PySM` package [271] to generate foreground maps, and choose the following reference frequency for foreground templates:

$$\nu_{0,\rm sync.} = 70\,\rm GHz, \qquad \nu_{0,\rm dust} = 353\,\rm GHz \tag{8.48}$$

We fix the dust temperature at $T_d = 19.6$ K, and for dust and synchrotron spectral indices nominal values we use:

$$\beta_d = 1.59, \qquad \beta_s = -3.1. \tag{8.49}$$

We take constant foreground parameters across the sky, although the effect of varying spectral parameters could be included within our framework. For details we refer the reader to [246].

`PySM` uses the `healpy` implementation of the HEALPix pixelisation scheme [3], and we use `nside` = 256 throughout this work. We use a mask corresponding to $\sim 10\%$ of the sky, corresponding to the SO SAT mask, as shown in Figure 8.3. When it comes to power spectrum reconstruction, we therefore consider multipoles from $\ell = 30$ to $\ell = 511$, given the limitation by the mask at low ℓ, and by the pixel size at high ℓ.

We consider two cosmological parameters, the tensor-to-scalar ration r which sets the amplitude of primordial B modes:

$$C^{BB}_{\ell,\,\rm primordial} = r \times C^{BB}_{\ell,\,\rm primordial}(r = 1), \tag{8.50}$$

[2] https://camb.readthedocs.io/en/latest/

[3] https://healpix.sourceforge.io/

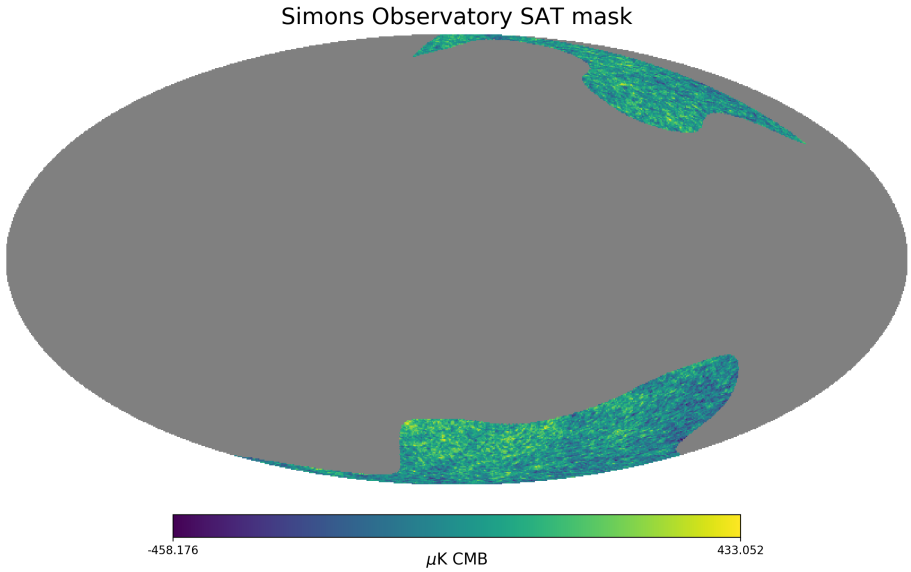

Figure 8.3 – Simons Observatory SAT mask on the CMB temperature map

and the lensing parameter which sets the delensing amplitude ($A_L = 1$ corresponds to no delensing and $A_L = 0$ corresponds to full delensing):

$$C^{BB}_{\ell,\,\mathrm{lensing}} = A_L \times C^{BB}_{\ell,\,\mathrm{lensing}}(A_L = 1). \tag{8.51}$$

We choose

$$r = 0, \qquad A_L = 1, \tag{8.52}$$

as our fiducial case. We explore other cases in section 8.2.3.

Finally, as we aim at modelling a ground-based experiment, we consider that sky only modulated terms, i.e. $\mathcal{C}_0$ and $\mathcal{S}_0$ in our model, can not be used due to atmospheric noise that dominates in this frequency regime [155, 253]. In what follows, we therefore use only $\mathcal{C}_4$ and $\mathcal{S}_4$, both in the simulated data and in the model. However, we point out that for a space mission such as LiteBIRD, it could be possible to recover all four mixed Stokes components.

8.2.2 Optimisation of the generalised spectral likelihood

In this section, we explore the parameter space described in the previous section: 18 instrumental parameters (6 for the HWPs and 12 for the bandpasses), as well as 2 foreground spectral parameters β_s and β_d. We start by fixing all instrumental parameters to their nominal values, and we only estimate foreground parameters, β_d and β_s, as in the Simons Observatory forecast study [269]. This constitutes our baseline scenario for uncertainties, residuals and bias on r, and we compare results obtained when estimating instrumental parameters to this case. We then gradually introduce instrumental parameters, as free parameters of the spectral likelihood Eq. (8.11). We do not consider priors in first instance, but will introduce them for specific cases when, and only if, it becomes necessary.

We consider the following cases, and corresponding abbreviations to identify them throughout this work:

- Spectral Energy Distribution (SED) parameters (foreground spectral indices) only
  $\rightarrow$ SED only
- SED + HWP central layer angle for all three HWP
  $\rightarrow$ SED + α_2
- SED + HWP layer thickness for all three HWP
  $\rightarrow$ SED + $\theta_{\rm hwp}$
- SED + HWP central layer angle + HWP layer thickness for all three HWP
  $\rightarrow$ SED + HWP
- SED + Band centres for all bandpasses
  $\rightarrow$ SED + ν_0
- SED + Bandwidths for all bandpasses
  $\rightarrow$ SED + $\Delta\nu$
- SED + Band centres + Bandwidths for all bandpasses
  $\rightarrow$ SED + Bandpass
- SED + All the above
  $\rightarrow$ SED + All

Method

For each case, once the generalised spectral likelihood is optimised, we compute the Hessian matrix $\mathcal{H}$ as defined in Eq. (8.14) at the peak of the likelihood. We compare the one-dimensional spectral likelihood where we fix all parameters but one to their nominal value, to a Gaussian function whose variance is determined by the diagonal of the Hessian matrix (i.e. the conditional uncertainty):

$$\sigma_i = \frac{1}{\sqrt{\mathcal{H}_{ii}}} \tag{8.53}$$

for any parameter i. We also compute the eigenvalues and eigenvectors decomposition of the Hessian matrix, to test for the presence of possible ill-conditioned directions or degeneracies in the considered parameter space.

Finally, we evaluate the error bars on spectral parameters using the diagonal of the inverse of the Hessian matrix $\mathbf{\Sigma}$, as defined in Eq. (8.14-8.15) (i.e. the marginalised uncertainty):

$$\sigma(\beta_i) = \sqrt{\mathbf{\Sigma}_{\beta_i,\beta_i}} \tag{8.54}$$

The errors on instrumental and foreground parameters are of primary importance as they determine the amplitudes of both statistical and systematic residuals, directly impacting our estimates of r. Generically, we expect that uncertainty on these parameters will increase as we increase the number of free instrumental parameters.

We emphasise however that there are fundamental differences in the way the data constraint both these types of parameters and what number of parameters

can be constrained. Indeed, the foreground parameters are usually specific to a sky component, be that dust or synchrotron, and therefore tend to affect only a single column of the generalised mixing matrix. In contrast, the instrumental parameters are rather frequency channel specific and determine the rows of the matrix. As a consequence, the constraints on the instrumental parameters do not benefit from the multi-frequency information as much as do the foreground parameters. In particular, the quality of the constraints do not improve with the increasing number of frequency bands (while the number of parameters will typically increase). In the simple case of instrumental parameters specific to only a single frequency channel, we expect that only one such parameter can be well constrained with the data. In fact, as we measure several mixed-Stokes maps per frequency channel (2 in this work, 4 in the general model), more parameters can be constrained but with significantly lower (and typically insufficient) precision. If instrumental parameters are relevant to more than a single frequency channel the number of potentially well constrained parameters increases. We note that these analytic insights are fully borne-out by our numerical results as we discuss in the following section.

SED only

We first apply the proposed method to the simplest case, considering only spectral parameters. We verify that the amended spectral likelihood behaves as expected, and that we are able to recover values of spectral parameters with a good precision. As shown in Figure 8.4, the one dimensional likelihood (all parameters fixed, but one) can be described by the Gaussian approximation, with a width estimated by the Hessian matrix. Uncertainties on spectral parameters in this case constitute our baseline scenario, and, in the following, we compare results obtained when considering broader a parameter space to these values, as shown in Figure 8.6 and Table 8.4.

HWP parameters

We then consider the following cases, involving only HWP parameters:

- SED + α_2
- SED + $\theta_{\rm hwp}$
- SED + HWP

In all these cases, we show an excellent agreement between the curvature of the one dimensional likelihood at the peak and the Gaussian approximation. This validates the approach to use the Hessian matrix as a measure of statistical uncertainty on recovered parameters, even in multi-parameter cases.

Moreover, we show, by computing its eigenvalues, that the Hessian matrix is positive definite, and find that in all these cases the parameters are well constrained, and that there are no degeneracies in the parameter space. We then compute the marginalised uncertainty on spectral parameters (defined in Eq. (8.54)) in these various cases. We find that there is no significant increase of the marginalised

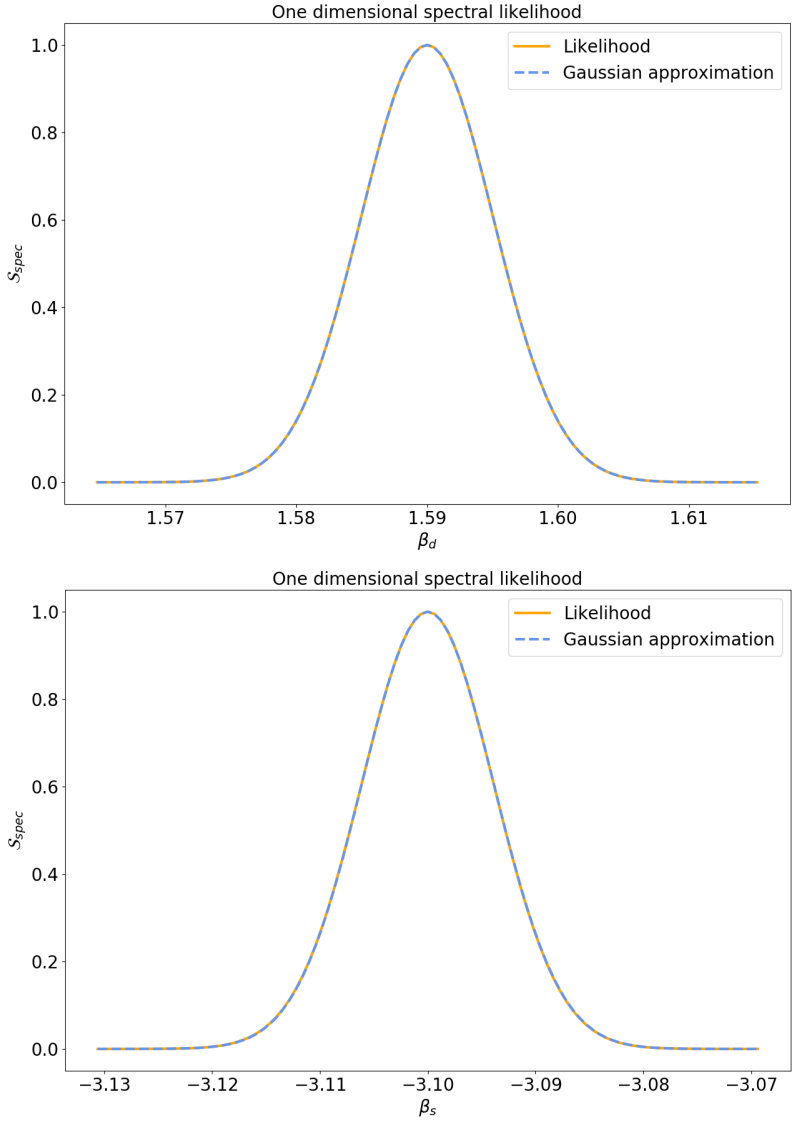

Figure 8.4 – One dimensional spectral likelihood for β_d (top) and β_s (bottom). We show that the Gaussian approximation given by the Hessian matrix describes very well the likelihood at its peak, in a one dimensional case. Note that the distribution does not need to be fully Gaussian, as long as it is the case close the peak, as it is here.

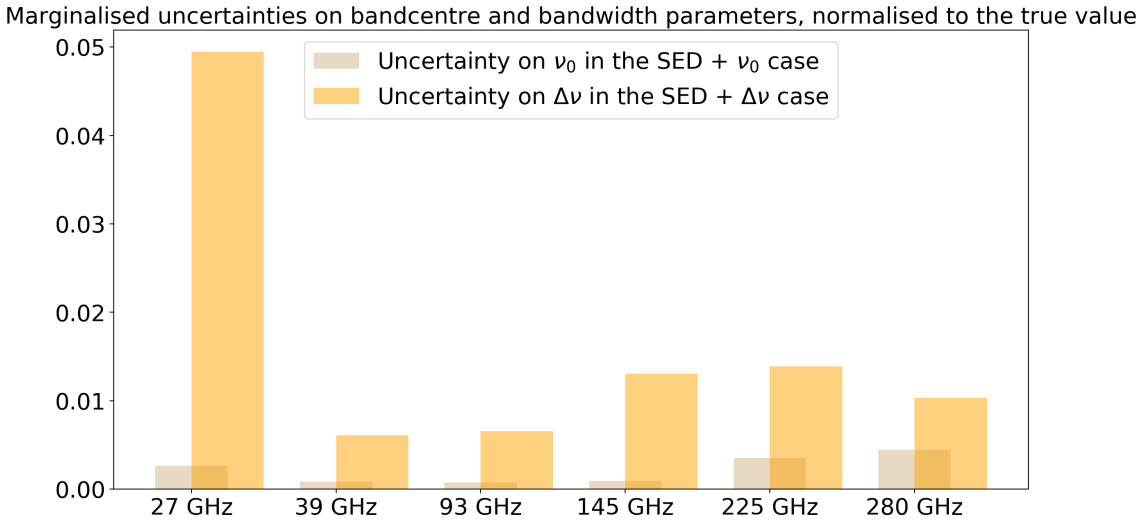

Figure 8.5 – 1-σ marginalised uncertainties on band centres ν_0 and bandwidths $\Delta\nu$, normalised to their true values. Uncertainties on bandwidths are larger than the ones on band centres, indicating that these parameters are less well constrained compared to band centres. For clarity reasons, we show here uncertainties with priors, but results are also true in the no-prior case.

uncertainty on spectral indices when adding HWP parameters compared to the {SED only} case, as shown in Table 8.4 and Figure 8.6.

We thus expect that when only HWP parameters are considered, the impact on foreground residuals and r estimation should be limited, as we will demonstrate in section 8.2.3. We therefore conclude that none of these cases would need priors to properly constrain HWP parameters.

Bandpass parameters

Having validated our framework with HWP parameters, we now consider bandpass parameters and investigate first the following cases:

- SED + ν_0
- SED + $\Delta\nu$
- SED + Bandpass

Without priors When considering either band centres or bandwidths in addition to foreground parameters (i.e {SED + ν_0} and {SED + $\Delta\nu$}), the system is not degenerate: its Hessian matrix is still formally positive definite as all eigenvalues are strictly positive. As shown in Figure 8.6 and Table 8.4, there is however a non negligible increase of the uncertainties on spectral parameters, especially β_d, when considering band centres ν_0. In contrast, instrumental parameters are better constrained for band centres ν_0 than for bandwidths $\Delta\nu$, as shown in Figure 8.5. This has an impact on the shape of foreground residuals as we will show in the next section.

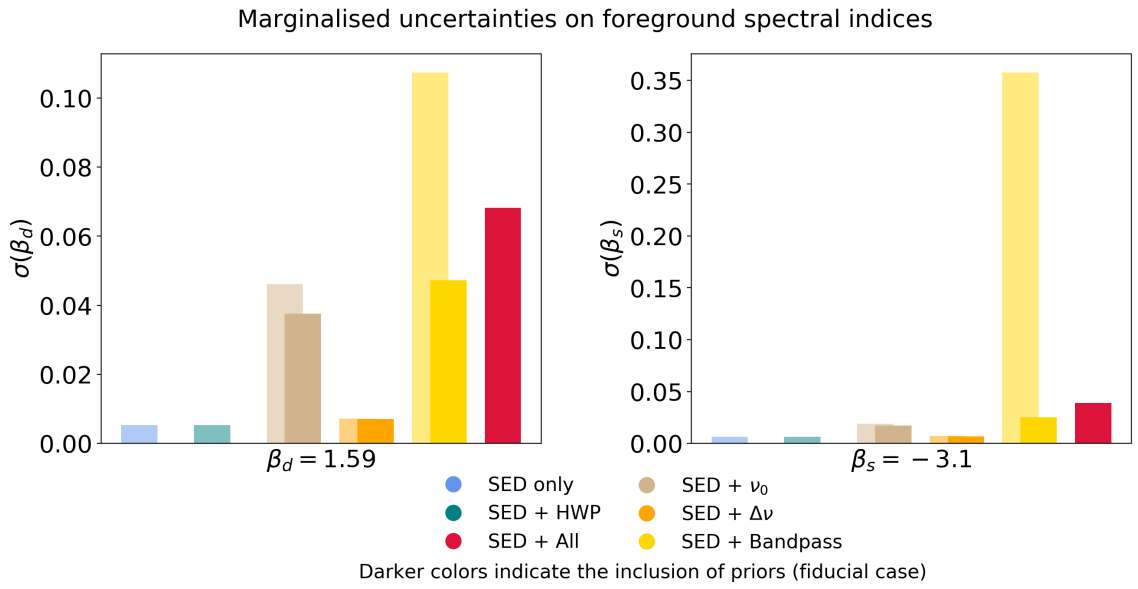

Figure 8.6 – Marginalised 1-σ uncertainties on foreground spectral indices. The inclusion of HWP parameters has a negligible impact on the uncertainty on spectral parameters, which is why we do not consider the inclusion of priors. However, the effect is much more important when including bandpass parameters, hence the inclusion of priors. The uncertainty on spectral parameters when considering only ν_0 or $\Delta\nu$ does not change much when adding priors, as shown in Table 8.4. However, we show that adding priors when all bandpass parameters are considered is required to limit uncertainty on foreground parameters and avoid degeneracies for instrumental parameters. In the case when all parameters (foregrounds, HWP and bandpass) are considered, priors are necessary because the system is otherwise degenerate.

Moreover, when adding all bandpass parameters together in the case {SED + Bandpass}, we expect the system to be degenerate as we do not have enough data to constrain 14 parameters (12 bandpass parameters + 2 spectral parameters). In this case indeed, the uncertainty on both spectral parameters and instrumental parameters increases significantly. The Hessian matrix is still positive definite, but some eigenvalues are numerically zero, with eigenvalues ranging from 10^4 to 10^{-2}. As expected, the marginalised errors on spectral parameters largely increase in this case, as shown in Figure 8.6 and Table 8.4.

Even in this latter case, the spectral likelihood is still well approximated by a Gaussian when we allow a single parameter to vary. However, for a given bandpass, its band centre and bandwidth are degenerate: the system is poorly constrained, and uncertainties on recovered parameters increase. This is well illustrated by the elongated shape of the likelihood in a 2d space where we consider ν_0 and $\Delta\nu$ for the same bandpass, as shown in Figure 8.7. To clearly see this degeneracy, the spectral likelihood is computed over only 100 random sky pixels (compared to 80,068 pixels in other results).

We thus show that adding bandpass parameters largely increases uncertainties on both spectral and instrumental parameters, while they still were at level comparable to the SED only case for HWP parameters. As outlined before, we therefore consider the inclusion of priors coming from bandpass calibration to

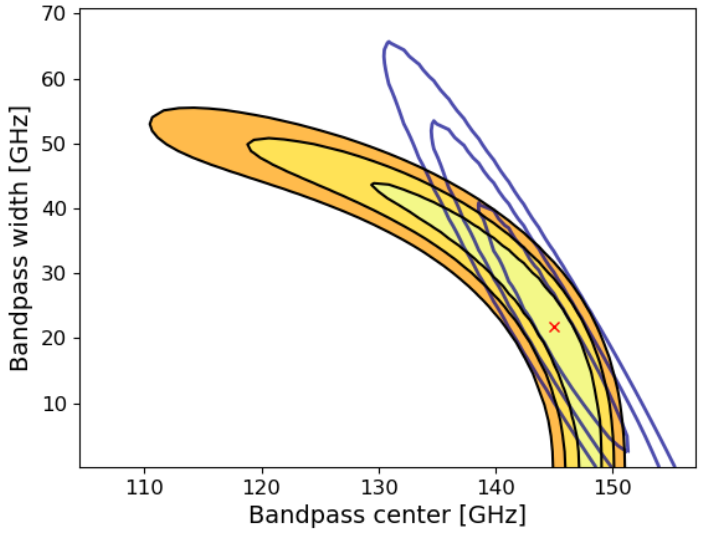

Figure 8.7 – Two-dimensional gridding of the generalised spectral likelihood, Eq. (8.11), estimated from 100 random sky pixels. We overplot in blue the Gaussian approximation given by the Hessian matrix, and show that in this case it fails to describe the likelihood. The red cross indicate true values of parameters.

alleviate this issue.

With priors To remove bandpass-associated degeneracies in the parameter space, we introduce Gaussian priors on ν_0 and $\Delta\nu$ as proposed in Eq. (8.13). The eigenvalue decomposition of the Hessian matrix allows us to decide which instrumental parameters should be constrained with priors. The lowest eigenvalues of the Hessian matrix are associated with eigenvectors combining bandpass parameters - both band centres and bandwidths, as shown in Figure 8.8. It is expected as we outlined above that, for a given bandpass, its width and centre are degenerated as shown in Figure 8.7.

In the absence of calibration data, we propose to test three levels of priors:

- Pessimistic: 5% on ν_0 and 8% on $\Delta\nu$;
- Fiducial: 1% on ν_0 and 5% on $\Delta\nu$;
- Optimistic: 0.5% on ν_0 and 1% on $\Delta\nu$.

The corresponding uncertainties on spectral parameters for these different choices are listed on Table 8.3. We also show uncertainties with and without priors on Figure 8.6 for the fiducial case. Priors are efficient to reduce uncertainties in all considered cases, but their effect is most sensitive when we consider all bandpass parameters, as expected since the system is otherwise almost degenerate.

Moreover, we note that introducing priors allows to reduce the range of eigenvalues by one to two orders of magnitude (depending on the level), demonstrating that priors are efficiently reducing degeneracies of the Hessian matrix.

	Priors	$\sigma(\beta_d = 1.59)$	$\sigma(\beta_s = -3.1)$
SED + Bandpass	No	0.108	0.358
	Pessimistic	0.0690	0.0419
	Fiducial	0.0472	0.0249
	Optimistic	0.0281	0.0161

Table 8.3 – Marginalised 1-σ uncertainties on spectral parameters when considering bandpass parameters for different choices of priors.

When it comes to the level of priors, even poorly constraining ones allow for a significant reduction of marginalised uncertainties on spectral parameters. However, the change in eigenvalues is not significant between pessimistic and fiducial cases, although it is better than in the no prior case. In what follows, unless otherwise specified, we choose to keep fiducial values as our nominal level of priors, as they are closer to currently achieved calibration performances.

This choice of priors is indeed achievable at least in the cases of limited numbers of detectors, for instance compared to calibration performances currently achieved with a Fourier Transform Spectrometer (FTS) on a typical CMB experiment. Accuracy of such measurements has been demonstrated to be at the level of 1 GHz for the POLARBEAR experiment [177] for example. Future experiments such as LiteBIRD will even require higher accuracy on bandpass calibration, up to 0.2 GHz [107], so priors at the level we propose should not be a limiting factor for future analysis.

Overall, this shows that the inclusion of priors is necessary and efficient to reduce marginalised uncertainties and lift degeneracies in the multi-parameter space. The level we propose is achievable with current calibration strategies. We also show in the next section that it reduces foreground residuals and bias on r.

All parameters

After including priors for bandpass parameters, we finally consider all instrumental parameters together in addition to foreground parameters:

- SED + All

In this case, if we do not include priors, the Hessian matrix is degenerate since it has a wide range of eigenvalues, and several of them are numerically zero, including a negative one, as shown in Figure 8.8. This is expected given the large number of parameters. We therefore once again include priors on bandpass parameters at the level discussed in the previous section, which suppresses the degeneracy as shown in Table 8.4. In the follow-up, unless otherwise specified, we always consider fiducial priors on bandpass parameters for the case {SED + All}.

Summary

In this first part of our work, we have studied parameter space degeneracies as well as statistical uncertainties on spectral parameters estimated by the Hessian matrix at the spectral likelihood peak. We showed that we can estimate

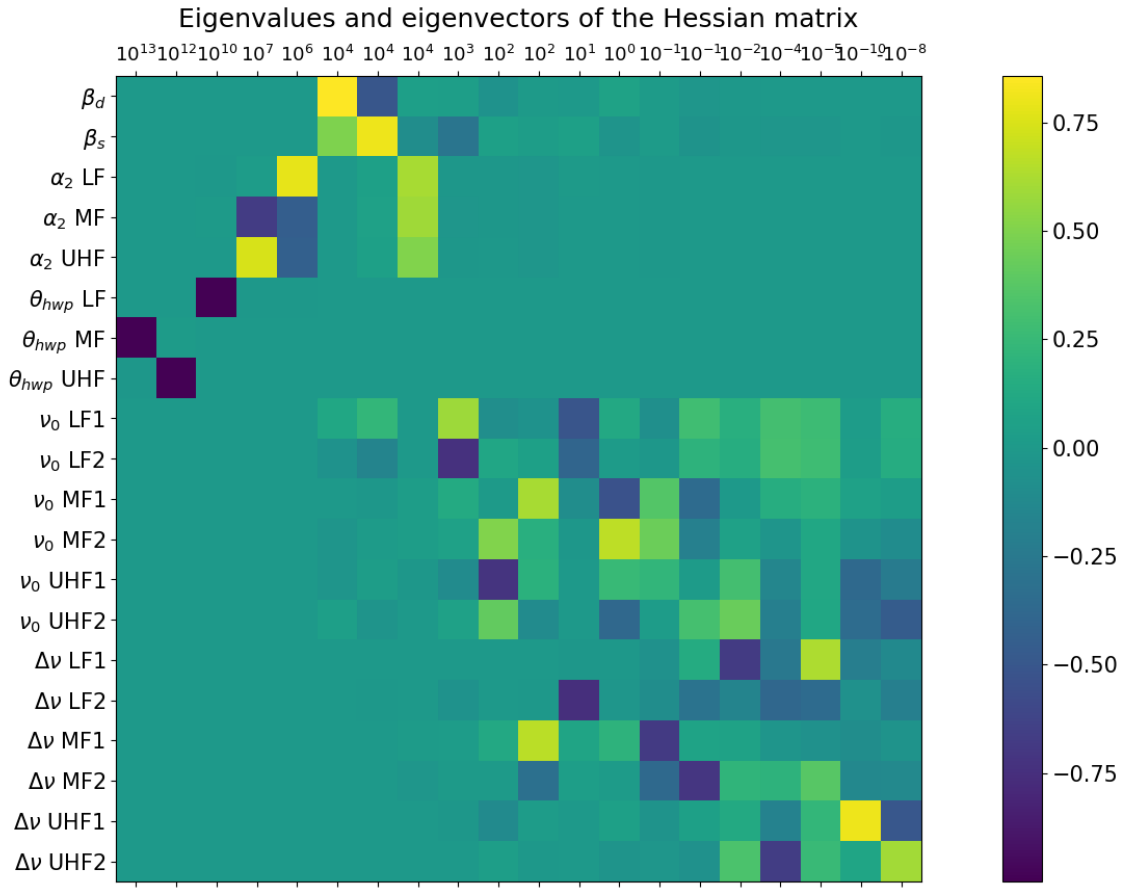

Figure 8.8 – Eigenvectors of the Hessian matrix, normalised to one, in the {SED + All} case, without priors. Each column of this matrix corresponds to one eigenvector, that is a linear combination of the parameters indicated on the vertical axis. On the horizontal axis, we quote orders of magnitude of eigenvalues associated with each eigenvector. We show that poorly constrained eigenvectors, i.e. the ones associated with low eigenvalues (on the right), correspond to combinations of bandpass parameters (both band centre and bandwidth). In particular, some of these eigenvalues are numerically zero, and the last one is negative, indicating degeneracies in the bandpass parameter space that calls for the inclusion of priors.

	Priors	$\sigma(\beta_d = 1.59)$	$\sigma(\beta_s = -3.1)$
SED only	No	5.291×10^{-3}	6.420×10^{-3}
SED + α_2	No	5.292×10^{-3}	6.423×10^{-3}
SED + $\theta_{\rm hwp}$	No	5.292×10^{-3}	6.422×10^{-3}
SED + HWP	No	5.300×10^{-3}	6.444×10^{-3}
SED + ν_0	No	4.609×10^{-2}	1.890×10^{-2}
SED + ν_0	**Yes**	3.761×10^{-2}	1.736×10^{-2}
SED + $\Delta\nu$	No	7.155×10^{-3}	7.129×10^{-3}
SED + $\Delta\nu$	**Yes**	7.014×10^{-3}	6.538×10^{-3}
SED + Bandpass	No	1.074×10^{-1}	3.577×10^{-1}
SED + Bandpass	**Yes**	4.721×10^{-2}	2.493×10^{-2}
SED + All	No	Degenerate	Degenerate
SED + All	**Yes**	6.825×10^{-2}	3.903×10^{-2}

Table 8.4 – Summary of 1-σ marginalised uncertainties on spectral parameters. Priors refer to the fiducial case: 1% on band centres (ν_0) and 5% on bandwidths ($\Delta\nu$).

HWP parameters with no significant increase of marginalised uncertainties, and without adding priors. This is because HWP parameters apply to more than one frequency band, and therefore we have enough leverage to constrain them. However, when it comes to bandpass parameters, we showed that it is necessary to introduce priors on both band centres and bandwidths to avoid degeneracies in the parameter space and maintain marginalised error bars on spectral parameters at a level at least comparable to the SED only case. This is due to the fact that we have two bandpass parameters (bandwidth and band centre) for only one frequency band, and therefore these two parameters are degenerate. In what follows, unless otherwise specified, we keep the following priors on bandpass parameters anytime these parameters are estimated: 1% on ν_0 and 5% on $\Delta\nu$.

Overall, and as we could have expected, we show that the more parameters we consider in the spectral likelihood, the higher statistical uncertainties. This will have an impact on the level of foreground residuals and estimation of r, as we will now demonstrate. All results are summarised in Table 8.4.

8.2.3 Residuals and constraints on tensor-to-scalar ratio

In this section, after optimising the generalised spectral likelihood Eq. (8.11-8.13) (without and with priors respectively) and fitting for both spectral and instrumental parameters, we reconstruct sky maps, estimate foreground residuals, and finally estimate their impact on the tensor-to-scalar ratio r.

Impact on foreground residuals

We compute foreground residuals following Eq. (8.24). We remind that, in our framework, they take into account the possible leakage of CMB to foregrounds since the CMB frequency-scaling can now be affected by the instrumental effects. We also include statistical uncertainties induced by instrumental parameters.

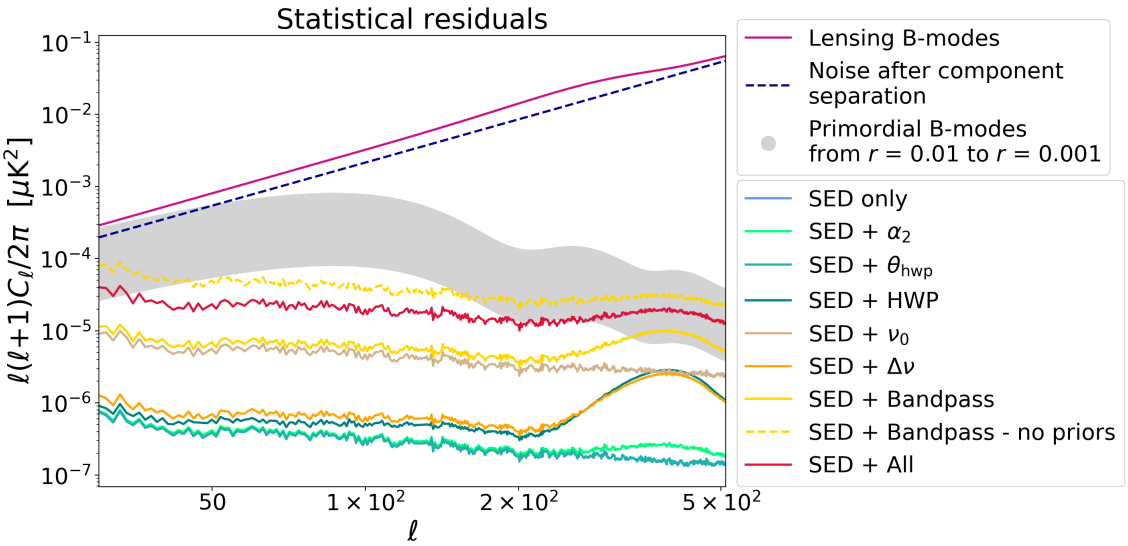

Figure 8.9 – Foreground statistical residuals on B-modes, for various instrumental parameter sets. As expected, statistical residuals scale as statistical uncertainty on the estimated parameters. The bump at high ℓ is due to statistical uncertainty dominated by uncertainty on instrumental parameters, resulting into a CMB E- to B-mode power spectra leakage.

Statistical residuals At first, we assume the same modelling to simulate and analyse data sets. In this case, we expect no systematic residuals, and we can therefore limit ourselves to statistical residuals as defined in Eq. (8.27). We compute foreground residuals for all cases we have studied in the previous section. Results are presented in Figure 8.9. As expected, the level of statistical residuals scales directly as the uncertainties on recovered parameters: the more parameters, the larger the uncertainties and the higher the statistical residuals. Including priors on bandpass parameters lowers the level of residuals as expected.

We note that, despite being very similar in shape at low ℓ, the various residual curves differ at high ℓ: the bump at small angular scales is due to the leakage of the CMB polarisation signal (E-modes) into residuals. We validate this by computing residuals without including CMB contributions, and show that this distinctive feature disappears, as shown in Figure 8.10.

The difference between various cases depends on the dominant source of uncertainty, i.e dominant terms in $\boldsymbol{\Sigma}$. When uncertainties on foreground spectral parameters are dominant, this has no impact on CMB residuals since foreground parameters, by definition, do not parametrise CMB. Otherwise, when uncertainties on instrumental parameters are dominant, the CMB contribution to residuals is boosted, hence the bump at high ℓ.

As we observed in section 8.2.2 (see Figure 8.6), marginalised uncertainties on spectral parameters in the {SED + ν_0} case are much higher than in the {SED only} case, while there is only a negligible increase in the case {SED + $\Delta\nu$}. As shown in Figure 8.9, statistical residuals at low ℓ in the {SED + ν_0} case are thus higher that in the {SED + $\Delta\nu$}. Moreover, in the {SED + ν_0} case, the dominant source of uncertainty is spectral parameter uncertainties, whereas it is instrumental parameter uncertainties in the {SED + $\Delta\nu$} case. This difference reflects in systematics residuals at high ℓ: in the {SED + $\Delta\nu$} case, they are indeed domi-

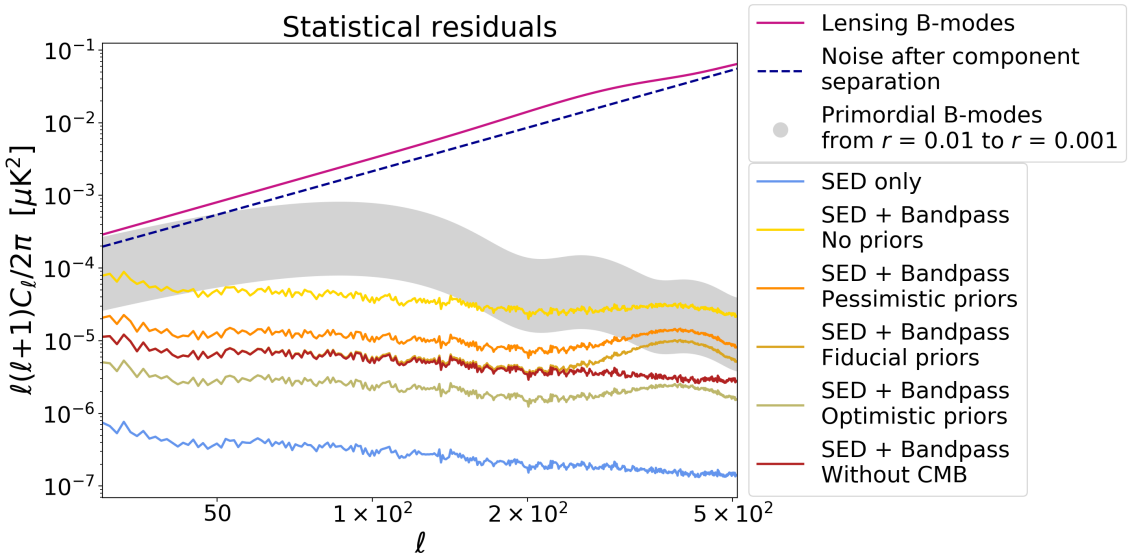

Figure 8.10 – Foreground statistical residuals with and without including CMB contribution. We also compare different level of priors on bandwidths, to show the effective reduction of statistical residuals by choosing more stringent priors. The case without CMB is considered with fiducial priors.

nated by CMB-sourced residuals, hence the bump, while they are dominated by pure foregrounds residuals in the {SED + ν_0} and therefore have no bump at high ℓ.

This effect could be reduced by having more stringent priors on instrumental parameters, as shown in Figure 8.10. Indeed, the presented framework can be used to motivate required specifications for calibration precision of different instrumental parameters. We leave a more detailed discussion of this option to future work.

Systematic residuals We now introduce a mismatch between simulated data and the model. As outlined in section 8.2.1, we investigate the effect of slowly varying, more realistic bandpasses in the data, while we keep a simple smoothed top-hat model. We consider the following cases:

- SED only
- SED + HWP
- SED + Bandpass
- SED + All

For each case, we compute residuals when introducing a discrepancy between bandpass data and model, with $a = 0.01$ and $b = 1$. We compare them to residuals in the same instrumental configuration, but with no bandpass variation in the input data. For both statistical (Eq. (8.27)) and systematic residuals (Eq. (8.26)), we verify that they behave as expected:

- no notable difference between statistical residuals, as they are unaffected by discrepancy between data and model;

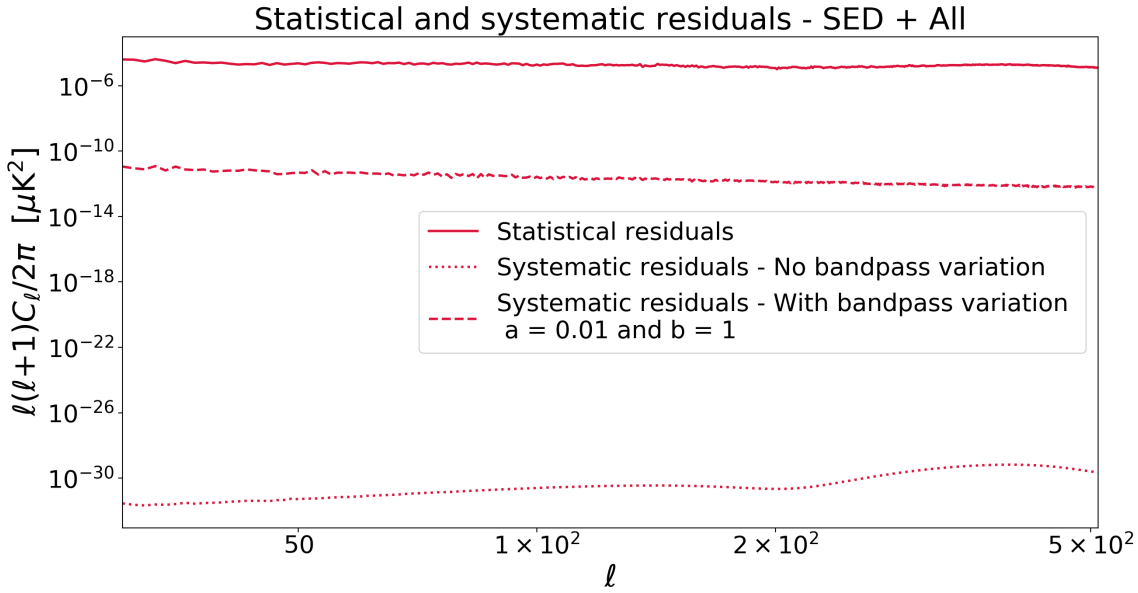

Figure 8.11 – Statistical and systematic residuals, showing the increase in systematic residuals when introducing a mismatch between bandpass in data and model in the {SED + All} case.

- increase of systematic residuals as they are precisely sensitive to the mismatch between data and its model.

We demonstrate that this is true in all cases, and show the result for one case ({SED + All}) in Figure 8.11 for reference.

Moreover, we expect the level of systematic residuals to depend on a and b (defined in section 8.2.1), as they set the amplitude and frequency of bandpass variations. The impact of higher systematic residuals on r estimation, and the level of bandpass variation we can tolerate compared to a smoothed, top-hat model, without having to take into account explicitly the effect is discussed hereafter.

Constraints on tensor-to-scalar ratio

Now that we have computed residuals for various cases, we move to the estimation of cosmological parameters, and in particular the tensor-to-scalar ratio r.

We use the cosmological likelihood introduced in Eq. (8.32) and consider that the theoretical covariance of the CMB signal only contains BB power and is only dependent on the tensor-to-scalar ratio r i.e. $\hat{\mathbf{C}} = \hat{\mathbf{C}}(r)$. We can thus determine the best fit for r as well as the uncertainty $\sigma(r)$ by minimising Eq. (8.32).

Contribution of residuals to the cosmological likelihood Residuals that we previously computed all contribute to the cosmological likelihood at different levels. High statistical residuals will increase the uncertainty $\sigma(r)$, while high systematic residuals will possibly bias the recovered value of r itself.

We first estimate r in the case assuming no model for the statistical residuals and the covariance given therefore as in Eq. (8.33). As no residual is accounted

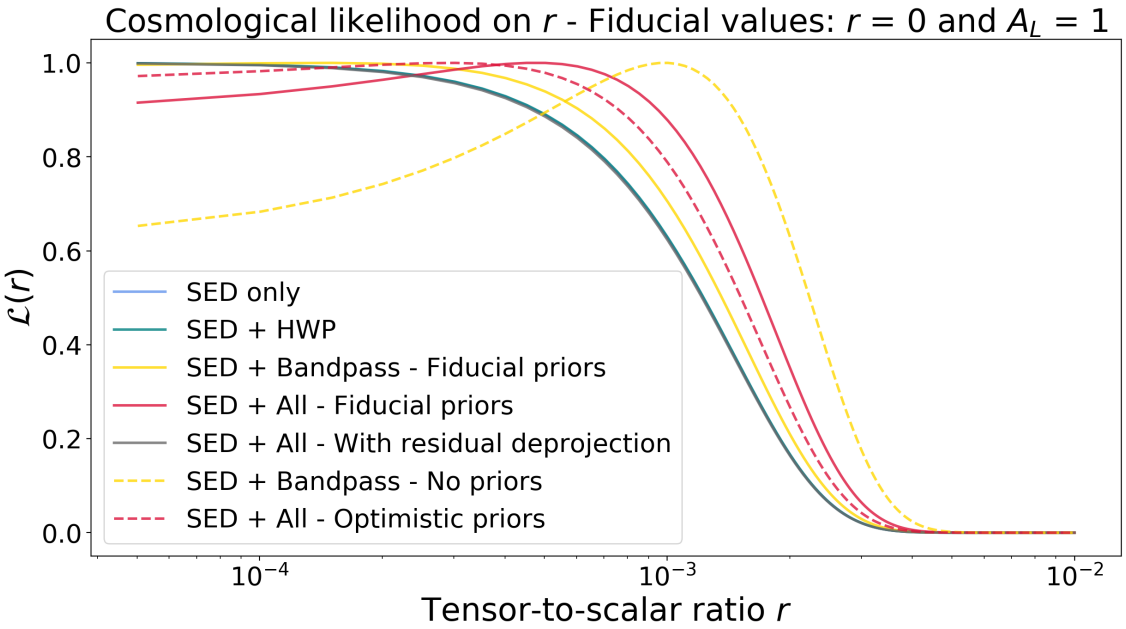

Figure 8.12 – Cosmological likelihoods (Eq. (8.32)) as a function of the tensor-to-scalar ratio r. We show that limiting statistical residuals by introducing priors reduces the bias on r. We also demonstrate that when it is possible to achieve statistical residuals deprojection because we have a precise enough model of the instrument, the estimation of r is significantly improved.

for in this case, both the statistical and systematic residuals may result in a bias on r which is expected to depend on the level of residuals. The results are shown in Figure 8.12 and we also quote values of r and $\sigma(r)$ for all instrumental parameter sets that we have considered in Table 8.5.

As expected, the higher the residuals, the bigger the bias on r. We can therefore suppress the bias by suppressing the residuals. This can be achieved with help of additional priors on instrumental parameters. As shown in Figure 8.12 and Table 8.5, this way is indeed efficient in reducing the bias on r and ensuring that it does not lead to an erroneous but statistically significant detection. Its downside is that it may call for high precision priors. This can be particularly demanding if the number of relevant instrumental effects is large.

The statistical residuals can be effectively marginalised, or deprojected, by using the model covariance in Eq. (8.34), therefore minimising potential bias of the measured value of r. In this case, we may hope that the need for high precision priors can at least partly be alleviated. This expectation is indeed confirmed in the cases studied here, as it is shown with a gray solid line in Figure 8.12. The loss of accuracy and precision seems to be in this case negligible. In more realistic cases and in the presence of a potentially significant mismatch between the assumed sky and instrument models, and the true ones, the deprojection may not be however as successful as in the simple cases studied here. We expect therefore that the calibration priors will continue to play a key role in the component separation process either in order to suppress the residuals, as in the first method described above, or to demonstrate that the deprojection was indeed performed successfully.

	$r(\times 10^{-5})$	$\sigma(r)(\times 10^{-3})$
SED only	0.819	1.47
SED + α_2	0.870	1.47
SED + $\theta_{\rm hwp}$	0.823	1.47
SED + HWP	1.15	1.47
SED + ν_0	8.40	1.48
SED + $\Delta\nu$	1.38	1.47
SED + Bandpass - no priors	98.6	1.51
SED + Bandpass - pessimistic priors	28.0	1.48
SED + Bandpass - fiducial priors	14.1	1.48
SED + Bandpass - optimistic priors	6.00	1.47
SED + All - fiducial priors	47.6	1.49
SED + All - optimistic priors	29.1	1.48

Table 8.5 – Best-fit values for r and $\sigma(r)$ without residuals deprojection. The input value is $r = 0$. Corresponding cosmological likelihood for some cases are shown in Figure 8.12.

	$A_L = 1$	$A_L = 0.5$
$r = 0$	$\sigma(r) = 1.49 \times 10{-}3$	$\sigma(r) = 1.05 \times 10{-}3$
$r = 0.01$	$\sigma(r) = 1.96 \times 10{-}3$	$\sigma(r) = 1.51 \times 10{-}3$

Table 8.6 – Uncertainties on r without residual deprojection, with varying tensor-to-scalar ratio r and lensing amplitude A_L, in the case of SED + All, including priors on bandpasses.

Results with other fiducial cosmological parameters We also test our framework with other values for fiducial cosmological parameters. We consider

- the effect of partial delensing with $A_L = 0.5$;
- the impact on the performance for a tensor-to-scalar ratio value consistent with what typical Stage 3 experiment plan to achieve, i.e. $r = 0.01$.

Here, we consider only the case with all instrumental parameters, including priors. Results without residual deprojection are shown in Figure 8.13 and Table 8.6. We show that in all considered cases, we correctly estimate the value of r within the uncertainty $\sigma(r)$, even if we do not deproject statistical residuals. The uncertainty on r is reduced when we assume partial delensing, as expected.

Overall, we demonstrate that results obtained with our framework are comparable with Simons Observatory forecast [269], as we recover $\sigma(r = 0) \sim 2 \times 10^{-3}$ with no delensing. When assuming $A_L = 0.5$, the reduction in $\sigma(r)$ is again consistent with SO expectations[4]. However, we emphasise again that the results are not directly comparable to SO forecasts, as we made simplifications in the instrument model, and did not include $1/f$ noise.

[4] One can refer for example to Tables 4 and 5 in [269]

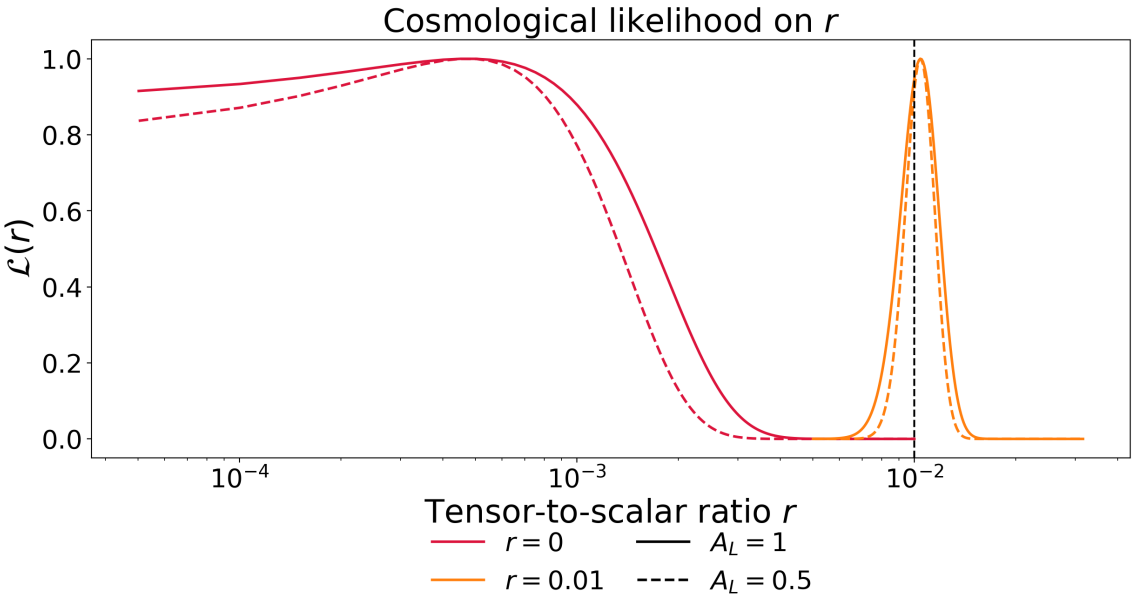

Figure 8.13 – Cosmological likelihood without residual deprojection, with varying tensor-to-scalar ratio r and lensing amplitude A_L, in the case of SED + All, including priors on bandpasses. $A_L = 1$ corresponds to no delensing and $A_L = 0.5$ to 50 % of delensing.

Impact of varying bandpass We have previously shown that bandpass parameters play a key role in the framework, and that their determination requires the inclusion of priors to control the level of uncertainties on recovered parameters. However, we have also emphasised that this is particularly difficult to find a good parametric modelling of bandpasses, as they are often more complex than the parametric model we have adopted. We therefore propose to go a step further to see how things are affected by mismodelling bandpasses. We consider a mismatch between bandpasses in simulated data and in the model, as outlined in section 8.2.3. This allows us to mimic the effect of having a real bandpass whose features are more complex that the top-hat model we use.

We first estimate r for the previously considered cases of systematic residuals, i.e with $a = 0.01$ and $b = 1$ with various instrumental configurations. Although we reported - as expected - an increase in systematic residuals, we find that this has no impact on the recovered value of r since systematic residuals are always below statistical residuals.

To investigate this effect further, we keep only the {SED + All} case, as this is the case where we expect the biggest impact. We consider various {a,b} combinations, compute residuals and estimate r in each case.

We show that, for a given value of a (amplitude of the bandpass variation), a smaller b leads to a larger increase in systematic residuals. As it corresponds to a low-frequency variation (see Figure 8.14), it shows that large-scale deviation from the assumed bandpass shape are more likely to affect the precision of the component separation, but higher frequency features in the bandpass are of less concern. It is therefore safe to characterise bandpass with a ~ 1 GHz sampling as this is most often the case [177, 280]. Moreover, for a given value of b, a bigger a increases systematics residuals: this is an expected effect, since a sets the

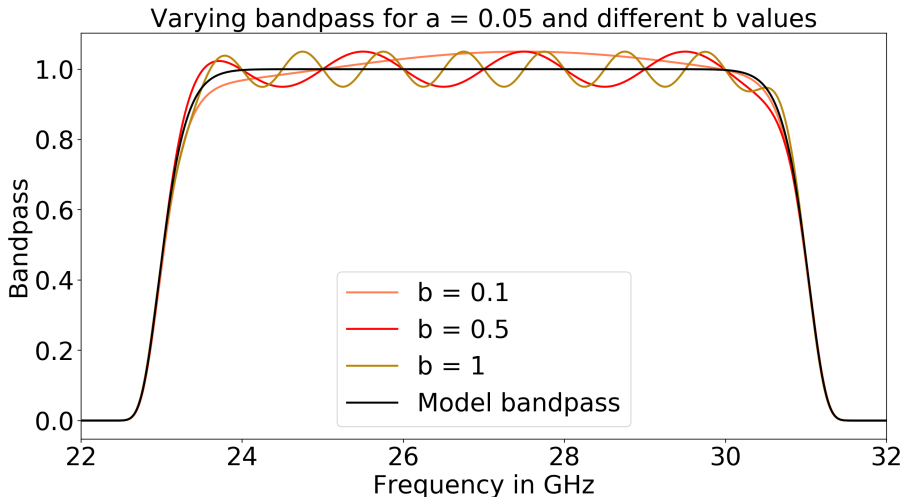

Figure 8.14 – Varying bandpass for $a = 0.05$ and different b values for the 27 GHz channel, following Eq. (8.47)

amplitude of bandpass variation. These two effects are demonstrated on Figure 8.15.

However, even with higher statistical residuals, the bias on the recovered value of r is insignificant, as it is within the uncertainty $\sigma(r)$. This is due to the fact that total residuals are still dominated by statistical residuals in the cases we considered.

8.2.4 Discussion

In this work, we addressed the issue of component separation within an instrumental framework, including a frequency-dependent optics chain. In particular, we focus on the interplay between HWP polarisation angle, bandpass and foregrounds spectral laws.

Using degeneracies of the Hessian matrix of the multi-parameter spectral likelihood, we demonstrated that it is necessary to include priors on instrumental parameters to properly constrain them. Although we have not explored a wide range of priors in this work, we demonstrate in a few chosen cases that their inclusion improves the performances of component separation. We also provide several metrics to decide on which priors to use and their required level: eigenvalues of the Hessian matrix, uncertainties on foreground spectral parameters and level on statistical residuals after component separation. We thus emphasise that the tool we propose is suited to inform calibration strategies and requirements, as it allows to forecast the impact on final cosmological parameters from calibration uncertainties.

We also addressed the impact of a mismatch between data and model, in the specific case of bandpasses. We show that for usual variations of bandpasses around a top-hat model, we can safely ignore these variations in the model without biasing cosmological parameters. Again, the tool we propose can be used to forecast the performance of data analysis given an experimental model, and assess whether a more complex one is required or not. Moreover, as we envisage experiments composed of thousands of detector arrays, the method we propose

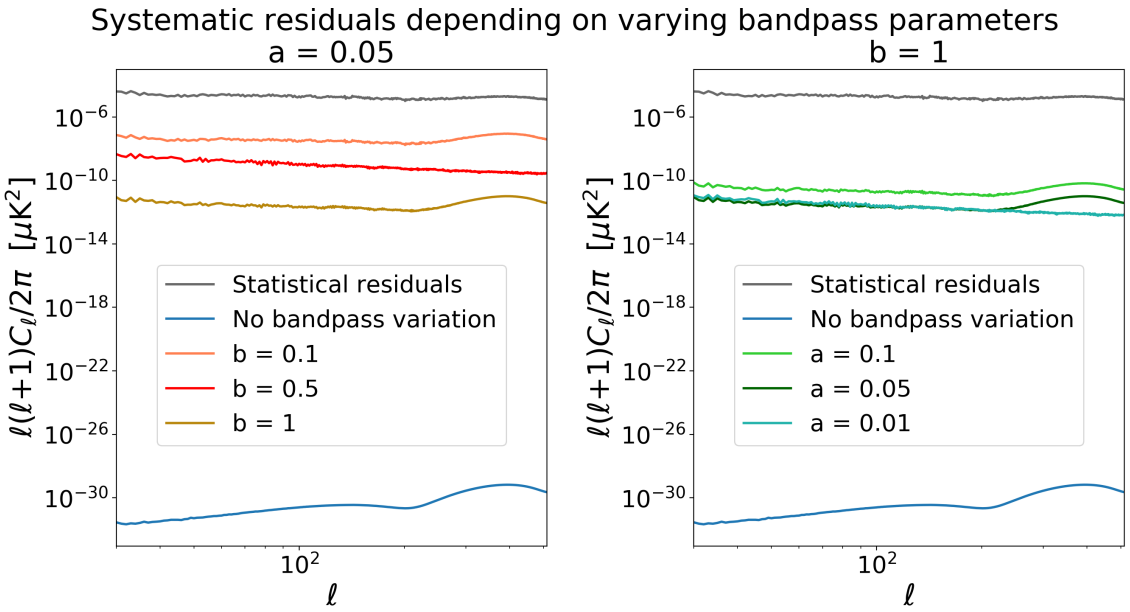

Figure 8.15 – Scaling of systematic residuals depending on bandpass variation, compared to statistical residuals. We consider here all 20 parameters.

is well suited to evaluate the impact of a dispersion of detector parameters (sinuous antenna, bandpass) on the data, while modelling them with only a single parameter, identical to all detectors and thus ignoring individual detector effects. Although this effect is not investigated here and is a potential limitation to the results we present, it is an extension that we plan on investigating in a future work.

Moreover, the proposed framework is flexible enough to accommodate a wide range of instrumental models, and is not limited to HWP and bandpass effects. We have for example introduced the sinuous antenna wobble angle, that we have not explored in this work but that could easily be considered. We also mentioned beam systematics and varying foreground spectral parameters that could be investigated within this framework in future work. Moreover, any of the instrument models that we propose (HWP, sinuous antenna, bandpass) can be replaced by lab measurements to simulate input data, while keeping a parametric instrument model in the model. This approach would be similar to what we did using varying bandpasses in simulated data. This would allow to assess the effect of an imperfect modelling of the instrument or a loose calibration on component separation performances.

Last but not least, while we have employed the framework in the context of forecasting, it can also be included in an actual data processing pipeline. In particular, as it requires an amended map-making process, we aim at including it in an end-to-end data analysis pipeline taking into account foreground and instrumental effects. In this case, the ensemble averaged likelihoods should be replaced by the actual likelihoods for actual data sets which are analysed.

Conclusion

After the progress in precision cosmology in the past 15 years, CMB science is preparing for a new step forward with the advent of new generation polarisation experiments. Primary science goals of this new generation of experiments include the observation of primordial B-modes that would be a smoking gun for inflation. Experiments are also designed to help unveiling the secrets of the Universe, dark energy and dark matter. In that respect, the development of multi messenger astrophysics and cross-correlation studies between data sets obtained from various cosmological observables allows to portray the Universe with an unprecedented accuracy.

Preparing for these new experiments requires to address new challenges. Technical ones in the first place, to reach an unprecedented on-sky sensitivity, but also data analysis ones. As the increased complexity of experimental design unavoidably introduces new instrumental and systematic effects, we need to ensure that this complexity does not degrade instrumental performances nor hinders our detection capabilities.

In this thesis, I first reviewed the core principles of cosmology and CMB science in Chapters 1 and 2, and I emphasised the importance of multi-probe cosmology in Chapter 3. In Chapter 4, I presented one of the most important challenges for CMB data analysis: the removal of diffuse galactic foreground contamination. This step of data analysis is the driver for the deployment of multi-frequency detector arrays. As I presented in Chapter 5, this calls for new technological developments and data analysis methods, that are being implemented in the context of new generation CMB polarisation experiments.

In this context, I have developed simulation and data analysis frameworks to address some of the key potential instrumental systematic effects for the new generation experiments. In Chapter 6, I emphasised my contribution to the POLARBEAR/Simons Array experiments, where I have helped to develop novel methods to estimate readout crosstalk by using planet scans. A map-domain version of this method was successfully applied in the context of the POLARBEAR-1 large patch data analysis in which I participated. I also proposed a time-domain framework for a parametric estimation of crosstalk parameters directly from timestreams, which would in principle allow for a day-to-day correction of crosstalk effects. I

have demonstrated this framework on a small subset of detectors, and I wish to continue to develop this method for future data sets. I also had the chance to be part of the preparation and deployment of Simons Array, by contributing to the installation and operation of the HWP in Chile in November 2019.

On another front, I derived in Chapter 7 an involved data model to take into account accurate modelling of optics chain elements. This allows to study the interplay of various optical elements with the frequency-dependent foreground emission, and to address issues in component separation arising from the complexity of the optics chain of the instrument. I demonstrated this framework in Chapter 8 in the context of parametric component separation forecast for a typical Stage 3 experiment. In particular, I emphasised the importance of instrumental calibration priors to reach the required precision on the unbiased estimation of cosmological parameters.

In the future, I intend to continue developing this component separation framework and integrate it in future data analysis pipeline for CMB polarisation experiments. In particular, as it requires an amended map-making procedure, I wish to participate in the development of novel map-making pipelines that would encompass the involved data model I developed. I would also like to integrate more instrumental effects in the framework, such as beam and gain effects, as well as the crosstalk formalism I proposed.

More generally, I plan to continue working at the interface between data analysis and instrument modelling, and to pursue the development of novel and disruptive methods for data analysis for increasingly complex instruments.

APPENDIX A

Spherical harmonics

Spherical harmonics play the same role on the sphere as the Fourier transform for plane waves: a basis of orthogonal functions allowing to decompose any field defined on the sphere. They are an unavoidable tool to anyone willing to describe CMB anisotropies. These functions are defined as the solutions of the Laplace operator:

$$\nabla^2 Y_{\ell m}(\theta, \phi) = -\ell(\ell+1) Y_{\ell m}(\theta, \phi), \tag{A.1}$$

where (θ, ϕ) are the usual angles of spherical coordinates. Spherical harmonics form an orthogonal basis on the sphere, with ℓ the degree of the harmonic, and m its mode, with $-\ell \leq m \leq \ell$. ℓ corresponds to the number of (geographical) parallels defined on the sphere by the mode, and $|m|$ to the number of meridians. In connection with CMB anisotropies, it is important to note that ℓ measures the angular scale of an anisotropy: a large ℓ means a small scale anisotropy, when a small ℓ corresponds to a large scale anisotropy, with $\ell = 0$ corresponding to full-sky, as it is shown for example in Figure A.1. The correspondence between angular scale θ and degree ℓ is roughly $\theta \sim \frac{180^\circ}{\ell}$.

Scalar transformation

For any scalar field $\mathcal{F}$ defined on the sphere - for example the CMB temperature field - this base can be used to expand it:

$$\mathcal{F}(\theta, \phi) = \sum_{\ell m}^{\infty} a_{\ell m} Y_{\ell m}(\theta, \varphi), \tag{A.2}$$

where the harmonic coefficients are given by

$$a_{\ell m} = \int_{4\pi} d\Omega Y^*_{\ell m}(\theta, \phi) \mathcal{F}(\theta, \phi). \tag{A.3}$$

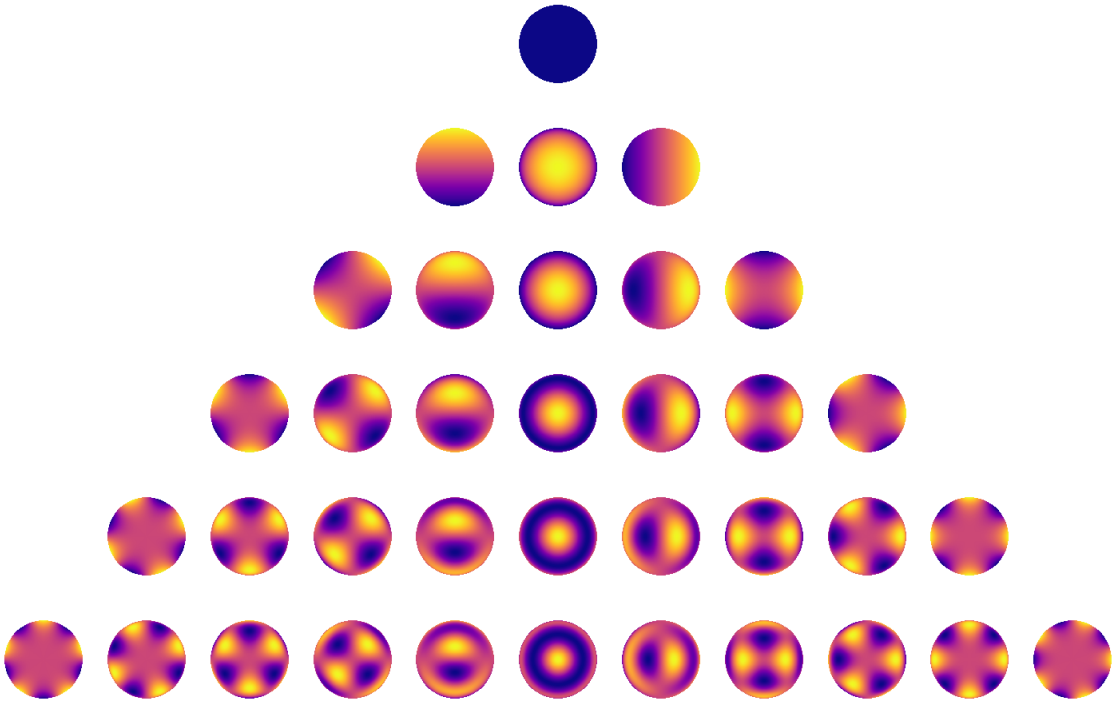

Figure A.1 – Spherical harmonics, from $\ell = 0$ (top) to $\ell = 5$ (bottom), with m ranging from $-\ell$ (left) to ℓ (right) for each ℓ
Credit: R. Luger using `starry` package [169]

Spin transformation

For a spin-2 field - for example a polarisation field - we introduce the spin-weighted spherical harmonics:

$$\mathcal{F}_{\pm 2}(\theta, \phi) = \sum_{\ell m} {}_{\pm 2}a_{\ell m} \, {}_{\pm 2}Y_{\ell m}(\theta, \phi), \tag{A.4}$$

where the coefficients are given by:

$${}_{\pm 2}a_{\ell m} = \int d\Omega Y^{\dagger}_{\ell m}(\theta, \phi) \mathcal{F}_{\pm 2}(\theta, \phi), \tag{A.5}$$

and ${}_{\pm 2}Y_{\ell m}$ are connected to $Y_{\ell m}$ through their covariant derivatives on the sphere, see for example in [110] for the complete algebra.

APPENDIX B

Gravitational waves

I do not intend to give an in-depth review of gravitational waves theory here, but rather to present a few important highlights to understand the physical meaning of gravitational waves observations[1]. For an extensive derivation, one can refer for example to [42, 82, 240].

Wave equation

As their name suggests, gravitational waves are... waves! Therefore, they follow a wave equation, similar to mechanical or electromagnetic waves equation, but derived in the framework of general relativity.

The space-time metric perturbed by gravitational waves is modelled as the Minkowski metric $\eta_{\mu\nu}$ plus a small perturbation $h_{\mu\nu}$

$$g_{\mu\nu} = \eta_{\mu\nu} + h_{\mu\nu}, \tag{B.1}$$

with $|h_{\mu\nu}| \ll 1$, and we limit ourselves to first order perturbations. For practical reasons, we introduce:

$$\begin{aligned} \bar{h}_{\mu\nu} &\equiv h_{\mu\nu} - \frac{h}{2}\eta_{\mu\nu} \\ h &\equiv \eta^{\mu\nu} h_{\mu\nu}. \end{aligned} \tag{B.2}$$

We impose the canonical harmonic gauge condition:

$$\partial_\mu \bar{h}^\mu_\nu = 0, \tag{B.3}$$

and we can then linearise and simplify Einstein field equation Eq. (1.17) to obtain:

$$\Box \bar{h}_{\mu\nu} = -\frac{16\pi G}{c^4} T_{\mu\nu}, \tag{B.4}$$

[1] This short review is based on lecture notes by Marios Petropoulos from his *Relativité Générale* course, École polytechnique, 2016.

which is the wave equation for gravitational waves, relating the metric perturbation $h_{\mu\nu}$ to the energy-momentum tensor of the source $T_{\mu\nu}$.

Propagation in vacuum

Once waves have been emitted, they propagate in vacuum, away from their source. We thus remove the source term $T_{\mu\nu}$ from the wave equation, and obtain the propagation equation in vacuum:

$$\Box \bar{h}_{\mu\nu} = 0. \tag{B.5}$$

To describe the gravitational waves field in vacuum, we impose further gauge restrictions, known as the traceless transverse gauge conditions:

$$\begin{aligned} \bar{h} &= 0\,(\text{traceless}) \\ u^{\mu}\bar{h}_{\mu\nu} &= 0\,(\text{transverse}), \end{aligned} \tag{B.6}$$

where u^{μ} is an arbitrary timelike vector.

If we assume that plane waves propagate along the z-axis, under the traceless transverse gauge condition, one can express them in a generic form:

$$h_{\mu\nu} = \begin{pmatrix} 0 & 0 & 0 & 0 \\ 0 & h_{+} & h_{\times} & 0 \\ 0 & h_{\times} & -h_{+} & 0 \\ 0 & 0 & 0 & 0 \end{pmatrix} e^{ikz}, \tag{B.7}$$

with k the wave number. h_{+} and $h_{\times}$ are the two independent polarisation states of the wave, that are analogue to polarisation states of the light.

Emission

Gravitational waves can only be generated if the source has a quadrupole moment. The generic expression for gravitational waves emitted by a source located at a distance r from the observer is indeed:

$$\bar{h}_{ij}(t, r) = \frac{2G}{c^4 r}\frac{dI^{ij}}{dt^2}(t_r) \tag{B.8}$$

where t_r is the retarded time and I^{ij} is the quadrupole moment of the source:

$$I^{ij}(t) = \frac{1}{c^2}\int d^3\mathbf{y} y^i y^j T^{00}(ct, \mathbf{y}), \tag{B.9}$$

where the unit vector $\mathbf{y}$ defines the space coordinates of the source. Here we note that the generation of a gravitational waves relies on the time-varying second moment of the energy-impulsion tensor T^{00}.

Bibliography

[1] K. N. Abazajian, K. Arnold, J. Austermann, B. A. Benson, C. Bischoff, J. Bock, J. R. Bond, J. Borrill, E. Calabrese, J. E. Carlstrom, C. S. Carvalho, C. L. Chang, H. C. Chiang, S. Church, A. Cooray, T. M. Crawford, K. S. Dawson, S. Das, M. J. Devlin, M. Dobbs, S. Dodelson, O. Doré, J. Dunkley, J. Errard, A. Fraisse, J. Gallicchio, N. W. Halverson, S. Hanany, S. R. Hildebrandt, A. Hincks, R. Hlozek, G. Holder, W. L. Holzapfel, K. Honscheid, W. Hu, J. Hubmayr, K. Irwin, W. C. Jones, M. Kamionkowski, B. Keating, R. Keisler, L. Knox, E. Komatsu, J. Kovac, C. L. Kuo, C. Lawrence, A. T. Lee, E. Leitch, E. Linder, P. Lubin, J. McMahon, A. Miller, L. Newburgh, M. D. Niemack, H. Nguyen, H. T. Nguyen, L. Page, C. Pryke, C. L. Reichardt, J. E. Ruhl, N. Sehgal, U. Seljak, J. Sievers, E. Silverstein, A. Slosar, K. M. Smith, D. Spergel, S. T. Staggs, A. Stark, R. Stompor, A. G. Vieregg, G. Wang, S. Watson, E. J. Wollack, W. L. K. Wu, K. W. Yoon, and O. Zahn. Neutrino physics from the cosmic microwave background and large scale structure. *Astroparticle Physics*, 63:66–80, March 2015. arXiv:1309.5383, doi:10.1016/j.astropartphys.2014.05.014. (not cited)

[2] Kevork Abazajian, George M. Fuller, and Mitesh Patel. Sterile neutrino hot, warm, and cold dark matter. *Physical Review D*, 64(2):023501, July 2001. arXiv:astro-ph/0101524, doi:10.1103/PhysRevD.64.023501. (cited p. 65)

[3] Viviana Acquaviva and Carlo Baccigalupi. Dark energy records in lensed cosmic microwave background. *Physical Review D*, 74(10):103510, November 2006. arXiv:astro-ph/0507644, doi:10.1103/PhysRevD.74.103510. (cited p. 64)

[4] R. Adam, I. Bartalucci, G. W. Pratt, P. Ade, P. André, M. Arnaud, A. Beelen, A. Benoît, A. Bideaud, N. Billot, H. Bourdin, O. Bourrion, M. Calvo, A. Catalano, G. Coiffard, B. Comis, A. D'Addabbo, M. De Petris, J. Démoclès, F. X. Désert, S. Doyle, E. Egami, C. Ferrari, J. Goupy, C. Kramer, G. Lagache, S. Leclercq, J. F. Macías-Pérez, S. Maurogordato, P. Mauskopf, F. Mayet, A. Monfardini, T. Mroczkowski, F. Pajot, E. Pascale, L. Perotto, G. Pisano, E. Pointecouteau, N. Ponthieu, V. Revéret, A. Ritacco, L. Rodriguez, C. Romero, F. Ruppin, K. Schuster, A. Sievers, S. Triqueneaux,

C. Tucker, M. Zemcov, and R. Zylka. Mapping the kinetic Sunyaev-Zel'dovich effect toward MACS J0717.5+3745 with NIKA. *Astronomy & Astrophysics*, 598:A115, February 2017. arXiv:1606.07721, doi:10.1051/0004-6361/201629182. (cited pp. 67 and 69)

[5] R. Adam, O. Hahn, F. Ruppin, P. Ade, P. André, M. Arnaud, I. Bartalucci, A. Beelen, A. Benoît, A. Bideaud, N. Billot, O. Bourrion, M. Calvo, A. Catalano, G. Coiffard, B. Comis, A. D'Addabbo, F. X. Désert, S. Doyle, C. Ferrari, J. Goupy, C. Kramer, G. Lagache, S. Leclercq, J. F. Lestrade, J. F. Macías-Pérez, G. Martinez Aviles, D. Martizzi, S. Maurogordato, P. Mauskopf, F. Mayet, A. Monfardini, F. Pajot, E. Pascale, L. Perotto, G. Pisano, E. Pointecouteau, N. Ponthieu, G. W. Pratt, V. Revéret, M. Ricci, A. Ritacco, L. Rodriguez, C. Romero, H. Roussel, K. Schuster, A. Sievers, S. Triqueneaux, C. Tucker, H. Y. Wu, and R. Zylka. Substructure and merger detection in resolved NIKA Sunyaev-Zel'dovich images of distant clusters. *Astronomy & Astrophysics*, 614:A118, June 2018. arXiv:1712.01836, doi:10.1051/0004-6361/201731950. (cited p. 67)

[6] R. Adam, O. Hahn, F. Ruppin, P. Ade, P. André, M. Arnaud, I. Bartalucci, A. Beelen, A. Benoît, A. Bideaud, N. Billot, O. Bourrion, M. Calvo, A. Catalano, G. Coiffard, B. Comis, A. D'Addabbo, F. X. Désert, S. Doyle, C. Ferrari, J. Goupy, C. Kramer, G. Lagache, S. Leclercq, J. F. Lestrade, J. F. Macías-Pérez, G. Martinez Aviles, D. Martizzi, S. Maurogordato, P. Mauskopf, F. Mayet, A. Monfardini, F. Pajot, E. Pascale, L. Perotto, G. Pisano, E. Pointecouteau, N. Ponthieu, G. W. Pratt, V. Revéret, M. Ricci, A. Ritacco, L. Rodriguez, C. Romero, H. Roussel, K. Schuster, A. Sievers, S. Triqueneaux, C. Tucker, H. Y. Wu, and R. Zylka. Substructure and merger detection in resolved NIKA Sunyaev-Zel'dovich images of distant clusters. *Astronomy & Astrophysics*, 614:A118, June 2018. arXiv:1712.01836, doi:10.1051/0004-6361/201731950. (cited p. 67)

[7] Nabila Aghanim, Subhabrata Majumdar, and Joseph Silk. Secondary anisotropies of the CMB. *Reports on Progress in Physics*, 71(6):066902, June 2008. arXiv:0711.0518, doi:10.1088/0034-4885/71/6/066902. (cited p. 46)

[8] Charles Alcock and Bohdan Paczyński. An evolution free test for non-zero cosmological constant. *Nature*, 281(5730):358–359, October 1979. URL: https://doi.org/10.1038/281358a0, doi:10.1038/281358a0. (cited p. 79)

[9] Stephon Alexander and Evan McDonough. Primordial circular polarization in the cosmic microwave background. *Physics Letters B*, 789:197–202, February 2019. arXiv:1811.05953, doi:10.1016/j.physletb.2018.12.037. (cited p. 158)

[10] R. A. Alpher, H. Bethe, and G. Gamow. The Origin of Chemical Elements. *Physical Review*, 73(7):803–804, April 1948. doi:10.1103/PhysRev.73.803. (cited p. 36)

[11] Luca Amendola and Shinji Tsujikawa. *Dark Energy: Theory and Observations*. Cambridge University Press, 2010. (cited p. 13)

[12] Philippe André, Carlo Baccigalupi, Anthony Banday, Domingos Barbosa, Belen Barreiro, James Bartlett, Nicola Bartolo, Elia Battistelli, Richard Battye, George Bendo, Alain Benoît, Jean-Philippe Bernard, Marco Bersanelli, Matthieu Béthermin, Pawel Bielewicz, Anna Bonaldi, François Bouchet, François Boulanger, Jan Brand, Martin Bucher, Carlo Burigana, Zhen-Yi Cai, Philippe Camus, Francisco Casas, Viviana Casasola, Guillaume Castex, Anthony Challinor, Jens Chluba, Gayoung Chon, Sergio Colafrancesco, Barbara Comis, Francesco Cuttaia, Giuseppe D'Alessandro, Antonio Da Silva, Richard Davis, Miguel de Avillez, Paolo de Bernardis, Marco de Petris, Adriano de Rosa, Gianfranco de Zotti, Jacques Delabrouille, François-Xavier Désert, Clive Dickinson, Jose Maria Diego, Joanna Dunkley, Torsten Enßlin, Josquin Errard, Edith Falgarone, Pedro Ferreira, Katia Ferrière, Fabio Finelli, Andrew Fletcher, Pablo Fosalba, Gary Fuller, Silvia Galli, Ken Ganga, Juan García-Bellido, Adnan Ghribi, Martin Giard, Yannick Giraud-Héraud, Joaquin Gonzalez-Nuevo, Keith Grainge, Alessand ro Gruppuso, Alex Hall, Jean-Christophe Hamilton, Marijke Haverkorn, Carlos Hernandez-Monteagudo, Diego Herranz, Mark Jackson, Andrew Jaffe, Rishi Khatri, Martin Kunz, Luca Lamagna, Massimiliano Lattanzi, Paddy Leahy, Julien Lesgourgues, Michele Liguori, Elisabetta Liuzzo, Marcos Lopez-Caniego, Juan Macias-Perez, Bruno Maffei, Davide Maino, Anna Mangilli, Enrique Martinez-Gonzalez, Carlos J. A. P. Martins, Silvia Masi, Marcella Massardi, Sabino Matarrese, Alessandro Melchiorri, Jean-Baptiste Melin, Aniello Mennella, Arturo Mignano, Marc-Antoine Miville-Deschênes, Alessandro Monfardini, Anthony Murphy, Pavel Naselsky, Federico Nati, Paolo Natoli, Mattia Negrello, Fabio Noviello, Créidhe O'Sullivan, Francesco Paci, Luca Pagano, Rosita Paladino, Nathalie Palanque-Delabrouille, Daniela Paoletti, Hiranya Peiris, Francesca Perrotta, Francesco Piacentini, Michel Piat, Lucio Piccirillo, Giampaolo Pisano, Gianluca Polenta, Agnieszka Pollo, Nicolas Ponthieu, Mathieu Remazeilles, Sara Ricciardi, Matthieu Roman, Cyrille Rosset, Jose-Alberto Rubino-Martin, Maria Salatino, Alessandro Schillaci, Paul Shellard, Joseph Silk, Alexei Starobinsky, Radek Stompor, Rashid Sunyaev, Andrea Tartari, Luca Terenzi, Luigi Toffolatti, Maurizio Tomasi, Neil Trappe, Matthieu Tristram, Tiziana Trombetti, Marco Tucci, Rien Van de Weijgaert, Bartjan Van Tent, Licia Verde, Patricio Vielva, Ben Wand elt, Robert Watson, and Stafford Withington. PRISM (Polarized Radiation Imaging and Spectroscopy Mission): an extended white paper. *Journal of Cosmology and Astroparticle Physics*, 2014(2):006, February 2014. arXiv:1310.1554, doi:10.1088/1475-7516/2014/02/006. (cited p. 72)

[13] K. Arnold and The POLARBEAR Collaboration. The bolometric focal plane array of the POLARBEAR CMB experiment. In *Proceedings of SPIE*, volume 8452 of *Society of Photo-Optical Instrumentation Engineers (SPIE) Conference Series*, page 84521D. SPIE, 2012. doi:10.1117/12.927057. (cited p. 128)

[14] J. Aumont, L. Conversi, C. Thum, H. Wiesemeyer, E. Falgarone, J. F. Macías-

Pérez, F. Piacentini, E. Pointecouteau, N. Ponthieu, J. L. Puget, C. Rosset, J. A. Tauber, and M. Tristram. Measurement of the Crab nebula polarization at 90 GHz as a calibrator for CMB experiments. *Astronomy & Astrophysics*, 514:A70, May 2010. arXiv:0912.1751, doi:10.1051/0004-6361/200913834. (cited p. 131)

[15] Jonathan Aumont, J. Macías-Pérez, Alessia Ritacco, N. Ponthieu, and A. Mangilli. Absolute calibration of the polarisation angle for future cmb b-mode experiments from current and future measurements of the crab nebula. *Astronomy & Astrophysics*, 634, 01 2020. doi:10.1051/0004-6361/201833504. (cited pp. 75, 152, and 161)

[16] Abdolali Banihashemi, Nima Khosravi, and Amir H. Shirazi. Phase transition in the dark sector as a proposal to lessen cosmological tensions. *Physical Review D*, 101(12):123521, June 2020. arXiv:1808.02472, doi:10.1103/PhysRevD.101.123521. (cited p. 20)

[17] C. Bao, B. Gold, C. Baccigalupi, J. Didier, S. Hanany, A. Jaffe, B. R. Johnson, S. Leach, T. Matsumura, A. Miller, and D. O'Dea. The Impact of the Spectral Response of an Achromatic Half-wave Plate on the Measurement of the Cosmic Microwave Background Polarization. *The Astrophysical Journal*, 747(2):97, March 2012. arXiv:1112.3057, doi:10.1088/0004-637X/747/2/97. (cited p. 160)

[18] Rennan Barkana. Possible interaction between baryons and dark-matter particles revealed by the first stars. *Nature*, 555(7694):71–74, March 2018. arXiv:1803.06698, doi:10.1038/nature25791. (cited p. 83)

[19] Darcy Barron, Yuji Chinone, Akito Kusaka, Julian Borril, Josquin Errard, Stephen Feeney, Simone Ferraro, Reijo Keskitalo, Adrian T. Lee, Natalie A. Roe, Blake D. Sherwin, and Aritoki Suzuki. Optimization study for the experimental configuration of CMB-S4. *Journal of Cosmology and Astroparticle Physics*, 2018(2):009, February 2018. arXiv:1702.07467, doi:10.1088/1475-7516/2018/02/009. (cited p. 110)

[20] N. Bartolo, E. Komatsu, S. Matarrese, and A. Riotto. Non-Gaussianity from inflation: theory and observations. *Physical Reports*, 402(3-4):103–266, November 2004. arXiv:astro-ph/0406398, doi:10.1016/j.physrep.2004.08.022. (cited p. 73)

[21] N. Bartolo, S. Matarrese, and A. Riotto. Non-Gaussianity and the Cosmic Microwave Background Anisotropies. *Advances in Astronomy*, 2010:157079, January 2010. arXiv:1001.3957, doi:10.1155/2010/157079. (cited p. 72)

[22] Nicola Bartolo, Ahmad Hoseinpour, Sabino Matarrese, Giorgio Orlando, and Moslem Zarei. CMB circular and B -mode polarization from new interactions. *Physical Review D*, 100(4):043516, August 2019. arXiv:1903.04578, doi:10.1103/PhysRevD.100.043516. (cited p. 158)

[23] Bruce Bassett and Renée Hlozek. *Baryon acoustic oscillations*. Cambridge University Press, 2010. (cited p. 79)

[24] Richard A. Battye, Rod D. Davies, and Jochen Weller. Neutral hydrogen surveys for high-redshift galaxy clusters and protoclusters. *Monthly Notices of the Royal Astronomical Society*, 355(4):1339–1347, December 2004. arXiv:astro-ph/0401340, doi:10.1111/j.1365-2966.2004.08416.x. (cited p. 82)

[25] Daniel Baumann. TASI Lectures on Inflation. *arXiv e-prints*, July 2009. arXiv:0907.5424. (cited pp. 24 and 26)

[26] Robert H. Becker, Xiaohui Fan, Richard L. White, Michael A. Strauss, Vijay K. Narayanan, Robert H. Lupton, James E. Gunn, James Annis, Neta A. Bahcall, J. Brinkmann, A. J. Connolly, István Csabai, Paul C. Czarapata, Mamoru Doi, Timothy M. Heckman, G. S. Hennessy, Željko Ivezić, G. R. Knapp, Don Q. Lamb, Timothy A. McKay, Jeffrey A. Munn, Thomas Nash, Robert Nichol, Jeffrey R. Pier, Gordon T. Richards, Donald P. Schneider, Chris Stoughton, Alexand er S. Szalay, Aniruddha R. Thakar, and D. G. York. Evidence for Reionization at z∼6: Detection of a Gunn-Peterson Trough in a z=6.28 Quasar. *Astronomical Journal*, 122(6):2850–2857, December 2001. arXiv:astro-ph/0108097, doi:10.1086/324231. (cited p. 21)

[27] C. L. Bennett, R. S. Hill, G. Hinshaw, M. R. Nolta, N. Odegard, L. Page, D. N. Spergel, J. L. Weiland, E. L. Wright, M. Halpern, N. Jarosik, A. Kogut, M. Limon, S. S. Meyer, G. S. Tucker, and E. Wollack. First-Year Wilkinson Microwave Anisotropy Probe (WMAP) Observations: Foreground Emission. *The Astrophysical Journal, Supplement*, 148(1):97–117, September 2003. arXiv:astro-ph/0302208, doi:10.1086/377252. (cited p. 104)

[28] Peter G. Bergmann. Summary of the chapel hill conference. *Rev. Mod. Phys.*, 29:352–354, Jul 1957. URL: https://link.aps.org/doi/10.1103/RevModPhys.29.352, doi:10.1103/RevModPhys.29.352. (cited p. 88)

[29] José Luis Bernal, Licia Verde, and Adam G. Riess. The trouble with H_0. *Journal of Cosmology and Astroparticle Physics*, 2016(10):019, Oct 2016. arXiv:1607.05617, doi:10.1088/1475-7516/2016/10/019. (cited p. 10)

[30] M. Betoule, R. Kessler, J. Guy, J. Mosher, D. Hardin, R. Biswas, P. Astier, P. El-Hage, M. Konig, S. Kuhlmann, J. Marriner, R. Pain, N. Regnault, C. Balland, B. A. Bassett, P. J. Brown, H. Campbell, R. G. Carlberg, F. Cellier-Holzem, D. Cinabro, A. Conley, C. B. D'Andrea, D. L. DePoy, M. Doi, R. S. Ellis, S. Fabbro, A. V. Filippenko, R. J. Foley, J. A. Frieman, D. Fouchez, L. Galbany, A. Goobar, R. R. Gupta, G. J. Hill, R. Hlozek, C. J. Hogan, I. M. Hook, D. A. Howell, S. W. Jha, L. Le Guillou, G. Leloudas, C. Lidman, J. L. Marshall, A. Möller, A. M. Mourão, J. Neveu, R. Nichol, M. D. Olmstead, N. Palanque-Delabrouille, S. Perlmutter, J. L. Prieto, C. J. Pritchet, M. Richmond, A. G. Riess, V. Ruhlmann-Kleider, M. Sako, K. Schahmaneche, D. P. Schneider, M. Smith, J. Sollerman, M. Sullivan, N. A. Walton, and C. J. Wheeler. Improved cosmological constraints from a joint analysis of the SDSS-II and SNLS supernova samples. *Astronomy & Astrophysics*,

568:A22, Aug 2014. arXiv:1401.4064, doi:10.1051/0004-6361/201423413. (cited p. 9)

[31] M. G. Betti, M. Biasotti, A. Boscá, F. Calle, N. Canci, G. Cavoto, C. Chang, A. G. Cocco, A. P. Colijn, J. Conrad, N. D'Ambrosio, N. De Groot, P. F. de Salas, M. Faverzani, A. Ferella, E. Ferri, P. Garcia-Abia, I. García-Cortés, G. Garcia Gomez-Tejedor, S. Gariazzo, F. Gatti, C. Gentile, A. Giachero, J. E. Gudmundsson, Y. Hochberg, Y. Kahn, A. Kievsky, M. Lisanti, C. Mancini-Terracciano, G. Mangano, L. E. Marcucci, C. Mariani, J. Martínez, M. Messina, A. Molinero-Vela, E. Monticone, A. Moroño, A. Nucciotti, F. Pand olfi, S. Parlati, S. Pastor, J. Pedrós, C. Pérez de los Heros, O. Pisanti, A. D. Polosa, A. Puiu, I. Rago, Y. Raitses, M. Rajteri, N. Rossi, I. Rucandio, R. Santorelli, K. Schaeffner, C. G. Tully, M. Viviani, F. Zhao, and K. M. Zurek. Neutrino physics with the PTOLEMY project: active neutrino properties and the light sterile case. *Journal of Cosmology and Astroparticle Physics*, 2019(7):047, July 2019. arXiv:1902.05508, doi:10.1088/1475-7516/2019/07/047. (cited p. 92)

[32] BICEP2 Collaboration. Detection of B-Mode Polarization at Degree Angular Scales by BICEP2. *Physical Review Letters*, 112(24):241101, June 2014. arXiv:1403.3985, doi:10.1103/PhysRevLett.112.241101. (cited p. 101)

[33] The BICEP2 Collaboration and the Keck Array Collaboration. BICEP2 / Keck Array IX: New bounds on anisotropies of CMB polarization rotation and implications for axionlike particles and primordial magnetic fields. *Physical Review D*, 96(10):102003, November 2017. arXiv:1705.02523, doi:10.1103/PhysRevD.96.102003. (cited pp. 74 and 75)

[34] BICEP2/Keck Collaboration and Planck Collaboration. Joint Analysis of BICEP2/Keck Array and Planck Data. *Physical Review Letters*, 114(10):101301, March 2015. arXiv:1502.00612, doi:10.1103/PhysRevLett.114.101301. (cited p. 102)

[35] M. Birkinshaw, S. F. Gull, and H. Hardebeck. The Sunyaev-Zeldovich effect towards three clusters of galaxies. *Nature*, 309:34–35, May 1984. doi:10.1038/309034a0. (cited p. 67)

[36] Nikita Blinov, Kevin J. Kelly, Gordan Krnjaic, and Samuel D. McDermott. Constraining the Self-Interacting Neutrino Interpretation of the Hubble Tension. *Phys. Rev. Letters*, 123(19):191102, Nov 2019. arXiv:1905.02727, doi:10.1103/PhysRevLett.123.191102. (cited p. 10)

[37] Céline Bœhm, Céline Degrande, Olivier Mattelaer, and Aaron C. Vincent. Circular polarisation: a new probe of dark matter and neutrinos in the sky. *Journal of Cosmology and Astroparticle Physics*, 2017(5):043, May 2017. arXiv:1701.02754, doi:10.1088/1475-7516/2017/05/043. (cited p. 158)

[38] S. Borgani. *Cosmology with Clusters of Galaxies*, volume 740, page 24. Nova Science Publishers, 2008. doi:10.1007/978-1-4020-6941-3_9. (cited p. 78)

[39] Alexandre Boucaud, Marc Huertas-Company, Caroline Heneka, Emille E. O. Ishida, Nima Sedaghat, Rafael S. de Souza, Ben Moews, Hervé Dole, Marco Castellano, Emiliano Merlin, Valerio Roscani, Andrea Tramacere, Madhura Killedar, Arlindo M. M. Trindade, and Collaboration COIN. Photometry of high-redshift blended galaxies using deep learning. *Monthly Notices of the Royal Astronomical Society*, 491(2):2481–2495, January 2020. arXiv:1905.01324, doi:10.1093/mnras/stz3056. (cited p. 80)

[40] Judd D. Bowman, Alan E. E. Rogers, Raul A. Monsalve, Thomas J. Mozdzen, and Nivedita Mahesh. An absorption profile centred at 78 megahertz in the sky-averaged spectrum. *Nature*, 555(7694):67–70, March 2018. arXiv:1810.05912, doi:10.1038/nature25792. (cited p. 83)

[41] Emory F. Bunn, Matias Zaldarriaga, Max Tegmark, and Angelica de Oliveira-Costa. E/B decomposition of finite pixelized CMB maps. *Physical Review D*, 67(2):023501, January 2003. arXiv:astro-ph/0207338, doi:10.1103/PhysRevD.67.023501. (cited pp. 45 and 46)

[42] Alessandra Buonanno. Course 1 - Gravitational Waves. In Francis Bernardeau, Christophe Grojean, and Jean Dalibard, editors, *Particle Physics and Cosmology: The Fabric of Spacetime*, volume 86 of *Les Houches*, pages 3 – 52. Elsevier, 2007. ISSN: 0924-8099. URL: http://www.sciencedirect.com/science/article/pii/S0924809907800278, doi:10.1016/S0924-8099(07)80027-8. (cited p. 207)

[43] Scott Burles, Kenneth M. Nollett, and Michael S. Turner. Big-Bang Nucleosynthesis: Linking Inner Space and Outer Space. *arXiv e-prints*, pages astro–ph/9903300, Mar 1999. arXiv:astro-ph/9903300. (cited pp. 18 and 19)

[44] Robert R. Caldwell, Vera Gluscevic, and Marc Kamionkowski. Cross-correlation of cosmological birefringence with CMB temperature. *Physical Review D*, 84(4):043504, August 2011. arXiv:1104.1634, doi:10.1103/PhysRevD.84.043504. (cited p. 74)

[45] M. Calvo, A. Benoît, A. Catalano, J. Goupy, A. Monfardini, N. Ponthieu, E. Barria, G. Bres, M. Grollier, G. Garde, J. P. Leggeri, G. Pont, S. Triqueneaux, R. Adam, O. Bourrion, J. F. Macías-Pérez, M. Rebolo, A. Ritacco, J. P. Scordilis, D. Tourres, A. Adane, G. Coiffard, S. Leclercq, F. X. Désert, S. Doyle, P. Mauskopf, C. Tucker, P. Ade, P. André, A. Beelen, B. Belier, A. Bideaud, N. Billot, B. Comis, A. D'Addabbo, C. Kramer, J. Martino, F. Mayet, F. Pajot, E. Pascale, L. Perotto, V. Revéret, A. Ritacco, L. Rodriguez, G. Savini, K. Schuster, A. Sievers, and R. Zylka. The NIKA2 Instrument, A Dual-Band Kilopixel KID Array for Millimetric Astronomy. *Journal of Low Temperature Physics*, 184(3-4):816–823, August 2016. arXiv:1601.02774, doi:10.1007/s10909-016-1582-0. (cited p. 111)

[46] David Camarena and Valerio Marra. Local determination of the hubble constant and the deceleration parameter. *Phys. Rev. Research*, 2:013028, Jan 2020. URL: https://link.aps.org/doi/10.1103/

PhysRevResearch.2.013028, doi:10.1103/PhysRevResearch.2.013028. (cited p. 11)

[47] Chiara Caprini and Daniel G. Figueroa. Cosmological backgrounds of gravitational waves. *Classical and Quantum Gravity*, 35(16):163001, August 2018. arXiv:1801.04268, doi:10.1088/1361-6382/aac608. (cited p. 90)

[48] Jean-François Cardoso, Maude Le Jeune, Jacques Delabrouille, Marc Betoule, and Guillaume Patanchon. Component Separation With Flexible Models—Application to Multichannel Astrophysical Observations. *IEEE Journal of Selected Topics in Signal Processing*, 2(5):735–746, November 2008. doi:10.1109/JSTSP.2008.2005346. (cited p. 104)

[49] B. J. Carr. Baryonic dark matter. *Comments on Astrophysics*, 14(5):257–280, Feb 1990. (cited p. 13)

[50] Sean M. Carroll. Quintessence and the rest of the world: Suppressing long-range interactions. *Phys. Rev. Lett.*, 81:3067–3070, Oct 1998. URL: https://link.aps.org/doi/10.1103/PhysRevLett.81.3067, doi:10.1103/PhysRevLett.81.3067. (cited p. 74)

[51] Hsin-Yu Chen, Maya Fishbach, and Daniel E. Holz. A two per cent Hubble constant measurement from standard sirens within five years. *Nature*, 562(7728):545–547, Oct 2018. arXiv:1712.06531, doi:10.1038/s41586-018-0606-0. (cited p. 10)

[52] H. Y. Cheng. The strong CP problem revisited. *Physical Reports*, 158(1):1–89, Jan 1988. doi:10.1016/0370-1573(88)90135-4. (cited pp. 12 and 65)

[53] J. Chluba, M. H. Abitbol, N. Aghanim, Y. Ali-Haimoud, M. Alvarez, K. Basu, B. Bolliet, C. Burigana, P. de Bernardis, J. Delabrouille, E. Dimastrogiovanni, F. Finelli, D. Fixsen, L. Hart, C. Hernandez-Monteagudo, J. C. Hill, A. Kogut, K. Kohri, J. Lesgourgues, B. Maffei, J. Mather, S. Mukherjee, S. P. Patil, A. Ravenni, M. Remazeilles, A. Rotti, J. A. Rubino-Martin, J. Silk, R. A. Sunyaev, and E. R. Switzer. New Horizons in Cosmology with Spectral Distortions of the Cosmic Microwave Background. *arXiv e-prints*, September 2019. arXiv:1909.01593. (cited pp. 17 and 70)

[54] J. Chluba and R. A. Sunyaev. The evolution of CMB spectral distortions in the early Universe. *Monthly Notices of the Royal Astronomical Society*, 419(2):1294–1314, January 2012. arXiv:1109.6552, doi:10.1111/j.1365-2966.2011.19786.x. (cited p. 68)

[55] Jens Chluba. Science with CMB spectral distortions. *arXiv e-prints*, page arXiv:1405.6938, May 2014. arXiv:1405.6938. (cited p. 70)

[56] S. K. Choi, J. Austermann, K. Basu, N. Battaglia, F. Bertoldi, D. T. Chung, N. F. Cothard, S. Duff, C. J. Duell, P. A. Gallardo, J. Gao, T. Herter, J. Hubmayr, M. D. Niemack, T. Nikola, D. Riechers, K. Rossi, G. J. Stacey, J. R. Stevens, E. M. Vavagiakis, M. Vissers, and S. Walker. Sensitivity of the

Prime-Cam Instrument on the CCAT-Prime Telescope. *Journal of Low Temperature Physics*, 199(3-4):1089–1097, March 2020. arXiv:1908.10451, doi:10.1007/s10909-020-02428-z. (cited p. 111)

[57] Steve K. Choi, Matthew Hasselfield, Shuay-Pwu Patty Ho, Brian Koopman, Marius Lungu, and The ACT Collaboration. The Atacama Cosmology Telescope: A Measurement of the Cosmic Microwave Background Power Spectra at 98 and 150 GHz. *arXiv e-prints*, page arXiv:2007.07289, July 2020. arXiv:2007.07289. (cited p. 57)

[58] John Clarke and Alex I. Braginski. *The SQUID Handbook*, volume 1. Wiley-ICH, 2006. (cited p. 115)

[59] Alain Coc, Elisabeth Vangioni-Flam, Pierre Descouvemont, Abderrahim Adahchour, and Carmen Angulo. Updated Big Bang Nucleosynthesis Compared with Wilkinson Microwave Anisotropy Probe Observations and the Abundance of Light Elements. *The Astrophysical Journal*, 600(2):544–552, Jan 2004. arXiv:astro-ph/0309480, doi:10.1086/380121. (cited p. 18)

[60] The ALICE Collaboration. The ALICE experiment at the CERN LHC. *Journal of Instrumentation*, 3(08):S08002–S08002, aug 2008. doi:10.1088/1748-0221/3/08/s08002. (cited p. 93)

[61] The CMB-S4 Collaboration. CMB-S4 Science Book, First Edition. *arXiv e-prints*, page arXiv:1610.02743, October 2016. arXiv:1610.02743. (cited p. 115)

[62] The CMB-S4 Collaboration. CMB-S4 Technology Book, First Edition. *arXiv e-prints*, June 2017. arXiv:1706.02464. (cited p. 124)

[63] The IceCube Collaboration, Fermi-LAT, MAGIC, AGILE, ASAS-SN, HAWC, H.E.S.S., INTEGRAL, Kanata, Kiso, Kapteyn, Liverpool Telescope, Subaru, Swift/NuSTAR, VERITAS, and VLA/17B-403. Multimessenger observations of a flaring blazar coincident with high-energy neutrino IceCube-170922A. *Science*, 361(6398):eaat1378, July 2018. arXiv:1807.08816, doi:10.1126/science.aat1378. (cited p. 93)

[64] The LiteBIRD Collaboration. LiteBIRD: an all-sky cosmic microwave background probe of inflation. *Astro2020 APC White Paper*, page 17, 2020. (cited p. 125)

[65] The T2K Collaboration. Constraint on the Matter-Antimatter Symmetry-Violating Phase in Neutrino Oscillations. *arXiv e-prints*, October 2019. arXiv:1910.03887. (cited pp. 92 and 93)

[66] Edward Collett and Society of Photo-optical Instrumentation Engineers. *Field guide to polarization*. SPIE, Bellingham, Wash., 2005. OCLC: 435912084. (cited p. 152)

[67] F. Combes and D. Pfenniger. Perspectives for detecting cold H_2_ in outer galactic disks. *Astronomy and Astrophysics*, 327:453–466, Nov 1997. arXiv:astro-ph/9707217. (cited p. 13)

[68] P. C. Cortes, R. M. Crutcher, and W. D. Watson. Line Polarization of Molecular Lines at Radio Frequencies: The Case of DR 21(OH). *The Astrophysical Journal*, 628(2):780–788, August 2005. arXiv:astro-ph/0504258, doi:10.1086/430815. (cited p. 100)

[69] William R. Coulton and David N. Spergel. The bispectrum of polarized galactic foregrounds. *Journal of Cosmology and Astrophysics*, 2019(10):056, October 2019. arXiv:1901.04515, doi:10.1088/1475-7516/2019/10/056. (cited p. 101)

[70] A. T. Crites, J. W. Henning, and The South Pole Telescope Collaboration. Measurements of E-Mode Polarization and Temperature-E-Mode Correlation in the Cosmic Microwave Background from 100 Square Degrees of SPTpol Data. *The Astrophysical Journal*, 805(1):36, May 2015. arXiv:1411.1042, doi:10.1088/0004-637X/805/1/36. (cited p. 142)

[71] M. Crocce, A. J. Ross, I. Sevilla-Noarbe, E. Gaztanaga, J. Elvin-Poole, and Dark Energy Survey Collaboration. Dark Energy Survey year 1 results: galaxy sample for BAO measurement. *Monthly Notices of the Royal Astronomical Society*, 482(2):2807–2822, January 2019. arXiv:1712.06211, doi:10.1093/mnras/sty2522. (cited p. 79)

[72] Kevin T. Crowley, Sara M. Simon, Max Silva-Feaver, Neil Goeckner-Wald, Aamir Ali, Jason Austermann, Michael L. Brown, Yuji Chinone, Ari Cukierman, Bradley Dober, Shannon M. Duff, Jo Dunkley, Josquin Errard, Giulio Fabbian, Patricio A. Gallardo, Shuay-Pwu Patty Ho, Johannes Hubmayr, Brian Keating, Akito Kusaka, Nialh McCallum, Jeff McMahon, Federico Nati, Michael D. Niemack, Giuseppe Puglisi, Mayuri Sathyanarayana Rao, Christian L. Reichardt, Maria Salatino, Praween Siritanasak, Suzanne Staggs, Aritoki Suzuki, Grant Teply, Daniel B. Thomas, Joel N. Ullom, Clara Vergès, Michael R. Vissers, Benjamin Westbrook, Edward J. Wollack, Zhilei Xu, and Ningfeng Zhu. Studies of systematic uncertainties for Simons Observatory: detector array effects. In *Proceedings of SPIE*, volume 10708 of *Society of Photo-Optical Instrumentation Engineers (SPIE) Conference Series*, page 107083Z, July 2018. arXiv:1808.10491, doi:10.1117/12.2313414. (cited pp. 141 and 148)

[73] G. D'Alessandro, L. Mele, F. Columbro, L. Pagano, F. Piacentini, P. de Bernardis, and S. Masi. Systematic effects induced by half-wave plate precession into measurements of the cosmic microwave background polarization. *Astronomy & Astrophysics*, 627:A160, July 2019. arXiv:1906.07010, doi:10.1051/0004-6361/201834495. (not cited)

[74] Leverett Davis, Jr. and Jesse L. Greenstein. The Polarization of Starlight by Aligned Dust Grains. *The Astrophysical Journal*, 114:206, September 1951. doi:10.1086/145464. (cited p. 96)

[75] Pablo F. de Salas and Sergio Pastor. Relic neutrino decoupling with flavour oscillations revisited. *Journal of Cosmology and Astroparticle Physics*, 2016(7):051, July 2016. arXiv:1606.06986, doi:10.1088/1475-7516/2016/07/051. (cited p. 64)

[76] J. Delabrouille, J. F. Cardoso, M. Le Jeune, M. Betoule, G. Fay, and F. Guilloux. A full sky, low foreground, high resolution CMB map from WMAP. *Astronomy & Astrophysics*, 493(3):835–857, January 2009. arXiv:0807.0773, doi:10.1051/0004-6361:200810514. (cited p. 105)

[77] Eleonora Di Valentino, Eric V. Linder, and Alessandro Melchiorri. Vacuum phase transition solves the H_0 tension. *Physical Review D*, 97(4):043528, Feb 2018. arXiv:1710.02153, doi:10.1103/PhysRevD.97.043528. (cited p. 10)

[78] Eleonora Di Valentino, Alessandro Melchiorri, and Joseph Silk. Reconciling Planck with the local value of H_0 in extended parameter space. *Physics Letters B*, 761:242–246, Oct 2016. arXiv:1606.00634, doi:10.1016/j.physletb.2016.08.043. (cited p. 10)

[79] Eleonora Di Valentino, Ankan Mukherjee, and Anjan A. Sen. Dark Energy with Phantom Crossing and the H_0 tension. *arXiv e-prints*, page arXiv:2005.12587, May 2020. arXiv:2005.12587. (cited p. 20)

[80] R. H. Dicke, P. J. E. Peebles, P. G. Roll, and D. T. Wilkinson. Cosmic Black-Body Radiation. *The Astrophysical Journal*, 142:414–419, July 1965. doi:10.1086/148306. (not cited)

[81] Clive Dickinson, Y. Ali-Haïmoud, A. Barr, E. S. Battistelli, A. Bell, L. Bernstein, S. Casassus, K. Cleary, B. T. Draine, R. Génova-Santos, S. E. Harper, B. Hensley, J. Hill-Valler, Thiem Hoang, F. P. Israel, L. Jew, A. Lazarian, J. P. Leahy, J. Leech, C. H. López-Caraballo, I. McDonald, E. J. Murphy, T. Onaka, R. Paladini, M. W. Peel, Y. Perrott, F. Poidevin, A. C. S. Readhead, J. A. Rubiño-Martín, A. C. Taylor, C. T. Tibbs, M. Todorović, and Matias Vidal. The State-of-Play of Anomalous Microwave Emission (AME) research. *New Astronomy Review*, 80:1–28, February 2018. arXiv:1802.08073, doi:10.1016/j.newar.2018.02.001. (cited p. 99)

[82] Alain Dirkes. Gravitational waves — A review on the theoretical foundations of gravitational radiation. *International Journal of Modern Physics A*, 33:1830013, May 2018. arXiv:1802.05958, doi:10.1142/S0217751X18300132. (cited p. 207)

[83] M. A. Dobbs, M. Lueker, K. A. Aird, A. N. Bender, B. A. Benson, L. E. Bleem, J. E. Carlstrom, C. L. Chang, H. M. Cho, J. Clarke, T. M. Crawford, A. T. Crites, D. I. Flanigan, T. de Haan, E. M. George, N. W. Halverson, W. L. Holzapfel, J. D. Hrubes, B. R. Johnson, J. Joseph, R. Keisler, J. Kennedy, Z. Kermish, T. M. Lanting, A. T. Lee, E. M. Leitch, D. Luong-Van, J. J. McMahon, J. Mehl, S. S. Meyer, T. E. Montroy, S. Padin, T. Plagge, C. Pryke, P. L. Richards, J. E. Ruhl, K. K. Schaffer, D. Schwan, E. Shirokoff, H. G. Spieler, Z. Staniszewski, A. A. Stark, K. Vanderlinde, J. D. Vieira, C. Vu, B. Westbrook, and R. Williamson. Frequency multiplexed superconducting quantum interference device readout of large bolometer arrays for cosmic microwave background measurements. *Review of Scientific Instruments*, 83(7):073113–073113–24, July 2012. arXiv:1112.4215, doi:10.1063/1.4737629. (cited pp. 114 and 142)

[84] B. Dober, D. T. Becker, D. A. Bennett, S. A. Bryan, S. M. Duff, J. D. Gard, J. P. Hays-Wehle, G. C. Hilton, J. Hubmayr, J. A. B. Mates, C. D. Reintsema, L. R. Vale, and J. N. Ullom. Microwave SQUID multiplexer demonstration for cosmic microwave background imagers. *Applied Physics Letters*, 111(24):243510, December 2017. arXiv:1710.04326, doi:10.1063/1.5008527. (cited pp. 116 and 142)

[85] P. J. Doe, J. Kofron, E. L. McBride, R. G. H. Robertson, L. J Rosenberg, G. Rybka, S. Doelman, A. Rogers, J. A. Formaggio, D. Furse, N. S. Oblath, B. H. LaRoque, M. Leber, B. Monreal, M. Bahr, D. M. Asner, A. M. Jones, J. Fernandes, B. A. VanDevender, R. Patterson, R. Bradley, and T. Thuemmler. Project 8: Determining neutrino mass from tritium beta decay using a frequency-based method. *arXiv e-prints*, September 2013. arXiv:1309.7093. (cited p. 92)

[86] B. T. Draine and Brandon S. Hensley. On the Shapes of Interstellar Grains: Modeling Extinction and Polarization by Speroids and Continuous Distributions of Ellipsoids. *arXiv e-prints*, October 2017. arXiv:1710.08968. (cited p. 98)

[87] Raymond H. DuHamel. Dual polarized sinuous antennas, April 1987. Library Catalog: Google Patents. URL: https://patents.google.com/patent/US4658262A/en. (cited p. 117)

[88] EBEX Collaboration, Asad M. Aboobaker, Peter Ade, Derek Araujo, François Aubin, Carlo Baccigalupi, Chaoyun Bao, Daniel Chapman, Joy Didier, Matt Dobbs, Christopher Geach, Will Grainger, Shaul Hanany, Kyle Helson, Seth Hillbrand, Johannes Hubmayr, Andrew Jaffe, Bradley Johnson, Terry Jones, Jeff Klein, Andrei Korotkov, Adrian Lee, Lorne Levinson, Michele Limon, Kevin MacDermid, Tomotake Matsumura, Amber D. Miller, Michael Milligan, Kate Raach, Britt Reichborn-Kjennerud, Ilan Sagiv, Giorgio Savini, Locke Spencer, Carole Tucker, Gregory S. Tucker, Benjamin Westbrook, Karl Young, and Kyle Zilic. The EBEX Balloon-borne Experiment—Optics, Receiver, and Polarimetry. *The Astrophysical Journal, Supplement*, 239(1):7, Nov 2018. arXiv:1703.03847, doi:10.3847/1538-4365/aae434. (cited p. 160)

[89] Albert Einstein. Näherungsweise Integration der Feldgleichungen der Gravitation. *Sitzungsberichte der Königlich Preußischen Akademie der Wissenschaften (Berlin*, pages 688–696, January 1916. (cited p. 88)

[90] Albert Einstein. Cosmological considerations in the general theory of relativity. *Sitzungsber.Preuss.Akad.Wiss.Berlin (Math.Phys.)*, 142, 1917. (cited pp. 2 and 5)

[91] Albert Einstein. Über Gravitationswellen. *Sitzungsberichte der Königlich Preußischen Akademie der Wissenschaften (Berlin*, pages 154–167, January 1918. (cited p. 88)

[92] Torsten A. Enßlin, Sebastian Hutschenreuter, Valentina Vacca, and Niels Oppermann. The Galaxy in circular polarization: All-sky radio predic-

tion, detection strategy, and the charge of the leptonic cosmic rays. *Physical Review D*, 96(4):043021, August 2017. arXiv:1706.08539, doi:10.1103/PhysRevD.96.043021. (cited p. 158)

[93] H. K. Eriksen, A. J. Banday, K. M. Górski, and P. B. Lilje. On Foreground Removal from the Wilkinson Microwave Anisotropy Probe Data by an Internal Linear Combination Method: Limitations and Implications. *The Astrophysical Journal*, 612(2):633–646, September 2004. arXiv:astro-ph/0403098, doi:10.1086/422807. (cited p. 104)

[94] H. K. Eriksen, J. B. Jewell, C. Dickinson, A. J. Band ay, K. M. Górski, and C. R. Lawrence. Joint Bayesian Component Separation and CMB Power Spectrum Estimation. *The Astrophysical Journal*, 676(1):10–32, March 2008. arXiv:0709.1058, doi:10.1086/525277. (cited pp. 106 and 169)

[95] J. Errard, F. Stivoli, and R. Stompor. Publisher's Note: Framework for performance forecasting and optimization of CMB B-mode observations in the presence of astrophysical foregrounds [Phys. Rev. D 84, 063005 (2011)]. *Physical Review D*, 84(6):069907, Sep 2011. arXiv:1105.3859, doi:10.1103/PhysRevD.84.069907. (cited pp. 106, 169, 171, and 174)

[96] J. Errard and R. Stompor. Astrophysical foregrounds and primordial tensor-to-scalar ratio constraints from cosmic microwave background B-mode polarization observations. *Physical Review D*, 85(8):083006, April 2012. arXiv:1203.5285, doi:10.1103/PhysRevD.85.083006. (cited pp. 106, 170, 171, and 175)

[97] c. Fabry and A. Pérot. Théorie et applications d'une nouvelle methode de spectroscopie interférentielle. *Ann. Chim. Phys.*, 16(7), 1899. (cited p. 90)

[98] Amand Faessler, Rastislav Hodák, Sergey Kovalenko, and Fedor Šimkovic. Can one measure the Cosmic Neutrino Background? *International Journal of Modern Physics E*, 26:1740008, January 2017. arXiv:1602.03347, doi:10.1142/S0218301317400080. (cited p. 92)

[99] George B. Field. The Spin Temperature of Intergalactic Neutral Hydrogen. *The Astrophysical Journal*, 129:536, May 1959. doi:10.1086/146653. (cited p. 83)

[100] Douglas P. Finkbeiner, Marc Davis, and David J. Schlegel. Extrapolation of Galactic Dust Emission at 100 Microns to Cosmic Microwave Background Radiation Frequencies Using FIRAS. *The Astrophysical Journal*, 524(2):867–886, October 1999. arXiv:astro-ph/9905128, doi:10.1086/307852. (cited p. 98)

[101] D. J. Fixsen, E. S. Cheng, D. A. Cottingham, Jr. Eplee, R. E., R. B. Isaacman, J. C. Mather, S. S. Meyer, P. D. Noerdlinger, R. A. Shafer, R. Weiss, E. L. Wright, C. L. Bennett, N. W. Boggess, T. Kelsall, S. H. Moseley, R. F. Silverberg, G. F. Smoot, and D. T. Wilkinson. Cosmic Microwave Background Dipole Spectrum Measured by the COBE FIRAS Instrument. *The Astrophysical Journal*, 420:445, Jan 1994. doi:10.1086/173575. (cited p. 71)

[102] Brent Follin, Lloyd Knox, Marius Millea, and Zhen Pan. First detection of the acoustic oscillation phase shift expected from the cosmic neutrino background. *Physical Review Letters*, 115:091301, Aug 2015. URL: https://link.aps.org/doi/10.1103/PhysRevLett.115.091301, doi:10.1103/PhysRevLett.115.091301. (cited p. 17)

[103] Alexander Friedmann. Über die Krümmung des Raumes. *Zeitschrift fur Physik*, 10:377–386, Jan 1922. doi:10.1007/BF01332580. (cited p. 6)

[104] Y. Fukuda, T. Hayakawa, E. Ichihara, K. Inoue, K. Ishihara, H. Ishino, Y. Itow, T. Kajita, J. Kameda, S. Kasuga, K. Kobayashi, Y. Kobayashi, Y. Koshio, M. Miura, M. Nakahata, S. Nakayama, A. Okada, K. Okumura, N. Sakurai, M. Shiozawa, Y. Suzuki, Y. Takeuchi, Y. Totsuka, S. Yamada, M. Earl, A. Habig, E. Kearns, M. D. Messier, K. Scholberg, J. L. Stone, L. R. Sulak, C. W. Walter, M. Goldhaber, T. Barszczxak, D. Casper, W. Gajewski, P. G. Halverson, J. Hsu, W. R. Kropp, L. R. Price, F. Reines, M. Smy, H. W. Sobel, M. R. Vagins, K. S. Ganezer, W. E. Keig, R. W. Ellsworth, S. Tasaka, J. W. Flanagan, A. Kibayashi, J. G. Learned, S. Matsuno, V. J. Stenger, D. Takemori, T. Ishii, J. Kanzaki, T. Kobayashi, S. Mine, K. Nakamura, K. Nishikawa, Y. Oyama, A. Sakai, M. Sakuda, O. Sasaki, S. Echigo, M. Kohama, A. T. Suzuki, T. J. Haines, E. Blaufuss, B. K. Kim, R. Sanford, R. Svoboda, M. L. Chen, Z. Conner, J. A. Goodman, G. W. Sullivan, J. Hill, C. K. Jung, K. Martens, C. Mauger, C. McGrew, E. Sharkey, B. Viren, C. Yanagisawa, W. Doki, K. Miyano, H. Okazawa, C. Saji, M. Takahata, Y. Nagashima, M. Takita, T. Yamaguchi, M. Yoshida, S. B. Kim, M. Etoh, K. Fujita, A. Hasegawa, T. Hasegawa, S. Hatakeyama, T. Iwamoto, M. Koga, T. Maruyama, H. Ogawa, J. Shirai, A. Suzuki, F. Tsushima, M. Koshiba, M. Nemoto, K. Nishijima, T. Futagami, Y. Hayato, Y. Kanaya, K. Kaneyuki, Y. Watanabe, D. Kielczewska, R. A. Doyle, J. S. George, A. L. Stachyra, L. L. Wai, R. J. Wilkes, and K. K. Young. Evidence for Oscillation of Atmospheric Neutrinos. *Phys. Rev. Letters*, 81(8):1562–1567, Aug 1998. arXiv:hep-ex/9807003, doi:10.1103/PhysRevLett.81.1562. (cited p. 14)

[105] R. Génova-Santos, J. A. Rubiño-Martín, R. Rebolo, A. Peláez-Santos, C. H. López-Caraballo, S. Harper, R. A. Watson, M. Ashdown, R. B. Barreiro, B. Casaponsa, C. Dickinson, J. M. Diego, R. Fernández-Cobos, K. J. B. Grainge, C. M. Gutiérrez, D. Herranz, R. Hoyland, A. Lasenby, M. López-Caniego, E. Martínez-González, M. McCulloch, S. Melhuish, L. Piccirillo, Y. C. Perrott, F. Poidevin, N. Razavi-Ghods, P. F. Scott, D. Titterington, D. Tramonte, P. Vielva, and R. Vignaga. QUIJOTE scientific results - I. Measurements of the intensity and polarisation of the anomalous microwave emission in the Perseus molecular complex. *Monthly Notices of the Royal Astronomical Society*, 452(4):4169–4182, October 2015. arXiv:1501.04491, doi:10.1093/mnras/stv1405. (cited p. 99)

[106] Y. Gershon, T. andNir. Cp violation in the quark sector. http://pdg.lbl.gov/2019/reviews/rpp2019-rev-cp-violation.pdf, 2019. (cited p. 92)

[107] Tommaso Ghigna, Tomotake Matsumura, Guillaume Patanchon, Hirokazu

Ishino, and Masashi Hazumi. Requirements for future CMB satellite missions: photometric and band-pass response calibration. *arXiv e-prints*, page arXiv:2004.11601, April 2020. arXiv:2004.11601. (cited p. 191)

[108] Héctor Gil-Marín, Will J. Percival, Joel R. Brownstein, Chia-Hsun Chuang, Jan Niklas Grieb, Shirley Ho, Francisco-Shu Kitaura, Claudia Maraston, Francisco Prada, Sergio Rodríguez-Torres, Ashley J. Ross, Lado Samushia, David J. Schlegel, Daniel Thomas, Jeremy L. Tinker, and Gong-Bo Zhao. The clustering of galaxies in the SDSS-III Baryon Oscillation Spectroscopic Survey: RSD measurement from the LOS-dependent power spectrum of DR12 BOSS galaxies. *Monthly Notices of the Royal Astronomical Society*, 460(4):4188–4209, August 2016. arXiv:1509.06386, doi:10.1093/mnras/stw1096. (cited p. 81)

[109] Héctor Gil-Marín, Will J. Percival, Licia Verde, Joel R. Brownstein, Chia-Hsun Chuang, Francisco-Shu Kitaura, Sergio A. Rodríguez-Torres, and Matthew D. Olmstead. The clustering of galaxies in the SDSS-III Baryon Oscillation Spectroscopic Survey: RSD measurement from the power spectrum and bispectrum of the DR12 BOSS galaxies. *Monthly Notices of the Royal Astronomical Society*, 465(2):1757–1788, February 2017. arXiv:1606.00439, doi:10.1093/mnras/stw2679. (cited p. 81)

[110] J. Grain, M. Tristram, and R. Stompor. Polarized CMB power spectrum estimation using the pure pseudo-cross-spectrum approach. *Physical Review D*, 79(12):123515, June 2009. arXiv:0903.2350, doi:10.1103/PhysRevD.79.123515. (cited pp. 46 and 206)

[111] R. Graziani, M. Rigault, N. Regnault, Ph. Gris, A. Möller, P. Antilogus, P. Astier, M. Betoule, S. Bongard, M. Briday, J. Cohen-Tanugi, Y. Copin, H. M. Courtois, D. Fouchez, E. Gangler, D. Guinet, A. J. Hawken, Y. L. Kim, P. F. Léget, J. Neveu, P. Ntelis, Ph. Rosnet, and E. Nuss. Peculiar velocity cosmology with type Ia supernovae. *arXiv e-prints*, January 2020. arXiv:2001.09095. (cited p. 87)

[112] L. Grigori, R. Stompor, and M. Szydlarski. A parallel two-level preconditioner for cosmic microwave background map-making. In *SC '12: Proceedings of the International Conference on High Performance Computing, Networking, Storage and Analysis*, pages 1–10, 2012. (not cited)

[113] LHC Dark Matter Working Group. Dark Matter Benchmark Models for Early LHC Run-2 Searches: Report of the ATLAS/CMS Dark Matter Forum. *arXiv e-prints*, page arXiv:1507.00966, July 2015. arXiv:1507.00966. (cited p. 94)

[114] Mario Hamuy, M. M. Phillips, Jose Maza, Nicholas B. Suntzeff, R. A. Schommer, and R. Aviles. A Hubble Diagram of Distant Type 1a Supernovae. *Astronomical Journal*, 109:1, January 1995. doi:10.1086/117251. (cited p. 85)

[115] Nick Hand, Graeme E. Addison, Eric Aubourg, Nick Battaglia, Elia S. Battistelli, Dmitry Bizyaev, J. Richard Bond, Howard Brewington, Jon

Brinkmann, Benjamin R. Brown, Sudeep Das, Kyle S. Dawson, Mark J. Devlin, Joanna Dunkley, Rolando Dunner, Daniel J. Eisenstein, Joseph W. Fowler, Megan B. Gralla, Amir Hajian, Mark Halpern, Matt Hilton, Adam D. Hincks, Renée Hlozek, John P. Hughes, Leopoldo Infante, Kent D. Irwin, Arthur Kosowsky, Yen-Ting Lin, Elena Malanushenko, Viktor Malanushenko, Tobias A. Marriage, Danica Marsden, Felipe Menanteau, Kavilan Moodley, Michael D. Niemack, Michael R. Nolta, Daniel Oravetz, Lyman A. Page, Nathalie Palanque-Delabrouille, Kaike Pan, Erik D. Reese, David J. Schlegel, Donald P. Schneider, Neelima Sehgal, Alaina Shelden, Jon Sievers, Cristóbal Sifón, Audrey Simmons, Stephanie Snedden, David N. Spergel, Suzanne T. Staggs, Daniel S. Swetz, Eric R. Switzer, Hy Trac, Benjamin A. Weaver, Edward J. Wollack, Christophe Yeche, and Caroline Zunckel. Evidence of Galaxy Cluster Motions with the Kinematic Sunyaev-Zel'dovich Effect. *Physical Review Letters*, 109(4):041101, July 2012. arXiv:1203.4219, doi:10.1103/PhysRevLett.109.041101. (cited p. 67)

[116] F. K. Hansen, A. J. Banday, H. K. Eriksen, K. M. Górski, and P. B. Lilje. Foreground Subtraction of Cosmic Microwave Background Maps Using WI-FIT (Wavelet-Based High-Resolution Fitting of Internal Templates). *The Astrophysical Journal*, 648(2):784–796, September 2006. arXiv:astro-ph/0603308, doi:10.1086/506015. (cited p. 103)

[117] D. Hanson, S. Hoover, A. Crites, and The South Pole Telescope Collaboration. Detection of B-Mode Polarization in the Cosmic Microwave Background with Data from the South Pole Telescope. *Physical Review Letters*, 111(14):141301, October 2013. arXiv:1307.5830, doi:10.1103/PhysRevLett.111.141301. (cited p. 56)

[118] Kathleen Harrington, Joseph Eimer, David T. Chuss, Matthew Petroff, Joseph Cleary, Martin DeGeorge, Theodore W. Grunberg, Aamir Ali, John W. Appel, Charles L. Bennett, Michael Brewer, Ricardo Bustos, Manwei Chan, Jullianna Couto, Sumit Dahal, Kevin Denis, Rolando Dünner, Thomas Essinger-Hileman, Pedro Fluxa, Mark Halpern, Gene Hilton, Gary F. Hinshaw, Johannes Hubmayr, Jeffrey Iuliano, John Karakla, Tobias Marriage, Jeffrey McMahon, Nathan J. Miller, Carolina Nuñez, Ivan L. Padilla, Gonzalo Palma, Lucas Parker, Bastian Pradenas Marquez, Rodrigo Reeves, Carl Reintsema, Karwan Rostem, Deniz Augusto Nunes Valle, Trevor Van Engelhoven, Bingjie Wang, Qinan Wang, Duncan Watts, Janet Weiland , Edward Wollack, Zhilei Xu, Ziang Yan, and Lingzhen Zeng. Variable-delay polarization modulators for the CLASS telescopes. In *Proceedings of SPIE*, volume 10708 of *Society of Photo-Optical Instrumentation Engineers (SPIE) Conference Series*, page 107082M, July 2018. arXiv:1807.03807, doi:10.1117/12.2313614. (cited p. 113)

[119] E. R. Harrison. Fluctuations at the Threshold of Classical Cosmology. *Physical Review D*, 1(10):2726–2730, May 1970. doi:10.1103/PhysRevD.1.2726. (cited p. 37)

[120] Michael G. Hauser and Eli Dwek. The cosmic infrared background: Measurements and implications. *Annual Review of Astronomy and Astrophysics*,

39:249–307, January 2001. arXiv:astro-ph/0105539, doi:10.1146/annurev.astro.39.1.249. (cited p. 84)

[121] Stephen Hawking. Gravitationally collapsed objects of very low mass. *Monthly Notices of the Royal Astronomical Society*, 152:75, Jan 1971. doi:10.1093/mnras/152.1.75. (cited p. 12)

[122] Shawn W. Henderson, Zeeshan Ahmed, Jason Austermann, Daniel Becker, Douglas A. Bennett, David Brown, Saptarshi Chaudhuri, Hsiao-Mei Sherry Cho, John M. D'Ewart, Bradley Dober, Shannon M. Duff, John E. Dusatko, Sofia Fatigoni, Josef C. Frisch, Jonathon D. Gard, Mark Halpern, Gene C. Hilton, Johannes Hubmayr, Kent D. Irwin, Ethan D. Karpel, Sarah S. Kernasovskiy, Stephen E. Kuenstner, Chao-Lin Kuo, Dale Li, John A. B. Mates, Carl D. Reintsema, Stephen R. Smith, Joel Ullom, Leila R. Vale, Daniel D. Van Winkle, Michael Vissers, and Cyndia Yu. Highly-multiplexed microwave SQUID readout using the SLAC Microresonator Radio Frequency (SMuRF) electronics for future CMB and sub-millimeter surveys. In *SPIE Proceedings*, volume 10708 of *Society of Photo-Optical Instrumentation Engineers (SPIE) Conference Series*, page 1070819, July 2018. arXiv:1809.03689, doi:10.1117/12.2314435. (cited pp. 116 and 142)

[123] J. W. Henning, J. T. Sayre, C. L. Reichardt, and The SPT Collaboration. Measurements of the Temperature and E-mode Polarization of the CMB from 500 Square Degrees of SPTpol Data. *The Astrophysical Journal*, 852(2):97, January 2018. arXiv:1707.09353, doi:10.3847/1538-4357/aa9ff4. (cited p. 148)

[124] Brandon S. Hensley and Philip Bull. Mitigating Complex Dust Foregrounds in Future Cosmic Microwave Background Polarization Experiments. *The Astrophysical Journal*, 853(2):127, January 2018. Publisher: American Astronomical Society. doi:10.3847/1538-4357/aaa489. (cited p. 101)

[125] Roger H. Hildebrand, Larry Kirby, Jessie L. Dotson, Martin Houde, and John E. Vaillancourt. Dispersion of Magnetic Fields in Molecular Clouds. I. *The Astrophysical Journal*, 696(1):567–573, May 2009. arXiv:0811.0813, doi:10.1088/0004-637X/696/1/567. (cited p. 97)

[126] Charles A. Hill, Shawn Beckman, Yuji Chinone, Neil Goeckner-Wald, Masashi Hazumi, Brian Keating, Akito Kusaka, Adrian T. Lee, Frederick Matsuda, Richard Plambeck, Aritoki Suzuki, and Satoru Takakura. Design and development of an ambient-temperature continuously-rotating achromatic half-wave plate for CMB polarization modulation on the POLARBEAR-2 experiment. *arXiv:1607.07399 [astro-ph]*, page 99142U, July 2016. arXiv: 1607.07399. URL: http://arxiv.org/abs/1607.07399, doi:10.1117/12.2232280. (cited pp. 138, 154, and 180)

[127] Henk Hoekstra and Bhuvnesh Jain. Weak gravitational lensing and its cosmological applications. *Annual Review of Nuclear and Particle Science*, 58(1):99–123, 2008. arXiv:https://doi.org/10.1146/annurev.nucl.58.110707.171151, doi:10.1146/annurev.nucl.58.110707.171151. (cited p. 80)

[128] Wayne Hu. Weak lensing of the CMB: A harmonic approach. *Physical Review D.*, 62(4):043007, August 2000. arXiv:astro-ph/0001303, doi:10.1103/PhysRevD.62.043007. (cited pp. 49 and 57)

[129] Wayne Hu. Lecture Notes on CMB Theory: From Nucleosynthesis to Recombination. *arXiv e-prints*, February 2008. arXiv:0802.3688. (not cited)

[130] Wayne Hu and Scott Dodelson. Cosmic Microwave Background Anisotropies. *Annual Review of Astronomy and Astrophysics*, 40:171–216, January 2002. arXiv:astro-ph/0110414, doi:10.1146/annurev.astro.40.060401.093926. (cited p. 41)

[131] Edwin Hubble. A Relation between Distance and Radial Velocity among Extra-Galactic Nebulae. *Proceedings of the National Academy of Science*, 15(3):168–173, Mar 1929. doi:10.1073/pnas.15.3.168. (cited p. 5)

[132] Kiyotomo Ichiki. CMB foreground: A concise review. *Progress of Theoretical and Experimental Physics*, 2014(6):06B109, June 2014. doi:10.1093/ptep/ptu065. (cited p. 104)

[133] Kiyotomo Ichiki, Hiroaki Kanai, Nobuhiko Katayama, and Eiichiro Komatsu. Delta-map method of removing CMB foregrounds with spatially varying spectra. *Progress of Theoretical and Experimental Physics*, 2019(3):033E01, March 2019. arXiv:1811.03886, doi:10.1093/ptep/ptz009. (cited p. 103)

[134] Donghui Jeong and Marc Kamionkowski. Gravitational Waves, CMB Polarization, and the Hubble Tension. *Phys. Rev. Letters*, 124(4):041301, Jan 2020. arXiv:1908.06100, doi:10.1103/PhysRevLett.124.041301. (cited p. 10)

[135] Elmar K. Jessberger, Thomas Stephan, Detlef Rost, Peter Arndt, Mischa Maetz, Frank J. Stadermann, Don E. Brownlee, John P. Bradley, and Gero Kurat. *Properties of Interplanetary Dust: Information from Collected Samples*, pages 253–294. Springer Berlin Heidelberg, Berlin, Heidelberg, 2001. URL: https://doi.org/10.1007/978-3-642-56428-4_6, doi:10.1007/978-3-642-56428-4_6. (cited p. 97)

[136] B. R. Johnson, J. Collins, M. E. Abroe, P. A. R. Ade, J. Bock, J. Borrill, A. Boscaleri, P. de Bernardis, S. Hanany, A. H. Jaffe, T. Jones, A. T. Lee, L. Levinson, T. Matsumura, B. Rabii, T. Renbarger, P. L. Richards, G. F. Smoot, R. Stompor, H. T. Tran, C. D. Winant, J. H. P. Wu, and J. Zuntz. MAXIPOL: Cosmic Microwave Background Polarimetry Using a Rotating Half-Wave Plate. *The Astrophysical Journal*, 665(1):42–54, August 2007. arXiv:astro-ph/0611394, doi:10.1086/518105. (cited p. 132)

[137] B. R. Johnson, J. Collins, M. E. Abroe, P. A. R. Ade, J. Bock, J. Borrill, A. Boscaleri, P. de Bernardis, S. Hanany, A. H. Jaffe, T. Jones, A. T. Lee, L. Levinson, T. Matsumura, B. Rabii, T. Renbarger, P. L. Richards, G. F. Smoot, R. Stompor, H. T. Tran, C. D. Winant, J. H. P. Wu, and J. Zuntz.

MAXIPOL: Cosmic Microwave Background Polarimetry Using a Rotating Half-Wave Plate. *The Astrophysical Journal*, 665(1):42–54, Aug 2007. arXiv:astro-ph/0611394, doi:10.1086/518105. (cited p. 160)

[138] Nick Kaiser. Clustering in real space and in redshift space. *Monthly Notices of the Royal Astronomical Society*, 227:1–21, July 1987. doi:10.1093/mnras/227.1.1. (cited p. 81)

[139] Marc Kamionkowski. How to Derotate the Cosmic Microwave Background Polarization. *Physical Review Letters*, 102(11):111302, March 2009. arXiv:0810.1286, doi:10.1103/PhysRevLett.102.111302. (cited p. 75)

[140] Marc Kamionkowski and Ely D. Kovetz. The Quest for B Modes from Inflationary Gravitational Waves. *Annual Review of Astronomy and Astrophysics*, 54:227–269, September 2016. arXiv:1510.06042, doi:10.1146/annurev-astro-081915-023433. (not cited)

[141] A. Kashlinsky. Cosmic infrared background and early galaxy evolution [review article]. *Physical Reports*, 409(6):361–438, April 2005. arXiv:astro-ph/0412235, doi:10.1016/j.physrep.2004.12.005. (cited p. 84)

[142] Nobuhiko Katayama and Eiichiro Komatsu. Simple Foreground Cleaning Algorithm for Detecting Primordial B-mode Polarization of the Cosmic Microwave Background. *The Astrophysical Journal*, 737(2):78, August 2011. arXiv:1101.5210, doi:10.1088/0004-637X/737/2/78. (cited p. 103)

[143] Zigmund D. Kermish and The POLARBEAR Collaboration. The POLARBEAR experiment. In *Proceedings of SPIE*, volume 8452 of *Society of Photo-Optical Instrumentation Engineers (SPIE) Conference Series*, page 84521C, September 2012. arXiv:1210.7768, doi:10.1117/12.926354. (cited pp. 128 and 138)

[144] Soma King and Philip Lubin. Circular polarization of the CMB: Foregrounds and detection prospects. *Physical Review D*, 94(2):023501, July 2016. arXiv:1606.04112, doi:10.1103/PhysRevD.94.023501. (cited p. 158)

[145] Tetsu Kitayama, Shutaro Ueda, Shigehisa Takakuwa, Takahiro Tsutsumi, Eiichiro Komatsu, Takuya Akahori, Daisuke Iono, Takuma Izumi, Ryohei Kawabe, Kotaro Kohno, Hiroshi Matsuo, Naomi Ota, Yasushi Suto, Motozaku Takizawa, and Kohji Yoshikawa. The Sunyaev-Zel'dovich effect at 5″: RX J1347.5-1145 imaged by ALMA. *Publications of the ASJ*, 68(5):88, October 2016. arXiv:1607.08833, doi:10.1093/pasj/psw082. (cited p. 67)

[146] A. Kogut. SYNCHROTRON SPECTRAL CURVATURE FROM 22 MHz TO 23 GHz. *The Astrophysical Journal*, 753(2):110, jun 2012. doi:10.1088/0004-637x/753/2/110. (cited p. 100)

[147] A. Kogut, J. Dunkley, C. L. Bennett, O. Doré, B. Gold, M. Halpern, G. Hinshaw, N. Jarosik, E. Komatsu, M. R. Nolta, N. Odegard, L. Page, D. N. Spergel, G. S. Tucker, J. L. Weiland, E. Wollack, and E. L. Wright. Three-Year Wilkinson Microwave Anisotropy Probe (WMAP) Observations: Foreground Polarization. *The Astrophysical Journal*, 665(1):355–362, August 2007. arXiv:0704.3991, doi:10.1086/519754. (cited p. 100)

[148] A. Kogut, D. J. Fixsen, D. T. Chuss, J. Dotson, E. Dwek, M. Halpern, G. F. Hinshaw, S. M. Meyer, S. H. Moseley, M. D. Seiffert, D. N. Spergel, and E. J. Wollack. The Primordial Inflation Explorer (PIXIE): a nulling polarimeter for cosmic microwave background observations. *Journal of Cosmology and Antiparticle Physics*, 2011(7):025, July 2011. arXiv:1105.2044, doi:10.1088/1475-7516/2011/07/025. (cited p. 71)

[149] Eiichiro Komatsu and David N. Spergel. Acoustic signatures in the primary microwave background bispectrum. *Physical Review D*, 63(6):063002, March 2001. arXiv:astro-ph/0005036, doi:10.1103/PhysRevD.63.063002. (cited p. 73)

[150] Kunimoto Komatsu, Tomotake Matsumura, Hiroaki Imada, Hirokazu Ishino, Nobuhiko Katayama, and Yuki Sakurai. Demonstration of the broadband half-wave plate using the nine-layer sapphire for the CMB polarization experiment. *arXiv e-prints*, page arXiv:1905.13520, May 2019. arXiv:1905.13520. (cited pp. 117, 152, and 181)

[151] Kunimoto Komatsu, Tomotake Matsumura, Hiroaki Imada, Hirokazu Ishino, Nobuhiko Katayama, and Yuki Sakurai. Demonstration of the broadband half-wave plate using the nine-layer sapphire for the CMB polarization experiment. *arXiv:1905.13520 [astro-ph]*, May 2019. arXiv:1905.13520. URL: http://arxiv.org/abs/1905.13520. (cited p. 154)

[152] J. M. Kovac, E. M. Leitch, C. Pryke, J. E. Carlstrom, N. W. Halverson, and W. L. Holzapfel. Detection of polarization in the cosmic microwave background using DASI. *Nature*, 420(6917):772–787, December 2002. arXiv:astro-ph/0209478, doi:10.1038/nature01269. (cited p. 56)

[153] N. Krachmalnicoff, C. Baccigalupi, J. Aumont, M. Bersanelli, and A. Mennella. Characterization of foreground emission on degree angular scales for CMB B-mode observations . Thermal dust and synchrotron signal from Planck and WMAP data. *Astronomy & Astrophysics*, 588:A65, April 2016. arXiv:1511.00532, doi:10.1051/0004-6361/201527678. (cited p. 97)

[154] N. Krachmalnicoff, E. Carretti, C. Baccigalupi, G. Bernardi, S. Brown, B. M. Gaensler, M. Haverkorn, M. Kesteven, F. Perrotta, S. Poppi, and L. Staveley-Smith. S-PASS view of polarized Galactic synchrotron at 2.3 GHz as a contaminant to CMB observations. *Astronomy & Astrophysics*, 618:A166, October 2018. arXiv:1802.01145, doi:10.1051/0004-6361/201832768. (cited pp. 96, 100, and 101)

[155] A. Kusaka, T. Essinger-Hileman, J. W. Appel, P. Gallardo, K. D. Irwin, N. Jarosik, M. R. Nolta, L. A. Page, L. P. Parker, S. Raghunathan, J. L. Sievers, S. M. Simon, S. T. Staggs, and K. Visnjic. Modulation of cosmic microwave background polarization with a warm rapidly rotating half-wave plate on the Atacama B-Mode Search instrument. *Review of Scientific Instruments*, 85(2):024501, February 2014. doi:10.1063/1.4862058. (cited pp. 113, 132, and 184)

[156] David Langlois. Inflation, Quantum Fluctuations and Cosmological Perturbations. In *NATO Advanced Science Institutes (ASI) Series B*, volume 188 of *NATO Advanced Science Institutes (ASI) Series B*, page 235, January 2005. arXiv:hep-th/0405053. (not cited)

[157] S. M. Leach, J. F. Cardoso, C. Baccigalupi, R. B. Barreiro, M. Betoule, J. Bobin, A. Bonaldi, J. Delabrouille, G. de Zotti, C. Dickinson, H. K. Eriksen, J. González-Nuevo, F. K. Hansen, D. Herranz, M. Le Jeune, M. López-Caniego, E. Martínez-González, M. Massardi, J. B. Melin, M. A. Miville-Deschênes, G. Patanchon, S. Prunet, S. Ricciardi, E. Salerno, J. L. Sanz, J. L. Starck, F. Stivoli, V. Stolyarov, R. Stompor, and P. Vielva. Component separation methods for the PLANCK mission. *Astronomy & Astrophysics*, 491(2):597–615, November 2008. arXiv:0805.0269, doi:10.1051/0004-6361:200810116. (cited p. 95)

[158] Henrietta S. Leavitt. 1777 variables in the Magellanic Clouds. *Annals of Harvard College Observatory*, 60:87–108.3, January 1908. (cited p. 85)

[159] Henrietta S. Leavitt and Edward C. Pickering. Periods of 25 Variable Stars in the Small Magellanic Cloud. *Harvard College Observatory Circular*, 173:1–3, March 1912. (cited p. 85)

[160] Georges Lemaître. Un Univers homogène de masse constante et de rayon croissant rendant compte de la vitesse radiale des nébuleuses extra-galactiques. *Annales de la Société Scientifique de Bruxelles*, 47:49–59, Jan 1927. (cited p. 5)

[161] Julien Lesgourgue and Licia Verde. Neutrinos in cosmology. http://pdg.lbl.gov/2019/reviews/rpp2019-rev-neutrinos-in-cosmology.pdf, 2019. (not cited)

[162] Julien Lesgourgues. TASI Lectures on Cosmological Perturbations. *arXiv e-prints*, page arXiv:1302.4640, February 2013. arXiv:1302.4640. (not cited)

[163] Antony Lewis and Anthony Challinor. Weak gravitational lensing of the CMB. *Physics Reports*, 429(1):1–65, June 2006. arXiv:astro-ph/0601594, doi:10.1016/j.physrep.2006.03.002. (cited pp. 49, 58, and 63)

[164] LHCb collaboration. Observation of *CP* violation in charm decays. *arXiv e-prints*, page arXiv:1903.08726, March 2019. arXiv:1903.08726. (cited p. 94)

[165] Hong Li, Si-Yu Li, Yang Liu, Yong-Ping Li, Yifu Cai, Mingzhe Li, Gong-Bo Zhao, Cong-Zhan Liu, Zheng-Wei Li, He Xu, Di Wu, Yong-Jie Zhang, Zu-Hui Fan, Yong-Qiang Yao, Chao-Lin Kuo, Fang-Jun Lu, and Xinmin Zhang. Probing Primordial Gravitational Waves: Ali CMB Polarization Telescope. *arXiv e-prints*, October 2017. arXiv:1710.03047. (cited p. 121)

[166] E. M. Lifshitz. On the gravitational stability of the expanding universe. *Zhurnal Eksperimentalnoi i Teoreticheskoi Fiziki*, 16:587–602, January 1946. (cited p. 37)

[167] LIGO Scientific Collaboration and Virgo Collaboration. Observation of Gravitational Waves from a Binary Black Hole Merger. *Physical Review Letters*, 116(6):061102, February 2016. arXiv:1602.03837, doi:10.1103/PhysRevLett.116.061102. (cited pp. 88 and 90)

[168] LIGO Scientific Collaboration, Virgo Collaboration, Fermi GBM, INTEGRAL, IceCube Collaboration, AstroSat Cadmium Zinc Telluride Imager Team, IPN Collaboration, The Insight-Hxmt Collaboration, ANTARES Collaboration, The Swift Collaboration, AGILE Team, The 1M2H Team, The Dark Energy Camera GW-EM Collaboration, the DES Collaboration, The DLT40 Collaboration, GRAWITA: GRAvitational Wave Inaf TeAm, The Fermi Large Area Telescope Collaboration, ATCA: Australia Telescope Compact Array, ASKAP: Australian SKA Pathfinder, Las Cumbres Observatory Group, OzGrav, DWF (Deeper, Wider, Faster Program), AST3, CAASTRO Collaborations, The VINROUGE Collaboration, MASTER Collaboration, J-GEM, GROWTH, JAGWAR, Caltech- NRAO, TTU-NRAO, NuSTAR Collaborations, Pan-STARRS, The MAXI Team, TZAC Consortium, KU Collaboration, Nordic Optical Telescope, ePESSTO, GROND, Texas Tech University, SALT Group, TOROS: Transient Robotic Observatory of the South Collaboration, The BOOTES Collaboration, MWA: Murchison Widefield Array, The CALET Collaboration, IKI-GW Follow-up Collaboration, H.E.S.S. Collaboration, LOFAR Collaboration, LWA: Long Wavelength Array, HAWC Collaboration, The Pierre Auger Collaboration, ALMA Collaboration, Euro VLBI Team, Pi of the Sky Collaboration, The Chandra Team at McGill University, DFN: Desert Fireball Network, ATLAS, High Time Resolution Universe Survey, RIMAS, RATIR, and SKA South Africa/MeerKAT. Multi-messenger Observations of a Binary Neutron Star Merger. *The Astrophysical Journal Letters*, 848(2):L12, October 2017. arXiv:1710.05833, doi:10.3847/2041-8213/aa91c9. (cited p. 90)

[169] Rodrigo Luger. Starry. https://rodluger.github.io/starry/latest/, May 2019. (cited p. 206)

[170] Roger Lynds. The Absorption-Line Spectrum of 4c 05.34. *The Astrophysical Journal*, 164:L73, March 1971. doi:10.1086/180695. (cited p. 81)

[171] N. Macellari, E. Pierpaoli, C. Dickinson, and J. E. Vaillancourt. Galactic foreground contributions to the 5-year Wilkinson Microwave Anisotropy Probe maps. *Monthly Notices of the Royal Astronomical Society*, 418(2):888–905, December 2011. arXiv:1108.0205, doi:10.1111/j.1365-2966.2011.19542.x. (cited p. 99)

[172] D. Maino, A. Farusi, C. Baccigalupi, F. Perrotta, A. J. Banday, L. Bedini, C. Burigana, G. De Zotti, K. M. Górski, and E. Salerno. All-sky astrophysical component separation with Fast Independent Component Analysis (FASTICA). *Monthly Notices of the Royal Astronomical Society*, 334(1):53–68, July 2002. arXiv:astro-ph/0108362, doi:10.1046/j.1365-8711.2002.05425.x. (cited p. 106)

[173] A. Manzotti. Future cosmic microwave background delensing with galaxy surveys. *Physical Review D*, 97(4):043527, February 2018. arXiv:1710.11038, doi:10.1103/PhysRevD.97.043527. (cited p. 63)

[174] David J. E. Marsh. Axion cosmology. *Physics Reports*, 643:1–79, July 2016. arXiv:1510.07633, doi:10.1016/j.physrep.2016.06.005. (cited pp. 12 and 65)

[175] J. C. Mather, E. S. Cheng, Jr. Eplee, R. E., R. B. Isaacman, S. S. Meyer, R. A. Shafer, R. Weiss, E. L. Wright, C. L. Bennett, N. W. Boggess, E. Dwek, S. Gulkis, M. G. Hauser, M. Janssen, T. Kelsall, P. M. Lubin, Jr. Moseley, S. H., T. L. Murdock, R. F. Silverberg, G. F. Smoot, and D. T. Wilkinson. A Preliminary Measurement of the Cosmic Microwave Background Spectrum by the Cosmic Background Explorer (COBE) Satellite. *The Astrophysical Journal*, 354:L37, May 1990. doi:10.1086/185717. (cited p. 20)

[176] J. S. Mathis, W. Rumpl, and K. H. Nordsieck. The size distribution of interstellar grains. *The Astrophysical Journal*, 217:425–433, October 1977. doi:10.1086/155591. (cited p. 96)

[177] F. Matsuda, L. Lowry, A. Suzuki, M. Aguilar Fáundez, K. Arnold, D. Barron, F. Bianchini, K. Cheung, Y. Chinone, T. Elleflot, G. Fabbian, N. Goeckner-Wald, M. Hasegawa, D. Kaneko, N. Katayama, B. Keating, A. T. Lee, M. Navaroli, H. Nishino, H. Paar, G. Puglisi, P. L. Richards, J. Seibert, P. Siritanasak, O. Tajima, S. Takatori, C. Tsai, and B. Westbrook. The POLARBEAR Fourier transform spectrometer calibrator and spectroscopic characterization of the POLARBEAR instrument. *Review of Scientific Instruments*, 90(11):115115, November 2019. arXiv:1904.02901, doi:10.1063/1.5095160. (cited pp. 161, 191, and 199)

[178] Tomotake Matsumura. Mitigation of the spectral dependent polarization angle response for achromatic half-wave plate. *arXiv e-prints*, page arXiv:1404.5795, April 2014. arXiv:1404.5795. (cited pp. 160 and 161)

[179] Tomotake Matsumura, Shaul Hanany, Peter Ade, Bradley R. Johnson, Terry J. Jones, Prashanth Jonnalagadda, and Giorgio Savini. Performance of three- and five-stack achromatic half-wave plates at millimeter wavelengths. *Applied Optics*, 48(19):3614, July 2009. URL: https://www.osapublishing.org/abstract.cfm?URI=ao-48-19-3614, doi:10.1364/AO.48.003614. (cited p. 154)

[180] Tomotake Matsumura, Shaul Hanany, Peter Ade, Bradley R. Johnson, Terry J. Jones, Prashanth Jonnalagadda, and Giorgio Savini. Performance

of three- and five-stack achromatic half-wave plates at millimeter wavelengths. *Applied Optics*, 48(19):3614, July 2009. arXiv:0806.1518, doi:10.1364/AO.48.003614. (cited p. 180)

[181] Sabino Matterese. Lecture notes on Primordial non-gaussianity, XIIIth School of Cosmology - Cargèse. http://www.cpt.univ-mrs.fr/~cosmo/EC2017/Presentations/Matarrese.pdf, November 2017. (cited p. 72)

[182] A. A. Michelson and E. W. Morley. On the relative motion of the Earth and the luminiferous ether. *American Journal of Science*, 34(203):333–345, November 1887. doi:10.2475/ajs.s3-34.203.333. (cited p. 90)

[183] P. W. Milonni. *The Quantum vacuum: An Introduction to quantum electrodynamics*. Academic Press, 1994. (cited p. 13)

[184] Yuto Minami, Hiroki Ochi, Kiyotomo Ichiki, Nobuhiko Katayama, Eiichiro Komatsu, and Tomotake Matsumura. Simultaneous determination of the cosmic birefringence and miscalibrated polarization angles from CMB experiments. *Progress of Theoretical and Experimental Physics*, 2019(8), 2019. _eprint: https://academic.oup.com/ptep/article-pdf/2019/8/083E02/29117835/ptz079.pdf. URL: https://doi.org/10.1093/ptep/ptz079, doi:10.1093/ptep/ptz079. (cited p. 75)

[185] M. A. Miville-Deschênes, G. Lagache, F. Boulanger, and J. L. Puget. Statistical properties of dust far-infrared emission. *Astronomy & Astrophysics*, 469(2):595–605, July 2007. arXiv:0704.2175, doi:10.1051/0004-6361:20066962. (cited p. 101)

[186] Silvia Mollerach, Diego Harari, and Sabino Matarrese. CMB polarization from secondary vector and tensor modes. *Physical Review D*, 69(6):063002, March 2004. arXiv:astro-ph/0310711, doi:10.1103/PhysRevD.69.063002. (cited p. 48)

[187] Paulo Montero-Camacho and Christopher M. Hirata. Exploring circular polarization in the CMB due to conventional sources of cosmic birefringence. *Journal of Cosmology and Astroparticle Physics*, 2018(8):040, August 2018. arXiv:1803.04505, doi:10.1088/1475-7516/2018/08/040. (cited p. 158)

[188] Tony Mroczkowski, Simon Dicker, Jack Sayers, Erik D. Reese, Brian Mason, Nicole Czakon, Charles Romero, Alexander Young, Mark Devlin, Sunil Golwala, Phillip Korngut, Craig Sarazin, James Bock, Patrick M. Koch, Kai-Yang Lin, Sandor M. Molnar, Elena Pierpaoli, Keiichi Umetsu, and Michael Zemcov. A Multi-wavelength Study of the Sunyaev-Zel'dovich Effect in the Triple-merger Cluster MACS J0717.5+3745 with MUSTANG and Bolocam. *The Astrophysical Journal*, 761(1):47, December 2012. arXiv:1205.0052, doi:10.1088/0004-637X/761/1/47. (cited p. 67)

[189] J. M. Nagy, P. A. R. Ade, M. Amiri, S. J. Benton, A. S. Bergman, R. Bihary, J. J. Bock, J. R. Bond, S. A. Bryan, H. C. Chiang, C. R. Contaldi,

O. Doré, A. J. Duivenvoorden, H. K. Eriksen, M. Farhang, J. P. Filippini, L. M. Fissel, A. A. Fraisse, K. Freese, M. Galloway, A. E. Gambrel, N. N. Gandilo, K. Ganga, J. E. Gudmundsson, M. Halpern, J. Hartley, M. Hasselfield, G. Hilton, W. Holmes, V. V. Hristov, Z. Huang, K. D. Irwin, W. C. Jones, C. L. Kuo, Z. D. Kermish, S. Li, P. V. Mason, K. Megerian, L. Moncelsi, T. A. Morford, C. B. Netterfield, M. Nolta, I. L. Padilla, B. Racine, A. S. Rahlin, C. Reintsema, J. E. Ruhl, M. C. Runyan, T. M. Ruud, J. A. Shariff, J. D. Soler, X. Song, A. Trangsrud, C. Tucker, R. S. Tucker, A. D. Turner, J. F. Van Der List, A. C. Weber, I. K. Wehus, D. V. Wiebe, and E. Y. Young. A New Limit on CMB Circular Polarization from SPIDER. *The Astrophysical Journal*, 844(2):151, August 2017. arXiv:1704.00215, doi:10.3847/1538-4357/aa7cfd. (cited p. 158)

[190] Namikawa et al. Evidence for the Cross-correlation between Cosmic Microwave Background Polarization Lensing from POLARBEAR and Cosmic Shear from Subaru Hyper Suprime-Cam. *arXiv e-prints*, Apr 2019. arXiv:1904.02116. (cited p. 135)

[191] Toshiya Namikawa. CMB internal delensing with general optimal estimator for higher-order correlations. *Physical Review D*, 95(10):103514, May 2017. arXiv:1703.00169, doi:10.1103/PhysRevD.95.103514. (cited p. 63)

[192] Toshiya Namikawa, Yilun Guan, Omar Darwish, Blake D. Sherwin, Simone Aiola, Nicholas Battaglia, James A. Beall, Daniel T. Becker, J. Richard Bond, Erminia Calabrese, Grace E. Chesmore, Steve K. Choi, Mark J. Devlin, Joanna Dunkley, Rolando Dünner, Anna E. Fox, Patricio A. Gallardo, Vera Gluscevic, Dongwon Han, Matthew Hasselfield, Gene C. Hilton, Adam D. Hincks, Renée Hložek, Johannes Hubmayr, Kevin Huffenberger, John P. Hughes, Brian J. Koopman, Arthur Kosowsky, Thibaut Louis, Marius Lungu, Amanda MacInnis, Mathew S. Madhavacheril, Maya Mallaby-Kay, Loïc Maurin, Jeffrey McMahon, Kavilan Moodley, Sigurd Naess, Federico Nati, Laura B. Newburgh, John P. Nibarger, Michael D. Niemack, Lyman A. Page, Frank J. Qu, Naomi Robertson, Alessandro Schillaci, Neelima Sehgal, Cristóbal Sifón, Sara M. Simon, David N. Spergel, Suzanne T. Staggs, Emilie R. Storer, Alexander van Engelen, Jeff van Lanen, and Edward J. Wollack. Atacama Cosmology Telescope: Constraints on cosmic birefringence. *Physical Review D*, 101(8):083527, April 2020. arXiv:2001.10465, doi:10.1103/PhysRevD.101.083527. (cited p. 75)

[193] P. A. Oesch, G. Brammer, P. G. van Dokkum, G. D. Illingworth, R. J. Bouwens, I. Labbé, M. Franx, I. Momcheva, M. L. N. Ashby, G. G. Fazio, V. Gonzalez, B. Holden, D. Magee, R. E. Skelton, R. Smit, L. R. Spitler, M. Trenti, and S. P. Willner. A Remarkably Luminous Galaxy at z=11.1 Measured with Hubble Space Telescope Grism Spectroscopy. *The Astrophysical Journal*, 819(2):129, March 2016. arXiv:1603.00461, doi:10.3847/0004-637X/819/2/129. (cited p. 21)

[194] Takemi Okamoto and Wayne Hu. Cosmic microwave background lensing reconstruction on the full sky. *Physical Review D*, 67(8):083002,

April 2003. arXiv:astro-ph/0301031, doi:10.1103/PhysRevD.67.083002. (cited p. 61)

[195] J. P. Ostriker and P. J. E. Peebles. A Numerical Study of the Stability of Flattened Galaxies: or, can Cold Galaxies Survive? *The Astrophysical Journal*, 186:467–480, Dec 1973. doi:10.1086/152513. (cited p. 12)

[196] Ivan L. Padilla, Joseph R. Eimer, Yunyang Li, Graeme E. Addison, Aamir Ali, John W. Appel, Charles L. Bennett, Ricardo Bustos, Michael K. Brewer, Manwei Chan, David T. Chuss, Joseph Cleary, Jullianna Couto, Sumit Dahal, Kevin Denis, Rolando Dünner, Thomas Essinger-Hileman, Pedro Fluxá, Dominik Gothe, Saianeesh K. Haridas, Kathleen Harrington, Jeffrey Iuliano, John Karakla, Tobias A. Marriage, Nathan J. Miller, Carolina Núñez, Lucas Parker, Matthew A. Petroff, Rodrigo Reeves, Karwan Rostem, Robert W. Stevens, Deniz Augusto Nunes Valle, Duncan J. Watts, Janet L. Weiland, Edward J. Wollack, and Zhilei Xu. Two-year Cosmology Large Angular Scale Surveyor (CLASS) Observations: A Measurement of Circular Polarization at 40 GHz. *The Astrophysical Journal*, 889(2):105, February 2020. arXiv:1911.00391, doi:10.3847/1538-4357/ab61f8. (cited p. 158)

[197] Nathalie Palanque-Delabrouille, Christophe Yèche, Nils Schöneberg, Julien Lesgourgues, Michael Walther, Solène Chabanier, and Eric Armengaud. Hints, neutrino bounds, and WDM constraints from SDSS DR14 Lyman-α and Planck full-survey data. *Journal of Cosmology and Astroparticle Physics*, 2020(4):038, April 2020. arXiv:1911.09073, doi:10.1088/1475-7516/2020/04/038. (cited p. 65)

[198] S. Pancharatnam. Achromatic combinations of birefringent plates. *Proceedings of the Indian Academy of Sciences - Section A*, 41(4):130–136, April 1955. URL: https://doi.org/10.1007/BF03047097, doi:10.1007/BF03047097. (cited p. 180)

[199] Kanhaiya L. Pandey, Tanvi Karwal, and Subinoy Das. Alleviating the H_0 and σ_8 anomalies with a decaying dark matter model. *arXiv e-prints*, Feb 2019. arXiv:1902.10636. (cited p. 10)

[200] F. De Paolis, G. Ingrosso, Ph. Jetzer, and M. Roncadelli. A case for a baryonic dark halo. *Physical Review Letters*, 74:14–17, Jan 1995. URL: https://link.aps.org/doi/10.1103/PhysRevLett.74.14, doi:10.1103/PhysRevLett.74.14. (cited p. 13)

[201] J. Papež, L. Grigori, and R. Stompor. Solving linear equations with messenger-field and conjugate gradient techniques: An application to CMB data analysis. *Astronomy & Astrophysics*, 620:A59, November 2018. arXiv:1803.03462, doi:10.1051/0004-6361/201832987. (cited p. 119)

[202] P. J. E. Peebles and J. T. Yu. Primeval Adiabatic Perturbation in an Expanding Universe. *The Astrophysical Journal*, 162:815, December 1970. doi:10.1086/150713. (cited pp. 37 and 39)

[203] A. A. Penzias and R. W. Wilson. A Measurement of Excess Antenna Temperature at 4080 Mc/s. *The Astrophysical Journal*, 142:419–421, July 1965. doi:10.1086/148307. (cited p. 37)

[204] Will J. Percival and Martin White. Testing cosmological structure formation using redshift-space distortions. *Monthly Notices of the Royal Astronomical Society*, 393(1):297–308, February 2009. arXiv:0808.0003, doi:10.1111/j.1365-2966.2008.14211.x. (cited p. 81)

[205] S. Perlmutter, G. Aldering, G. Goldhaber, R. A. Knop, P. Nugent, P. G. Castro, S. Deustua, S. Fabbro, A. Goobar, D. E. Groom, I. M. Hook, A. G. Kim, M. Y. Kim, J. C. Lee, N. J. Nunes, R. Pain, C. R. Pennypacker, R. Quimby, C. Lidman, R. S. Ellis, M. Irwin, R. G. McMahon, P. Ruiz-Lapuente, N. Walton, B. Schaefer, B. J. Boyle, A. V. Filippenko, T. Matheson, A. S. Fruchter, N. Panagia, H. J. M. Newberg, W. J. Couch, and The Supernova Cosmology Project. Measurements of Ω and Λ from 42 High-Redshift Supernovae. *The Astrophysical Journal*, 517(2):565–586, Jun 1999. arXiv:astro-ph/9812133, doi:10.1086/307221. (cited p. 11)

[206] M. M. Phillips. The Absolute Magnitudes of Type IA Supernovae. *The Astrophysical Journal, Letters*, 413:L105, August 1993. doi:10.1086/186970. (cited p. 85)

[207] Planck Collaboration. Planck 2013 results. XV. CMB power spectra and likelihood. *Astronomy & Astrophysics*, 571:A15, November 2014. arXiv:1303.5075, doi:10.1051/0004-6361/201321573. (cited p. 177)

[208] Planck Collaboration. Planck 2013 results. XVI. Cosmological parameters. *Astronomy & Astrophysics*, 571:A16, November 2014. arXiv:1303.5076, doi:10.1051/0004-6361/201321591. (cited p. 52)

[209] Planck Collaboration. Planck 2013 results. XXX. Cosmic infrared background measurements and implications for star formation. *Astronomy & Astrophysics*, 571:A30, November 2014. arXiv:1309.0382, doi:10.1051/0004-6361/201322093. (cited p. 84)

[210] Planck Collaboration. Planck intermediate results. XIX. An overview of the polarized thermal emission from Galactic dust. *Astronomy & Astrophysics*, 576:A104, April 2015. arXiv:1405.0871, doi:10.1051/0004-6361/201424082. (cited pp. 96, 97, and 98)

[211] Planck Collaboration. Planck 2015 results. X. Diffuse component separation: Foreground maps. *Astronomy & Astrophysics*, 594:A10, September 2016. arXiv:1502.01588, doi:10.1051/0004-6361/201525967. (cited p. 101)

[212] Planck Collaboration. Planck 2015 results. XXVII. The second Planck catalogue of Sunyaev-Zeldovich sources. *Astronomy & Astrophysics*, 594:A27, September 2016. arXiv:1502.01598, doi:10.1051/0004-6361/201525823. (cited p. 67)

[213] Planck Collaboration. Planck intermediate results. L. Evidence of spatial variation of the polarized thermal dust spectral energy distribution and implications for CMB B-mode analysis. *Astronomy & Astrophysics*, 599:A51, March 2017. arXiv:1606.07335, doi:10.1051/0004-6361/201629164. (cited p. 100)

[214] Planck Collaboration. Planck 2018 results. IV. Diffuse component separation. *arXiv e-prints*, July 2018. arXiv:1807.06208. (cited p. 99)

[215] Planck Collaboration. Planck 2018 results. VI. Cosmological parameters. *arXiv e-prints*, Jul 2018. arXiv:1807.06209. (cited pp. 8, 9, 11, 18, 20, 21, 25, 65, and 183)

[216] Planck Collaboration. Planck 2018 results. X. Constraints on inflation. *arXiv e-prints*, page arXiv:1807.06211, July 2018. arXiv:1807.06211. (cited pp. 32 and 33)

[217] Planck Collaboration. Planck 2018 results. X. Constraints on inflation. *arXiv e-prints*, page arXiv:1807.06211, July 2018. arXiv:1807.06211. (cited p. 54)

[218] Planck Collaboration. Planck 2018 results. XI. Polarized dust foregrounds. *arXiv e-prints*, January 2018. arXiv:1801.04945. (cited pp. 97 and 102)

[219] Planck Collaboration. Planck 2018 results. IX. Constraints on primordial non-Gaussianity. *arXiv e-prints*, May 2019. arXiv:1905.05697. (cited pp. 72 and 73)

[220] Davide Poletti, Giulio Fabbian, Maude Le Jeune, Julien Peloton, Kam Arnold, Carlo Baccigalupi, Darcy Barron, Shawn Beckman, Julian Borrill, Scott Chapman, Yuji Chinone, Ari Cukierman, Anne Ducout, Tucker Elleflot, Josquin Errard, Stephen Feeney, Neil Goeckner-Wald, John Groh, Grantland Hall, Masaya Hasegawa, Masashi Hazumi, Charles Hill, Logan Howe, Yuki Inoue, Andrew H. Jaffe, Oliver Jeong, Nobuhiko Katayama, Brian Keating, Reijo Keskitalo, Theodore Kisner, Akito Kusaka, Adrian T. Lee, David Leon, Eric Linder, Lindsay Lowry, Frederick Matsuda, Martin Navaroli, Hans Paar, Giuseppe Puglisi, Christian L. Reichardt, Colin Ross, Praween Siritanasak, Nathan Stebor, Bryan Steinbach, Radek Stompor, Aritoki Suzuki, Osamu Tajima, Grant Teply, and Nathan Whitehorn. Making maps of cosmic microwave background polarization for B-mode studies: the POLARBEAR example. *Astronomy & Astrophysics*, 600:A60, April 2017. arXiv:1608.01624, doi:10.1051/0004-6361/201629467. (cited pp. 129 and 134)

[221] Vivian Poulin, Tristan L. Smith, Tanvi Karwal, and Marc Kamionkowski. Early Dark Energy can Resolve the Hubble Tension. *Phys. Rev. Letters*, 122(22):221301, Jun 2019. arXiv:1811.04083, doi:10.1103/PhysRevLett.122.221301. (cited p. 10)

[222] Jonathan R. Pritchard and Abraham Loeb. 21 cm cosmology in the 21st century. *Reports on Progress in Physics*, 75(8):086901, August 2012. arXiv:1109.6012, doi:10.1088/0034-4885/75/8/086901. (cited p. 82)

[223] M. J. Rees and D. W. Sciama. Large-scale Density Inhomogeneities in the Universe. *Nature*, 217(5128):511–516, February 1968. doi:10.1038/217511a0. (cited p. 48)

[224] Christian L. Reichardt. *Observing the Epoch of Reionization with the Cosmic Microwave Background*, volume 423 of *Astrophysics and Space Science Library*, page 227. Mesinger, Andrei, 2016. doi:10.1007/978-3-319-21957-8_8. (cited p. 55)

[225] Beth A. Reid, Lado Samushia, Martin White, Will J. Percival, Marc Manera, Nikhil Padmanabhan, Ashley J. Ross, Ariel G. Sánchez, Stephen Bailey, Dmitry Bizyaev, Adam S. Bolton, Howard Brewington, J. Brinkmann, Joel R. Brownstein, Antonio J. Cuesta, Daniel J. Eisenstein, James E. Gunn, Klaus Honscheid, Elena Malanushenko, Viktor Malanushenko, Claudia Maraston, Cameron K. McBride, Demitri Muna, Robert C. Nichol, Daniel Oravetz, Kaike Pan, Roland de Putter, N. A. Roe, Nicholas P. Ross, David J. Schlegel, Donald P. Schneider, Hee-Jong Seo, Alaina Shelden, Erin S. Sheldon, Audrey Simmons, Ramin A. Skibba, Stephanie Snedden, Molly E. C. Swanson, Daniel Thomas, Jeremy Tinker, Rita Tojeiro, Licia Verde, David A. Wake, Benjamin A. Weaver, David H. Weinberg, Idit Zehavi, and Gong-Bo Zhao. The clustering of galaxies in the SDSS-III Baryon Oscillation Spectroscopic Survey: measurements of the growth of structure and expansion rate at z = 0.57 from anisotropic clustering. *Monthly Notices of the Royal Astronomical Society*, 426(4):2719–2737, November 2012. arXiv:1203.6641, doi:10.1111/j.1365-2966.2012.21779.x. (cited p. 81)

[226] David M. Reiman and Brett E. Göhre. Deblending galaxy superpositions with branched generative adversarial networks. *Monthly Notices of the Royal Astronomical Society*, 485(2):2617–2627, May 2019. arXiv:1810.10098, doi:10.1093/mnras/stz575. (cited p. 80)

[227] Adam G. Riess, Alexei V. Filippenko, Peter Challis, Alejandro Clocchiatti, Alan Diercks, Peter M. Garnavich, Ron L. Gilliland, Craig J. Hogan, Saurabh Jha, Robert P. Kirshner, B. Leibundgut, M. M. Phillips, David Reiss, Brian P. Schmidt, Robert A. Schommer, R. Chris Smith, J. Spyromilio, Christopher Stubbs, Nicholas B. Suntzeff, and John Tonry. Observational Evidence from Supernovae for an Accelerating Universe and a Cosmological Constant. *Astronomical Journal*, 116(3):1009–1038, Sep 1998. arXiv:astro-ph/9805201, doi:10.1086/300499. (cited p. 11)

[228] Adam G. Riess, Lucas M. Macri, Samantha L. Hoffmann, Dan Scolnic, Stefano Casertano, Alexei V. Filippenko, Brad E. Tucker, Mark J. Reid, David O. Jones, Jeffrey M. Silverman, Ryan Chornock, Peter Challis, Wenlong Yuan, Peter J. Brown, and Ryan J. Foley. A 2.4% Determination of the Local Value of the Hubble Constant. *The Astrophysical Journal*, 826(1):56, Jul 2016. arXiv:1604.01424, doi:10.3847/0004-637X/826/1/56. (cited p. 9)

[229] M. Rigault, G. Aldering, M. Kowalski, Y. Copin, P. Antilogus, C. Aragon, S. Bailey, C. Baltay, D. Baugh, S. Bongard, K. Boone, C. Buton, J. Chen,

N. Chotard, H. K. Fakhouri, U. Feindt, P. Fagrelius, M. Fleury, D. Fouchez, E. Gangler, B. Hayden, A. G. Kim, P. F. Leget, S. Lombardo, J. Nordin, R. Pain, E. Pecontal, R. Pereira, S. Perlmutter, D. Rabinowitz, K. Runge, D. Rubin, C. Saunders, G. Smadja, C. Sofiatti, N. Suzuki, C. Tao, and B. A. Weaver. Confirmation of a Star Formation Bias in Type Ia Supernova Distances and its Effect on the Measurement of the Hubble Constant. *The Astrophysical Journal*, 802(1):20, March 2015. arXiv:1412.6501, doi:10.1088/0004-637X/802/1/20. (cited pp. 10 and 86)

[230] M. Rigault, V. Brinnel, G. Aldering, P. Antilogus, C. Aragon, S. Bailey, C. Baltay, K. Barbary, S. Bongard, K. Boone, C. Buton, M. Childress, N. Chotard, Y. Copin, S. Dixon, P. Fagrelius, U. Feindt, D. Fouchez, E. Gangler, B. Hayden, W. Hillebrandt, D. A. Howell, A. Kim, M. Kowalski, D. Kuesters, P. F. Leget, S. Lombardo, Q. Lin, J. Nordin, R. Pain, E. Pecontal, R. Pereira, S. Perlmutter, D. Rabinowitz, K. Runge, D. Rubin, C. Saunders, G. Smadja, C. Sofiatti, N. Suzuki, S. Taubenberger, C. Tao, and R. C. Thomas. Strong Dependence of Type Ia Supernova Standardization on the Local Specific Star Formation Rate. *arXiv e-prints*, page arXiv:1806.03849, June 2018. arXiv:1806.03849. (cited p. 86)

[231] A. Ritacco, N. Ponthieu, A. Catalano, R. Adam, P. Ade, P. André, A. Beelen, A. Benoît, A. Bideaud, N. Billot, O. Bourrion, M. Calvo, G. Coiffard, B. Comis, F. X. Désert, S. Doyle, J. Goupy, C. Kramer, S. Leclercq, J. F. Macías-Pérez, P. Mauskopf, A. Maury, F. Mayet, A. Monfardini, F. Pajot, E. Pascale, L. Perotto, G. Pisano, M. Rebolo-Iglesias, V. Revéret, L. Rodriguez, C. Romero, F. Ruppin, G. Savini, K. Schuster, A. Sievers, C. Thum, S. Triqueneaux, C. Tucker, and R. Zylka. Polarimetry at millimeter wavelengths with the NIKA camera: calibration and performance. *Astronomy & Astrophysics*, 599:A34, March 2017. arXiv:1609.02042, doi:10.1051/0004-6361/201629666. (cited p. 113)

[232] A. Ritacco, N. Ponthieu, A. Catalano, R. Adam, P. Ade, P. André, A. Beelen, A. Benoît, A. Bideaud, N. Billot, O. Bourrion, M. Calvo, G. Coiffard, B. Comis, F. X. Désert, S. Doyle, J. Goupy, C. Kramer, S. Leclercq, J. F. Macías-Pérez, P. Mauskopf, A. Maury, F. Mayet, A. Monfardini, F. Pajot, E. Pascale, L. Perotto, G. Pisano, M. Rebolo-Iglesias, V. Revéret, L. Rodriguez, C. Romero, F. Ruppin, G. Savini, K. Schuster, A. Sievers, C. Thum, S. Triqueneaux, C. Tucker, and R. Zylka. Polarimetry at millimeter wavelengths with the NIKA camera: calibration and performance. *Astronomy & Astrophysics*, 599:A34, March 2017. arXiv:1609.02042, doi:10.1051/0004-6361/201629666. (cited p. 132)

[233] M. S. Roberts and R. N. Whitehurst. The rotation curve and geometry of M31 at large galactocentric distances. *The Astrophysical Journal*, 201:327–346, Oct 1975. doi:10.1086/153889. (cited p. 12)

[234] Keir K. Rogers, Hiranya V. Peiris, Boris Leistedt, Jason D. McEwen, and Andrew Pontzen. Spin-SILC: CMB polarization component separation with spin wavelets. *Monthly Notives of the Royal Astronomical Society*,

463(3):2310–2322, December 2016. arXiv:1605.01417, doi:10.1093/mnras/stw2128. (cited p. 105)

[235] M. Rouble, M. Dobbs, A. Gilbert, J. Montgomery, G. Noble, and C. Vergès. Transformer-Coupled TES Frequency Domain Readout Prototype. *Journal of Low Temperature Physics*, February 2020. URL: https://doi.org/10.1007/s10909-020-02376-8, doi:10.1007/s10909-020-02376-8. (cited p. 117)

[236] Pilar Ruiz-Lapuente. *Dark Energy: Observational and Theoretical Approaches*. Cambridge University Press, 2010. (cited p. 13)

[237] R. K. Sachs and A. M. Wolfe. Perturbations of a Cosmological Model and Angular Variations of the Microwave Background. *The Astrophysical Journal*, 147:73, January 1967. doi:10.1086/148982. (cited p. 51)

[238] A. D. Sakharov. Violation of CP Invariance, C Asymmetry, and Baryon Asymmetry of the Universe. *Soviet Journal of Experimental and Theoretical Physics Letters*, 5:24, Jan 1967. (cited p. 17)

[239] Maria Salatino , Jacob Lashner, Martina Gerbino, Sara M. Simon, Joy Didier, Aamir Ali, Peter C. Ashton, Sean Bryan, Yuji Chinone, Kevin Coughlin, Kevin T. Crowley, Giulio Fabbian, Nicholas Galitzki, Neil Goeckner-Wald, Jon E. Gudmundsson, Charles A. Hill, Brian Keating, Akito Kusaka, Adrian T. Lee, Jeffrey McMahon, Amber D. Miller, Giuseppe Puglisi, Christian L. Reichardt, Grant Teply, Zhilei Xu, and Ningfeng Zhu. Studies of systematic uncertainties for Simons Observatory: polarization modulator related effects. In *Proceedings of SPIE*, volume 10708 of *Society of Photo-Optical Instrumentation Engineers (SPIE) Conference Series*, page 1070848, Jul 2018. arXiv:1808.07442. (cited pp. 152, 180, and 181)

[240] Bernard F. Schutz. Gravitational waves on the back of an envelope. *American Journal of Physics*, 52(5):412–419, May 1984. doi:10.1119/1.13627. (cited p. 207)

[241] Neelima Sehgal, Mathew S. Madhavacheril, Blake Sherwin, and Alexander van Engelen. Internal delensing of cosmic microwave background acoustic peaks. *Physical Review D*, 95(10):103512, May 2017. arXiv:1612.03898, doi:10.1103/PhysRevD.95.103512. (cited p. 63)

[242] Y. Sekimoto and The LiteBIRD collaboration. Concept design of the LiteBIRD satellite for CMB B-mode polarization. In *Proceedings of SPIE*, volume 10698 of *Society of Photo-Optical Instrumentation Engineers (SPIE) Conference Series*, page 106981Y, August 2018. doi:10.1117/12.2313432. (cited p. 110)

[243] Joseph Silk. Cosmic Black-Body Radiation and Galaxy Formation. *The Astrophysical Journal*, 151:459, February 1968. doi:10.1086/149449. (cited p. 42)

[244] Kendrick M. Smith, Duncan Hanson, Marilena LoVerde, Christopher M. Hirata, and Oliver Zahn. Delensing CMB polarization with external datasets. *Journal of Cosmology and Astroparticle Physics*, 2012(6):014, June 2012. arXiv:1010.0048, doi:10.1088/1475-7516/2012/06/014. (cited p. 63)

[245] F. Stivoli, J. Grain, S. M. Leach, M. Tristram, C. Baccigalupi, and R. Stompor. Maximum likelihood, parametric component separation and CMB B-mode detection in suborbital experiments. *Monthly Notices of the Royal Astronomical Society*, 408(4):2319–2335, Nov 2010. arXiv:1004.4756, doi:10.1111/j.1365-2966.2010.17281.x. (cited p. 174)

[246] Radek Stompor, Josquin Errard, and Davide Poletti. Forecasting performance of CMB experiments in the presence of complex foreground contaminations. *Physical Review D*, 94(8):083526, Oct 2016. arXiv:1609.03807. (cited pp. 106, 107, 165, 170, 171, 172, 174, 175, 176, 177, 178, and 183)

[247] Radek Stompor, Samuel Leach, Federico Stivoli, and Carlo Baccigalupi. Maximum likelihood algorithm for parametric component separation in cosmic microwave background experiments. *Monthly Notices of the Royal Astronomical Society*, 392(1):216–232, January 2009. arXiv:0804.2645, doi:10.1111/j.1365-2966.2008.14023.x. (cited pp. 107, 170, 172, and 177)

[248] I. A. Strukov, A. A. Brukhanov, D. P. Skulachev, and M. V. Sazhin. Anisotropy of the microwave background radiation. *Soviet Astronomy Letters*, 18(5):153, May 1992. (cited p. 124)

[249] Meng Su, Amit P. S. Yadav, and Matias Zaldarriaga. Impact of instrumental systematic contamination on the lensing mass reconstruction using the CMB polarization. *Physical Review D*, 79(12):123002, June 2009. arXiv:0901.0285, doi:10.1103/PhysRevD.79.123002. (cited p. 63)

[250] R. A. Sunyaev and Ya. B. Zeldovich. The Observations of Relic Radiation as a Test of the Nature of X-Ray Radiation from the Clusters of Galaxies. *Comments on Astrophysics and Space Physics*, 4:173, November 1972. (cited p. 47)

[251] A. Suzuki and The POLARBEAR Collaboration. The POLARBEAR-2 and the Simons Array Experiments. *Journal of Low Temperature Physics*, 184(3-4):805–810, August 2016. URL: https://link.springer.com/article/10.1007/s10909-015-1425-4, doi:10.1007/s10909-015-1425-4. (cited pp. 110 and 136)

[252] Aritoki Suzuki. *Multichroic Bolometric Detector Architecture for Cosmic Microwave Background Polarimetry Experiments*. PhD thesis, University of California, Berkeley, 2013. (cited p. 156)

[253] Satoru Takakura, Mario Aguilar, Yoshiki Akiba, Kam Arnold, Carlo Baccigalupi, Darcy Barron, Shawn Beckman, David Boettger, Julian Borrill, Scott Chapman, Yuji Chinone, Ari Cukierman, Anne Ducout, Tucker Elleflot, Josquin Errard, Giulio Fabbian, Takuro Fujino, Nicholas Galitzki,

Neil Goeckner-Wald, Nils W. Halverson, Masaya Hasegawa, Kaori Hattori, Masashi Hazumi, Charles Hill, Logan Howe, Yuki Inoue, Andrew H. Jaffe, Oliver Jeong, Daisuke Kaneko, Nobuhiko Katayama, Brian Keating, Reijo Keskitalo, Theodore Kisner, Nicoletta Krachmalnicoff, Akito Kusaka, Adrian T. Lee, David Leon, Lindsay Lowry, Frederick Matsuda, Tomotake Matsumura, Martin Navaroli, Haruki Nishino, Hans Paar, Julien Peloton, Davide Poletti, Giuseppe Puglisi, Christian L. Reichardt, Colin Ross, Praween Siritanasak, Aritoki Suzuki, Osamu Tajima, Sayuri Takatori, and Grant Teply. Performance of a continuously rotating half-wave plate on the POLARBEAR telescope. *Journal of Cosmology and Astroparticle Physics*, 2017(5):008, May 2017. arXiv:1702.07111, doi:10.1088/1475-7516/2017/05/008. (cited pp. 138, 153, 160, and 184)

[254] Satoru Takakura and the POLARBEAR collaboration. Performance of a continuously rotating half-wave plate on the POLARBEAR telescope. *Journal of Cosmology and Astro-Particle Physics*, 2017(5):008, May 2017. arXiv:1702.07111, doi:10.1088/1475-7516/2017/05/008. (cited pp. 113 and 129)

[255] Q. Y. Tang, P. S. Barry, T. W. Cecil, and E. Shirokoff. Fabrication of OMT-Coupled Kinetic Inductance Detector for CMB Detection. *Journal of Low Temperature Physics*, 199(1-2):362–368, January 2020. doi:10.1007/s10909-020-02341-5. (cited p. 111)

[256] Max Tegmark, Angélica de Oliveira-Costa, and Andrew J. Hamilton. High resolution foreground cleaned CMB map from WMAP. *Physical Review D*, 68(12):123523, December 2003. arXiv:astro-ph/0302496, doi:10.1103/PhysRevD.68.123523. (cited p. 105)

[257] The BICEP2 Collaboration and the Keck Array Collaboration. Constraints on Primordial Gravitational Waves Using Planck, WMAP, and New BICEP2/Keck Observations through the 2015 Season. *Physical Review Letters*, 121(22):221301, Nov 2018. arXiv:1810.05216, doi:10.1103/PhysRevLett.121.221301. (cited p. 54)

[258] The BICEP/Keck Collaboration. Optical characterization of the Keck Array and BICEP3 CMB Polarimeters from 2016 to 2019. *arXiv e-prints*, February 2020. arXiv:2002.05197. (cited p. 110)

[259] The CMB-S4 collaboration. CMB-S4 Science Book, First Edition. *arXiv e-prints*, page arXiv:1610.02743, Oct 2016. arXiv:1610.02743. (cited p. 124)

[260] The LIGO Scientific Collaboration and the Virgo Collaboration. A gravitational-wave measurement of the Hubble constant following the second observing run of Advanced LIGO and Virgo. *arXiv e-prints*, page arXiv:1908.06060, August 2019. arXiv:1908.06060. (cited p. 91)

[261] The Planck Collaboration. Planck 2013 results. XXX. Cosmic infrared background measurements and implications for star formation. *Astronomy & Astrophysics*, 571:A30, November 2014. arXiv:1309.0382, doi:10.1051/0004-6361/201322093. (cited p. 84)

[262] The POLARBEAR Collaboration. A Measurement of the Cosmic Microwave Background B-mode Polarization Power Spectrum at Sub-degree Scales with POLARBEAR. *The Astrophysical Journal*, 794(2):171, October 2014. arXiv:1403.2369, doi:10.1088/0004-637X/794/2/171. (cited pp. 131 and 134)

[263] The POLARBEAR Collaboration. Measurement of the Cosmic Microwave Background Polarization Lensing Power Spectrum with the POLARBEAR Experiment. *Physical Review Letter*, 113(2):021301, Jul 2014. arXiv:1312.6646, doi:10.1103/PhysRevLett.113.021301. (cited pp. 56, 131, and 134)

[264] The POLARBEAR Collaboration. A Measurement of the Cosmic Microwave Background B-mode Polarization Power Spectrum at Subdegree Scales from Two Years of POLARBEAR Data. *The Astrophysical Journal*, 848(2):121, Oct 2017. arXiv:1705.02907, doi:10.3847/1538-4357/aa8e9f. (cited pp. 131 and 134)

[265] The POLARBEAR Collaboration. Cross-correlation of POLARBEAR CMB Polarization Lensing with High-z Sub-mm Herschel-ATLAS galaxies. *arXiv e-prints*, Mar 2019. arXiv:1903.07046. (cited p. 135)

[266] The POLARBEAR collaboration. Internal delensing of Cosmic Microwave Background polarization B-modes with the POLARBEAR experiment. *arXiv e-prints*, page arXiv:1909.13832, September 2019. arXiv:1909.13832. (cited pp. 131 and 134)

[267] The POLARBEAR Collaboration. A measurement of the degree-scale CMB b-mode angular power spectrum with polarbear. *The Astrophysical Journal*, 897(1):55, jul 2020. doi:10.3847/1538-4357/ab8f24. (cited pp. 60, 131, 132, 134, 140, 141, and 145)

[268] The Simons Observatory Collaboration. The Simons Observatory: Astro2020 Decadal Project Whitepaper. *arXiv e-prints*, Jul 2019. arXiv:1907.08284. (cited p. 110)

[269] The Simons Observatory Collaboration. The Simons Observatory: science goals and forecasts. *Journal of Cosmology and Astroparticle Physics*, 2019(2):056, February 2019. arXiv:1808.07445, doi:10.1088/1475-7516/2019/02/056. (cited pp. 123, 156, 179, 180, 182, 184, and 198)

[270] The XENON1T Collaboration. Observation of Excess Electronic Recoil Events in XENON1T. *arXiv e-prints*, page arXiv:2006.09721, June 2020. arXiv:2006.09721. (cited p. 94)

[271] Ben Thorne, David Alonso, Sigurd Naess, and Jo Dunkley. PySM: Python Sky Model, April 2017. arXiv:1704.007. (cited p. 183)

[272] R. B. Tully, O. de Marseille, and J. R. Fisher. A New Method of Determining Distances to Galaxies. In *Bulletin of the AAS*, volume 7, page 426, June 1975. (cited p. 87)

[273] Shutaro Ueda, Tetsu Kitayama, Masamune Oguri, Eiichiro Komatsu, Takuya Akahori, Daisuke Iono, Takumi Izumi, Ryohei Kawabe, Kotaro Kohno, Hiroshi Matsuo, Naomi Ota, Yasushi Suto, Shigehisa Takakuwa, Motokazu Takizawa, Takahiro Tsutsumi, and Kohji Yoshikawa. A Cool Core Disturbed: Observational Evidence for the Coexistence of Subsonic Sloshing Gas and Stripped Shock-heated Gas around the Core of RX J1347.5-1145. *The Astrophysical Journal*, 866(1):48, October 2018. arXiv:1808.09232, doi:10.3847/1538-4357/aadd9d. (cited pp. 67 and 68)

[274] J.P. Uzan and P. Peter. *Cosmologie primordiale*. Échelles. Humensis, 2015. URL: https://books.google.fr/books?id=owiWDgAAQBAJ. (not cited)

[275] F. Vansyngel, F. Boulanger, T. Ghosh, B. Wandelt, J. Aumont, A. Bracco, F. Levrier, P. G. Martin, and L. Montier. Statistical simulations of the dust foreground to cosmic microwave background polarization. *Astronomy & Astrophysics*, 603:A62, July 2017. arXiv:1611.02577, doi:10.1051/0004-6361/201629992. (cited p. 98)

[276] Kyriakos Vattis, Savvas M. Koushiappas, and Abraham Loeb. Dark matter decaying in the late Universe can relieve the H_0 tension. *Physical Review D*, 99(12):121302, Jun 2019. arXiv:1903.06220, doi:10.1103/PhysRevD.99.121302. (cited p. 10)

[277] Clara Vergès, Josquin Errard, and Radek Stompor. Framework for analysis of next generation, polarised CMB data sets in the presence of galactic foregrounds and systematic effects. *arXiv e-prints*, page arXiv:2009.07814, September 2020. arXiv:2009.07814. (cited p. 152)

[278] Clara Vergès, Josquin Errard, and Radek Stompor. Forecasting the performance of next generation of cmb polarisation experiments in the presence of galactic foregrounds and selected systematic effects. 2020, in prep. (not cited)

[279] R. Vio and P. Andreani. Internal Linear Combination method for the separation of CMB from Galactic foregrounds in the harmonic domain. *arXiv e-prints*, November 2008. arXiv:0811.4277. (cited p. 104)

[280] J. T. Ward, D. Alonso, J. Errard, M. J. Devlin, and M. Hasselfield. The Effects of Bandpass Variations on Foreground Removal Forecasts for Future CMB Experiments. *The Astrophysical Journal*, 861(2):82, July 2018. arXiv:1803.07630, doi:10.3847/1538-4357/aac71f. (cited p. 199)

[281] David H. Weinberg, Romeel Davé, Neal Katz, and Juna A. Kollmeier. The Lyman-α Forest as a Cosmological Tool. In Stephen H. Holt and Christopher S. Reynolds, editors, *The Emergence of Cosmic Structure*, volume 666 of *American Institute of Physics Conference Series*, pages 157–169, May 2003. arXiv:astro-ph/0301186, doi:10.1063/1.1581786. (cited p. 82)

[282] J. M. Weisberg, J. H. Taylor, and L. A. Fowler. Gravitational waves from an orbiting pulsar. *Scientific American*, 245:74–82, October 1981. doi:10.1038/scientificamerican1081-74. (cited p. 88)

[283] Kenneth C. Wong, Sherry H. Suyu, Geoff C. F. Chen, Cristian E. Rusu, Martin Millon, Dominique Sluse, Vivien Bonvin, Christopher D. Fassnacht, Stefan Taubenberger, Matthew W. Auger, Simon Birrer, James H. H. Chan, Frederic Courbin, Stefan Hilbert, Olga Tihhonova, Tommaso Treu, Adriano Agnello, Xuheng Ding, Inh Jee, Eiichiro Komatsu, Anowar J. Shajib, Alessandro Sonnenfeld, Roger D. Bland ford, Leon V. E. Koopmans, Philip J. Marshall, and Georges Meylan. H0LiCOW XIII. A 2.4% measurement of H_0 from lensed quasars: 5.3σ tension between early and late-Universe probes. *arXiv e-prints*, Jul 2019. arXiv:1907.04869. (cited p. 9)

[284] S. A. Wouthuysen. On the excitation mechanism of the 21-cm (radio-frequency) interstellar hydrogen emission line. *Astronomical Journal*, 57:31–32, January 1952. doi:10.1086/106661. (cited p. 83)

[285] Ya. B. Zel'dovich and I. D. Novikov. The Hypothesis of Cores Retarded during Expansion and the Hot Cosmological Model. *Astronomicheskii Zhurnal*, 43:758, Jan 1966. (cited p. 12)

[286] Yaa B. Zeldovich. A hypothesis, unifying the structure and the entropy of the Universe. *Monthly Notices of the Royal Astronomical Society*, 160:1P, January 1972. doi:10.1093/mnras/160.1.1P. (cited p. 37)

[287] Andrea Zonca, Leo Singer, Daniel Lenz, Martin Reinecke, Cyrille Rosset, Eric Hivon, and Krzysztof Gorski. healpy: equal area pixelization and spherical harmonics transforms for data on the sphere in Python. *The Journal of Open Source Software*, 4(35):1298, March 2019. doi:10.21105/joss.01298. (cited p. 183)

[288] F. Zwicky. On the Masses of Nebulae and of Clusters of Nebulae. *The Astrophysical Journal*, 86:217, Oct 1937. doi:10.1086/143864. (cited p. 12)